Defining the Role of Aerobic Respiration in Uropathogenic *Escherichia coli* Physiology and Pathogenesis

By

Connor James Beebout

Dissertation

Submitted to the Faculty of the

Graduate School of Vanderbilt University

in partial fulfillment of the requirements

for the degree of

DOCTOR OF PHILOSOPHY

in

Microbe-Host Interactions

May 13, 2022

Nashville, Tennessee

Approved:

James E. Cassat, M.D., Ph.D.

David M. Aronoff, M.D.

Eric P. Skaar, Ph.D.

Gary A. Sulikowski, Ph.D.

Maria Hadjifrangiskou, Ph.D.

ACKNOWLEDGMENTS

This work would not be possible without the unyielding support of countless friends, family, colleagues, mentors, and institutions. First and foremost, I thank my mentor, Maria Hadjifrangiskou, for her steady support and guidance over the years that has facilitated my development into the scientist I am today, as well as all past and present members of our lab who have graciously provided their time, ideas, and advice throughout my graduate career. I thank the members of my thesis committee who helped steer me throughout my studies and offered insightful comments to help me improve my experiments, my critical thinking skills, and my ability to present and discuss my work. I thank Vanderbilt University and the Vanderbilt Medical Scientist Training Program for taking a chance on me, as well as the many faculty, staff, and fellow trainees in my department and the School of Medicine who have provided a collegial, collaborative, and engaging community. I thank Vanderbilt University, the National Institutes of Health, and the Ruth L. Kirschstein National Research Service Award for funding my work. And, of course, I thank my family and friends who have served an essential role during this time by keeping me grounded, pretending to care about *Escherichia coli*, and by selflessly supporting my decision to move across the country to pursue my academic dreams. I would particularly like to thank my parents, Karin and John, my stepfather, Rob, and my brother, Stephen, for providing a stable and supportive upbringing and for raising me to possess the ambition to pursue lofty goals as well as the pragmatism required to achieve them. Above all, I thank my wife, Alexandra, for her patience, dedication, and conversation. She has been a true partner for many years, and someone I cannot imagine life without.

TABLE OF CONTENTS

Page

ACKNOWLEDGMENTS…… iii

LIST OF TABLES…….. vii

LIST OF FIGURES……... viii

LIST OF ABBREVIATIONS AND SYMBOLS…… xi

Chapter

1. Introduction……..... 1

Overview…….. 1

Urinary tract infections……... 3

Uropathogenic *Escherichia coli*…… 6

UPEC pathogenic cycle…… 9

UPEC metabolism and pathogenesis are inextricably linked…… 11

Structure and function of the *Escherichia coli* electron transport chain…… 12

Outlook…….. 15

2. Respiratory Heterogeneity Shapes Biofilm Formation and Host Colonization in Uropathogenic *Escherichia coli*..…….. 16

Abstract…… 16

Introduction……... 17

Results……... 18

Discussion…… 38

Materials and Methods…… 40

Acknowledgments……..... 46

3. Subversion of Mitochondrial Metabolism Supports Intracellular Bacterial Pathogenesis During Urinary Tract Infection…….. 47

Abstract……..... 47

Introduction…… 47

Results……... 49

Discussion……. 65

Materials and Methods…… 68

Acknowledgments……..... 80

4. Cytochrome *bd* Promotes Biofilm Antibiotic Tolerance by Regulating Accumulation of Noxious Chemicals……... 81

Abstract……..... 81

Introduction……..... 82

Results…….. 84

Discussion…….. 103

Materials and Methods…….. 105

Acknowledgments……... 112

5. Conclusions and Future Directions…… 113

Conclusions…… 113

Future Directions…… 114

Appendix…….. 134

A. Normalized transcript counts of intracellularly infected urothelial cells. …… 134

B. Differential gene expression during intracellular infection of urothelial cells. ……..... 142

C. Biofilm mass spectrometry data…….. 148

REFERENCES…… 149

LIST OF TABLES

Table **Page**

Chapter 2: Respiratory Heterogeneity Shapes Biofilm Formation and Host Colonization in Uropathogenic *Escherichia coli*

1. Primers and probes used in Chapter 2……..... 40

Chapter 3: Subversion of Mitochondrial Metabolism Supports Intracellular Bacterial Pathogenesis During Urinary Tract Infection

2. Bacterial strains and plasmids used in Chapter 3…… 68
3. Primers and probes used in Chapter 3…… 69

Chapter 4: Cytochrome *bd* Promotes Biofilm Antibiotic Tolerance by Regulating Accumulation of Noxious Chemicals

4. Results of disk diffusion assays……..... 90
5. Primers used in Chapter 4……106

LIST OF FIGURES

Figure **Page**

Chapter 1: Introduction

1. *Escherichia coli* phylogenetic tree…… 8

Chapter 2: Respiratory Heterogeneity Shapes Biofilm Formation and Host Colonization in Uropathogenic *Escherichia coli*

2. Lateral expression of respiratory complexes in *Escherichia coli* biofilms…… 21
3. Expression of respiratory complexes compared to *gyrB*…… 22
4. Expression of respiratory oxidases as a function of the oxygen gradient……..... 23
5. PNA-FISH on respiratory oxidase deletion mutants……..... 23
6. Localization of *appC* transcript in biofilm cryosections…… 24
7. Localization of respiratory oxidase transcripts in biofilm wrinkles…… 25
8. Cytochrome *bd* organizes biofilm architecture and extracellular matrix production……... 27
9. Temporal development of colony biofilms by UTI89 and respiratory oxidase mutants…….. 28
10. Extrachromosomal complementation of Δ*cydAB* rescues biofilm defects…… 28
11. Analysis of Δ*appBC*Δ*cyoAB*::*kanR* colony biofilms…….. 29
12. Cytochrome *bd* provides nitrosative stress resistance…… 32
13. Respiratory heterogeneity provides a fitness advantage during urinary tract infection……..... 35
14. Ambient oxygen concentration influences respiratory oxidase transcript abundance…… 36
15. Expression of respiratory oxidases as a function of oxygen tension……..... 37

Chapter 3: Subversion of Mitochondrial Metabolism Supports Intracellular Bacterial Pathogenesis During Urinary Tract Infection

16. Cytochrome *bd* supports intracellular bacterial replication during bladder infection……..... 50
17. Deletion of cytochrome *bd* does not influence type 1 pilus production……. 51
18. Cytochrome *bd* does not impact adherence or invasion of urothelial cells…….. 51
19. Biochemical dissection of cytochrome *bd* reveals niche dependent contributions to bladder pathogenesis…….…… 54
20. Loss of cytochrome *bd* does not impair flagellar biosynthesis……... 55
21. UPEC uses aerobic respiration during intracellular infection of urothelial cells……..... 57
22. UPEC is not sensitive to rotenone or antimycin A…… 58
23. Expression of respiratory oxidases in intracellular bacterial populations……. 58
24. Intracellular bacterial infection enhances mitochondrial network fusion……..... 60
25. Intracellular infection of urothelial cells induces a shift toward aerobic glycolysis…….. 61
26. Intracellular infection modulates urothelial cell metabolism and immune signaling…..... 62
27. Shifts in urothelial cell metabolism are partially dependent on cytochrome *bd*……... 63
28. Reprogramming of host metabolism modulates urothelial cell survival during intracellular infection.....…. 64
29. Flow cytometry gating strategy…… 65
30. Proposed model……. 66

Chapter 4: Cytochrome *bd* Promotes Biofilm Antibiotic Tolerance by Regulating Accumulation of Noxious Chemicals

31. Loss of cytochrome *bd* increases biofilm antibiotic sensitivity……... 86
32. Cytochrome *bd* has minimal effect on planktonic antibiotic susceptibility…… 90
33. Cytochrome *bd* does not affect the rate of antibiotic-induced cell death in planktonic cells…. 93

34. Outer membrane charge is unaffected in Δ*cydAB* biofilm cells……..... 94

35. Cytochrome *bd* deficient biofilm cells have elevated uptake of noxious chemicals…… 96

36. Loss of cytochrome *bd* impairs efflux by diminishing respiratory flux……...… 99

37. AcrAB inactivation has minor effects on biofilm development……..... 101

38. Complementation restores TTC reduction in Δ*cydAB*……...… 102

39. Loss of cytochrome *bd* does not impair ATP generation…….. 103

Chapter 5: Conclusions and Future Directions

40. Inhibition of cytochrome *bd* potentiates antibiotics in UPEC colony biofilms……...… 119

41. Loss of cytochrome *bd* disrupts extracellular matrix organization……..……... 121

42. MALDI-IMS analysis of UPEC biofilms reveals spatial dysregulation of peptide species….. 122

43. Cytochrome *bd* may regulate σ^S abundance by modulating ArcB activity……..…... 124

44. Loss of cytochrome *bd* reduces cyclic di-GMP accumulation in biofilms……... 125

45. Cytochrome *bd* influences the spatial accumulation of cyclic di-GMP in biofilms……..... 126

46. Cytochrome *bd* is necessary but not sufficient for bacterial persistence in the bladder…..… 128

47. Proposed cross-feeding interactions between oxic and anoxic biofilm regions…… 129

48. Loss of cytochrome *bd* eliminates flagellar motility…… 131

LIST OF ABBREVIATIONS AND SYMBOLS

Δ	Deletion
ANOVA	Analysis of Variance
ATP	Adenosine Triphosphate
BSA	Bovine Serum Albumin
CCCP	Carbonyl Cyanide *m*-Chlorophenyl Hydrazone
cDNA	Complementary DNA
CFU	Colony Forming Unit
CLSM	Confocal Laser Scanning Microscopy
CLSI	Clinical & Laboratory Standards Institute
Cryo-EM	Cryogenic Electron Microscopy
C_T	Cycle Threshold
DAPI	4',6'-diamido-2-phenylindole
DMOG	Dimethyloxalylglycine
DMSO	Dimethyl Sulfoxide
DNA	Deoxyribonucleic Acid
DTT	Dithiothreitol
E. coli	*Escherichia Coli*
ECAR	Extracellular Acidification Rate
EDTA	Ethylenediaminetetraacetic Acid
EHEC	Enterohemorrhagic *Escherichia coli*
EPEC	Enteropathogenic *Escherichia coli*
EtBr	Ethidium Bromide
$FADH_2$	Flavin Adenine Dinucleotide
FCCP	Carbonyl Cyanide-*p*-trifluromethoxyphenylhydrazone
FDA	Food and Drug Administration
FSC	Forward Scatter
GFP	Green Fluorescent Protein
GSEA	Gene Set Enrichment Analysis
HRP	Horseradish Peroxidase
h.p.i.	Hours Post-Infection
IACUC	Institutional Animal Care and Use Committee
IBC	Intracellular Bacterial Community
K_D	Dissociation Constant
LB	Lysogeny Broth
LC-MS/MS	Liquid Chromatography Tandem Mass Spectrometry
MALDI-IMS	Matrix-Assisted Laser Desorption/Ionization Imaging Mass Spectrometry
MATE	Multidrug And Toxin Extrusion
Mb	Megabase
MFS	Major Facilitator Superfamily
MIC	Minimum Inhibitory Concentration
MLST	Multi-Locus Sequence Typing
MOPS	3-(*N*-morpholino)propanesulfonic acid
NADH	Nicotinamide Adenine Dinucleotide
NIH	National Institutes of Health
NMEC	Neonatal Meningitis *Escherichia coli*
NMR	Nuclear Magnetic Resonance

NO	Nitric Oxide
NSF	National Science Foundation
OCR	Oxygen Consumption Rate
OD_{600}	Optical Density at 600 nm
ori:ter	Origin of Replication to Terminus Ratio
PAGE	Polyacrylamide Gel Electrophoresis
PBS	Phosphate Buffered Saline
PCR	Polymerase Chain Reaction
PDB	Protein Data Bank
pEtN	Phosphoethanolamine
PMSF	Phenylmethylsulfonyl fluoride
PNA-FISH	Peptide-Nucleic Acid Fluorescence *in situ* Hybridization
PFA	Paraformaldehyde
PVC	Polyvinyl Chloride
REU	Rosetta Energy Units
RFU	Relative Fluorescence Units
RMSD	Root Mean Square Deviation
RNA	Ribonucleic Acid
RND	Resistance-Nodulation-Division
rRNA	Ribosomal RNA
RT-qPCR	Reverse Transcription Quantitative PCR
SD	Standard Deviation
SDS	Sodium Dodecyl Sulfate
SEM	Standard Error of the Mean
SSC	Side Scatter
TBST	Tris Buffered Saline Tween 20
TCA	Tricarboxylic Acid Cycle
TMAO	Trimethylamine Oxide
TTC	Triphenyl Tetrazolium Chloride
UPEC	Uropathogenic *Escherichia Coli*
UQ	Ubiquinone
UQH_2	Ubiquinol
YESCA	Yeast Extract-Casamino Acids

CHAPTER 1

Introduction

Denamur E, Clermont O, Bonacorsi S, and Gordon D. The population genetics of pathogenic *Escherichia coli*. Nature Reviews Microbiology 2021. PMID: 32826992.

OVERVIEW

Host-microbial symbioses are complex, co-evolved interactions that exert major influence over human health and disease (1). Given the incredible diversity of microbial life, human-microbial interactions are themselves highly variable and include commensal, mutualistic, and parasitic interactions (1). Until recent decades, infectious diseases have represented the greatest single threat to human health, and they remain among the most common causes of human morbidity and mortality (2). As such, research into microbe-host symbioses has been historically skewed toward focusing on parasitic interactions between humans and pathogens. Through Koch's postulates – the principle that a parasite is causal for a given disease if it is found in all diseased organisms, is not found in healthy organisms, and can cause disease upon introduction to a previously healthy organisms (3-5) – we have successfully identified the causal agent in hundreds of infectious diseases. Furthermore, through the molecular adaptation of Koch's postulates – the principle that a gene product is causal for a given disease if it is found in all disease-causing parasites, that inactivation of the gene attenuates virulence, and that restoration of the gene restores virulence (3-5) – researchers have identified the molecular mediators employed by many parasites to cause disease. These general approaches have served as the conceptual underpinnings of the field of microbial pathogenesis for decades and have dramatically

improved human health both by allowing physicians to precisely tailor treatment to target particular pathogens and by allowing researchers to develop new therapeutic and vaccine approaches to inhibit microbial pathogenesis (2).

Despite the undeniable success of this conceptual framework in describing the pathogenesis of many clinically important pathogens, it fails to adequately describe many others. In their classical formulation, Koch's postulates overlook organisms that cannot be cultured or only cause disease under certain circumstances, and they also fail to apply to the interconnected networks and ecological interactions underpinning host-microbiota interactions (1, 6-9). Furthermore, while the molecular formulation of Koch's postulates neatly describes the pathogenesis of organisms that use a discrete set of virulence factors to mediate disease (*e.g. Clostridioides difficile*, enterohemorrhagic *Escherichia coli*, *Bacillus anthracis*), the same formulation breaks down when confronted with organisms that lack a core set of virulence determinants. Accordingly, new conceptual frameworks are emerging that broaden our understanding of host-microbial interactions and provide a more complete understanding of the range of human-microbial symbioses that influence health and disease.

In this work, I investigate the pathogenesis of uropathogenic *E. coli* (UPEC). UPEC is the primary causative agent in urinary tract infections, making it one of the most successful bacterial pathogens worldwide (10-12). Rather than deploying a dedicated suite of virulence determinants to mediate disease, UPEC repurposes a wide array of survival and fitness factors such as flagella, iron acquisition systems, and core metabolic pathways that enable it to adapt to the urinary tract and inflict damage on the host (13-17). Instead of a linear gene-protein-disease pathway, during urinary tract infection a confluence of microbial and host factors contribute in a multifactorial manner to determining the ultimate outcome of this host-microbial interaction, with outcomes ranging from asymptomatic colonization to life-threatening infection. By broadening our conceptual frameworks and recognizing that UPEC pathogenesis is integrally connected with its metabolic state, this work expands our understanding of the interconnections between the physiology and metabolism of both host and pathogen while

identifying new targets for the development of therapeutic strategies that aim to treat bacterial infections not by killing pathogens, but by reprogramming bacterial metabolism to limit their virulent potential.

URINARY TRACT INFECTIONS

Urinary tract infections are among the most common human bacterial infections, afflicting an estimated 150 million people per year (12, 14). The prevalence of urinary tract infection is variable between sexes, with greater than 80 percent of cases occurring in females (17, 18). At least half of women will have a urinary tract infection during their lifetime, with approximately one quarter of those infected experiencing recurrent infection within six months (10, 12, 19, 20). This sexual dimorphism is believed to result from a combination of anatomic and behavioral factors that increase the likelihood of fecal flora being exposed to the bladder in females (*e.g.* short urethral-anal distance, incontinence, sexual activity, vaginal dysbiosis) (11, 20). Although nearly all cases of cystitis in young cohorts (less than 50 years old) occur in females, older males and females (greater than 50 years old) have similar rates of infection (20). The increased incidence of infection in older males is caused by increased rates of functional and anatomic abnormalities in this population, most commonly due to increased urinary retention resulting from prostatic hypertrophy as well as higher rates of catheterization (20).

Urinary tract infections manifest across a spectrum of clinical presentations, with patients most commonly experiencing acute symptomatic bladder infection that resolves with outpatient antibiotic therapy (20). Uncomplicated cystitis occurs in otherwise healthy young females (peak incidence between the ages of 15 to 34), and patients typically present with urinary frequency, urgency, and dysuria (10, 11, 18, 21). Complicating matters, many uropathogens can asymptomatically colonize the bladder leading to a condition called asymptomatic bacteriuria. Asymptomatic bacteriuria is observed in up to five percent of pre-menopausal and up to 50 percent of post-menopausal females (20, 22). Because asymptomatic bacteriuria is distinguished from cystitis solely based on the presence of subjective symptoms, it is frequently mistaken for cystitis and treated accordingly. Despite the conflation of these two conditions, asymptomatic bacteriuria is a benign condition that is not believed to precede

symptomatic urinary tract infection. As such, screening and treatment of asymptomatic bacteriuria is contraindicated except in specific circumstances where the risk of complications are increased (*i.e.* pregnancy and preceding urologic procedures) (22, 23).

In approximately one to five percent of cystitis cases, the causative uropathogen gains access to the kidney where it establishes a symptomatic infection called pyelonephritis (11, 18, 24). While pyelonephritis canonically results from urinary reflux and flagellum-dependent bacterial ascension from the bladder to the kidneys (25), in rare cases, pyelonephritis can occur in patients with bacteremia as a result of hematogenous spread (20). Pyelonephritis presents with many of the same symptoms as cystitis, but patients will also typically have fever and costovertebral angle tenderness (18, 20). Nausea, vomiting, rigors, and flank pain occur frequently in more severe pyelonephritis cases (18, 20). Although most cases resolve with antibiotic therapy, pyelonephritis is associated with elevated risk of severe outcomes including bacteremia, acute kidney injury, renal and perinephric abscess formation, renal scarring, urinary tract obstruction, and emphysematous infection (20, 24). Accordingly, pyelonephritis often requires inpatient monitoring and intravenous antibiotic therapy (20, 24).

Approximately 25% of pyelonephritis cases have coincident bacteremia (20). Although this bacteremia is generally transient, urosepsis, the most severe manifestation of urinary tract infection, can occur as the result of a dysregulated immune response to bacteria in the bloodstream that leads to hyperactivation of the immune system and uncontrolled cytokine release (26, 27). This hyperactivation of the immune system can cause patients to experience septic shock, in which profound cytokine-induced hypotension can result in multi-organ failure and death (26, 27). Urosepsis occurs most commonly among older patients, and the risk of urosepsis is increased by various factors and comorbidities including urinary obstruction, catherization, urogenital procedures, and immunosuppression (28).

Although urinary tract infections can generally be diagnosed clinically, urine dipstick, urinalysis, and urine culture are frequently included as part of a diagnostic work up to confirm infection and identify the causative uropathogen. Urine culture – performed by aerobically culturing urine on MacConkey and

blood agar and enumerating the number of bacterial colony-forming units (CFU) per mL urine – is the gold standard test for diagnosing urinary tract infection, with the presence of at least 10^5 CFU/mL urine in a symptomatic patient being considered diagnostic for cystitis. However, detecting as few as 10 CFU/mL urine has been shown to be highly predictive of disease in symptomatic patients (positive predictive value 92 percent) (20, 29). In addition to quantifying bacteriuria, subsequent antimicrobial susceptibility testing performed on the cultured bacteria allows antimicrobial treatment to be tailored to the identified uropathogen. While urine culture is the gold standard diagnostic test, it takes at least 24 hours to receive a result. As such, in practice urine dipstick and microscopic urinalysis are frequently used as the primary point-of-care diagnostic tests for suspected urinary tract infection (18, 20). A positive urine dipstick test shows elevated leukocyte esterase (derived from phagocytic influx into the infected bladder) and elevated nitrite (derived from the anaerobic conversion of nitrate to nitrite by *E. coli* and other Enterobacteriaceae). Consistent with these findings, microscopic urinalysis commonly reveals pyuria and bacteriuria in cases of cystitis. Although these tests are the most frequently used, they are often overinterpreted and lead to excessive treatment. Accordingly, expert statements and society guidelines recommend using urine dipstick and urinalysis solely to confirm clinically suspected urinary tract infection, and not as a standalone diagnostic test or as a part of a shotgun workup of a patient with an unexplained febrile illness (18, 20, 22).

Urinary tract infections are among the most common indications for antibiotic prescriptions in adult populations (21). Because most urinary tract infections and an overwhelming majority of uncomplicated urinary tract infections are caused by *E. coli*, treatment of cystitis is typically empirical (10-12, 20, 21). First-line antibiotics for uncomplicated cystitis include nitrofurantoin, trimethoprim-sulfamethoxazole, and fosfomycin (21). Fluoroquinolones have historically been a common treatment for cystitis but have fallen out of favor in recent years due to increasing rates of resistance and the recognition that these antibiotics ought to be reserved for other types of more severe infections (21). Pyelonephritis is typically treated with fluoroquinolones, cephalosporins, aminoglycosides, or trimethoprim-sulfamethoxazole (21). Oral antibiotics are appropriate for outpatient treatment of

pyelonephritis; however, patients requiring hospitalization should be treated with intravenous antibiotics (21). Because urinary tract infections are highly prevalent and typically treated empirically with broad-spectrum antibiotics, externalities such as damage to the microbiota and antibiotic resistance are significant concerns. Furthermore, due to the high and ever-changing rates of antibiotic resistance, treatment recommendations should be interpreted with caution, and treatment strategies should be tailored according to local prevalence of antibiotic resistant pathogens and the results of antimicrobial susceptibility testing, when available (20, 21).

UROPATHOGENIC *ESCHERICHIA COLI*

Uropathogenic *E. coli* (UPEC), the primary cause of urinary tract infections, is responsible for approximately 80 percent of urinary tract infections, making it one of the most successful human bacterial pathogens worldwide (10, 12, 21). *E. coli* is a Gram-negative, facultatively anaerobic γ-Proteobacteria in the family Enterobacteriaceae. As a result of its permissive culture conditions, fast growth rate, amenability to genetic alterations, and a constellation of historical contingencies, *E. coli* has served as a workhorse of molecular biology for nearly 100 years (30-32). Accordingly, *E. coli* is among the most well-characterized organisms on Earth. Many of the fundamental advances of molecular biology occurred using *E. coli*, including the discoveries of the essential processes and machinery required for life, the basic paradigms of genetic regulation, and the foundations of recombinant DNA technologies (30-32).

Although most research into *E. coli* has occurred using K-12 *E. coli* – a lab-adapted model strain – the species *E. coli* is remarkably diverse (**Figure 1**) (13, 33-35). The genome of *E. coli* ranges between 4.2 – 6.0 megabases (Mb) and encodes 3,900 – 5,800 genes (13, 33, 35). Only about 2,000 of these genes are conserved across the species *E. coli* (*i.e.* the core genome), with the remainder of the genome being comprised of non-conserved genes derived from a pan-genome containing at least 15,000 unique genes (13, 33-36). Given the vast diversity of *E. coli* genomes and high rates of horizontal gene transfer, genetic relationships within the species *E. coli* are often described through

multi-locus sequence typing (MLST). These approaches sort *E. coli* into nine core phylogenetic groups (A, B1, B2, C, D, E, F, G, H), five cryptic clades (Clades I – V) containing strains that are phenotypically indistinguishable but phylogenetically divergent from typical *E. coli* strains, and the erstwhile distinct genus *Shigella* (**Figure 1**) (13, 33, 35, 37). In addition to categorizing based on phylogenetic relationships, *E. coli* is split into commensal and pathogenic strains, with the pathogenic strains further divided into intestinal and extra-intestinal pathogens (**Figure 1**). The pathogenic strains of *E. coli* are described according to the type of disease they cause (35). These distinctions, termed pathotypes, are either subtypes of intestinal pathogenic *E. coli* – such as enteropathogenic *E. coli* (EPEC) and enterohemorrhagic *E. coli* (EHEC) – or subtypes of extra-intestinal pathogenic *E. coli* – such as uropathogenic *E. coli* (UPEC) and neonatal meningitis *E. coli* (NMEC) (35). While these designations largely track along genetic relationships (for example, UPEC is primarily found in the B2 and D phylogroups), pathotypes are widely spread throughout the phylogenetic tree, indicative of the remarkable degree of horizontal gene transfer has occurred across the species (**Figure 1**) (13, 33-35).

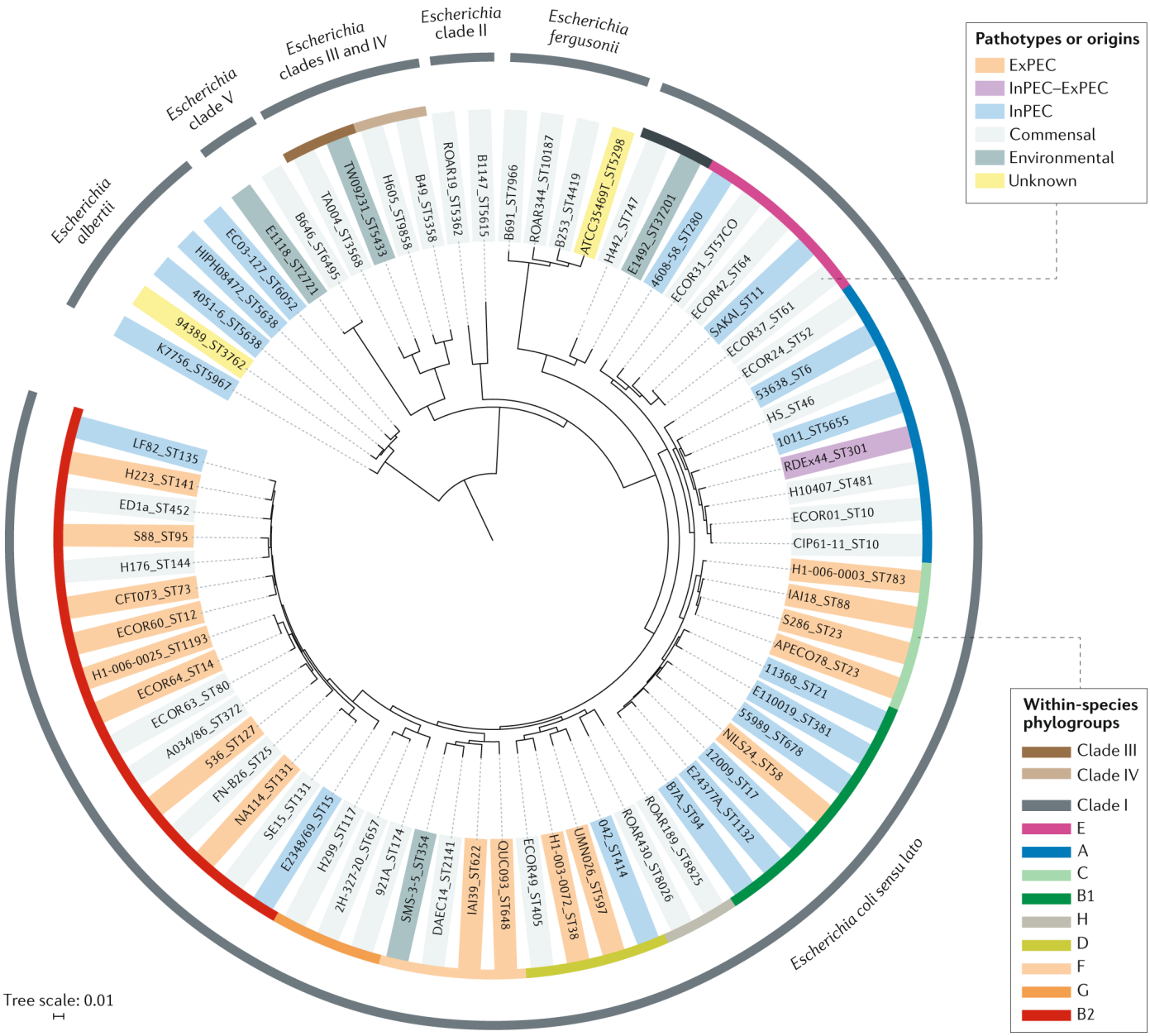

Figure 1: *Escherichia coli* phylogenetic tree. Phylogenetic tree of *E.* coli constructed by comparing the sequence of 1,302 core genome genes across 72 representative *Escherichia* strains rooted on *Escherichia albertii*. Strains are color-coded according to their phylogroup and pathotype. ExPEC, extraintestinal pathogenic *E. coli*; InPEC, intestinal pathogenic *E. coli*. This figure was reproduced from Figure 1 of the following article with permission of the publisher and copyright holder: Denamur *et al*. Nature Reviews Microbiology 2021. © Springer Nature Limited 2020 (35).

Unlike many other clinically important pathogens in which a single strain can cause distinct types of disease in diverse host niches (*e.g. Pseudomonas aeruginosa* (38) and *Staphylococcus aureus* (39)), *E. coli* pathogenesis is much more restricted, and a given strain or pathotype is only able to cause one type of disease in one niche. Intestinal pathogens are unable to cause disease in the urinary tract, for example, and extra-intestinal pathogens behave as commensals in the gut. Although some

pathotypes are genetically defined by carriage of genetic elements and virulence factors, others are purely phenomenological. For example, EHEC are defined by the carriage of a Shiga toxin encoding prophage that is the primary mediator of disease, whereas a strain is deemed UPEC if it was isolated from a patient with urinary tract infection irrespective of any genetic or phenotypic factor (13). As such, identifying and predicting the pathogenic potential of EHEC is relatively straightforward, but we lack a clear set of genetic or phenotypic features that define a strain as UPEC, and no set of factors can predict whether a given strain can cause disease in the urinary tract (13, 14, 16, 17). Accordingly, only a subset of *E. coli* pathotypes (*e.g.* EHEC) fulfill the classical and molecular Koch's postulates, while others (*e.g.* UPEC) cannot be neatly described by these frameworks. Consequently, there is an increasing recognition that the pathogenesis of UPEC (as well as many other bacteria) cannot simply be described by listing virulence factors and genetic elements. Instead, UPEC pathogenesis can only be described through by integrating bacterial virulence, metabolic, structural, and regulatory factors into a conceptual model that considers the dynamic nature of bacterial physiology in the context of an exceedingly complex host environment.

UPEC PATHOGENIC CYCLE

Like most strains of *E. coli*, UPEC primarily resides in the mammalian gut. In this niche, UPEC behaves as a stably colonizing commensal bacterium with minimal impact on host physiology or disease (13, 35, 40-42). Upon ascension to the bladder, however, UPEC can rapidly establish symptomatic infection. UPEC is thought to gain access to the urinary tract by ascending the urethra after periurethral contamination with fecal flora, but it can also be introduced into the bladder by instrumentation (*e.g.* catheters and surgical intervention) or activated from latent reservoirs within the bladder itself (11, 12, 20, 25, 43, 44). Upon entering the bladder UPEC uses type 1 pili, polymeric adhesive fibers assembled by the chaperone usher pathway, to adhere to mannosylated proteins on the bladder surface such as uroplakin Ia and $\alpha 3\beta 1$ integrins (45-52). Adherence to the bladder epithelium protects bacteria against shear stress imposed by micturition, and promotes the aggregation

of bacteria into extracellular, surface-associated multicellular bacterial communities termed biofilms (53-56). By forming biofilms in the urinary tract, UPEC establishes a stable niche, and, by secreting an extracellular matrix, physically protects bacteria from a wide array of external stressors, including antibiotics, complement, and phagocytes (53, 55, 57-59). Additionally, gradients of nutrients, waste, and signaling molecules form in biofilms as they expand due to the metabolic activity of biofilm residents in combination with physical limitations on diffusion (60-63). Consequently, bacteria in different regions of the biofilm are exposed to variable environmental conditions which causes them to differentiate into phenotypically distinct subpopulations. Phenotypic differentiation within biofilms greatly enhances biofilm resilience and stress tolerance by expanding the metabolic diversity of resident bacteria (60, 61, 63, 64). As a result of their remarkable stress tolerance, biofilms are a key survival strategy adopted by UPEC in the urinary tract (11, 53).

In addition to providing bacteria with a foothold in the bladder, adherence by type 1 pili facilitates the internalization of UPEC into urothelial cells (44, 47, 48, 65, 66). Upon binding to the urothelial cell surface, UPEC activates focal adhesin kinase, the Rho family GTPase Rac1, PI3K, adenylate cyclase, and other eukaryotic signaling pathways which collectively mediate a rearrangement of the actin network that facilitates bacterial internalization into urothelial cells through a zipper-like mechanism (46, 47, 67-70). Internalized UPEC are found in LAMP1 positive endocytic vesicles, from which they escape into the urothelial cell cytosol through as yet undefined mechanisms (44, 47, 67-69). During this time, the host cell limits bacterial invasion through a non-lytic toll-like receptor (TLR) 4-dependent expulsion mechanism (71-73). In addition to expelling bacteria, some urothelial cells will exfoliate and slough off the bladder surface as part of a suicide mechanism that limits bacterial proliferation (48, 74). Although exfoliation antagonizes bacterial growth in the bladder, it exposes underlying tissue layers for further rounds of infection and enhances the formation of persistent bacterial reservoirs in the bladder (43, 74, 75).

Once in the cytosol, UPEC rapidly expand to form large biofilm like cytoplasmic aggregates called intracellular bacterial communities (IBCs) (65, 76). IBCs undergo rapid clonal expansion within

bladder cells, forming communities containing thousands of bacteria (53, 77, 78). After approximately 12-16 hours of expansion, a subset of bacteria within the IBC form long filaments that escape from urothelial cells where they can reattach to the bladder surface and infect neighboring cells (11, 12, 53, 77, 79, 80). Through this transient intracellular lifecycle, UPEC gains access to a nutrient rich niche where it can rapidly replicate, protected from phagocytes and the toxic effects of immunity and antibiotics.

UPEC METABOLISM AND PATHOGENESIS ARE INEXTRICABLY LINKED

Although type 1 pili and other classical virulence factors are required for the completion of the UPEC infectious cycle in the bladder, despite our best attempts we are currently unable to distinguish pathogenic from non-pathogenic strains on a genetic or phenotypic level (14, 17). Many of the virulence factors present in UPEC are functionally redundant, not present in all pathogenic strains, and shared with non-pathogenic strains (11, 12, 14). Furthermore, these factors are not disease specific, but instead encode gene products such as flagella, iron acquisition systems, global regulatory elements, and core metabolic factors necessary for adaptation to a wide variety of environments inside and outside the human host (13-17, 81, 82). During its infectious cycle UPEC completely reorganizes its metabolism to adapt to a particular niche, and these metabolic shifts are accompanied by dramatic shifts in behavior, including transitioning from a benign commensal in the gut to a highly successful pathogen in the urinary tract (13-17, 41, 81, 82). Importantly, many of the key regulators of these metabolic shifts are also regulators of UPEC virulence determinants (11, 12, 14, 41, 83). Accordingly, in UPEC, metabolic state cannot be considered as distinct from virulence, but rather shifts in metabolism are coincident and share common cause with shifts in virulence potential. Metabolism is not simply a way for bacteria to obtain energy; metabolism is an integral component of virulence.

During the transition from the gut to the bladder, UPEC undergoes a wholesale metabolic reprogramming. Under healthy conditions the gut is anaerobic and most available nutrients are byproducts of mucin degradation by the microbiota. As such, *E. coli* uses anaerobic, carbohydrate-

based metabolism in this niche and specifically requires glycolysis, the Entner-Douderoff pathway, and sugar alcohol catabolism to support its energetic needs in the gut (41, 84, 85). By contrast, the bladder is hypoxic (dissolved oxygen concentration 4-6%) and most available carbon is in the form of small peptides and amino acids (41, 86). As such, rather than using anaerobic carbohydrate-based metabolism, in the bladder UPEC uses a form of aerobic metabolism in which amino acids are imported and shunted through the aerobic arm of the tricarboxylic acid (TCA) cycle, thereby supporting the energetic needs of UPEC and generating anabolic precursors used to drive gluconeogenesis and the synthesis of macromolecules (15, 41, 83, 87, 88). Consistent with this, transposon mutagenesis studies identified *ubiI* – an enzyme required for synthesis of the aerobic electron carrier ubiquinone – as a major regulator of UPEC biofilm formation and pathogenesis in the bladder (83, 89), and oxygen availability plays a central role in regulating UPEC biofilm formation (54, 90). While these studies revealed the requirement for aerobic respiration during bladder infection, prior to this work it remained unclear precisely how and why UPEC uses aerobic respiration to support its virulence and to colonize distinct niches in the urinary tract.

STRUCTURE AND FUNCTION OF THE *ESCHERICHIA COLI* ELECTRON TRANSPORT CHAIN

E. coli encodes a branched, modular respiratory chain that enables it to adapt its metabolism to a broad set of environmental conditions (91, 92). *E. coli* extracts electrons from a wide array of reduced electron donors (*e.g.* NADH, $FADH_2$, succinate, H_2) and, through the action of one of several dedicated dehydrogenases, transfers these electrons onto a lipid soluble electron carrier (ubiquinone, menaquinone, or demethylmenaquinone) which are differentially involved in aerobic and anaerobic respiration (91-93). This reduced quinol electron carrier then interacts with one of several terminal oxidases and reductases which transfer the electrons onto a terminal electron acceptor (91-93). Each step of this process is coupled to the transfer of protons into the periplasmic space via physical charge separation across the membrane or through direct proton pumping (91, 92). By generating a proton

gradient, the cell creates a source of potential energy that can be used to energize various membrane processes including ATP synthesis, solute transport, and flagellar rotation (92, 94).

As a facultative anaerobe, *E. coli* exhibits a high degree of flexibility in its metabolic and respiratory profile. In addition to using oxygen as an electron acceptor via one of three terminal respiratory oxidases, *E. coli* can grow using fermentation or by performing anaerobic respiration using one of five alternative terminal electron acceptors (nitrate, nitrite, TMAO, DMSO, and fumarate) paired with one of seven terminal reductases (90, 91, 93, 95). Because each electron acceptor has a different midpoint potential, they each have different potential energy yields, with oxygen being the most energetically favorable electron acceptor (92, 93). Consequently, *E. coli* has evolved a robust set of pathways that hierarchically regulate expression of respiratory enzymes according to the energetic state of the cell as well as the availability of preferred electron acceptors (92, 93). Interestingly, *E. coli* does not always structure its electron transport chain to maximize energetic yield; instead, *E. coli* frequently uses less efficient modes of electron transfer to increase metabolic flux, particularly during times of rapid growth (92, 93).

To define the role of aerobic respiration in UPEC physiology and pathogenesis, this work focuses on the terminal respiratory oxidases. By functioning as respiratory quinol:O_2 oxidoreductases that couple the flow of electrons to the reduction of molecular oxygen into water, these complexes catalyze the final step in the aerobic electron transport chain and are essential for aerobic respiration (91, 92). *E. coli* encodes three respiratory oxidases derived from two phylogenetically unrelated families (91, 92, 96). Cytochrome *bo*, a heme copper oxidase, is a true proton pump and as such is a highly energetically efficient enzyme (H^+/e^- = 2). By contrast, the two *bd*-type oxidases, cytochromes *bd* and *bd*$_2$, are not proton pumps and are accordingly less energetically efficient (H^+/e^- = 1) (91, 92, 96). However, the *bd*-type oxidases have a remarkably high oxygen affinity (K_D = 30 nM), which is approximately 1000-fold higher than that of cytochrome *bo* (91, 96, 97). As such, despite lower energetic efficiency, *bd*-type oxidases are efficient oxygen scavengers that allow *E. coli* to use aerobic respiration even under microaerobic conditions (91, 96, 97).

In addition to serving as integral components of the aerobic respiratory chain, the *bd*-type oxidases possess several non-respiratory activities including catalase activity, resistance to respiratory poisons (*e.g.* nitric oxide, carbon monoxide, hydrogen sulfide, and cyanide), and the ability to reversibly sequester and oxidatively degrade the innate immune effector nitric oxide (91, 92, 95, 96, 98-103). As a result, the *bd*-type oxidases are critical for the physiology and pathogenesis of a wide variety of bacteria including *Salmonella enterica*, *Klebsiella pneumoniae*, *Streptococcus agalactiae*, *Brucella abortus*, and *Mycobacterium tuberculosis* (96, 99). Although nearly all studies involving *bd*-type oxidases have occurred using cytochrome *bd*, many structural and biochemical properties are shared between the two *bd*-type oxidases (91, 96, 104-106). The *bd*-type oxidases exhibit a high degree of sequence and structural similarity representative of a shared evolutionary origin (91, 96, 104). Additionally, both *bd*-type oxidases are induced under low oxygen tensions, and, despite some initial controversy, both have been shown to exhibit an identical energetic efficiency (H^+/e^- = 1) (91, 96, 104-106). While recent studies have begun to tease apart differences in the structure, biochemical activity, and functional role of these two oxidases, little is known about the specific role of cytochrome bd_2, and future work will be required to adequately characterize differences in the function and regulation of the *bd*-type oxidases (91, 95, 104, 107, 108).

In this work I investigate the contribution of aerobic respiration to UPEC physiology and pathogenesis in the urinary tract. Through a systematic investigation of the three respiratory oxidases, I identify cytochrome *bd* as a central regulator of UPEC pathogenesis and biofilm formation. Loss of cytochrome *bd* leads to dramatic disruptions to biofilm development (**Chapter 2**), and consequently impairs the ability for UPEC to form robust biofilms capable of withstanding antibiotics and other exogenous threats (**Chapters 2 and 4**). In addition to facilitating the formation of biofilms within the urinary tract and enhancing bacterial resistance to nitric oxide and other innate immune defenses, cytochrome *bd* is also required during infection due to its role in promoting the intracellular replication of UPEC within urothelial cells (**Chapter 3**). Furthermore, by depleting oxygen from the hypoxic urothelial cell cytosol, cytochrome *bd* mediated respiration by intracellular bacteria shifts host cell

metabolism and alters the dynamics of the urothelial cell response to infection (**Chapter 3**). Collectively this work clarifies the role of aerobic respiration during urinary tract infection and defines the multifaceted role of cytochrome *bd* in UPEC physiology and pathogenesis. By revealing the metabolic basis for intracellular bacterial replication and a mechanism by which intracellular bacterial aerobic respiration subverts the host response to infection, this work identifies cytochrome *bd* as a potential drug target and suggests that modulation of bacterial metabolism is a potential therapeutic approach for the treatment of urinary tract infections and other bacterial diseases.

OUTLOOK

In recent years there has been a growing appreciation of the complexities of the host-pathogen interface, and an increasing understanding of the interconnectedness between bacterial metabolism, virulence, and host response to infection. The recognition that bacterial metabolism is more than simply a way for bacteria to obtain energy, and in fact represents an integral component of virulence, has forced a rethinking of our conceptual frameworks and expanded our understanding of microbial pathogenesis. Analogously, the field of immunology is coalescing around the idea that immune cell metabolism and effector function are integrally connected, and oncologists are increasingly recognizing the influence of cancer cell metabolism on treatment successes and failures (109-115). Consequently, there is an active effort to target metabolism as a means of modulating immune cell effector function and augmenting tumor sensitivity to therapy (113, 114, 116, 117). This evolution of our conceptual models collectively represents a paradigm shift in our understand of the role of metabolism in cellular function and dysfunction across the domains of life and suggests the possibility of modulating microbial metabolism as a mechanism for controlling bacterial behavior and limiting virulence in the post-antibiotic era.

CHAPTER 2

Respiratory Heterogeneity Shapes Biofilm Formation and Host Colonization in Uropathogenic *Escherichia coli*

Portions of this chapter have been adapted and reproduced from the following article with permission of the publisher under Creative Commons Attribution 4.0 International (CC BY 4.0) license:

Beebout CJ, Eberly AR, Werby SH, Reasoner SA, Brannon JR, De S, Fitzgerald MJ, Huggins MM, Clayton DB, Cegelski L, and M Hadjifrangiskou. Respiratory heterogeneity shapes biofilm formation and host colonization in uropathogenic *Escherichia coli. mBio* 2019. PMID: 30940709. © 2019 Beebout et al.

ABSTRACT

Escherichia coli encodes a flexible and modular electron transport chain that allows it to colonize a wide variety of environmentally diverse niches. Despite being a facultative anaerobe uropathogenic *E. coli* (UPEC), the leading cause of urinary tract infections, requires aerobic respiration to colonize the urinary tract and to form biofilms – multicellular bacterial communities encased in a self-secreted extracellular matrix. In this study, we aimed to define the role of aerobic respiration in UPEC physiology by characterizing the expression and utilization of respiratory enzymes across niches. Using planktonic, biofilm, and murine infection models, we determine that UPEC heterogeneously expresses respiratory enzymes within and across populations. In biofilms, we determine that two respiratory quinol oxidases – cytochrome *bd* and *bo* – are expressed in spatially distinct subpopulations organized along the biofilm oxygen gradient, and loss of cytochrome *bd* impairs biofilm development by impeding the production and organization of the extracellular matrix. In planktonic populations, UPEC heterogeneously expresses respiratory oxidases between cells, with a subset of cells primarily expressing cytochrome

bd. Despite low abundance of cytochrome *bd* expressing cells in planktonic populations, this subpopulation dominates during urinary tract infection, suggestive of a respiratory bet-hedging mechanism. These results demonstrate UPEC heterogeneously expresses respiratory enzymes across niches and identifies a central role for cytochrome *bd* in UPEC physiology and pathogenesis.

INTRODUCTION

Rather than existing as uniform populations, bacterial cultures, colonies, and biofilms contain phenotypically distinct subpopulations. This intra-strain heterogeneity can be irreversible, arising through the acquisition of mutations, or transient and reversible if it is brought about by stochastic differences in the abundance and activity of regulators in each individual cell or by metabolic adaptation to local environmental conditions. Cell-to-cell heterogeneity oftentimes confers a survival advantage to the population by allowing at least portion of the population to survive in different niches and during sudden changes in environmental conditions.

E. coli is a facultative anaerobe capable of utilizing multiple metabolic pathways to fulfill its energetic requirements. Despite encoding a flexible electron transport chain, previous studies demonstrate that aerobic respiration is required for biofilm formation and bladder colonization by uropathogenic *E. coli (*UPEC), the leading cause of urinary tract infection (41, 54, 83, 87-90). In aerobically respiring *E. coli*, respiratory quinol oxidases comprise essential components of the terminal electron transport chain that couple the flow of electrons to the reduction of molecular oxygen into water (91, 93). *E. coli* encodes two classes of respiratory oxidases with differing oxygen affinities: one low affinity heme copper oxidase, cytochrome *bo* (encoded by the *cyoABCDE* gene cluster), and two high affinity *bd*-type oxidases, cytochromes *bd* (*cydABX*) and bd_2 (*appBCX*) (91, 96). Studies in K-12 *E. coli* indicate that cytochrome *bo* is induced at high (atmospheric, 21%) oxygen tensions, whereas the *bd*-type oxidases are induced at low (hypoxic, <15%) oxygen tensions (91, 97). Due to their high oxygen affinity and resistance to various small molecule inhibitors of respiration, the *bd*-type oxidases are

primarily believed to serve as oxygen scavengers capable of facilitating aerobic respiration under hypoxic conditions such as those encountered during infection (91, 96).

In this work we use planktonic, biofilm, and murine infection models to characterize the expression of respiratory oxidases across niches and determine the contribution of aerobic respiratory complexes to UPEC physiology and pathogenesis. We report that UPEC heterogeneously expresses respiratory operons between and across niches. Through quantitative PCR and *in situ* labelling approaches, we determine that in biofilms this heterogenous expression of respiratory operons occurs within distinct subpopulations that are spatially organized by oxygen availability. This spatial organization of respiration is critical for biofilm development, with the high affinity respiratory oxidase cytochrome *bd* playing an outsized role in regulating extracellular matrix production and community organization. In planktonic populations, we similarly observe heterogenous expression of respiratory operons, with a minority of cells primarily expressing cytochrome *bd* under aerobic conditions. Although planktonic populations robustly express all three aerobic respiratory operons, only loss of cytochrome *bd* impairs UPEC virulence in a well-established murine model of urinary tract infection. *In situ* analysis of gene expression reveals a shift from heterogeneous expression of aerobic respiratory operons in planktonic populations to homogenous expression of cytochrome *bd* in urine-associated populations. These findings suggest that the bladder favors cytochrome *bd* expression and that respiratory heterogeneity in the input pool serves as a potential bet-hedging mechanism to provide a fitness advantage to uropathogenic strains upon introduction to the bladder. Our studies, performed on one of the most common human pathogens and a prolific biofilm producer, reveal the contribution of respiratory heterogeneity to bacterial physiology and unveil a potential avenue for targeting heterogeneity and homogenizing bacterial programming as a therapeutic approach.

RESULTS

Respiratory complexes are heterogeneously expressed in UPEC biofilms

Biofilms are multicellular bacterial communities that are encased in self-secreted extracellular matrix. The biofilm extracellular matrix – composed of exopolysaccharides, proteinaceous fibers, and extracellular DNA – spatially organizes biofilm bacteria and protects biofilm residents from predation, desiccation, assault by antimicrobial agents, and the immune system (53, 57, 61, 62). In addition to providing a physical barrier against external threats, the extracellular matrix serves as a barrier to diffusion which, in conjunction with the metabolic activity of resident bacteria, leads to the establishment of chemical gradients throughout the biofilm community (60, 63). Bacteria at different locales along the gradient respond to the microenvironment differently, and as a result differentiate into distinct and often metabolically cooperative subpopulations (60, 63, 118-120). Previous studies in *Pseudomonas aeruginosa* and *E. coli* indicated that oxygen gradients play a key role in regulating the differential expression of genes involved in biofilm formation and metabolic specialization (54, 121-123). Additionally, we previously determined that oxygen availability spatially organizes protein expression in biofilms, and that biofilm formation is greatly diminished under anaerobic conditions, irrespective of growth medium or the presence of alternative terminal electron acceptors (54, 90). From this, we hypothesized that differences in oxygen availability drive the phenotypic differentiation of biofilm bacteria into differentially respiring subpopulations, and that this phenotypic differentiation contributes to the spatial coordination of extracellular matrix production in biofilms.

To define the expression patterns of respiratory enzymes within biofilms, we first determined the relative abundance of aerobic and anaerobic respiratory transcripts in mature colony biofilms grown on yeast extract casamino acids (YESCA) agar – a commonly used biofilm growth medium that mimics the amino acid rich environment of the bladder (54, 124-126). Under these growth conditions UPEC forms elaborate rugose colony biofilms that quickly establish an oxygen gradient from the surface to the interior of the biofilm (**Figure 2A**) (122). Because previous studies identified differences in extracellular matrix abundance and in the localization of transcriptional regulators at the actively growing leading edge (periphery) and center of the colony (122, 127-129), we extracted RNA from the biofilm center and periphery and used RT-qPCR to quantify steady state transcript of each respiratory

operon encoded by *E. coli* (**Figures 2A and 3**) (91, 93). Although overall transcript abundance was significantly increased in the periphery relative to the center (**Figure 2E**) – consistent with the notion that cells at the periphery are more metabolically active – we observed a similar distribution of transcript at the center of the biofilm and the growing edge (**Figure 2B-D**). Consistent with previous studies demonstrating the importance of aerobic respiration in UPEC biofilms, the majority of detected transcript corresponded to aerobic respiratory components (**Figure 2B-C**). The most abundant transcript was that of *cydA* (**Figures 2B-D and 3**), a gene encoding a subunit of the high affinity respiratory oxidase cytochrome *bd*. The abundance of *cydA* transcript was approximately two-fold higher than the abundance of cytochrome *bo* encoding transcript *cyoA*, the second most abundance respiratory oxidase under the conditions tested (**Figure 2B-D**). Although most anaerobic respiratory operons exhibited nearly undetectable baseline expression levels, we detected high levels of transcript corresponding to fumarate reductase (*frdA*) and periplasmic nitrite reductase (*nrfA*) (**Figures 2B-D and 3**). These results reveal the presence of marked respiratory heterogeneity within UPEC biofilms and suggest that respiration via cytochrome *bd* may be preferred within biofilm communities.

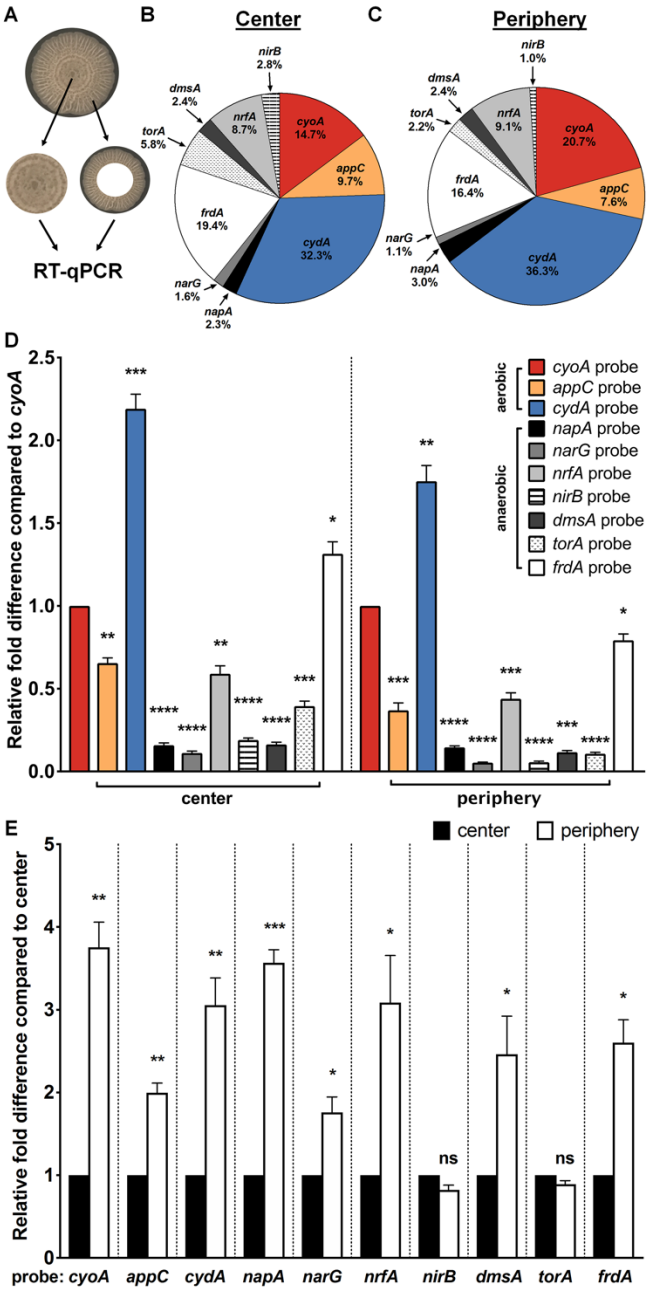

Figure 2: Lateral expression of respiratory complexes in *Escherichia coli* biofilms. (A) Image of a mature colony biofilm formed by UPEC strain UTI89 on YESCA agar without supplementation of alternative terminal electron acceptors. The center and periphery of colony biofilms, including both the surface and interior of each region, were harvested and subjected to RNA extraction and RT-qPCR using probes targeting each respiratory operon present in UPEC. (B – C) Pie charts indicating the relative abundance of detected respiratory transcripts in the biofilm center (B) and periphery (C). Aerobic respiratory operons are presented in color, whereas anaerobic respiratory operons are presented in grayscale (D) Graph depicting relative fold differences in respiratory transcript abundance in the biofilm center and periphery as compared to *cyoA* abundance in the same region. (E) Graph depicting relative fold difference in abundance of each transcript in the biofilm periphery as compared to abundance of the same transcript in the biofilm center. The graphs and pie charts depict the average of four biological replicates. Statistical analysis was performed in GraphPad Prism using a two-tailed paired t test. Data are presented as mean ± SEM. * $p < 0.05$, ** $p < 0.01$, *** $p < 0.001$, **** $p < 0.0001$.

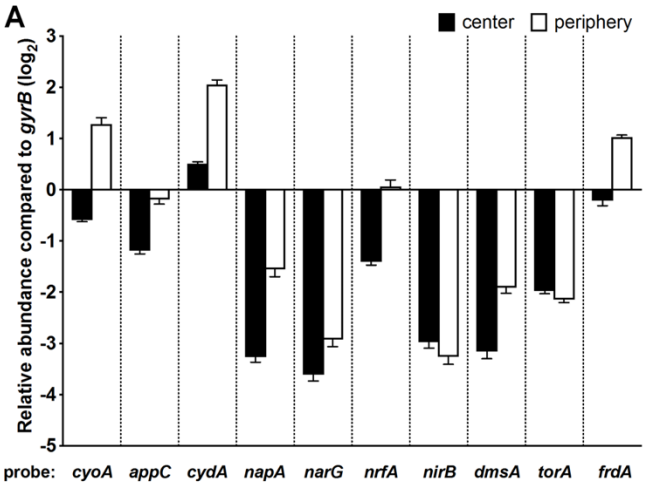

B

		cyoA	appC	cydA	napA	narG	nrfA	nirB	dmsA	torA	frdA
Center	Ct (GOI)	26.50	28.47	27.95	31.21	31.75	30.20	29.92	29.51	30.67	28.63
	Ct (*gyrB*)	26.13	27.46	28.43	27.95	28.22	28.39	26.54	26.29	28.16	28.05
Periphery	Ct (GOI)	24.98	27.91	26.26	29.86	31.68	28.62	30.96	28.59	31.66	27.13
	Ct (*gyrB*)	26.25	27.69	28.35	28.24	28.55	28.68	26.85	26.67	28.56	28.27

Figure 3: Expression of respiratory complexes compared to *gyrB*. (A) Graph depicting relative abundance of each respiratory transcript in the center and periphery of day 11 colony biofilms as compared to *gyrB*. (B) Average C_T values for each transcript in the center and periphery of colony biofilms. Data are presented as mean ± SEM. All data are representative of four biological replicates.

Respiratory oxidase expression is spatially organized along the biofilm oxygen gradient

To define the spatial organization of respiratory oxidase expression, we performed peptide nucleic acid fluorescence *in situ* hybridization (PNA-FISH) on cryosections of mature colony biofilms using probes targeting each respiratory oxidase operon (*cyoA*, *appC*, and *cydA*) as well as *rrsH* as an endogenous control (**Figure 4**). Because cryosectioning captures both macroscopic and microscopic architecture of biofilms with minimal disruption to the overall structure or organization of the resident bacteria, this approach allows us to define the *in situ* distribution of transcripts in unperturbed communities (**Figure 4A-B**). Each PNA-FISH probe was designed using the validated probe sequences used for qPCR to ensure comparable hybridization efficiencies, and the specificity of each probe was confirmed using both RT-qPCR and through staining of planktonic cells (**Figure 5**). SYTO 9 staining of sections was used as an additional control to localize the entire biofilm community and account for possible hybridization inconsistencies with the *rrsH* control probe (**Figures 4E, K and 6**). To account

for possible mislocalization of signal due to biofilm breakage during the cryosectioning and staining procedure, we focused our analysis on regions devoid of significant breaks in the cryosection.

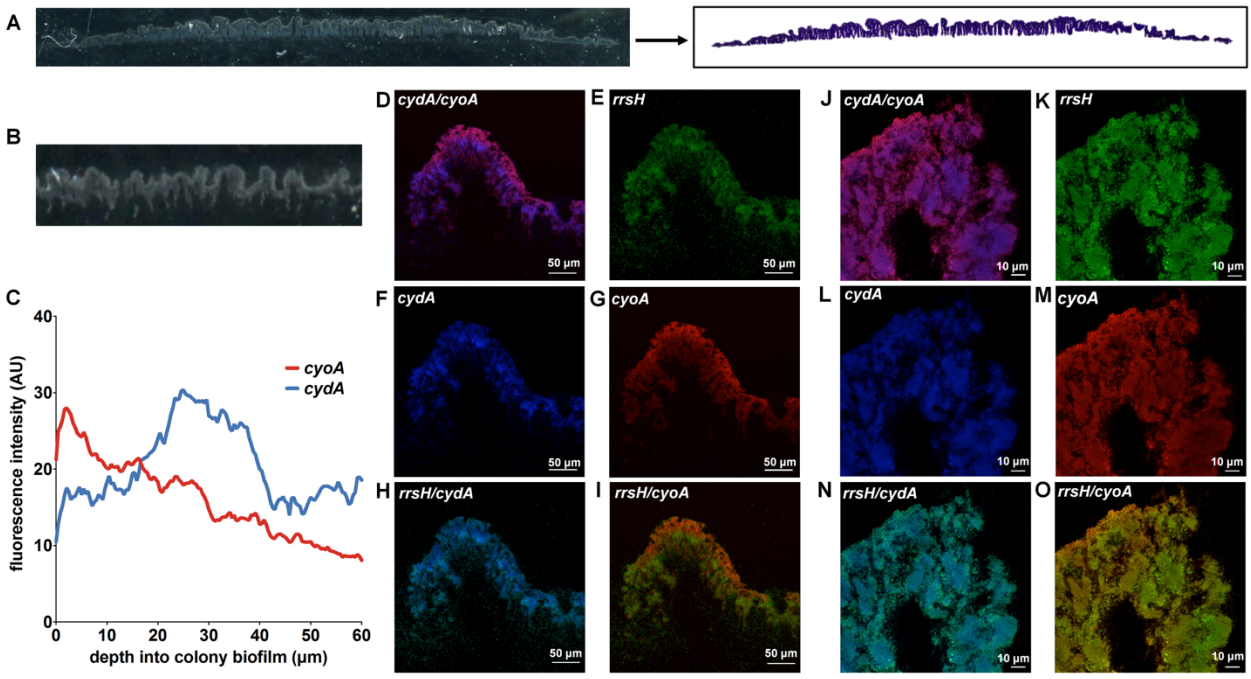

Figure 4: Expression of respiratory oxidases as a function of the oxygen gradient. (A) Representative images depicting a biofilm cryosection before (left) and after (right) fixation and crystal violet staining. (B) Magnified image of a cryosection allows visualization of architectural features of the biofilm (C) Fluorescence intensity of *cyoA* and *cydA* PNA-FISH probes was quantified on ImageJ. Data are presented as the average fluorescence intensity as a function of depth obtained from four images, each with five measurements per image. (D – O) Representative images of PNA-FISH stained biofilm cryosections at 20x magnification (D – I) and 63x magnification (J – O). Cryosections were stained with PNA-FISH probes targeting *cyoA* and *cydA* with *rrsH* (16S rRNA) as an endogenous control. Images are representative of three biological replicates.

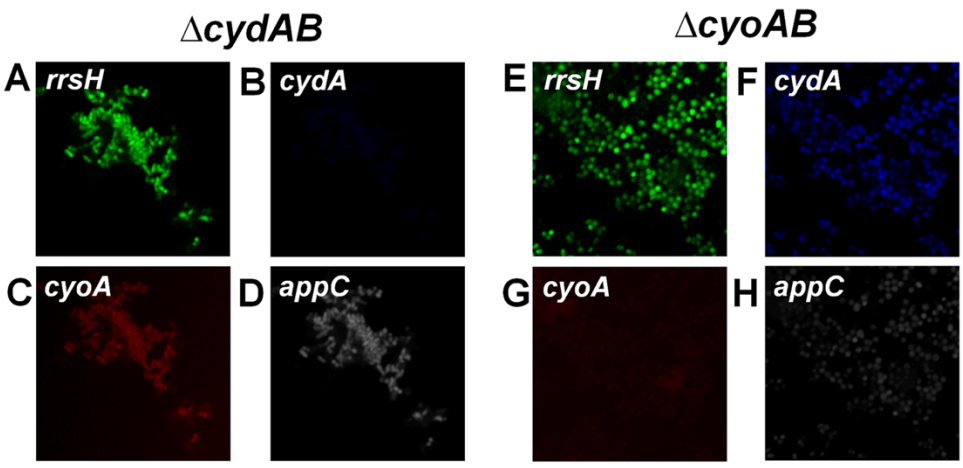

Figure 5: PNA-FISH on respiratory oxidase deletion mutants. Representative images of Δ*cydAB* (A – D) and Δ*cyoAB* (E – H) cells stained with PNA-FISH probes to assess specificity.

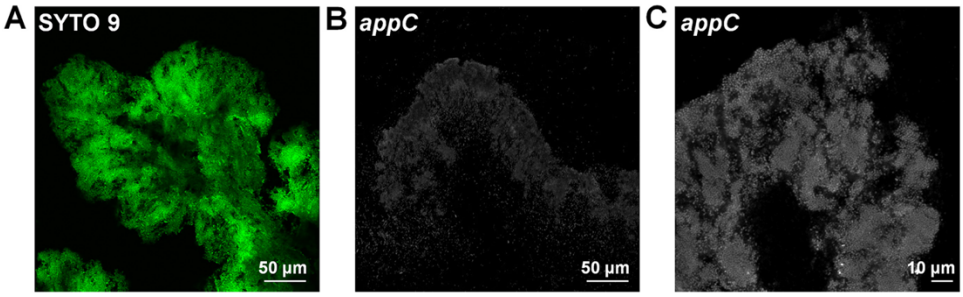

Figure 6: Localization of *appC* transcript in biofilm cryosections. (A) Representative image of SYTO 9 stained biofilm cryosection at 20x magnification. (B – C) Representative images of biofilm cryosections stained with an *appC* PNA-FISH probe at 20x (B) and 63x (C) magnification.

Consistent with previous observations demonstrating that the highest oxygen abundance is at the air-exposed surface of the biomass (121, 122), we observed that *cyoA* transcript was most abundant in bacteria lining air-exposed surfaces of the biofilm (**Figure 4C-D, G, I-J, M, O**). In contrast, the highest abundance of *cydA* transcript was found in densely packed clusters of bacteria in the interior of the biofilm (**Figure 4C-D, F, H, J, L, N**). Although cytochromes *bd* and bd_2 are both induced under oxygen-limited conditions (96, 105), we observe different transcript distribution for these two gene clusters. Rather than organizing along the oxygen gradient, *appBC* transcript was observed to be evenly distributed throughout the community (**Figure 6**). Interestingly, we observe basal expression of cytochrome *bo* across the community with enrichment of cytochrome *bd* in pockets of cells in the interior (**Figure 4J-O**), suggesting that individual cells may express multiple respiratory oxidases simultaneously within biofilms. Additionally, while many biofilm wrinkles are empty or sparsely populated with *rrsH* staining cells, we observe other wrinkles that are densely populated (**Figure 7**). We observe reduced intensity of respiratory oxidase staining in the interior of those populated wrinkles (**Figure 7**), suggesting that respiration in the deeper layers of the biofilm respiration occurs anaerobically (121, 130). Based on our RT-qPCR results (**Figure 2B-D**), we predict that respiration in the populated wrinkles may be occurring via fumarate reductase or periplasmic nitrite reductase. Given the known role of aerobic respiration in UPEC biofilm formation (54, 83, 90), we focused the remainder of these studies on understand the contribution of cytochrome *bd* to biofilm architecture.

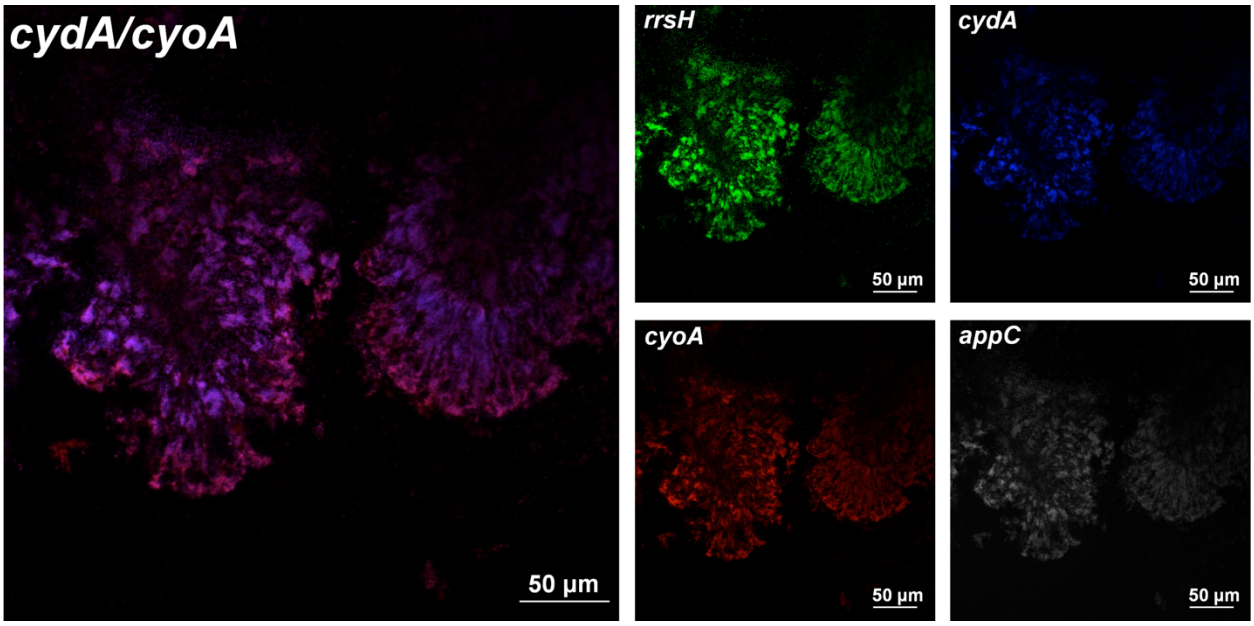

Figure 7: Localization of respiratory oxidase transcripts in biofilm wrinkles. Representative image of a PNA-FISH stained cryosection depicting a biofilm wrinkle with a central region filled with *rrsH* stained cells at 20x magnification.

Loss of cytochrome *bd* alters biofilm architecture, development, and extracellular matrix abundance

The highly ordered spatial organization of cytochrome *bo* and cytochrome *bd* in biofilms raised the hypothesis that subpopulations expressing each of these respiratory oxidases uniquely contribute to overall biofilm architecture. To test this hypothesis, we created isogenic deletion mutants lacking cytochrome *bo* (Δ*cyoAB*), cytochrome *bd* (Δ*cydAB*), or cytochrome bd_2 (Δ*appBC*) and compared biofilms formed by the resulting strains (**Figure 8A**). Colony biofilms formed by the parental strain expand to an average diameter of 16.8 mm over an 11-day incubation period and exhibit elaborate rugose architecture with distinct central and peripheral regions (**Figures 8A and 9**). Strains lacking cytochrome *bo* and cytochrome bd_2 exhibited inverse phenotypes relative to one another, with the Δ*cyoAB* colony biofilms expanding more than the parental strain (average diameter: 19.9 mm) and the Δ*appBC* colony biofilms appearing more compact and with apparently higher rugosity (**Figures 8A and 9**). Strikingly, while Δ*cyoAB* and Δ*appBC* only displayed minor architectural changes, Δ*cydAB* colony biofilms exhibited pronounced defects both in development and architecture (**Figures 8A and 9**).

Colony biofilms from all strains grew at a similar rate for the first 72 hours (**Figure 9**). However, Δ*cydAB* colony growth was significantly stunted between days 3 and 11, with radial expansion remaining at an average diameter of 10.3 mm and colonies exhibiting a wet mass approximately 50 percent of the parental strain after 7 days of growth, even though the CFU produced by the two strains were comparable at this time point (**Figures 8B, D and 9**). Complementation of Δ*cydAB* with an extra-chromosomal construct expressing *cydABX* under its native promoter rescued the deletion phenotype, indicating that the defects observed in the Δ*cydAB* mutant stem solely from the removal of the *cydABX* cluster (**Figure 10**). Deletion of both *cyoAB* and *appBC* from the same strain led to an early onset of rugose phenotype (**Figure 11**). Together, these results demonstrate that cytochrome *bd* is a key contributor to biofilm development and suggest that loss of cytochrome *bd* alters the synthesis and organization of the extracellular matrix.

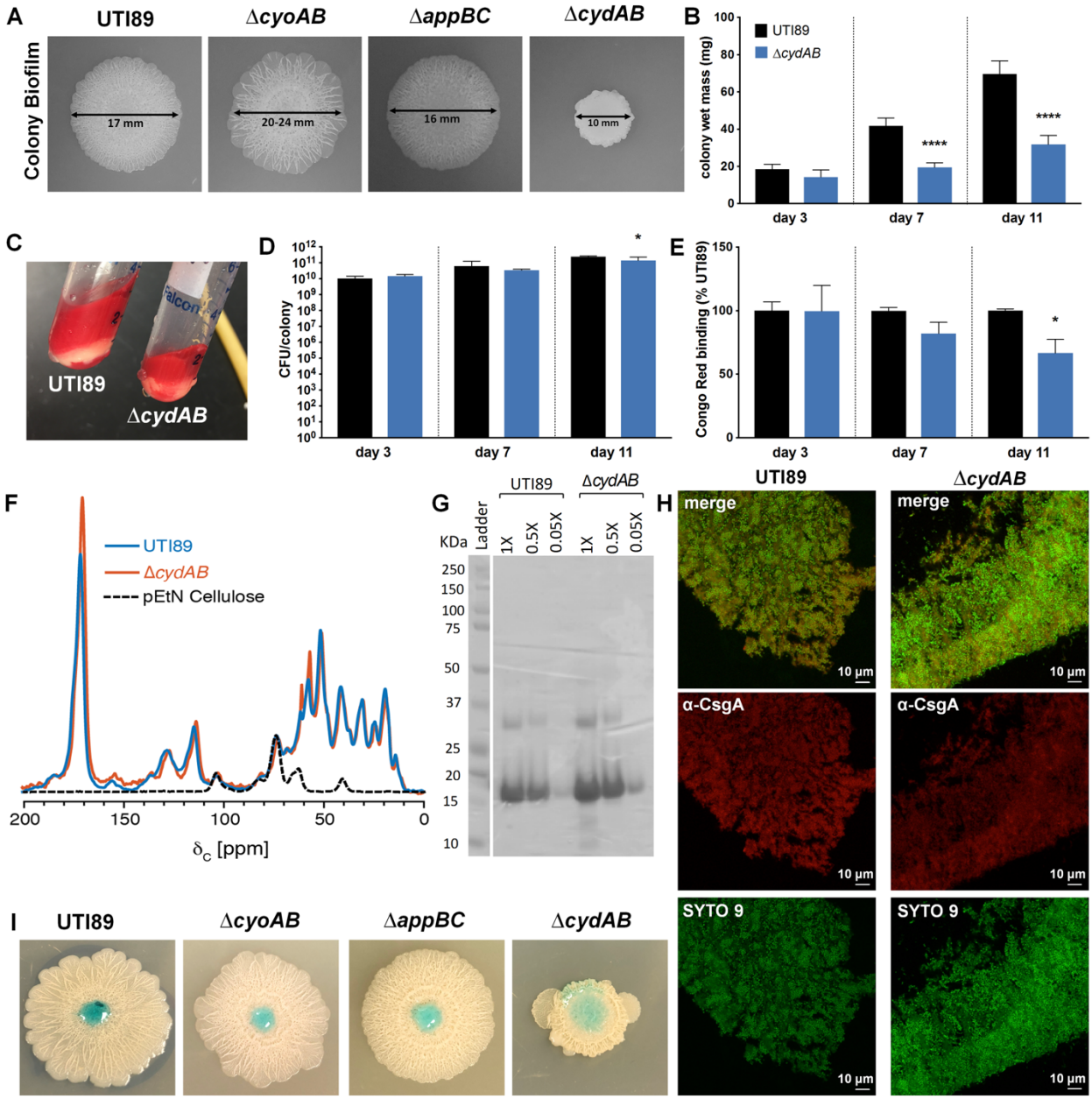

Figure 8. Cytochrome *bd* organizes biofilm architecture and extracellular matrix production. (A) Colony biofilms of UTI89 and respiratory oxidase mutants grown on YESCA agar for 11 days. Images are representative of at least 30 biological replicates. (B) Graph depicting wet mass of individual colony biofilms at days 3, 7, and 11 of growth. Data is the average of five biological replicates per day. Data are presented as mean ± SD. (C) Image depicting gross changes to extracellular matrix abundance between UTI89 and Δ*cydAB* colony biofilms. extracellular matrix is stained red by the presence of Congo Red in the growth medium. (D) CFU per colony biofilm was measured at days 3, 7, and 11 of growth. Data are presented as mean ± SD. Data are representative of five biological replicates. (E) Congo Red binding as a percentage of binding in UTI89. Data are presented as mean ± SEM. (F) Solid-state NMR spectra of the extracellular matrix of UTI89 (blue), Δ*cydAB* (orange), and isolated pEtN cellulose (black). (G) SDS-PAGE gel of UTI89 and Δ*cydAB* extracellular matrix. extracellular matrix was treated with 98% formic acid and vacuum centrifuged prior to analysis to dissociate curli amyloid fibers. (H) Immunofluorescence images of curli (α-CsgA, red) localization in UTI89 and Δ*cydAB* colony biofilm cryosections. (I) Colored water droplets were added to the top of day 11 colony biofilms to probe biofilm barrier function. All statistical analysis was performed in GraphPad Prism using a two-tailed unpaired t test. * $p < 0.05$, ** $p < 0.01$, *** $p < 0.001$, **** $p < 0.0001$.

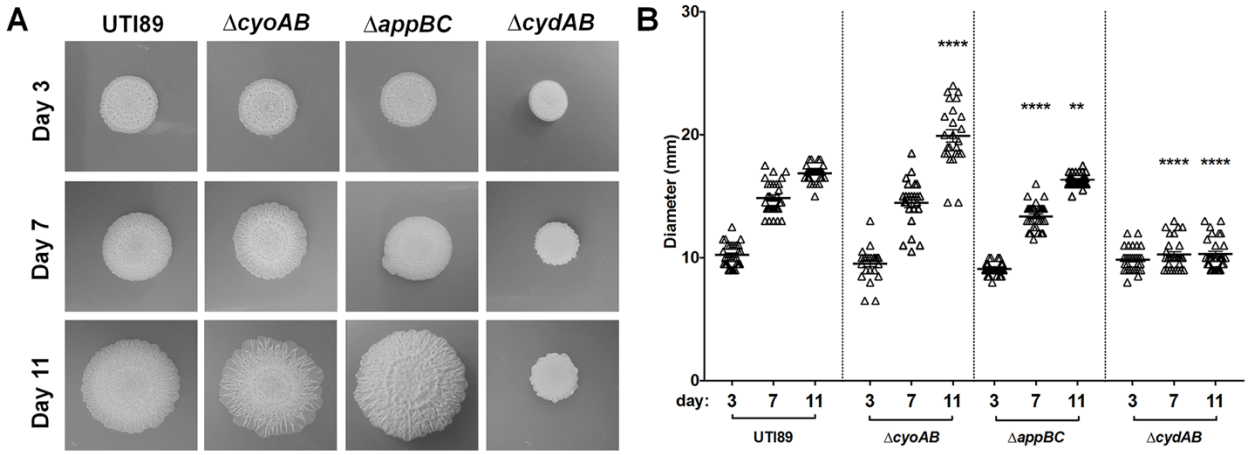

Figure 9: Temporal development of colony biofilms by UTI89 and respiratory oxidase mutants. (A) Representative images of UTI89 and respiratory oxidase mutant colony biofilms grown on YESCA agar taken on day 3, 7, and 11 of growth. (B) Graph depicting colony biofilm diameter at day 3, 7, and 11 of growth. Each point represents an individual colony biofilm. Data are representative of at least 30 biological replicates. Statistical analysis was performed in GraphPad Prism using Welch's t test. * $p < 0.05$, ** $p < 0.01$, *** $p < 0.001$, **** $p < 0.0001$.

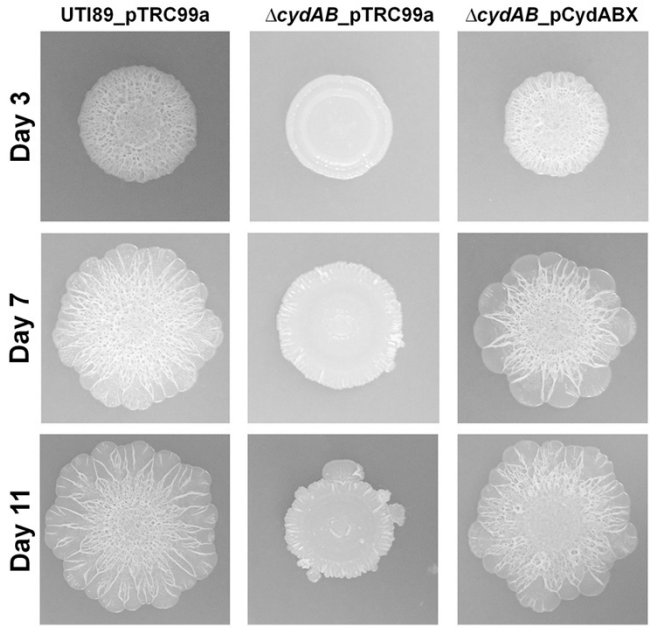

Figure 10: Extrachromosomal complementation of Δ*cydAB* rescues biofilm defects. Representative images on UTI89_pTRC99a, Δ*cydAB*_pTRC99a, and complemented Δ*cydAB*_pCydABX under the control of a native promoter. Images were taken of colony biofilms grown on YESCA agar at days 3, 7, and 11 of growth. Images are representative of at least five biological replicates.

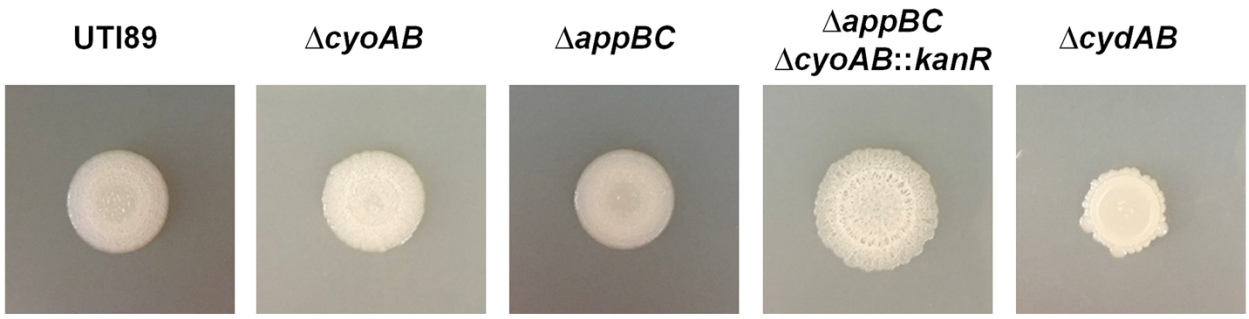

Figure 11: Analysis of Δ*appBC*Δ*cyoAB*::*kanR* colony biofilms. Comparison of colony biofilms formed by UTI89, Δ*cyoAB,* Δ*appBC*, Δ*appBC*Δ*cyoAB*::*kanR*, and Δ*cydAB* after six days of growth on YESCA agar. Images are representative of five biological replicates.

Under the growth conditions used, the extracellular matrix of *E. coli* comprises primarily of cellulose and curli amyloid fibers (131). Previous solid-state nuclear magnetic resonance (NMR) spectroscopy analyses on intact extracellular matrix material defined the contributions of cellulose and curli to the *E. coli* biofilm extracellular matrix, and determined that curli and cellulose are present in a 6 to 1 ratio (131). More recently, the extracellular matrix cellulose was determined to be a chemically modified form of cellulose, specifically phosphoethanolamine (pEtN) cellulose (132). To interrogate the effects of cytochrome *bd* on curli and exopolysaccharide production, we extracted extracellular matrix and performed solid-state NMR analysis to evaluate the abundance of curli and cellulose components (**Figure 8F-G**). The NMR spectra obtained for the parental and Δ*cydAB* extracellular matrix are very similar overall, indicating a comparable protein to polysaccharide ratio between the samples (**Figure 8F**). Consistent with this analysis, we do not observe changes in protein composition between the parent and Δ*cydAB* extracellular matrix samples when analyzed on SDS-PAGE gels (**Figure 8G**). We additionally do not observe any overt alterations to curli abundance or localization between UTI89 and Δ*cydAB* biofilm cryosections using immunofluorescence (**Figure 8H**). Despite the similar composition, the total amount of extracellular matrix recovered was reduced in Δ*cydAB* biofilms, indicative of a decrease in extracellular matrix production (**Figure 8C**). When quantified by Congo Red depletion assays, Δ*cydAB* colony biofilms exhibited a trend toward reduced total extracellular matrix abundance at 7 days (82.1% of parental), and significantly reduced abundance at 11 days (66.6% of parental) (**Figure 8E**). Because the protein to polysaccharide ratio and curli abundance are unchanged between

the parent and Δ*cydAB*, these data are suggestive of a change to the overall mixture of matrix components in Δ*cydAB*, with particular reductions in the abundance of non-curli and non-pEtN cellulose extracellular matrix components.

The extracellular matrix plays a central role in biofilm physiology by providing physical protection against exogenous insults, serving as a structural scaffold, and helping to establish chemical gradients which lead to metabolic differentiation and subpopulation formation (60, 63, 124, 133). As such, disruptions to the matrix can have catastrophic consequences for the biofilm community. We hypothesized that alterations to extracellular matrix abundance and architecture in the Δ*cydAB* mutant would render the biofilm more susceptible to exogenous insults. To investigate this possibility, we probed the barrier function of the respiratory oxidase mutant biofilms by applying a drop of colored water to the surface of mature colony biofilms (**Figure 8I**) (134). While the parental strain, Δ*cyoAB*, and Δ*appBC* biofilms repelled the drop, the solution readily penetrated Δ*cydAB* biofilms, demonstrating that the alterations to Δ*cydAB* biofilm architecture and extracellular matrix abundance increases penetrance of aqueous solutions.

Loss of cytochrome *bd* increases population sensitivity to nitrosative stress

Together, our studies indicate that cytochrome *bd* is highly expressed in biofilms, and that loss of the cytochrome *bd*-expressing subpopulation impairs barrier function and reduces extracellular matrix abundance. These data suggest that the cytochrome *bd*-expressing subpopulation plays a critical role in promoting extracellular matrix synthesis and providing structural integrity to the community. However, it is also possible that cytochrome *bd* is preferentially expressed in the biofilm because cytochrome *bd* provides protection against oxidative and nitrosative stress – byproducts of biofilm metabolism (135, 136) and components of the innate immune response (99, 102, 103). In addition to functioning as a respiratory quinol:O_2 oxidoreductase, previous studies demonstrated that cytochrome *bd* has catalase activity, is capable of oxidizing the respiratory inhibitor nitric oxide, and is insensitive to nitrosative stress due to its unusually fast nitric oxide dissociation rate (99). By contrast,

cytochrome *bo* affords no protection against nitrosative stress and is irreversibly inhibited by nitric oxide (99).

Given these additional functions of cytochrome *bd*, we performed growth curves at ambient oxygen concentration and evaluated the effects of nitrosative and oxidative stress on the fitness of cells lacking each respiratory oxidase as compared to the parental strain. Without the addition of stressors, both Δ*cydAB* and Δ*cyoAB* mutants exhibited a delay in growth, but growth of Δ*appBC* closely mirrored the parental strain (**Figures 12A, D**). Despite the delay, all strains reached a similar maximal CFU/mL by the end of the experiment (**Figure 12A**). ATP measurements of normalized samples taken from each strain during logarithmic phase revealed no significant overall differences in ATP concentrations, suggesting this growth delay is not caused by impaired ATP generation (**Figure 12G**). Next, to determine whether loss of cytochrome *bd* impairs resistance to oxidative and nitrosative stress, we measured growth with and without these stressors. Consistent with the reported catalase activity of cytochrome *bd*, significant increases in the doubling time of both Δ*cydAB* and Δ*appBC* were observed after treatment with 1 mM H_2O_2 (**Figure 12B, E**). Although previous studies in K-12 *E. coli* demonstrated that treatment with 1 mM H_2O_2 reduced the growth rate of Δ*cyoAB* by ~70 percent relative to wild-type (137), we did not observe significant reductions in growth rate of Δ*cyoAB* after treatment (**Figures 12B, E**). Addition of the nitric oxide donor NOC-12 to planktonic cultures induced an apparent growth delay in all strains, but only significantly reduced the growth rate of Δ*cydAB* (**Figures 12C, F**). Whereas treatment with NOC-12 increased the doubling time from 27 to 39 minutes in UTI89, in Δ*cydAB* the doubling time increased from 37 to 106 minutes after treatment (**Figure 12F**). Together, these data demonstrate that although cytochrome *bd* is dispensable for energy generation during planktonic growth, loss of cytochrome *bd* sensitizes bacteria to oxidative and nitrosative stress, consistent with previous studies on K-12 *E. coli* and the multi-drug resistant strain ST131 (102, 103).

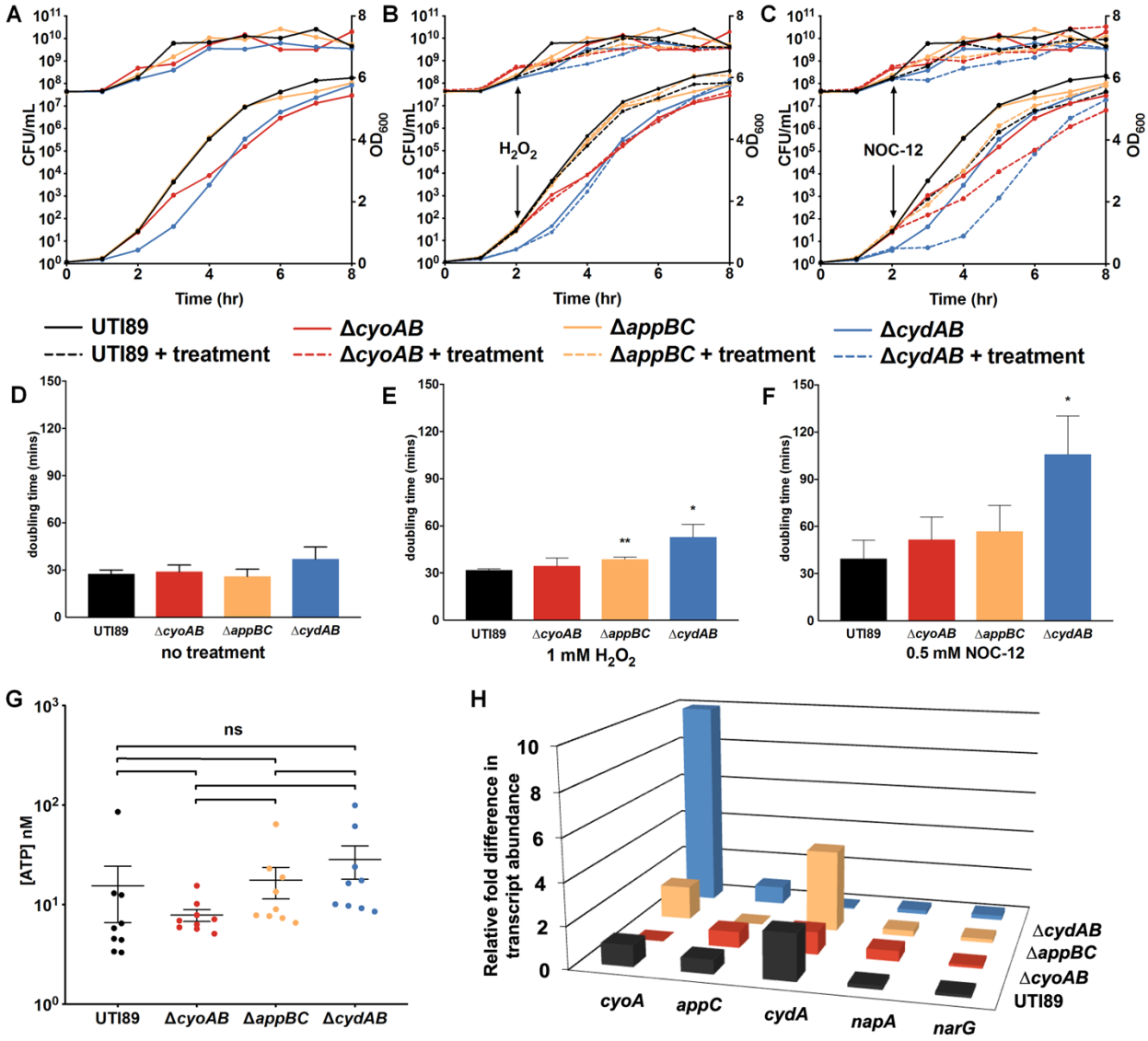

Figure 12: Cytochrome *bd* provides nitrosative stress resistance. (A – C) Growth curves for UTI89, Δ*cyoAB*, Δ*appBC*, and Δ*cydAB* as measured by CFU per mL (upper lines, left axis) and OD_{600} (lower lines, right axis) with no treatment (A), treated with 1 mM hydrogen peroxide (B), or treated with 0.5 mM of nitric oxide donor NOC-12 (C). (D – F) Doubling time in minutes of each strain between hours 2 and 4 was calculated using CFU per mL data shown in (A – C). (D) no treatment, (E) 1 mM hydrogen peroxide, (F) 0.5 mM NOC-12. (G) ATP levels measured from logarithmic cultures of each strain normalized to OD_{600} = 0.5. (H) RT-qPCR data depicting relative fold difference in respiratory transcript abundance in the center of day 11 colony biofilms in UTI89 and respiratory oxidase mutant strains. In UTI89 (black), data is presented as relative fold difference in abundance of each transcript as compared to *cyoA* abundance. In each mutant strain, data are presented as relative fold difference in transcript abundance as compared to the abundance of the same transcript in UTI89. Statistical analysis was performed on GraphPad Prism using a two-tailed unpaired t test. All data are presented as mean ± SEM and are representative of at least three biological replicates.

While there was a trend toward increased doubling time in all strains after treatment with NOC-12, treatment of Δ*cydAB* increased doubling time approximately 3-fold relative to its untreated control.

This observation suggests that during aerobic growth cytochrome *bd* serves as a nitric oxide sink that reversibly sequesters nitric oxide and protects the more efficient cytochrome *bo*-mediated respiration. Accordingly, loss of cytochrome *bd* would decrease nitrosative stress resistance and render the dominant respiratory complex, cytochrome *bo*, susceptible to irreversible inhibition by nitric oxide. As such, treatment of Δ*cydAB* with nitric oxide would poison all preformed cytochrome *bo* complexes in the membrane and force the bacteria to synthesize new oxidases prior to resuming growth. Consistent with this hypothesis, we observe a marked increase (~10-fold relative to UTI89) of *cyoA* transcript in the interior of Δ*cydAB* colony biofilms, where nitric is expected to be most abundant (**Fig 12H**). These results contrast previous studies in K-12 *E. coli*, in which loss of cytochrome *bd* induces a marked upregulation of *appBC* (105). These observations demonstrate that the regulation of respiratory oxidases in UPEC is distinct from that previously defined in K-12 and suggest that cytochrome *bd* may serve as a nitric oxide sink in biofilms. In conjunction with the disrupted biofilm architecture and altered extracellular matrix abundance in Δ*cydAB* biofilms, these data suggest that cytochrome *bd*-expressing subpopulations are critical, not only for directing extracellular matrix biosynthesis, but also for withstanding harmful metabolic byproducts while in the biofilm state.

Heterogeneous expression of respiratory oxidases at the population level

Our data thus far indicate that in addition to heterogeneity in respiratory oxidase expression in the biofilm state, heterogeneous expression of respiratory oxidases must also be occurring in the planktonic population. Our planktonic studies revealed a lag in growth of the Δ*cyoAB* and the Δ*cydAB* mutants when these strains were grown under ambient oxygen concentrations, suggesting that in each culture there are subpopulations – like in the biofilm – that stochastically or deterministically express different respiratory components. Such a bet-hedging approach could provide UPEC with the flexibility to quickly adapt to a given niche, be it different locales in the genitourinary tract or in the gastrointestinal tract during host colonization. In the context of urinary tract infection, *E. coli* traverse from the nearly anoxic gut to the perineum, where it encounters atmospheric oxygen concentrations, prior to ascending

the urethra to enter the hypoxic bladder, where the dissolved urinary oxygen concentration is 4-6% (86). This microbial journey is performed by planktonic cells, which can then expand into multicellular communities on and within bladder epithelial cells, as well as on urinary catheters (12, 53).

The high abundance of *cydA* transcript in the hypoxic areas of the biofilm, in conjunction with the defects observed in aerobically grown Δ*cydAB* planktonic cultures, raised the hypothesis that a cytochrome *bd*-expressing subpopulation exists in the planktonic state under ambient oxygen conditions and that this cytochrome *bd*-expressing subpopulation exhibits the greatest fitness advantage during infection. To test this hypothesis, we first analyzed transcript abundance in aerobic cultures used for inoculation during murine infections with RT-qPCR and PNA-FISH (**Figure 13**). Under these conditions, the majority of transcript corresponds to *cyoA* (69.7%), with *cydA* and *appC* transcripts each comprising approximately 15% of detected transcripts (**Figure 13A**). Transcript abundance was altered by decreasing ambient oxygen concentrations, with *cydA* becoming the most abundant transcript in 12%, 8% and 4% oxygen, the latter being the concentration of dissolved oxygen concentration in the urine (**Figures 13A-B and 14**) (86). This shift in transcript abundance is largely due to a marked induction of *cydABX* expression under hypoxic conditions (**Figure 15**). PNA-FISH analysis revealed the presence of bacteria which uniquely express cytochrome *bo* (**Figure 13F**), cytochrome *bd* (**Figure 13E**), or cytochrome bd_2 (**Figure 13G**), as well as some cells that have transcript of all three operons (**Figure 13C, E-G**). Intriguingly, we observed dividing cells in which each daughter had distinct respiratory oxidase transcript abundance (**Figure 13C, inset**), suggesting that asymmetric distribution of respiratory transcripts during division may be a mechanism by which these subpopulations are generated. This hypothesis is supported by previous studies in *E. coli* demonstrating that respiratory oxidases exhibit unusually noisy gene expression, and that asymmetric cell division is a major generator of heterogeneity (138-140).

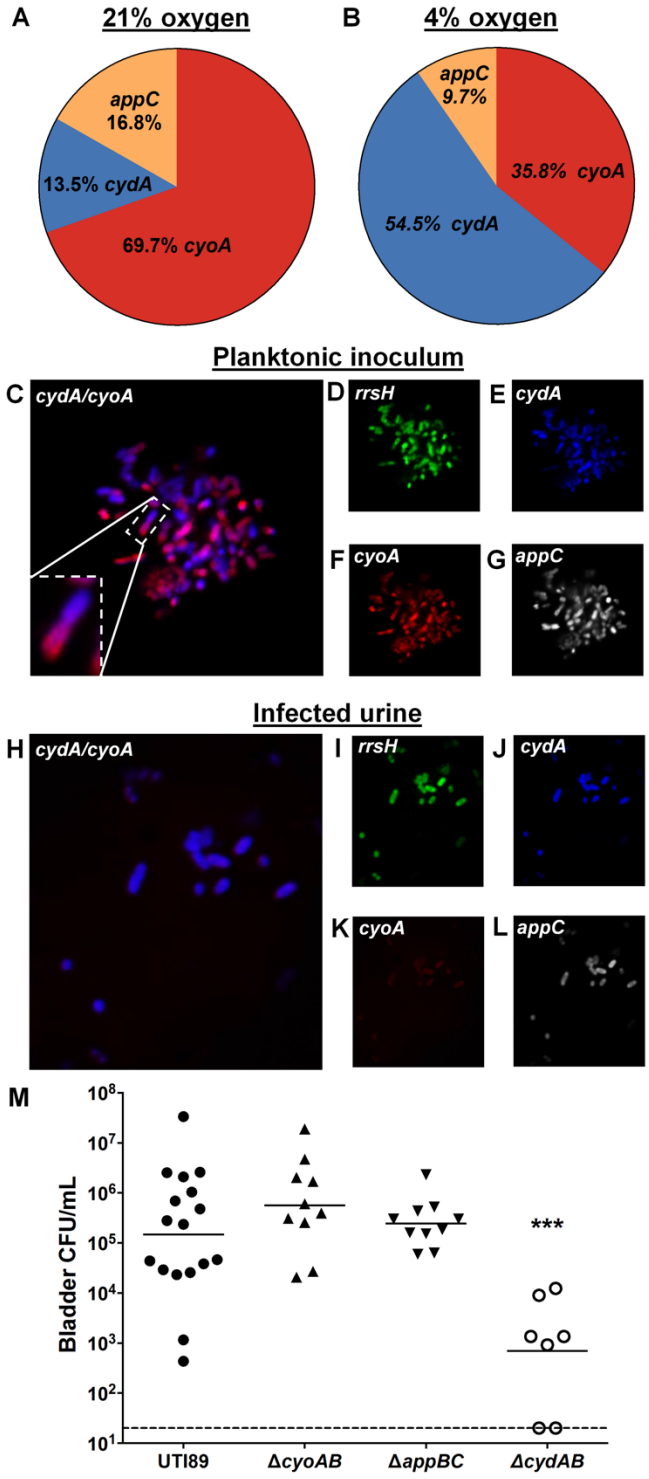

Figure 13: Respiratory heterogeneity provides a fitness advantage during urinary tract infection. (A – B) Pie charts depicting relative abundance of *cydA*, *cyoA*, and *appC* transcripts detected using RT-qPCR in planktonic cultures grown at 21% oxygen in the manner used to prepare cultures to inoculate mice (A), as well as planktonic cultures grown at 4% oxygen (B). Data are representative of three biological replicates. (C – G) PNA-FISH was used to detect respiratory oxidase transcripts from cultures used to inoculate mice. Data is representative of three biological replicates. (H – L) PNA-FISH was used to detected respiratory oxidase transcripts in the urine of mice infected with UTI89. Urine was pooled from 20 mice. (M) Graph depicting bladder titers obtained from mice infected with UTI89 or respiratory oxidase mutant strains at 24 hours post infection. Each point represents a mouse. Statistical analysis was performed in GraphPad Prism using a two-tailed Mann-Whitney test. Line represents geometric mean. *** $p < 0.001$.

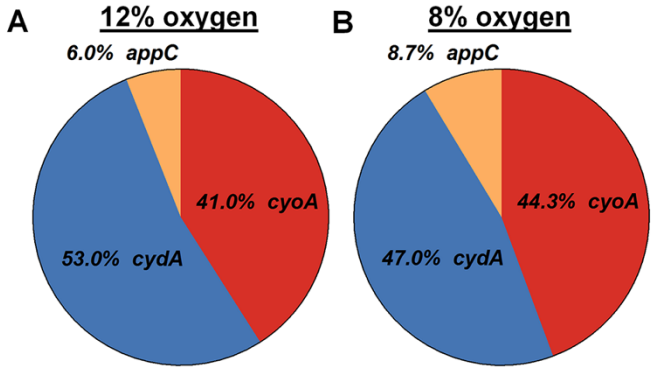

Figure 14: Ambient oxygen concentration influences respiratory oxidase transcript abundance. Pie charts depicting relative abundance of *cydA*, *cyoA*, and *appC* transcripts detected using RT-qPCR in planktonic cultures grown at 12% (A) or 8% oxygen (B). Data is representative of three biological replicates.

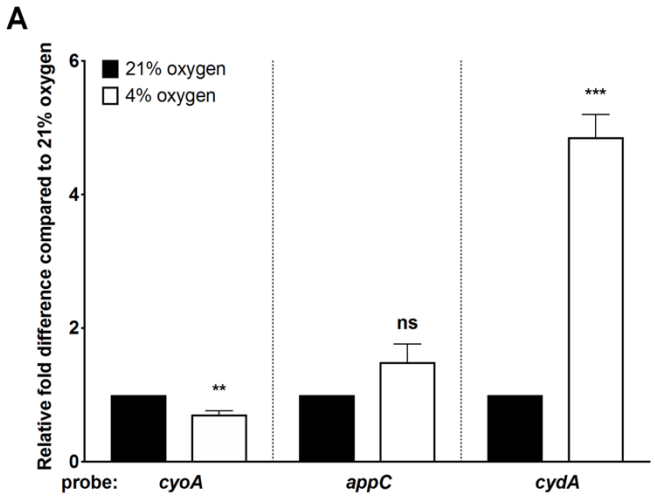

C

		cyoA	*appC*	*cydA*
21% O_2	**Ct (GOI)**	26.91	31.02	30.67
	Ct (*gyrB*)	27.14	27.95	28.50
4% O_2	**Ct (GOI)**	25.13	29.78	24.73
	Ct (*gyrB*)	24.96	26.91	24.91

Figure 15: Expression of respiratory oxidases as a function of oxygen tension. (A) RT-qPCR data depicting relative fold difference in abundance of each respiratory oxidase transcript of planktonic bacteria grown at 4% oxygen as compared to 21% oxygen. (B) Relative abundance of each transcript at 21% and 4% oxygen as compared to *gyrB*. (C) Raw Ct values for each transcript at 21% and 4% oxygen. Data are presented as mean ± SEM. All data are representative of three biological replicates.

Expression of cytochrome *bd* is dominant during acute urinary tract infection

Previous studies reported that deletion of cytochrome *bd* impairs UPEC virulence in a murine model of urinary tract infection (102). To gauge the contribution of each respiratory oxidase during infection, we evaluated the fitness of Δ*cyoAB,* Δ*appBC*, and Δ*cydAB* mutants compared to the parent

strain in a murine model of acute urinary tract infection. Consistent with the previous report (102), Δ*cydAB* exhibited a ~2 log decrease in bladder colonization by 24 hours relative to the parent strain, while the mutants deleted for *cyoAB* and *appBC* colonize mice at the same level as the parent strain (**Figure 13M**). Subsequent PNA-FISH on pooled urine obtained from mice infected with the parent strain revealed a marked enrichment in cytochrome *bd*-expressing cells and a corresponding reduction in the number of cells expressing cytochrome *bo* (**Figure 13H-L**). This suggests that the bladder environment either induces transcription of *cydABX* or that only subpopulations of bacteria expressing *cydABX* are capable of efficiently colonizing the bladder. Together these data reveal the presence of subpopulations of bacteria that differentially express respiratory oxidases as a potential bet-hedging mechanism to promote adaptation to low oxygen availability and bladder colonization.

DISCUSSION

Cytochrome *bd* is a multifunctional protein that is central to respiration and can maintain activity in the face of nitrosative stress (99). As such, bacteria expressing cytochrome *bd* presumably exhibit a fitness advantage during growth conditions that are low in oxygen or high in metabolic byproducts that increase nitric oxide concentration. The biofilm state, while protecting the bacterial residents from predation and desiccation, constitutes a high-density environment with several chemical gradients that result from the consumption and production of metabolites. Accordingly, expressing an enzyme that can facilitate tolerance to metabolic byproducts, such as nitric oxide, would ensure that biofilm residents do not perish as a consequence of their own metabolic excretions. Our study elucidates the distribution of respiratory oxidase expression in the biofilm state and indicates that the bulk of biofilm residents express cytochrome *bd*, particularly in the densely populated interior. The cytochrome *bd*-expressing bacteria are not necessarily using cytochrome *bd* for respiration, as many of them also have low levels of cytochrome *bo* and bd_2 transcripts (**Figures 4-6**). Rather, the production of cytochrome *bd* may be leveraged towards providing tolerance to nitrosative stress, which irreversibly inhibits cytochrome *bo*. Indeed, in Δ*cydAB* biofilms we observe a marked increase in cytochrome *bo* expression (**Figure 12H**),

suggesting that loss of cytochrome *bd* impairs nitric oxide tolerance and that increased production of cytochrome *bo* may be a compensatory mechanism that allows biofilm bacteria to respire in the presence of high levels of nitric oxide.

In addition to acting as a respiratory inhibitor, nitric oxide regulates cyclic di-GMP abundance and thereby governs the switch from motility to aggregation and biofilm expansion (141, 142). Consequently, if cytochrome *bd* decreases nitric oxide availability, it would indirectly influence extracellular matrix production. Consistent with this hypothesis, loss of the cytochrome *bd*-expressing subpopulation reduces extracellular matrix abundance and leads to gross alterations of biofilm architecture (**Figure 8**). From this, we speculate that the cytochrome *bd*-expressing subpopulation may promote biosynthesis of the extracellular matrix by influencing the nitric oxide – cyclic di-GMP signaling axis.

Most importantly, this work revealed the presence of planktonic subpopulations that express distinct respiratory oxidases during growth. In conjunction with the observation that only cytochrome *bd* expression is critical for fitness during infection, this finding suggests that basal expression of cytochrome *bd* under aerobic conditions serves as a bet-hedging mechanism that promotes the expansion of bacteria during the transition from the aerobic perineum to the hypoxic bladder. In addition to allowing for efficient respiration in the hypoxic bladder, expression of cytochrome *bd* provides resistance against nitrosative stress – a metabolic byproduct and component of the innate immune response – and promotes the formation of resilient biofilm communities. Alternatively, cytochrome *bd* may serve as an oxygen scavenger, thereby reducing oxygen tension and allowing distinct UPEC subpopulations to utilize anaerobic respiratory pathways. Consistent with this hypothesis, the alternative terminal electron acceptors nitrate and TMAO are known to be present in the urine, and the anaerobic reduction of nitrate to nitrite by *Enterobacteriaceae* is the basis of a commonly used clinical test used to diagnose urinary tract infection. Together our observations characterize expression of respiratory oxidases across niches, define the contribution of aerobic respiratory operons to biofilm formation and bladder colonization, and suggest the presence of respiratory bet-hedging behavior in

UPEC. These data clarify the role of respiration in UPEC physiology and suggest the possibility of targeting heterogeneity as a method for homogenizing bacterial populations and impeding their ability to colonize the urinary tract.

MATERIALS AND METHODS

Bacterial Strains

All studies were performed in *E. coli* cystitis isolate UTI89 (44). All gene deletions (Δ*cyoAB*, Δ*appBC*, and Δ*cydAB*) were performed using the λ-red recombinase system (143). Complementation constructs were created in plasmid pTRC99a with *cydABX* under the control of its native promoter as previously described (144). Primers used for gene deletions and complementation plasmid construction are listed in **Table 1**.

Primer/Probe	Sequence (5' → 3')	Purpose
cydA_KO_Fwd	ATGATGTTAGATATAGTCGAACTGTCGCGCTTA CAGTTTGCCTTGACCGCGATGTACGTGTAGGCT GGAGCTGCTTC	*cydAB* knockout
cydB_KO_Rev	GTTACGTTCAATATCTTCTTTGGTGATACGACC GAACATTTTCCAGTCATATGAATATCCTCCTTAG	*cydAB* knockout
cydA_KO_Test_Fwd	GATCAAATTGGTGAGATCGTGAC	*cydAB* knockout
cydB_KO_Test_Rev	CTAACAGAAGTGCCATCACG	*cydAB* knockout
cydA1_Fwd_XbaI	CTGCAGTCTAGACTGGTCAAGTTATCCATCATT CACT	*cydABX* complementation
cydX_Rev_SacI	CGTATTGAGCTC/TTGCGATAATCTTACTCATCA GATGTC	*cydABX* complementation
appC_KO_Fwd	ATGTGGGATGTCATTGATTTATCGCGCTGGCAG TTTGCTCTGACCGCGGTGTAGGCTGGAGCTGC TTC	*appBC* knockout
appB_KO_Rev	TTAGTACAGCTCGTTTTCGTTACGGCGGAGAGT TTCTGTCGTCATGCCATATGAATATCCTCCTTAG	*appBC* knockout
appC_KO_Test_Fwd	ACGCAGACGTCACGGCG	*appBC* knockout
appB_KO_Test_Rev	TGCACAGTCAGGTGCCAGC	*appBC* knockout
cyoB_KO_Fwd	TCAGTTGCCATTTTTCAGCCCTGCCTTAGTAATC TCATCGGTGTAGGCTGGAGCTGCTTC	*cyoAB* knockout
cyoA_KO_Rev	GTCATTATTTGCAGGCACTGTATTGCTCAGTGG CTGTAATTCTGCGCTGCATATGAATATCCTCCTT AG	*cyoAB* knockout
cyoB_KO_Test_Fwd	CATCCAGATAAGACCGGAAGTG	*cyoAB* knockout

cyoA_KO_Test_Rev	GCAACATATGTGACCTGATAGC	*cyoAB* knockout
cyoA_Fwd	CAATGCCCTGTTCCGGGTAGATG	qPCR
cyoA_Rev	ACGGTACCTATCTTAATCATCATCTTCC	qPCR
cyoA probe	NED-TCGTCGTGTGCCAGCGGCTTG	qPCR
appC_Fwd	CGATGTCGCATTACGCTCG	qPCR
appC_Rev	GGTGCAGGTTCTGTTTGCCACT	qPCR
appC probe	NED-CTGCGTATGAAGTCGCGCAAG	qPCR
cydA_Fwd	GTGGCTACCGGTCTGACCATG	qPCR
cydA_Rev	CCAACCGAAGAAGAACAGACCTAC	qPCR
cydA probe	FAM-CGCTGGCAATCGAAGGTCTGATG	qPCR
narG_Fwd	TCTCGCTATACTGGACACCTGA	qPCR
narG_Rev	CCGTATAGTCCACCGGATTCAT	qPCR
narG probe	NED-TGCCGTCTGCGCCGCAGT	qPCR
napA_Fwd	CTTCCGCGTGTGGTACTGC	qPCR
napA_Rev	GTGCCGCTCGGGATATTCC	qPCR
napA probe	FAM-CGTCTGCCTGCGGACATGGTGGTGAC	qPCR
nrfA_Fwd	GGTCAGTGCCATGTGGAGT	qPCR
nrfA_Rev	CGACAGGGAGTTAGTCCAGTCA	qPCR
nrfA probe	NED-CCGTGGGATGACGGCATGAAAGTCGAA	qPCR
nirB_Fwd	CTGGTGCTGAACGCTATCG	qPCR
nirB_Rev	ATAGCAGCAATCAGGTCGC	qPCR
nirB probe	FAM-AACTGCCGGACAGCGCGCAAATCTG	qPCR
frdA_Fwd	CCTCGACCTGCGTCACCTCGGC	qPCR
frdA_Rev	TTCTGGCACGAATGGCGTA	qPCR
frdA probe	FAM-CGGATCGACGCCAACGTA	qPCR
dmsA_Fwd	GCT ATC TCG ATG CTG GCG A	qPCR
dmsA_Rev	GTTCAATGGCATCGGTCCAC	qPCR
dmsA probe	NED-CGGCGCGCGCGAAGGTTCATACAGCTTAC	qPCR
torA_Fwd	CGTGGATGATTGTCGTTCTGG	qPCR
torA_Rev	TTGTCGTGAACAGGCGGA	qPCR
torA probe	NED-GGCTGGCACTATAACGGCGCAGGCAC	qPCR
gyrB_Fwd	GATGCGCGTGAAGGCCTGATTG	qPCR
gyrB_Rev	CACGGGCACGGGCAGCATC	qPCR
gyrB probe	VIC-ACGAACTGCTGGCGGA	qPCR
cyoA PNA	CGTCGTGTGCCA – Lys (Atto425)	PNA-FISH
cydA PNA	CGATTGCCAGCG – Lys (Cy5)	PNA-FISH
appC PNA	TGCGCGACTTCATA – Lys (TexasRed)	PNA-FISH
rrsH PNA	AGTAATTCCGATTAACG – Lys (Atto532)	PNA-FISH

Table 1: Primers and probes used in Chapter 2.

Growth conditions

For all analyses, strains were propagated overnight at 37°C with shaking in Lysogeny broth (LB) (Fisher) at pH 7.4. To form colony biofilms, 10 µL of overnight culture was spotted onto 1.2x Yeast Extract/Casamino Acids (YESCA) agar (122) and allowed to grow at room temperature. Growth curves to assess tolerance to nitrosative or oxidative stress were performed in LB broth at 37˚C with shaking, starting from an overnight culture normalized to optical density at 600 nm (OD_{600}) = 0.05. At 2 hours post-inoculation, cultures were split into equal volumes and treated with 0.5 mM NOC-12, 1 mM H_2O_2, or left unperturbed. OD_{600} and CFU per mL measurements were taken every hour for 8 hours.

RT-qPCR

RNA was extracted from day 11 colony biofilms or planktonic cultures using the RNeasy kit (Qiagen). RNA was DNase treated using Turbo DNase I (Invitrogen), and reverse transcribed using SuperScript III Reverse Transcriptase (Invitrogen). cDNA was amplified in an Applied Biosystems StepOne Plus Real-Time PCR machine using TaqMan MGB chemistry with the primers and probes listed in **Table 1**. All reactions were performed in triplicate with four different cDNA concentrations (100, 50, 25, or 12.5 ng per reaction). Relative fold difference in transcript abundance was determined using the $\Delta\Delta C_T$ method (145) with target transcripts normalized to *gyrB* abundance from a total of 3 – 4 biological replicates.7

Peptide nucleic acid fluorescence *in situ* hybridization (PNA-FISH)

Day 11 biofilms were flash frozen in Tissue-Tek O.C.T. compound (Electron Microscopy Sciences) and cryosectioned as described previously (118). The PNA-FISH hybridization protocol was adapted from Almeida *et al* (146). Biofilm cryosections were fixed in 4% paraformaldehyde (PFA) for 30 minutes at room temperature, then dehydrated for 10 minutes in 50% ethanol. After dehydration, 100 µL of

hybridization solution (see below for details) was applied to the slides. All hybridizations were performed at 60˚C for 30 minutes. Next, slides were submerged in pre-warmed wash solution for 30 minutes, mounted using ProLong Diamond (ThermoFisher), and imaged using a Zeiss 710 confocal laser scanning microscope (CLSM). For planktonic cells, 1 mL of culture was sedimented, fixed in 4% PFA, resuspended in 50% ethanol, incubated at -20˚C for 30 minutes, and resuspended in 100 µL hybridization solution. After hybridization, cells were pelleted, resuspended in 500 µL pre-warmed wash solution, and incubated at 60˚C for 30 minutes. Finally, cells were pelleted and resuspended in 100 µL sterile water before being applied to microscope slides for imaging. Wash solution contained 5 mM Tris-HCl pH 7.4, 15 mM NaCl, and 1% Triton X-100. Hybridization solution contained 10% w/v dextran sulfate, 30% formamide, 50 mM Tris-HCl pH 7.4, 10 mM NaCl, 5 mM EDTA, 0.1% Triton X-100, and 200 nM of each PNA-FISH probe. Probe sequences were based on the probes used for qPCR (efficiency of hybridization: *rrsH*: 81; *cydA*: 107; *cyoA*: 115; *appC*: 73) and were synthesized by PNA Bio (Newbury Park, CA).

ATP measurements

ATP was quantified from mid-log (4 hours after subculture) planktonic cultures using Cell-Glo Titer kit (Promega). Cultures were normalized to OD_{600} = 0.5, pelleted, and resuspended in PBS. 50 µL of bacterial suspension was mixed with an equal volume of Cell-Glo Titer reagent and incubated shaking at room temperature for 15 minutes. After incubation, luminescence was measured on a SpectraMax i3 plate reader (Molecular Devices). Luminescence was converted to concentration of ATP using a standard curve on the same plate.

Extracellular matrix extraction

Extracellular matrix was extracted using established methods (131). Briefly, biofilms were grown on YESCA agar containing 25 µg/mL Congo Red. After 60 hours, biofilms were homogenized in cold 10 mM Tris-HCl pH 7.4 using an Omni Tissue Homogenizer (motor speed 9) five times for one minute per

cycle. Next, the homogenate was centrifuged three times for 10 minutes at 5,000*g* to remove cells. The supernatant was spiked with NaCl (final concentration 170 mM) and centrifuged for one hour at 13,000*g* to pellet the matrix. The extracellular matrix pellet was washed in 10 mM Tris-HCl pH 7.4 with 4% SDS and incubated at room temperature rocking overnight. Next, the suspended extracellular matrix was centrifuged at 13,000*g* for one hour, resuspended in cold 10 mM Tris-HCl pH 7.4, and centrifuged at 30,000*g* for 20 minutes. Pelleted extracellular matrix was resuspended in Milli-Q water and flash frozen.

Congo Red depletion assays

Extracellular matrix abundance was quantified using Congo Red depletion assays adapted from established protocols (147). Colony biofilms grown on YESCA agar were harvested into PBS at specific time points and homogenized. 40 µg/mL Congo Red (final concentration) was added to homogenized biofilms, which were then incubated at 37˚C for 1 hour. After incubation, extracellular matrix was pelleted by centrifugation, the supernatant was removed, and supernatant absorbance (490 nm) was measured using a SpectraMax i3 plate reader (Molecular Devices).

Solid-state NMR measurements

All NMR experiments were performed in an 89 mm bore 11.7T magnet using either an HCN Agilent probe with a DD2 console (Agilent Technologies) or a home-built four-frequency transmission line probe with a Varian console. Samples were spun at 7143 Hz in either 36 µL capacity 3.2 mm Zirconia rotors or thin-walled 5 mm outer diameter Zirconia rotors. The temperature was maintained at 5˚C with an FTS chiller (FTS Thermal Products, SP Scientific, Warminster, PA) supplying nitrogen at -10˚C. The field strength for ^{13}C cross polarization was 50 kHz with a 10% ^{1}H linear ramp centered at 57 kHz. The CPMAS recycle time was 2 s for all experiments. ^{1}H decoupling was performed with continuous wave decoupling. ^{13}C chemical shifts were referenced to tetramethylsilane as 0 ppm using a solid adamantine sample at 38.5 ppm. The 15.6 mg wild-type ^{13}C CPMAS spectrum was the result of 32,768 scans and

the 8.3 mg mutant spectrum was the result of 100,000 scans. NMR spectra were processed with 80 Hz line broadening.

SDS-PAGE gels

A portion of the lyophilized extracellular matrix sample used for solid-state NMR analysis was resuspended in 98% formic acid and vacuum centrifuged. The samples were then reconstituted in SDS-PAGE sample buffer containing 8 M urea and 50 mM DTT and further diluted to desired concentrations. All samples were centrifuged briefly at 10,000*g* to remove any insoluble material and used for electrophoresis. The gels were stained with instant blue and de-stained in water.

Immunofluorescence

Immunofluorescence targeting CsgA, the major curli subunit, was performed as previously described (54). Biofilm cryosections were fixed in 4% PFA for 30 minutes at room temperature and blocked overnight in 5% BSA at 4˚C. Sections were washed in PBS, incubated with rabbit α-CsgA antibodies (GenScript) (1:1000) at room temperature for 1 hour, washed in PBS, and incubated with AlexaFluor 647 goat α-rabbit IgG (ThermoFisher) (1:1000) at room temperature for 1 hour. Slides were counterstained with SYTO 9 and imaged using CLSM.

Murine infections

Murine infections were performed as described previously (148). In brief, UTI89 and each mutant strain were inoculated individually into 5 mL LB medium and grown shaking at 37˚C for 4 hours. Next, this culture was diluted 1:1000 into 10 mL fresh media and grown statically at 37˚C for 24 hours. After 24 hours, this culture was diluted 1:1000 into 10 mL fresh media and grown for another 24 hours at 37˚C statically. Next, 7 – 8 week old C3H/HeN female mice were transurethrally inoculated with 50 µL PBS containing 10^7 CFU bacteria. Mice were sacrificed at 24 hours post infection after which bladders were removed and homogenized for CFU enumeration. All animal studies were approved by the Vanderbilt

University Medical Center Institutional Animal Care and Use Committee (IACUC) (protocol numbers M/12/191 and M1500017-01) and carried out in accordance with all recommendations in the Guide for the Care and Use of Laboratory Animals of the National Institutes of Health and the IACUC.

Statistical analysis

All statistical analyses were performed in GraphPad Prism using the most appropriate test. Details of test used, error bars, and statistical significance cutoffs are presented in figure legends.

ACKNOWLEDGMENTS

We thank Dr. Jonathan Schmitz, Dr. Gerald Van Horn, Dr. Mariana X. Byndloss, and members of the Hadjifrangiskou laboratory for critical evaluation of the manuscript and helpful discussions. This work was supported by the following NIH grants**:** R01 AI107052 (MH), DiaComp DK076169 (MH), T32 GM007347 (CJB), K08 DK106472 (DBC) and the Vanderbilt University Medical Center Pediatric Urology Research Fund. LC acknowledges support from the National Science Foundation CAREER Award 1453247. SHW is a recipient of an NSF Predoctoral Fellowship.

CHAPTER 3

Subversion of Mitochondrial Metabolism Supports Intracellular Bacterial Pathogenesis During Urinary Tract Infection

At the time this dissertation was submitted, a modified version of this chapter was submitted for publication and was undergoing peer review with the following title:

Beebout CJ, Robertson GL, Reinfeld BI, Blee AM, Morales GH, Brannon JR, Chazin WJ, Rathmell WK, Rathmell JC, Gama V, and Hadjifrangiskou M. Subversion of mitochondrial metabolism supports intracellular bacterial pathogenesis during urinary tract infection. Under Review 2022.

ABSTRACT

Urinary tract infections are among the most common human bacterial infections and place a significant burden on healthcare systems due to associated morbidity, cost, and antibiotic use. Despite being a facultative anaerobe, uropathogenic *Escherichia coli* (UPEC), the primary cause of urinary tract infections, requires aerobic respiration to establish infection in the bladder. Here, we provide evidence that the widely conserved respiratory oxidase cytochrome *bd* is required for intracellular infection of urothelial cells. We show that intracellular oxygen scavenging by cytochrome *bd* alters mitochondrial physiology by reducing the efficiency of mitochondrial respiration, stabilizing the hypoxia inducible transcription factor HIF-1, and promoting a shift toward aerobic glycolysis. This bacterially induced reprogramming of host metabolism antagonizes apoptosis, thereby protecting intracellular bacteria from urothelial cell exfoliation and preserving their replicative niche. These results reveal the metabolic basis for intracellular bacterial pathogenesis during urinary tract infection and identify subversion of mitochondrial metabolism as a bacterial strategy to facilitate persistence within the urinary tract.

INTRODUCTION

Urinary tract infections are among the most common human bacterial infections, afflicting an estimated 150 million people per year (10-12). Urinary tract infections manifest across a spectrum of

clinical presentations, with patients most commonly experiencing acute bladder infection that resolves with outpatient antibiotic therapy (20). In a minority of cases, pathogenic bacteria can gain access to the kidneys and bloodstream where they can establish severe, potentially life-threatening infections (20). Nearly two-thirds of women will experience urinary tract infection during their lifetime, and a quarter of those infected will experience recurrent infection within six months (10, 11). As a result of the high rates of infection and recurrence, urinary tract infections are a major cause of morbidity and a key driver of antibiotic prescriptions.

Uropathogenic *E. coli* (UPEC), the primary cause of urinary tract infections, is responsible for approximately 80% of urinary tract infections, making it one of the most successful human bacterial pathogens worldwide (10, 12, 21). During bladder infection UPEC enters a transient intracellular lifecycle, where it replicates to form multicellular communities within the cytosol of urothelial cells (10-12, 44, 47, 65). This intracellular lifecycle allows bacteria to replicate to high numbers in a protected and nutrient-rich niche prior to escaping and infecting neighboring cells (44, 47, 65, 80). Although decades of research have meticulously defined the stages of UPEC pathogenesis in the bladder, relatively little is known regarding how bacteria adapt their metabolism to thrive within urothelial cells (81, 82).

Despite being a facultative anaerobe, previous work established that oxygen plays a central role in the ability of UPEC to colonize the bladder and form stress tolerant biofilms in the urinary tract (**Chapter 2**) (15, 54, 89, 90, 95, 149). Although *E. coli* encodes three respiratory oxidases capable of mediating aerobic respiration – a heme copper oxidase, cytochrome *bo*, and two *bd*-type oxidases, cytochromes *bd* and *bd*$_2$ – only loss of cytochrome *bd* impacts bacterial fitness in the bladder (91, 95, 102). Unlike cytochrome *bo*, the *bd*-type oxidases have a remarkably high oxygen affinity, allowing them to support respiration under microaerobic conditions such as those encountered during infection (91, 92, 96). Additionally, while cytochrome *bd* canonically functions as a respiratory quinol:O_2 oxidoreductase, this complex also possesses non-respiratory activities including the ability to reversibly sequester and oxidatively degrade the respiratory poison and innate immune effector nitric oxide (99,

103). Consequently, cytochrome *bd* plays a central role in the physiology and pathogenesis of a wide array of human pathogens including *Salmonella enterica*, *Klebsiella pneumoniae*, *Streptococcus agalactiae*, and *Mycobacterium tuberculosis* (96, 99).

In this work, we investigate the contribution of bacterial aerobic respiration to urinary tract infection pathogenesis. We determine that oxygen scavenging by cytochrome *bd* supports intracellular bacterial pathogenesis during bladder infection both by supporting bacterial replication and by depleting oxygen from the urothelial cell cytosol. Intracellular bacterial aerobic respiration alters mitochondrial physiology, stabilizes the hypoxia inducible transcription factor HIF-1, and reprograms urothelial cell metabolism. This metabolic shift antagonizes apoptosis and protects intracellular bacteria from urothelial cell exfoliation. These findings define the metabolic underpinnings of intracellular bacterial pathogenesis during urinary tract infection and reveal a mechanism by which bacterial aerobic respiration reprograms host cell metabolism to support bacterial survival in the urinary tract.

RESULTS

Cytochrome *bd* supports intracellular bacterial replication during bladder infection

Although previous work established that cytochrome *bd* is necessary for bladder colonization, the mechanisms underlying this requirement remain unclear. To define the contribution of cytochrome *bd* to colonization of the urinary tract, we infected mice with wild-type cystitis isolate UTI89, an isogenic mutant lacking cytochrome *bd* (Δ*cydAB*), or Δ*cydAB* complemented with the cytochrome *bd* encoding operon (*cydABX*) under native transcriptional control (95, 149) and enumerated bacterial bladder titer during the first six hours of infection. Loss of cytochrome *bd* causes a reduction in bacterial titer within one hour of infection that is rescued by extrachromosomal complementation, demonstrating cytochrome *bd* is necessary for the initial establishment of bladder infection (**Figure 16A**). Interestingly, this reduction in titer increases in magnitude over time, indicating cytochrome *bd* is required for expansion of bacterial populations in the bladder (**Figure 16A**).

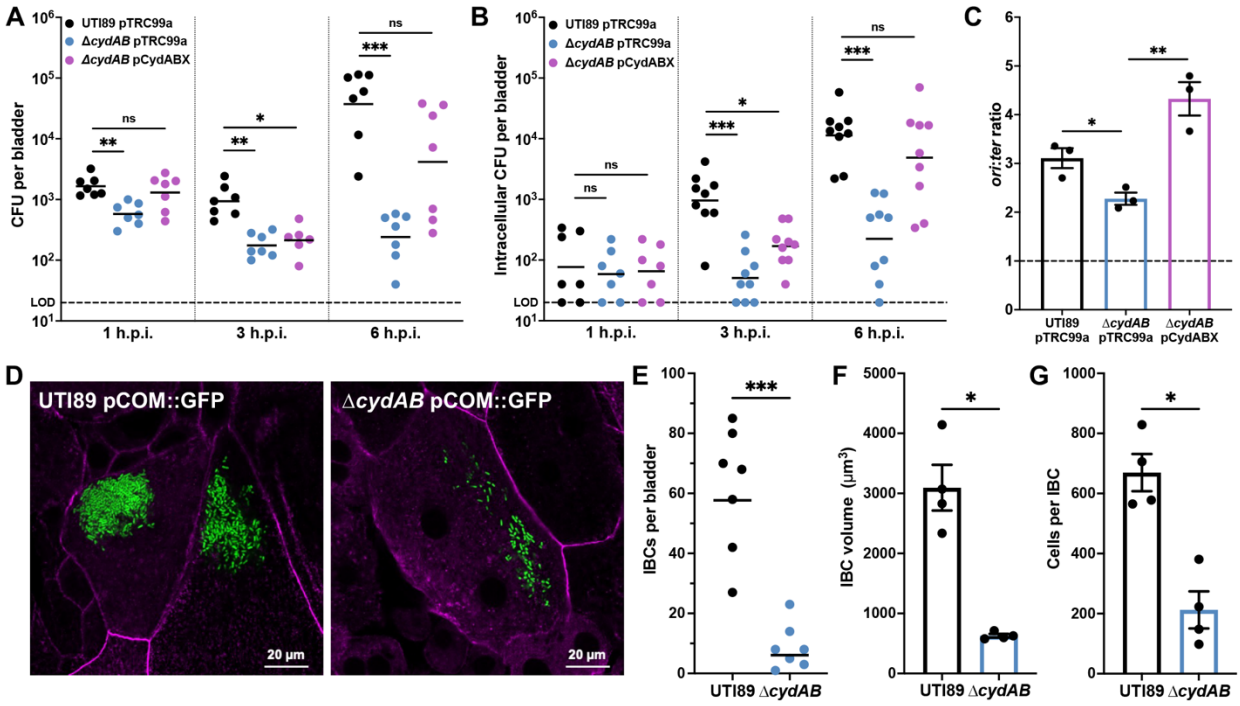

Figure 16: Cytochrome *bd* supports intracellular bacterial replication during bladder infection. (A) Bladder bacterial titer 1-, 3-, and 6-hours post-infection (h.p.i.); geometric mean; Kruskal-Wallis test. (B) Bladder intracellular bacterial titer 1, 3, and 6 h.p.i.; geometric mean; Kruskal-Wallis test. (C) *ori*:*ter* copy number ratio of intracellular bacteria 3 h.p.i; mean ± SEM, unpaired t test. (D) Representative images of wild-type and Δ*cydAB* IBCs 6 h.p.i.; green, bacteria; magenta, actin. (E) Number of IBCs per bladder; geometric mean; Mann-Whitney test. (F-G) Quantification of the volume (F) and number of cells per IBC (G); mean ± SEM; Mann-Whitney test. Experiments were performed with a minimum of three biological replicates. Each point represents a biological replicate. * $p < 0.05$, ** $p < 0.01$, *** $p < 0.001$, **** $p < 0.0001$.

During the first six hours of infection, UPEC uses type 1 pili to adhere to urothelial cells, invade into the cytosol, and replicate to form densely populated intracellular bacterial communities (IBCs) (47-49, 78). Wild-type and Δ*cydAB* display a similar, mannose-sensitive hemagglutination titer, indicating both strains elaborate functional type 1 pili (50) (**Figure 17A**). In addition, we observe similar abundance and polymerization of the primary type 1 pilus subunit FimA between strains, demonstrating cytochrome *bd* does not impact type 1 pilus production (**Figure 17B-D**). Consistent with these findings, gentamicin protection assays reveal that Δ*cydAB* and a strain encoding cytochrome *bd* as its sole respiratory oxidase (Δ*appBC*Δ*cyoAB*) are equally efficient at adherence and invasion of urothelial cells, indicating cytochrome *bd* does not impact the ability of UPEC to adhere to or invade urothelial cells *in*

vitro (**Figure 18**). These results suggest cytochrome *bd* facilitates the expansion of bacterial bladder populations by supporting intracellular pathogenesis.

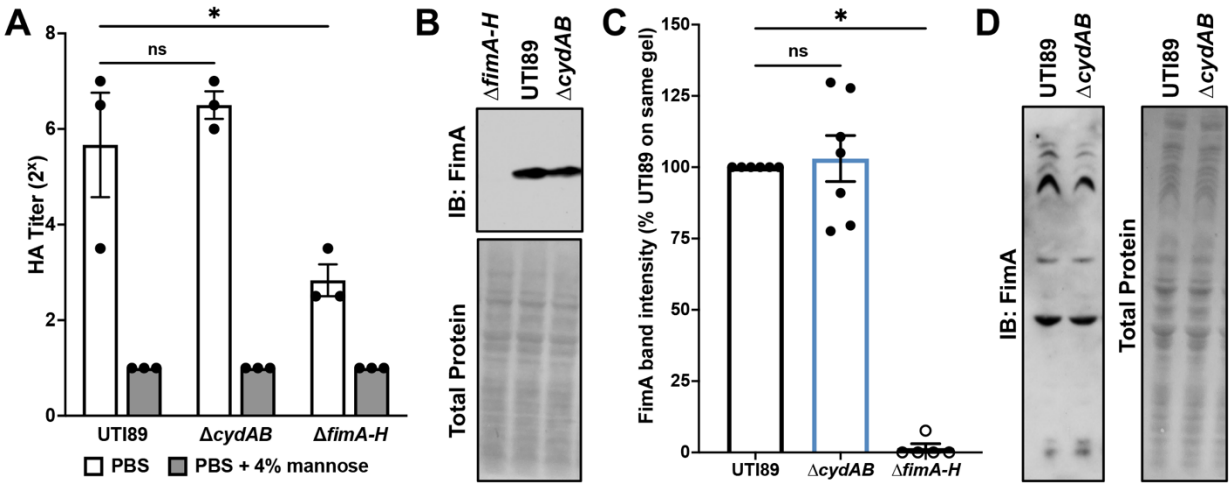

Figure 17: Deletion of cytochrome *bd* does not influence type 1 pilus production. (A) Bacterial hemagglutination titer with or without the competitive FimH inhibitor D-mannose; mean ± SEM; one-way ANOVA. (B) Anti-FimA immunoblot performed on normalized samples boiled in acidified SDS to depolymerize type 1 pili. (C) Quantification of FimA band intensity normalized to percent of UTI89 on the same gel; mean ± SEM; Kruskal-Wallis test. (D) Anti-FimA immunoblot performed on normalized samples with polymerized type 1 pili. Experiments were performed with a minimum of three biological replicates. Each point represents a biological replicate. * $p < 0.05$, ** $p < 0.01$, *** $p < 0.001$, **** $p < 0.0001$.

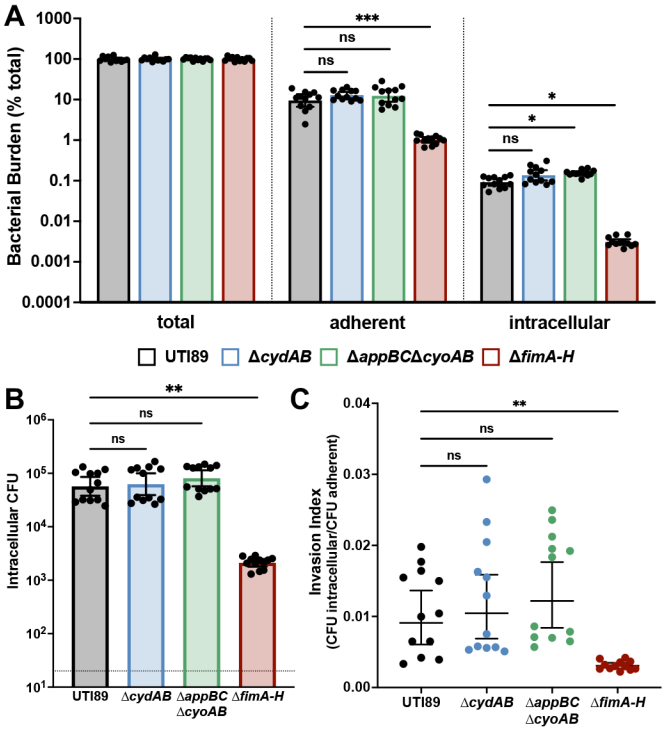

Figure 18: Cytochrome *bd* does not impact adherence or invasion of urothelial cells. (A) Relative titer of adherent and intracellular bacterial in infected urothelial cells; geometric mean ± 95% C.I.; Kruskal-Wallis test. (B) Intracellular bacterial colony forming units (CFUs); geometric mean ± 95% C.I.; Kruskal-Wallis test. (C) Invasion index; geometric mean ± 95% C.I.; Kruskal-Wallis test. Experiments were performed with a minimum of three biological replicates. Each point represents a biological replicate. * $p < 0.05$, ** $p < 0.01$, *** $p < 0.001$, **** $p < 0.0001$.

To define the role of cytochrome *bd* during intracellular infection of urothelial cells, we quantified intracellular bacterial bladder titer across the first six hours of infection. Wild-type and Δ*cydAB* have indistinguishable intracellular titers one hour post-infection, indicating cytochrome *bd* similarly does not impact bacterial invasion of urothelial cells *in vivo* (**Figure 16B**) (78). Whereas intracellular titers of wild-type and the complemented strain (Δ*cydAB* pCydABX) increase rapidly during the first six hours of infection, Δ*cydAB* intracellular titers remain static between one and three hours and only increase modestly thereafter, indicating loss of cytochrome *bd* impairs intracellular bacterial replication (**Figure 16B**). To validate these findings, we extracted genomic DNA from intracellular bacteria three hours post-infection and performed qPCR to quantify the copy number ratio of the origin of replication and terminus (*ori*:*ter* ratio) as a proxy for chromosomal replication rate (150). UPEC lacking cytochrome *bd* have a reduced *ori:ter* ratio as compared to wild-type, indicating cytochrome *bd* is required for efficient replication of intracellular bacteria (**Figure 16C**). Consistent with these results, loss of cytochrome *bd* causes gross deficiencies in the formation of IBCs (**Figure 16D**). Mice infected with Δ*cydAB* have nearly 10-fold fewer IBCs per bladder than those infected with wild-type (**Figure 16E**). Additionally, the IBCs formed by Δ*cydAB* are smaller and less populated than wild-type IBCs (**Figure 16F-G**). Together these data demonstrate that cytochrome *bd* is required for UPEC intracellular pathogenesis during bladder infection.

Biochemical dissection of cytochrome *bd* reveals niche dependent contributions to bladder pathogenesis

Cytochrome *bd* is a multifunctional respiratory complex that plays a critical role in the physiology and pathogenesis of a diverse group of bacteria (96, 99). In addition to functioning as a respiratory

oxidase, cytochrome *bd* possesses non-respiratory activities, most notably the ability to reversibly sequester and oxidatively degrade nitric oxide (99, 103). Because both respiration and nitric oxide tolerance are critical for UPEC colonization of the bladder (15, 89, 102), we sought to create a cytochrome *bd* variant that functionally separates the respiratory and non-respiratory activities of cytochrome *bd*, allowing us to biochemically define the contribution of cytochrome *bd* to intracellular bacterial pathogenesis.

Lysine-252 (K252) is a universally conserved periplasmic residue of CydA that facilitates quinol binding and aids in the coordination of heme b_{558}, the prosthetic group that accepts electrons from quinols (**Figure 19A**) (151, 152). Because this residue forms hydrogen bonds with heme b_{558} yet lacks contacts with heme *d*, the prosthetic group that interacts with nitric oxide (99, 152), we hypothesized that disrupting K252 would inhibit respiration without influencing the non-respiratory activities of cytochrome *bd*. Consistent with this, previous work demonstrated that a CydA_K252A variant has impaired quinol oxidation (V_{max} = 5% wild-type CydA) but near wild-type abundance of heme *d* (151). Furthermore, Rosetta predicts minimal destabilization of the CydA_K252A protein relative to wild-type CydA (Cartesian $\Delta\Delta G$ = 3.46 REU). Together, these analyses suggest the CydA_K252A variant has impaired respiratory activity but retains the ability to detoxify nitric oxide.

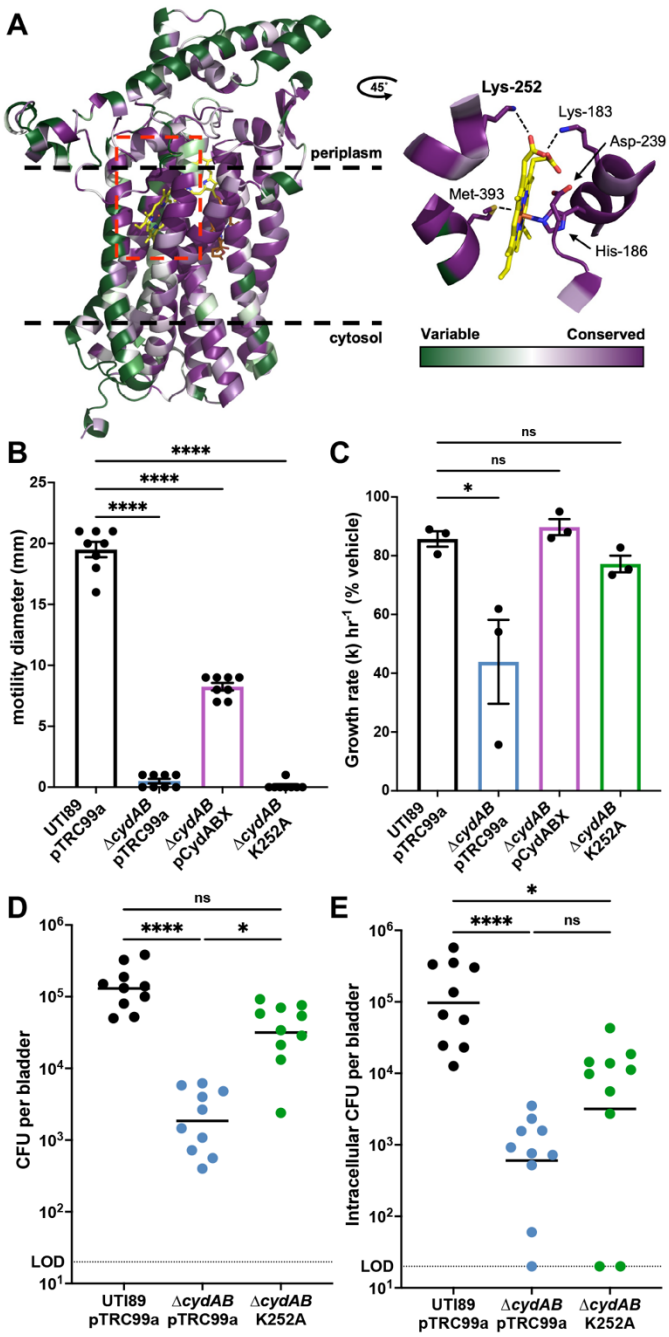

Figure 19: Biochemical dissection of cytochrome *bd* reveals niche dependent contributions to bladder pathogenesis. (A) Left, full-length model of cytochrome *bd* subunit CydA color coded according to ConSurf amino acid conservation score. Right, magnified image of the region surrounding heme b_{558} from a CydA cryo-EM structure (PDB ID: 6rko) depicting the coordinating residues. Dashed lines indicate approximate bounds of the inner membrane. Red box denotes magnified region shown in the right panel. (B) Flagellar motility radius; mean ± SEM; one-way ANOVA. (C) Bacterial growth rate in NOC-12 treated cultures compared to vehicle treated controls; mean ± SEM; one-way ANOVA. (D) Bladder bacterial titer 6 h.p.i.; geometric mean; Kruskal-Wallis test. (E) Bladder intracellular bacterial titer 6 h.p.i.; geometric mean; Kruskal-Wallis test. Each point represents a biological replicate. * p < 0.05, ** p <0.01, *** p <0.001, **** p <0.0001.

We then interrogated the energetics and nitric oxide sensitivity of Δ*cydAB* complemented with either pCydABX or CydA_K252A. Respiratory activity was assessed by measuring flagellar motility, a process energized by quinol oxidation via the proton gradient. Loss of cytochrome *bd* eliminates flagellar motility without impeding flagellar biosynthesis, indicating quinol oxidation by cytochrome *bd* energizes flagellar rotation (**Figure 19B and 20**). CydA_K252A fails to restore flagellar motility, in agreement with previous work indicating CydA_K252A does not substantially contribute to quinol oxidation (**Figure 19B**) (151). Nitric oxide sensitivity was assessed by measuring growth inhibition after treatment with nitric oxide donor NOC-12. Whereas deletion of cytochrome *bd* exacerbates nitric oxide mediated growth inhibition, complementation with either pCydABX or CydA_K252A restores nitric oxide tolerance to wild-type levels (**Figure 19C**). Collectively, these data demonstrate that the respiratory and non-respiratory activities of cytochrome *bd* are functionally separable, and that CydA_K252A is a respiration deficient variant that retains the ability to detoxify nitric oxide. Because cytochrome *bd* is widely distributed among pathogenic bacteria and K252 is universally conserved, we anticipate the CydA_K252A variant will have broad applicability toward studying the contribution of cytochrome *bd* to bacterial physiology.

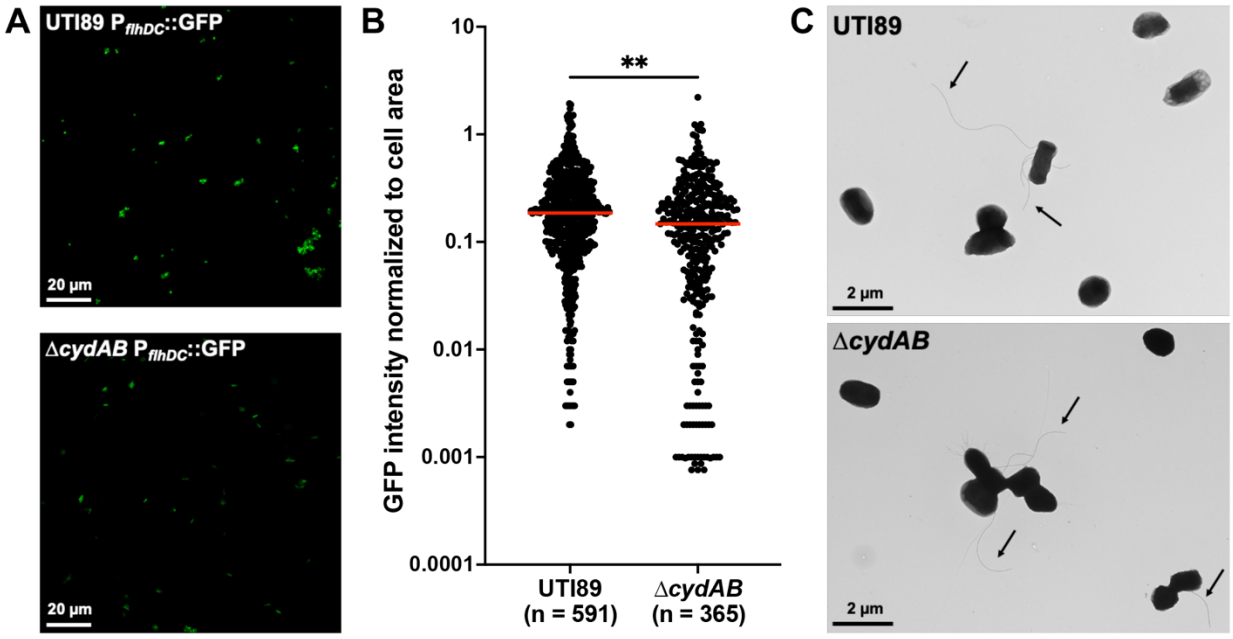

Figure 20: Loss of cytochrome *bd* does not impair flagellar biosynthesis. (A) Representative images of wild-type and Δ*cydAB* transformed with a transcriptional reporter for FlhDC, the master regulator of flagellar expression. (B) GFP intensity normalized to cell area; median; unpaired t test. (C) Representative transmission electron microscopy images of bacterial cells. Arrows indicate flagella. Images are representative of three biological replicates. * $p < 0.05$, ** $p < 0.01$, *** $p < 0.001$, **** $p < 0.0001$.

We next leveraged CydA_K252A to biochemically define the role of cytochrome *bd* in bladder pathogenesis. At six hours post-infection, complementation with CydA_K252A restores total bladder titers to wild-type levels, suggesting cytochrome *bd* supports colonization of the bladder lumen through its non-respiratory activities, presumably by detoxifying nitric oxide (**Figure 19D**). This is consistent with the fact that urine contains high concentrations of nitrogenous waste, and bacterial infection induces a robust influx of phagocytes into the bladder (74). Unexpectedly, complementation with CydA_K252A fails to restore intracellular bladder titers to wild-type levels, indicating cytochrome *bd* mediated quinol oxidation is required for intracellular pathogenesis (**Figure 19E**). These results demonstrate that the biochemical mechanisms by which cytochrome *bd* promotes bladder pathogenesis are niche dependent, and that cytochrome *bd* mediated respiration is specifically required during intracellular infection.

UPEC uses aerobic respiration during intracellular infection of urothelial cells

Based on the observation that cytochrome *bd* mediated quinol oxidation supports intracellular bacterial pathogenesis, we sought to quantify intracellular bacterial aerobic respiration. To do so, we measured the oxygen consumption rate (OCR) of intracellularly infected urothelial cells and observe a consistently elevated OCR relative to mock infected controls (**Figure 21A**). Importantly, because the respiratory chain of *E. coli* differs substantially from that encoded by mammalian cells, *E. coli* is insensitive to the complex I and III inhibitors rotenone and antimycin A (**Figure 22**) (91, 153, 154). As such, these agents specifically inhibit mammalian mitochondrial respiration and allow a direct measure of non-mitochondrial (*i.e.* bacterial) OCR. We observe a 69% increase in non-mitochondrial OCR of

intracellularly infected cells, indicating the elevated OCR is caused by intracellular bacterial oxygen consumption and not an off-target effect on mitochondrial respiration (**Figure 21B**).

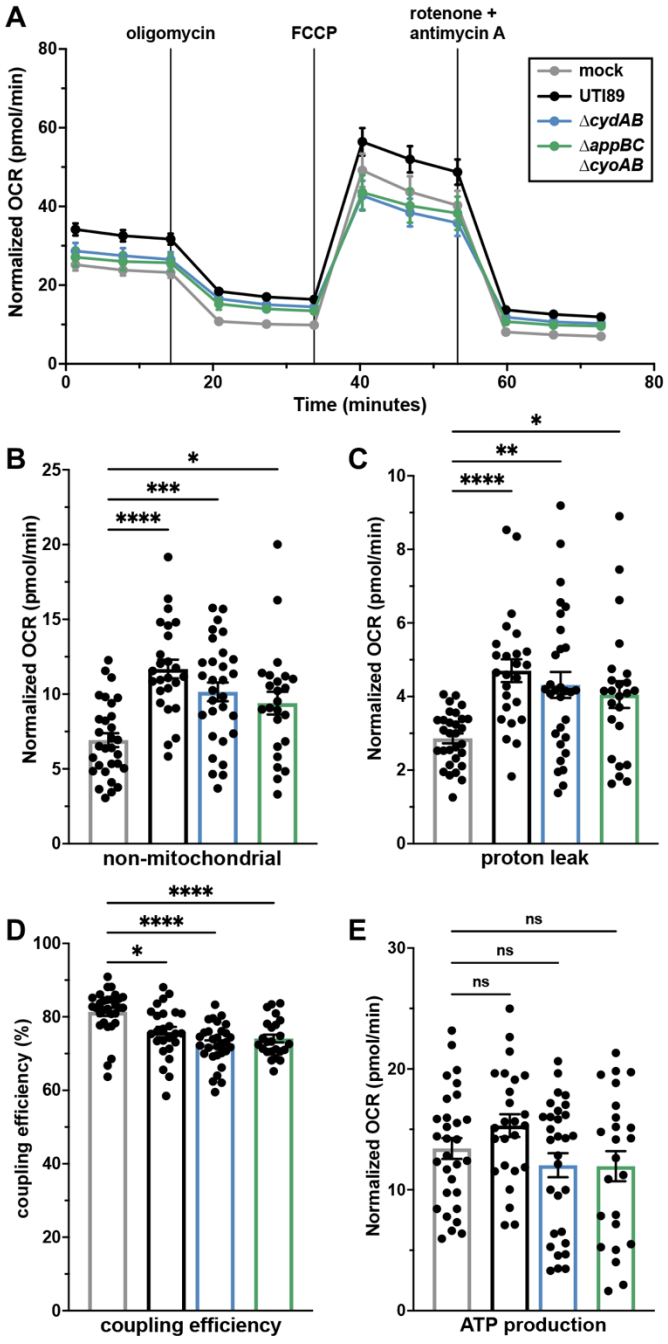

Figure 21: UPEC uses aerobic respiration during intracellular infection of urothelial cells. (A) Oxygen consumption rate (OCR) of intracellularly infected urothelial cells; mean ± SEM. (B-E) non-mitochondrial OCR (B), proton leak (C), mitochondrial coupling efficiency (D), and ATP production (E) measured by extracellular flux assays; mean ± SEM; Brown-Forsythe and Welch ANOVA. Each point in (B-E) represents a biological replicate. * $p < 0.05$, ** $p < 0.01$, *** $p < 0.001$, **** $p < 0.0001$.

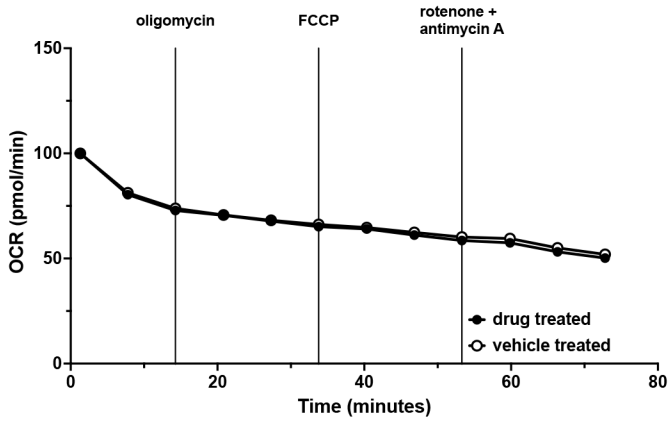

Figure 22: UPEC is not sensitive to rotenone or antimycin A. OCR readings of wild-type UPEC treated with vehicle (open circles) or treated with oligomycin, FCCP, and rotenone/antimycin A (closed circles) presented as percent OCR of time = 0; mean ± SEM. Data was fit to a one phase decay model ($R^2 > 0.9$ for both groups) and statistically analyzed by comparing *k* ($p = 0.6402$). Data is representative of five biological replicates, each with at least three technical replicates.

To determine the specific contribution of cytochrome *bd* to intracellular bacterial respiration, we measured OCR in urothelial cells intracellularly infected with Δ*cydAB* or Δ*appBC*Δ*cyoAB*. Both Δ*cydAB* and Δ*appBC*Δ*cyoAB* infected cells exhibit an intermediate phenotype between wild-type and mock infected cells, and the increase in non-mitochondrial OCR is partially reduced relative to wild-type infected cells (**Figure 21A-B**), indicating UPEC can use multiple respiratory oxidases during intracellular infection. Consistent with this, RT-qPCR analyses reveal intracellular bacterial populations have robust expression of both cytochromes *bd* and *bo*, and transcript encoding both respiratory oxidases is homogenously distributed within IBCs (Pearson correlation: 16S rRNA-*cyoA* = 0.93; 16S rRNA-*cydA* = 0.94) (**Figure 23**). Together these results suggest UPEC uses a mixed respiratory program to facilitate aerobic respiration within urothelial cells.

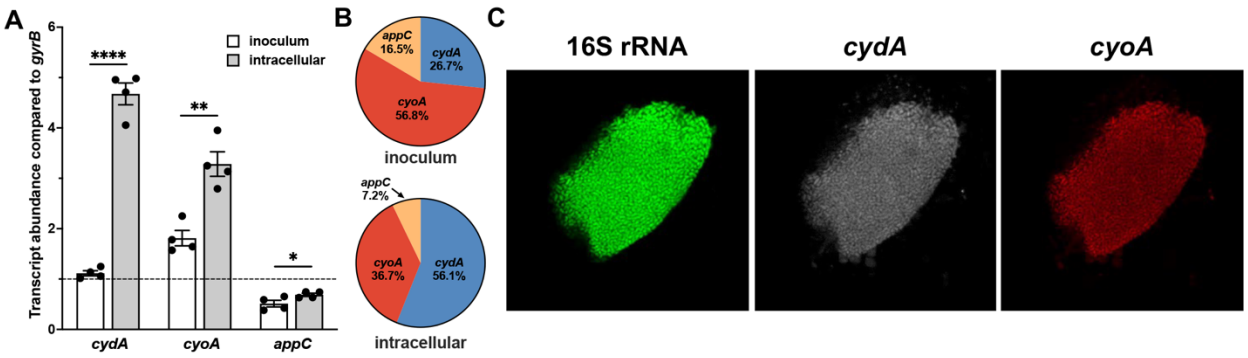

Figure 23: Expression of respiratory oxidases in intracellular bacterial populations. (A) Abundance of respiratory oxidase transcripts in the inoculum used for infections and intracellular bacterial populations compared to *gyrB*. Dotted line indicates *gyrB* abundance; mean ± SEM; unpaired t test. (B) Relative abundance of respiratory oxidase transcript in the inoculum and intracellular populations. (C) Representative peptide nucleic acid *in situ* hybridization (PNA-FISH) image of IBCs. Experiments were performed with a minimum of three biological replicates. Each point represents a biological replicate. * $p < 0.05$, ** $p < 0.01$, *** $p < 0.001$, **** $p < 0.0001$.

We next determined the influence of intracellular bacterial respiration on mitochondrial metabolism by interrogating mitochondrial electron transport chain efficiency. Intracellularly infected urothelial cells have increased proton leak and decreased coupling efficiency relative to mock infected cells, indicating intracellular infection impairs mitochondrial respiration (**Figure 21C-D**). Despite disruptions to the electron transport chain, intracellularly infected urothelial cells have similar ATP production as mock infected cells (**Figure 21E**), suggesting a compensatory mechanism allows urothelial cells maintain their energetic state during intracellular infection.

To further characterize the influence of intracellular infection on mitochondrial physiology, we performed structured illumination microscopy on intracellularly infected urothelial cells to analyze mitochondrial network morphology. In contrast to the punctate mitochondria observed in mock infected cells, we observe tubular mitochondrial networks in intracellularly infected cells (**Figure 24A**). Mitochondrial size and major axis length are increased in intracellularly infected cells as compared to mock infected cells (**Figure 24B-D**), indicating intracellular infection leads to an acute enhancement in mitochondrial fusion. Because mitochondrial fusion increases electron transport chain efficiency (155-157), these results suggest intracellularly infected urothelial cells may increase mitochondrial fusion to compensate for inefficient respiration.

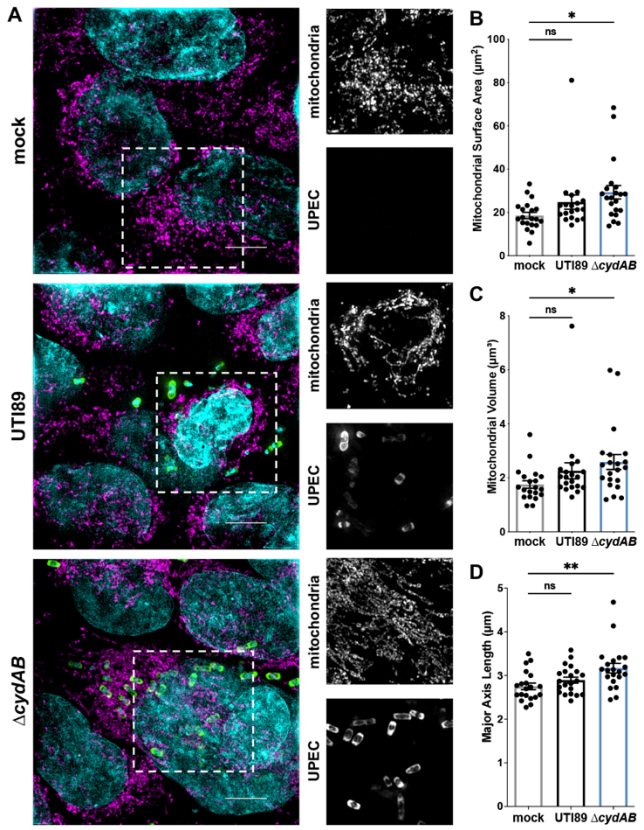

Figure 24: Intracellular bacterial infection enhances mitochondrial network fusion. (A) Representative structured illumination microscopy images of intracellularly infected or mock infected urothelial cells. Scale bar, 5 μm. Dashed box indicates area of interest shown in single color panels at right; cyan, DAPI; magenta, mitochondria; green, bacteria. (B-D) Quantification of mitochondrial surface area (B), volume (C), and major axis length (D) of intracellularly infected urothelial cells; mean ± SEM; one-way ANOVA. Each point represents the average value for an individual cell. Experiments were performed on at least three biological replicates. * $p < 0.05$, ** $p < 0.01$, *** $p < 0.001$, **** $p < 0.0001$.

Intracellular bacterial respiration induces a shift toward aerobic glycolysis

The oxygen affinity of cytochrome *bd* is approximately 1000-fold higher than that of both cytochrome *bo* and human cytochrome *c* oxidase, suggesting cytochrome *bd* promotes intracellular pathogenesis by allowing UPEC to scavenge oxygen in the hypoxic cytosol (91, 158). As such, we predicted intracellular bacterial oxygen consumption would deplete cytosolic oxygen, impede mitochondrial respiration, and induce a shift toward aerobic glycolysis. Indeed, several studies have identified Warburg-like metabolic shifts associated with intracellular bacterial infection of immune cells, and urothelial cells upregulate genes involved in glucose metabolism in response to IBC formation (81, 82, 156, 157). To test whether intracellular infection depletes cytosolic oxygen and promotes a shift toward aerobic glycolysis, we performed immunoblots on urothelial cells to quantify the abundance of

the hypoxia inducible transcription factor HIF-1. Consistent with this hypothesis, intracellularly infected cells have a 30% increase in HIF-1α protein abundance relative to mock infected cells (**Figure 25A**), indicating intracellular infection stabilizes HIF-1.

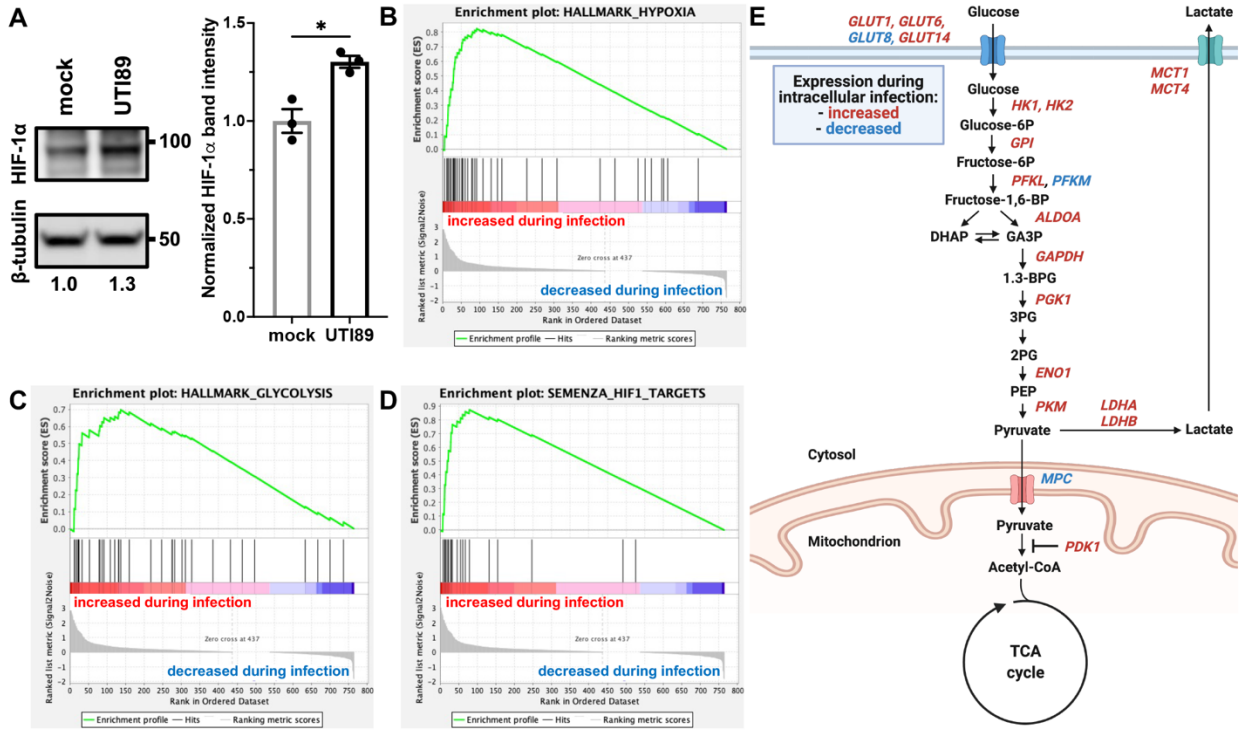

Figure 25: Intracellular infection of urothelial cells induces a shift toward aerobic glycolysis. (A) Right, HIF-1α immunoblot performed on intracellularly infected or mock infected urothelial cells. Left, Quantification of HIF-1α band intensity normalized to β-tubulin; mean ± SEM; unpaired t test. (B-D) Gene set enrichment analyses of hypoxia hallmark genes (B), glycolysis hallmark genes (C), and HIF-1 target genes (D). (E) Schematic depicting metabolic genes with significant differences in transcript abundance between intracellularly infected and mock infected cells. Each point represents a biological replicate. Experiments were performed with a minimum of three biological replicates.

To determine the metabolic consequences of intracellular infection, we next extracted RNA from intracellularly infected urothelial cells and transcriptionally profiled a panel of genes involved in metabolism and cellular stress response. In agreement with immunoblot data, gene set enrichment analyses reveal that intracellularly infected urothelial cells have elevated abundance of hypoxia and glycolysis related transcripts, including canonical HIF-1 targets (**Figure 25B-D and Appendices A-B**). Intracellularly infected cells have increased abundance of transcript encoding 3 glucose transporters, 9 glycolytic enzymes, lactate dehydrogenase, and two lactate exporters (**Figure 25E, 26A, and**

Appendices A-B). In addition, we observe decreased abundance of transcript encoding the mitochondrial pyruvate importers *MPC1* and *MPC2* as well as increased abundance of transcript encoding *PDK1* – a kinase that inactivates pyruvate dehydrogenase and antagonizes oxidative phosphorylation (**Figure 25E and 26A**).

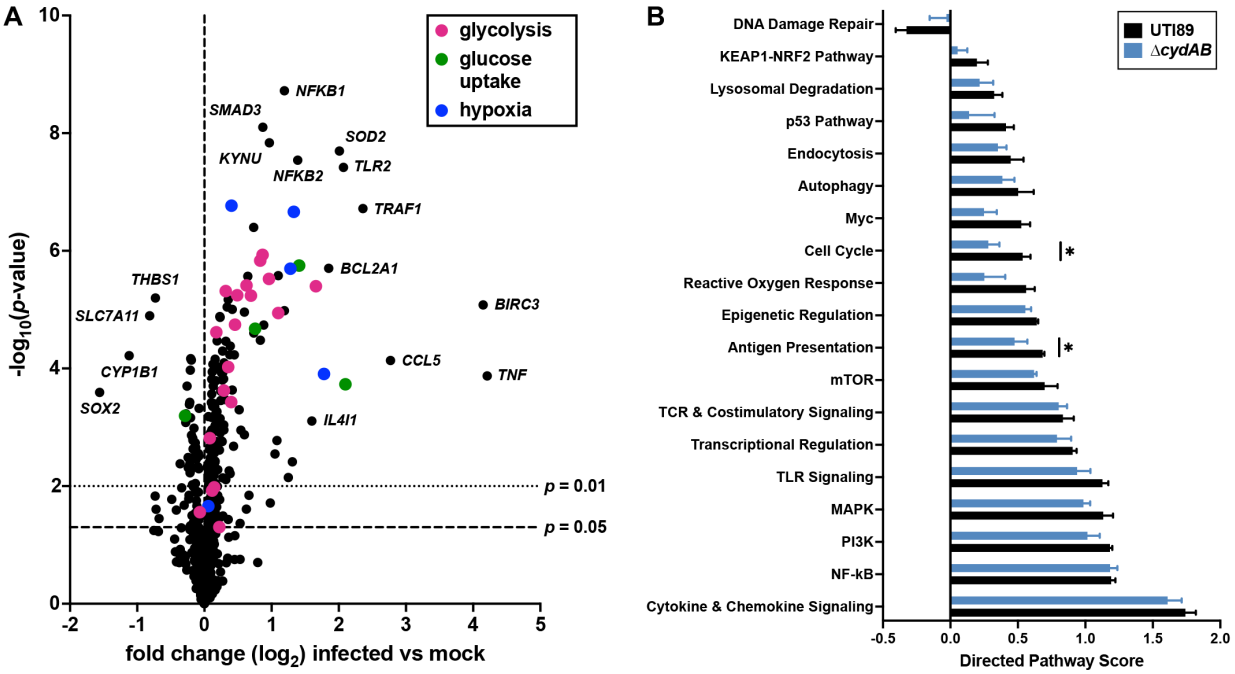

Figure 26: Intracellular infection modulates urothelial cell metabolism and immune signaling. (A) Volcano plot depicting changes in transcript abundance between wild-type and mock infected urothelial cells. Transcripts involved in glycolysis, glucose uptake, and hypoxia are denoted by color. (B) Directed pathway expression score for pathways not directly involved in central metabolism in wild-type and Δ*cydAB* infected compared to mock infected urothelial cells; mean ± SEM; unpaired t test. Data is representative of at least three biological replicates per group. * $p < 0.05$, ** $p < 0.01$, *** $p < 0.001$, **** $p < 0.0001$.

To define the role of cytochrome *bd* in these metabolic changes, we compared gene expression between wild-type and Δ*cydAB* infected urothelial cells. Intracellular infection with wild-type or Δ*cydAB* similarly increases the expression of pathways involved in the canonical urothelial cell response to infection – including NF-κB signaling, TLR signaling, and cytokine and chemokine signaling – suggesting infection with either strain elicits a similar overall immune response (**Figure 26B and Appendices A-B**) (71, 74). By contrast, deletion of cytochrome *bd* partially abrogates the increased expression of HIF-1 regulated metabolic genes (**Figure 27A-F and Appendices A-B**) and decreases

the extracellular acidification rate (ECAR) of intracellularly infected urothelial cells, a proxy for lactate secretion (**Figure 27G**), demonstrating intracellular bacterial respiration is necessary for this metabolic shift. Intriguingly, although both cytochromes *bd* and *bo* contribute to intracellular bacterial respiration (**Figures 21 and 23**), the basal ECAR of Δ*appBC*Δ*cyoAB* infected cells is similar to wild-type infected cells, indicating oxygen scavenging by cytochrome *bd* is primarily responsible for these alterations in urothelial cell metabolism (**Figure 27G**). Together, these results indicate intracellular bacterial respiration depletes oxygen from the urothelial cell cytosol, stabilizes HIF-1, and reprograms the metabolism of infected cells.

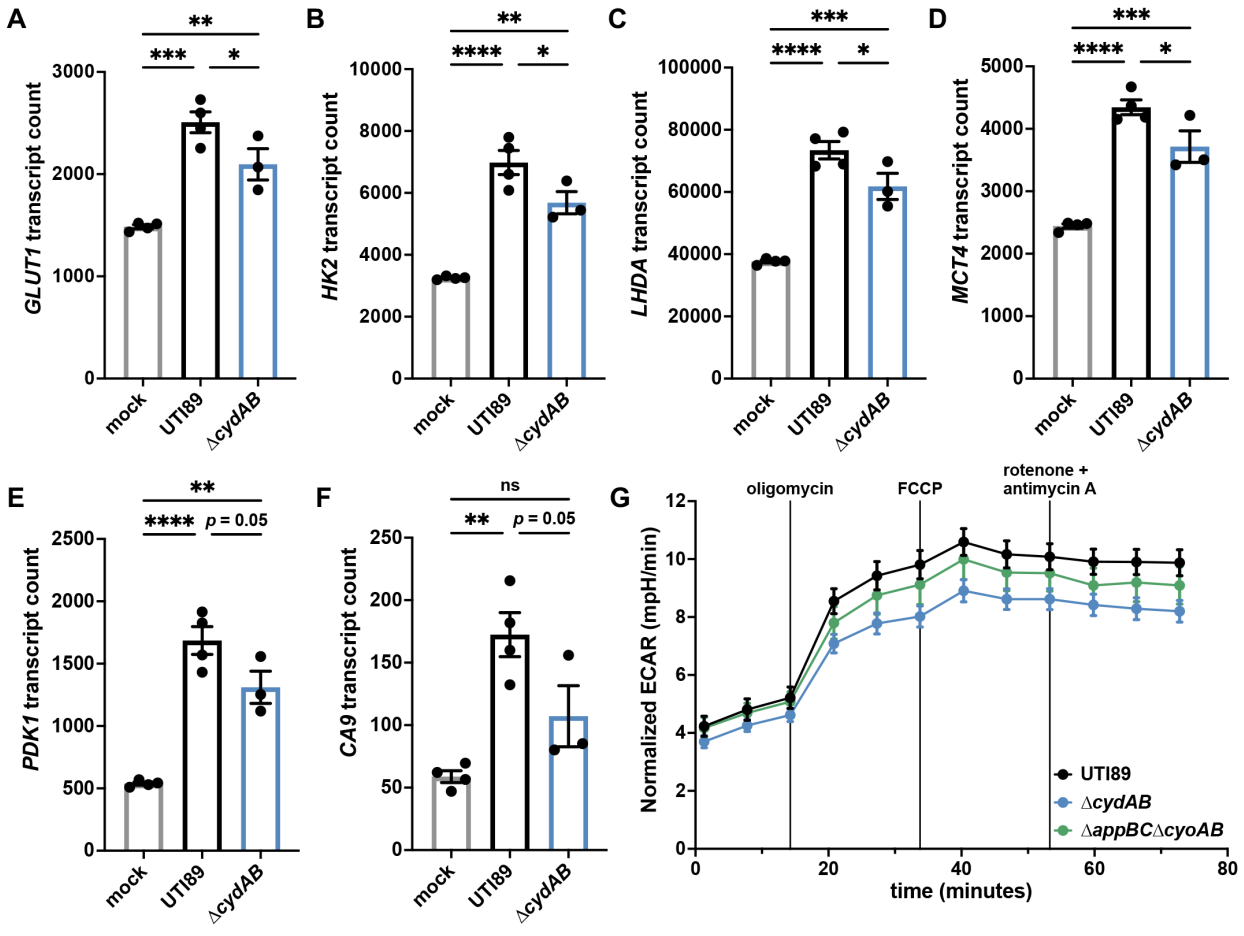

Figure 27: Shifts in urothelial cell metabolism are partially dependent on cytochrome *bd.* (A-F) Normalized counts of select HIF-1 regulated metabolic transcripts; mean ± SEM; one-way ANOVA. (F) Extracellular acidification rate (ECAR) of intracellularly infected urothelial cells; mean ± SEM. Each point represents a biological replicate. Experiments were performed on at least three biological replicates. * $p < 0.05$, ** $p < 0.01$, *** $p < 0.001$, **** $p < 0.0001$.

Intracellular bacterial respiration modulates urothelial cell survival

Previous work demonstrates that shifts toward aerobic glycolysis antagonize pro-apoptotic proteins and delay the onset of apoptosis in cancer and immune cells (159-161). As such, we hypothesized that HIF-1 dependent metabolic changes induced by intracellular infection would impede apoptosis, delay exfoliation of urothelial cells, and allow bacteria sufficient time to complete their intracellular lifecycle. To test this, urothelial cells were intracellularly infected with GFP-labelled UPEC, stained with the apoptosis marker annexin V, and analyzed by flow cytometry (**Figures 28A and 29**). Strikingly, intracellularly infected cells are approximately five-fold less likely to undergo apoptosis than uninfected cells in the same well (odds ratio 0.19; $p < 0.0001$) (**Figure 28A-B**). Consistent with these findings, during intracellular infection we observe increased mitochondrial fusion and increased transcript of two anti-apoptotic factors, *BIRC3* and *BCL2A1* (**Figures 24 and 26A**). These results indicate intracellular bacterial infection antagonizes apoptosis in urothelial cells.

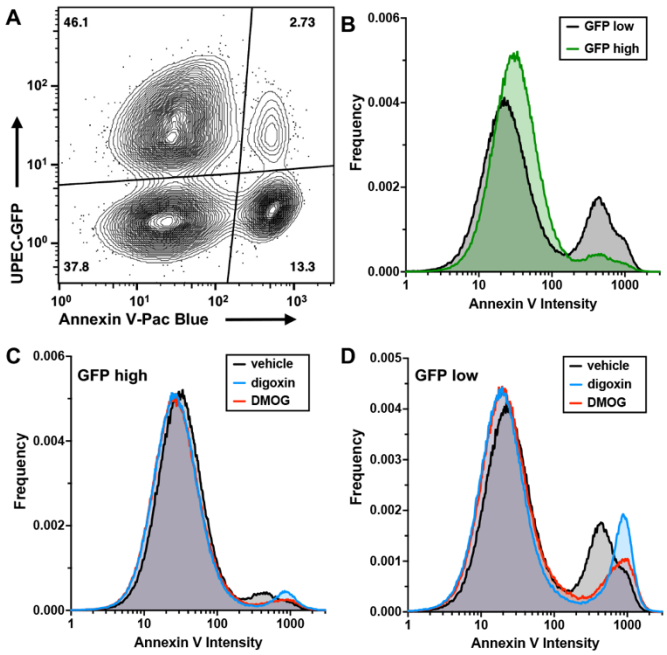

Figure 28: Reprogramming of host metabolism modulates urothelial cell survival during intracellular infection. (A) Representative flow cytometry plot depicting annexin V staining in intracellularly infected (GFP^{high}) and uninfected (GFP^{low}) urothelial cells from the same well. (B) Plot depicting annexin V staining intensity in intracellularly infected (GFP^{high}) and uninfected (GFP^{low}) urothelial cells. (C-D) Histograms depicting annexin V staining intensity in GFP^{high} (C) and GFP^{low} (D) urothelial cells treated with DMSO vehicle, DMOG, or digoxin at the time of infection. Experiments were performed with three biological replicates. * $p < 0.05$, ** $p < 0.01$, *** $p < 0.001$, **** $p < 0.0001$.

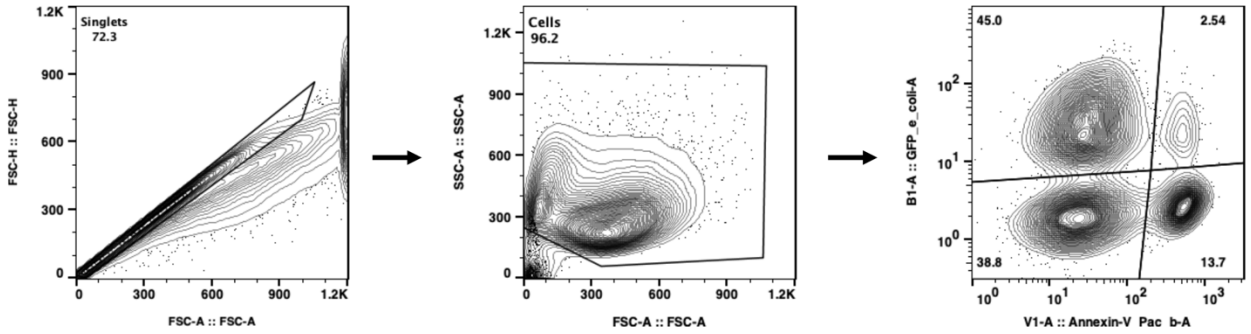

Figure 29: Flow cytometry gating strategy. Single cells were selected by gating on FSC-A and FSC-H. Debris and bacteria were subsequently excluded by gating out the FSC-A^{low}, SSC-A^{low} population. The remaining population was analyzed for UPEC (GFP) and annexin V (Pacific Blue). Because we are interested in quantifying cell death, dead cells were not specifically excluded from analyses.

To determine whether HIF-1 dependent metabolic changes influence urothelial cell fate during intracellular infection, we treated urothelial cells with dimethyloxalylglycine (DMOG) or digoxin at the time of infection to pharmacologically stabilize or inhibit HIF-1, respectively. Treatment with DMOG, a prolyl hydroxylase inhibitor that post-translationally stabilizes HIF-1α, reduces the number of apoptotic cells relative to vehicle treated controls (odds ratio 0.62, $p < 0.0001$) (**Figure 28C-D**), indicating HIF-1 dependent metabolic changes protect urothelial cells from apoptosis during intracellular infection. In agreement with these data, previous work demonstrates that stabilization of HIF-1 prior to infection has cytoprotective effects during urinary tract infection (162). By contrast, treatment with digoxin, a potent inhibitor of *HIF1A* translation, increases annexin V staining intensity without increasing the number of apoptotic cells (mean staining intensity of GFP^{high}/annexin^{high} cells: 586 and 821 RFU for vehicle and digoxin treated, respectively), suggesting inhibition of HIF-1 signaling accelerates the induction of apoptosis without causing more cells to commit to cell death pathways (**Figure 28C-D**). Together, these data indicate intracellular infection antagonizes urothelial cell apoptosis and identify HIF-1 as a regulator of urothelial cell fate during bladder infection.

DISCUSSION

These results collectively demonstrate that aerobic respiration is essential for the intracellular pathogenesis of UPEC during bladder infection. Although the need for aerobic metabolism during urinary tract infection is well established, it has remained unclear precisely how and why UPEC deploys aerobic respiratory enzymes during infection (87-89, 95). In this work, we determine that UPEC uses cytochrome *bd* to support bladder pathogenesis in a niche dependent manner, and that aerobic respiration supports the replication of bacteria during intracellular infection. Furthermore, intracellular bacterial aerobic respiration reprograms host cell metabolism, thereby protecting intracellular bacteria from urothelial exfoliation and preserving their replicative niche. From these data, we propose that although bladder infection induces a robust inflammatory response that initiates exfoliation of urothelial cells and limits bacterial proliferation, intracellular infection antagonizes urothelial cell apoptosis by reprogramming host cell metabolism (**Figure 30**). This bifurcation of urothelial cell fate allows UPEC to complete its intracellular pathogenic cascade while simultaneously exposing underlying bladder tissue layers for subsequent rounds of infection, thereby facilitating bacterial persistence in the bladder.

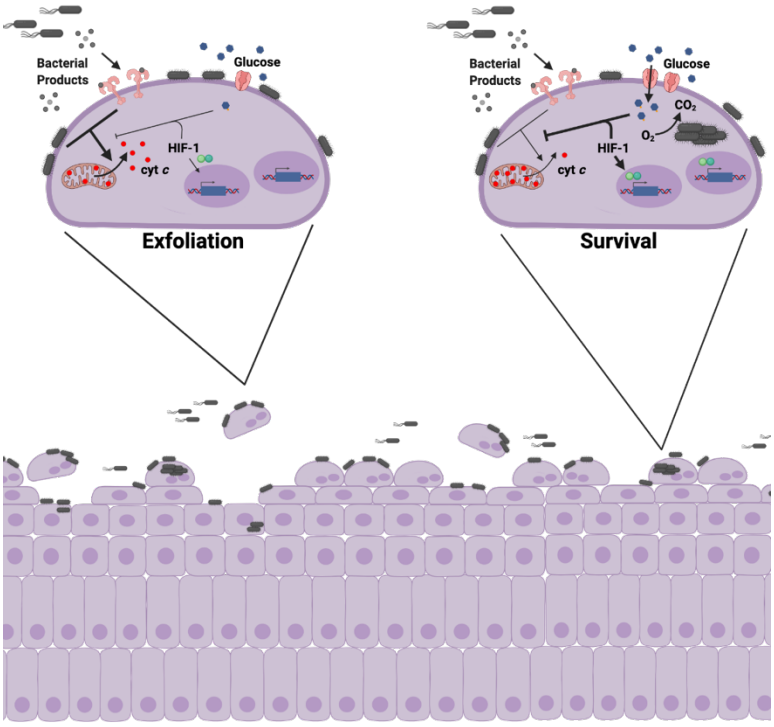

Figure 30: Proposed model. Schematic depicting the proposed model of how intracellular infection modulates urothelial cell metabolism and survival. Left, during bladder infection UPEC induces a strong

inflammatory response that triggers urothelial cell apoptosis and exfoliation. Urothelial cell exfoliation exposes underlying tissue layers to infection and promotes bacterial persistence in the bladder. Right, by consuming oxygen and activating HIF-1 signaling, intracellular bacterial aerobic respiration alters urothelial cell metabolism and antagonizes apoptosis, allowing UPEC to complete its intracellular infection cascade and evade exfoliation.

Our findings add to a growing body of work suggesting reprogramming of bacterial metabolism is a potential therapeutic strategy for treating bacterial infections and increasing the efficacy of antibiotics (41, 163-166). In the context of UPEC, previous work demonstrates that deletion of cytochrome *bd* reduces fitness in the bladder, impairs biofilm formation, and sensitizes bacteria to innate immune defenses and antibiotics (95, 102, 103, 149). Importantly, deletion of cytochrome *bd* does not kill UPEC, but rather reprograms its metabolism in a manner that impedes virulence in the bladder without influencing its ability to survive in the anaerobic gut (41, 87, 95, 149). As such, inhibition of cytochrome *bd* is expected to impose relatively minimal selective pressures on UPEC. Furthermore, several potent natural small molecule inhibitors of *E. coli* cytochrome *bd* have been identified, and inhibition of cytochrome *bd* is a promising strategy for the treatment of *Mycobacterium tuberculosis* (107, 167-169). In combination with data presented in this work, these studies collectively identify cytochrome *bd* as a target for the development of antimicrobial approaches to aid in the treatment of urinary tract infection and other bacterial diseases.

This study additionally has implications for clinical medicine, as it suggests that increases in urinary glucose will increase the risk of urinary tract infection by reducing urothelial exfoliation, facilitating intracellular bacterial replication, and promoting the formation of bacterial reservoirs in the bladder tissue. Consistent with this, diabetes is a known risk factor for urinary tract infection and increases in hemoglobin A1c are independently associated with increased risk of urinary tract infection in a dose-dependent manner (20, 170). Additionally, dapagliflozin – a sodium-glucose transport protein 2 (SGLT2) inhibitor that induces glycosuria – is associated with increased risk of urinary tract infection, and the United States Food and Drug Administration (FDA) has issued a warning regarding increased risk of severe urinary tract infections in patients taking SGLT2 inhibitors (20, 171-173). Future work is

needed to clarify the impact of glycosuria on bacterial pathogenesis in the bladder, particularly in the context of diabetes and use of SGLT2 inhibitors.

The results of this study clarify the role of aerobic respiration and cytochrome *bd* in UPEC pathogenesis in the urinary tract while simultaneously expanding our understanding of the metabolic requirements of intracellular bacteria. Through an integrated investigation of metabolism at the host-pathogen interface, this work identifies the metabolic basis for UPEC intracellular replication during bladder infection and reveals a mechanism by which UPEC subverts urothelial cell metabolism to enhance its intracellular pathogenesis and evade host defenses in the urinary tract.

MATERIALS AND METHODS

Bacterial Strains

All studies were performed in uropathogenic *E. coli* cystitis isolate UTI89 and isogenic derivatives created using the λ–Red recombinase system (143). Genetically manipulated strains, complementation constructs, plasmids, primers, and probes are listed in **Tables 2 and 3**. All deletion mutants and most plasmids were created and validated in previous studies (see **Table 2**). CydA_K252A was generated using the Q5 Site-Directed Mutagenesis Kit (New England BioLabs) according to manufacturer's protocols and verified by Sanger sequencing. Bacterial strains are stored at -80˚C in 50% glycerol and propagated from a single colony overnight in shaking lysogeny broth (LB) at 37˚C unless otherwise noted. Antibiotics were added during routine culture and during experiments as needed to maintain plasmids. For mouse and cell culture infections, bacterial cultures were grown in 10 mL static LB for 24 hours at 37˚C, sub-cultured 1:1,000 into 10 mL fresh LB and grown statically for another 24 hours. Cultures were normalized to optical density at 600 nm (OD_{600}) = 3.4 in PBS and diluted 1:10 in PBS prior to infection.

Name	Description	Source
UTI89	Wild-type UPEC cystitis isolate	Mulvey et al 2001; doi: 10.1128/IAI.69.7.4572-4579.2001

UTI89Δ*cydAB*	Cytochrome *bd* deletion mutant	Beebout et al 2019; doi: 10.1128/mBio.02400-18
UTI89Δ*appBC*Δ*cyoAB*	Cytochrome bd_2 and cytochrome *bo* deletion mutant	Beebout et al 2021; doi: 10.1038/s41522-021-00210-x
UTI89Δ*fimA-H*	Type 1 pilus deletion mutant	Kostakioti and Hadjifrangiskou et al 2012; doi: 10.1128/IAI.00283-12
pTRC99a	Empty vector	Amann et al 1988; doi: 10.1016/0378-1119(88)90440-4
pCydABX	Cytochrome *bd* complementation construct under native transcriptional control (pTRC99a derived)	Beebout et al 2019; doi: 10.1128/mBio.02400-18
CydA_K252A	Cytochrome *bd* complementation construct containing CydA_K252A variant under native transcriptional control (pTRC99a derived)	This study
pCOM::GFP	GFP expression plasmid	Lee and Falkow 1998; doi: 10.1128/IAI.66.8.3964-3967.1998
P_{flhDC}::GFP	FlhDC transcriptional reporter	Wright et al 2005; doi: 10.1128/IAI.73.11.7657-7668.2005

Table 2: Bacterial strains and plasmids used in Chapter 3.

Name	Sequence	Purpose	Source
cyoA_Fwd	CAATGCCCTGTTCCGGGTAGATG	qPCR	Beebout et al 2019; doi: 10.1128/mBio.02400-18
cyoA_Rev	ACGGTACCTATCTTAATCATCATCTTCC	qPCR	(95) Beebout et al 2019; doi: 10.1128/mBio.02400-18
cyoA probe	NED-TCGTCGTGTGCCAGCGGCTTG	qPCR	Beebout et al 2019; doi: 10.1128/mBio.02400-18
appC_Fwd	CGATGTCGCATTACGCTCG	qPCR	Beebout et al 2019; doi: 10.1128/mBio.02400-18
appC_Rev	GGTGCAGGTTCTGTTTGCCACT	qPCR	Beebout et al 2019; doi: 10.1128/mBio.02400-18
appC probe	NED-CTGCGTATGAAGTCGCGCAAG	qPCR	Beebout et al 2019; doi: 10.1128/mBio.02400-18
cydA_Fwd	GTGGCTACCGGTCTGACCATG	qPCR	Beebout et al 2019; doi: 10.1128/mBio.02400-18
cydA_Rev	CCAACCGAAGAAGAACAGACCTAC	qPCR	Beebout et al 2019; doi: 10.1128/mBio.02400-18
cydA probe	FAM-CGCTGGCAATCGAAGGTCTGATG	qPCR	Beebout et al 2019; doi: 10.1128/mBio.02400-18
gyrB_Fwd	GATGCGCGTGAAGGCCTGATTG	qPCR	Beebout et al 2019; doi: 10.1128/mBio.02400-18

gyrB_Rev	CACGGGCACGGGCAGCATC	qPCR	Beebout et al 2019; doi: 10.1128/mBio.02400-18
gyrB probe	VIC-ACGAACTGCTGGCGGA	qPCR	Beebout et al 2019; doi: 10.1128/mBio.02400-18
oriC_Fwd	CGCAACAGCATGGCGATAAC	qPCR	Haugan et al 2018; doi: 10.1038/s41598-018-33264-7
oriC_Rev	TTCGATCACCCCTGCATACA	qPCR	Haugan et al 2018; doi: 10.1038/s41598-018-33264-7
terC_Fwd	TCAACGTGCGAGCGATGAAT	qPCR	Haugan et al 2018; doi: 10.1038/s41598-018-33264-7
terC_Rev	TTGAGCTGCGATTCATCGAG	qPCR	Haugan et al 2018; doi: 10.1038/s41598-018-33264-7
rrsH PNA	AGTAATTCCGATTAACG – Lys (Atto532)	PNA-FISH	Beebout et al 2019; doi: 10.1128/mBio.02400-18
cydA PNA	CGATTGCCAGCG – Lys (Cy5)	PNA-FISH	Beebout et al 2019; doi: 10.1128/mBio.02400-18
cyoA PNA	CGTCGTGTGCCA – Lys (Atto425)	PNA-FISH	Beebout et al 2019; doi: 10.1128/mBio.02400-18
CydA_K252A_Fwd	GCAGAAAACCGCTCTGGCTGCTATCGAAG	CydA mutagenesis	This study
CydA_K252A_Rev	ACGTCGCCCATTTCGTAG	CydA mutagenesis	This study
SDM_seq_Fwd	GTCTGTTATTGTTCTGGGTGATG	CydA mutagenesis	This study
SDM_seq_Rev	CGTAAGGGATCTGGATCGC	CydA mutagenesis	This study

Table 3: Primers and probes used in Chapter 3.

Cell Lines

Cell culture infections were performed using 5637 human transitional bladder epithelial cells (ATCC HTB-9) originally derived from a 68-year-old white male with Grade II bladder carcinoma. 5637 cells (hereafter referred to as urothelial cells) were propagated and infected in RPMI 1640 (Gibco) supplemented with 10% fetal bovine serum (Gibco) unless otherwise noted. Urothelial cells were grown to confluence prior to infection.

Animal Models

All animal studies conform to regulatory standards and were approved by the Vanderbilt University Medical Center Institutional Animal Care and Use Committee (IACUC) (protocol: M1500017). Mice were co-housed in cages containing five animals, and each cage was randomly allocated to experimental groups. Mouse infections were performed as described previously (148). 6- to 7-week-old female C3H/HeN mice (Envigo) were transurethrally inoculated with 10^7 colony forming units (CFUs) of UPEC in 50 µL PBS. At pre-determined time points, mice were sacrificed, and organs were harvested into ice-cold, sterile PBS prior to endpoint experiments.

Mouse infections

As described previously, 6- to 7-week-old female C3H/HeN mice (Envigo) were transurethrally inoculated with 10^7 colony forming units (CFUs) of UPEC in 50 µL PBS (148). At pre-determined time points, mice were sacrificed, and organs were harvested into ice-cold, sterile PBS prior to endpoint experiments. To quantify total CFU per organ, organs were homogenized using an Omni tissue homogenizer and serially diluted. To quantify intracellular CFUs, bladders were washed in PBS and treated with 100 µg/mL gentamicin in PBS for 90 minutes. After gentamicin treatment bladders were washed in PBS, homogenized, serially diluted, and plated to quantify CFUs. For confocal laser scanning microscopy, bladders were stretched in PBS and fixed overnight at 4˚C in 3.2% paraformaldehyde. After fixation, bladders were washed in PBS, counter stained with Alexa Fluor 647 Phalloidin (ThermoFisher Scientific) and mounted with ProLong Diamond Antifade (ThermoFisher Scientific). Microscopy was performed on a Zeiss LSM 710 Confocal Microscope. IBCs were enumerated by manual counting using fluorescence microscopy and analyzed using BiofilmQ (v0.2.2) (174). Z-stacks were loaded into BiofilmQ, and intensity was normalized for each Z-stack analyzed. Global parameters of each IBCs were analyzed using default settings.

Cell culture infections

As described previously, for infection experiments bacteria were added to urothelial cell monolayers at a multiplicity of infection (MOI) of 5-10, centrifuged at 600 x *g* for 5 minutes to facilitate and synchronize attachment, and incubated for two hours at 37˚C in 5% CO_2 (47, 175). For intracellular infections, monolayers were washed thoroughly with PBS, and fresh RPMI 1640 containing 100 µg/mL gentamicin (Gibco) was added to each well to kill extracellular bacteria. Monolayers were incubated another two hours and washed with PBS prior to endpoint experiments. To quantify total CFUs, monolayers were lysed with 0.1% Triton X-100 (Fisher) and serially diluted. To quantify adherent CFUs, monolayers were washed three times in PBS to remove extracellular bacteria, lysed with 0.1% Triton X-100, and serially diluted. To quantify intracellular CFUs, monolayers were washed three times in PBS, and PBS containing 100 µg/mL gentamicin was added to each well to kill extracellular bacteria. After another 2 hours of incubation, monolayers were washed three times in PBS, lysed with 0.1% Triton X-100, and serially diluted.

Hemagglutination assays

Elaboration of type 1 pili was determined using mannose sensitive hemagglutination assays, as previously described (50). Cultures were grown statically at 37˚C for 24 hours in LB, sub-cultured 1:1,000 and grown another 24 hours statically at 37˚C. Cultures were normalized to OD_{600} = 1.0 in PBS, concentrated 10x, and resuspended in PBS or PBS with 4% mannose to competitively bind the type 1 pilus adhesin FimH. Concentrated culture was added to a 96 well plate and diluted in two-fold increments. Next, guinea pig erythrocytes (Innovative Research) were washed in PBS and suspended in PBS or PBS with 4% mannose. Normalized erythrocytes were added to diluted bacterial culture and incubated statically overnight at 4˚C. Hemagglutination titer was determined by measuring the lowest dilution that visibly inhibited hemagglutination.

Immunoblots

For FimA immunoblots, bacterial cultures were grown statically at 37˚C for 24 hours in LB, sub-cultured 1:1,000, grown another 24 hours statically at 37˚C, and normalized to OD_{600} = 1.0. Samples were boiled in SDS or boiled in acidified SDS to depolymerize FimA subunits. After transfer, membranes were stained with Ponceau S to ensure similar loading, blocked in 1% BSA 1% milk in TBST, and blotted with 1:5,000 rabbit FimA antisera (176) overnight at 4˚C. Membranes were then treated with 1:10,000 goat anti-rabbit IgG HRP conjugate (Promega) and developed using SuperSignal West Chemiluminescent Substrate (ThermoFisher Scientific). For HIF-1α immunoblots, urothelial cells were intracellularly infected or mock infected as described above and transferred to 4% oxygen to increase HIF-1α abundance. Cells lysed in RIPA buffer (Millipore Sigma) containing 0.2 μM PMSF and 50 μg total protein was loaded per sample. Membranes were blocked in 5% milk-TBST, blotted with 1:1,000 anti-HIF-1α (Cell Signaling Technologies; Rabbit mAb 14179) or 1:1,000 anti-β-tubulin (Cell Signaling Technologies; Rabbit mAb 2128) in 5% BSA-TBST with 0.02% sodium azide overnight at 4˚C, and treated with 1:5,000 goat anti-rabbit IgG HRP conjugate (Promega) in 5% milk-TBST. Membranes were stained with Ponceau S to ensure similar transfer and developed using SuperSignal West Chemiluminescent Substrate (ThermoFisher Scientific). Protein levels were calculated by normalizing HIF-1α band density to β-tubulin band density on imageJ.

Quantitative PCR

RNA was extracted using TRIzol Reagent (Invitrogen) according to manufacturer's protocols. 20 μg nuclease free glycogen (Millipore Sigma) was added to facilitate RNA precipitation. RNA was DNase treated using Turbo DNase I (Invitrogen), and reverse transcribed using SuperScript III Reverse Transcriptase (Invitrogen). cDNA was amplified in an Applied Biosystems StepOne Plus Real-Time PCR machine using TaqMan reagents. Relative fold difference in transcript abundance was determined using the $\Delta\Delta C_T$ method (145). Transcripts were normalized to *gyrB* abundance. For *ori*:*ter* qPCR, genomic DNA (gDNA) was isolated and treated with RNAse A using the Wizard Genomic DNA Purification Kit (Promega) following manufacturer's protocols. qPCR was performed using SYBR Green

(Applied Biosystems), and the *ori*:*ter* ratio was calculated by comparing the abundance of origin of replication and terminus sequences to gDNA extracted from late stationary phase bacteria (expected *ori*:*ter* ratio = 1) using the $\Delta\Delta C_T$ method (145, 150). All qPCR experiments were performed using cDNA or gDNA from at least three biological replicates. Each reaction was performed in technical triplicate at two different cDNA or gDNA concentrations. All primers and probes were validated in previous studies and are listed in **Table 3**.

Modeling of CydA

A full-length model of CydA was generated using Rosetta (v3.12) (177). The RosettaCM – Comparative Modeling protocol was followed as described (178) using the CydA FASTA sequence NCBI NP_415261.2 and templates PDB ID: 6rko and PDB ID: 6rx4 (152, 179). A transmembrane span file was generated using the RosettaMP application Span From PDB (MPSpanFromPDB) for PDB ID: 6rko (180, 181). The final model with the lowest score out of 1,000 was selected and used as the input for subsequent stability calculations and amino acid conservation analysis. Heme groups were manually added to the full-length model generated by RosettaCM for representative purposes. To do so, the full-length model was overlayed with a published cryo-EM structure (PDB ID: 6rko) using the ChimeraX (v1.2) MatchMaker tool and atom coordinates of 6rko were saved relative to the full-length model. Coordinates for the heme groups were then copied from 6rko into the full-length model. From MatchMaker, the root mean square deviation (RMSD) across all atom pairs was 1.128 Å.

Amino acid conservation analysis

CydA amino acid evolutionary sequence conservation was analyzed using ConSurf (182-184) and mapped onto the full-length model of CydA. Homolog search was performed using the HHMER algorithm and the UNIREF-90 database. 500 homologs with 50-99% sequence identity were automatically selected and aligned using the MAFFT-L-INS-I method. Conservation scores were calculated using a Bayesian method with the best fit evolutionary model (LG). Final graphical

representations and images were generated using PyMOL Molecular Graphics System (v2.0.7; Schrödinger, LLC).

Stability calculations of CydA_K252A

The free energy change of the CydA_K252A variant compared to wild-type CydA was modeled using Rosetta (v2021.38) (177). The Cartesian ΔΔG protocol was followed as described (185, 186) using the full-length model of CydA as the input, including all-atom refinement using the Rosetta Relax application (187-190) and using the mpframework_smooth_fa_2012_cart weights for membrane proteins (180). The relaxed model with the lowest score out of 100 was selected and the Rosetta energy change (ΔΔG) was then calculated as the average score difference between three iterations of CydA_K252A and wild-type models: $\Delta\Delta G = \Delta G_{K252A} - \Delta G_{WT}$. The final ΔΔG value was reported for the CydA_K252A variant in Rosetta energy units (REU). A mutation is classified as stabilizing if the change in free energy is ≤ -1, as destabilizing if the change is ≥ 1, and neutral if it falls between these values, with larger absolute values predicted to be more significant.

Analysis of flagellar motility

Flagellar motility was assessed by stabbing overnight cultures into 0.25% LB agar supplemented with 0.001% triphenyl tetrazolium chloride (TTC) and 100 µg/mL ampicillin. Plates were incubated for 7 hours at 37˚C, and flagellar motility was quantified by measuring the diameter of motility front. To analyze expression of the flagellar master regulator FlhDC, UTI89 and Δ*cydAB* were transformed with a FlhDC transcriptional reporter (P_{flhDC}::GFP), grown to mid-logarithmic phase, and imaged using confocal laser scanning microscopy. Expression of *flhDC* was determined by measuring GFP intensity on imageJ and normalizing to cell area. To visualize flagella, cells were extracted from 11-day old colony biofilms grown on 1.2X yeast extract casamino acids (YESCA) agar and normalized in PBS. Bacterial samples were fixed with 1% glutaraldehyde (Electron Microscopy Sciences) and allowed to absorb onto freshly glow discharged formvar/carbon-coated copper grids for 10 minutes. Grids were

then washed in dH_2O and stained with 1% aqueous uranyl acetate (Ted Pella Inc.) for one minute. Excess liquid was gently wicked off and grids were allowed to air dry. Samples were viewed on a JEOL 1200EX transmission electron microscope (JEOL USA) equipped with an AMT 8-megapixel digital camera (Advanced Microscopy Techniques).

Nitric oxide growth inhibition assay

Overnight cultures were diluted to OD_{600} = 0.05 in LB containing 100 µg/mL ampicillin. After two hours of growth, cultures were split into two flasks. One flask was treated with 0.5 mM nitric oxide donor NOC-12 (Millipore Sigma), and the other flask was treated with 0.1 M NaOH vehicle. OD was measured every hour for 8 hours. Data were fit to the Gompertz growth equation ($R^2 > 0.99$ for all replicates) on GraphPad Prism, and growth inhibition was calculated by quantifying the percent change in growth rate constant (*k*) in NOC-12 and vehicle treated controls.

PNA-FISH

Peptide nucleic acid *in situ* hybridization (PNA-FISH) experiments were performed as described previously (95, 146). Infected bladders were harvested six hours post-infection, stretched in PBS, and fixed in 3.2% paraformaldehyde at 4˚C overnight (148). Bladders were washed in PBS and treated with PNA-FISH probes complementary to RNA encoding *cydA* (cytochrome *bd*), *cyoA* (cytochrome *bo*), and *rrsH* (16S rRNA) in hybridization solution for 60 minutes at 60˚C. After hybridization, bladders were washed in 60˚C wash solution for 30 minutes, mounted in ProLong Diamond (Invitrogen), and imaged by confocal laser scanning microscopy. Pearson correlation between 16S rRNA, *cydA*, and *cyoA* staining intensity was determined using the Coloc2 plug-in on FIJI with default settings. Wash solution: 5 mM Tris-HCl (pH 7.4), 15 mM NaCl, and 1% Triton X-100. Hybridization solution: 10% (w/v) dextran sulfate, 30% formamide, 50 mM Tris-HCl (pH 7.4), 10 mM NaCl, 5 mM EDTA, 0.1% Triton X-100, 200 nM each PNA-FISH probe.

Extracellular flux assays

Extracellular flux assays were performed using an Agilent Seahorse XFe96 Analyzer with the Mito Stress Test kit (Agilent) (191). HTB-9 urothelial cells were grown to confluency in an Agilent Seahorse XF96 cell culture microplate and infected at an MOI of 5-10 as described above. Cultures were incubated at 37˚C in 5% CO_2 for 2 hours, washed in PBS, and the media was replaced with Seahorse XF RPMI (Agilent) containing 100 µg/µL gentamicin, 10 mM glucose, 2 mM glutamine, and 1 mM pyruvate. After changing the media, cells were incubated for one hour in 5% CO_2 and transferred to a non-CO_2 incubator for one hour. Cells were treated with oligomycin (1.5 µM), FCCP (0.5 µM), and rotenone/antimycin A (0.5 µM). Raw OCR and ECAR values were normalized using Seahorse Wave software (Agilent) to the number of eukaryotic cells per well as determined by a Cytation 5 imaging reader (BioTek). Bacterial extracellular flux assays were adapted from previous reports (192). Agilent Seahorse XF96 cell culture microplates were coated in 15 µL 1 mg/mL poly-D-lysine (Millipore Sigma) in 100 mM Tris HCl pH 8.4. After overnight drying, plates were washed twice in sterile water. To assess the impact of mitochondrial targeting drugs on bacterial OCR, cultures were grown to mid-logarithmic phase in Seahorse XF RPMI (Agilent) containing 10 mM glucose, 2 mM glutamine, and 1 mM pyruvate. 10^7 CFU were added to each well, and attachment was facilitated by centrifugation at 4,000 rpm for 10 minutes. Bacteria were treated with oligomycin (1.5 µM), FCCP (0.5 µM), and rotenone/antimycin A (0.5 µM) or mock treated with vehicle. Following standard quality control practices, each well was inspected prior to analysis for flags, failures, or aberrant response to drug treatment, and a subset of wells was excluded from subsequent analysis. Criteria were established prior to analysis and applied evenly across samples without consideration of experimental group. Parameter calculation was performed using Seahorse Analytics software (Agilent).

Mitochondrial imaging and analysis

Urothelial cells were intracellularly infected at an MOI 5-10 or mock infected as described above. Cells were washed in PBS and fixed in 4% paraformaldehyde for 20 minutes at room temperature followed

by permeabilization in 1% Triton-X-100 for 5 minutes at room temperature. After blocking in 10% BSA, immunostaining was performed with anti-HSP60 (1:200; Cell Signaling Technologies; 12165S) and anti-rabbit IgG Alexa Fluor 546 (1:500; ThermoFisher Scientific; A10040). Super-resolution mitochondrial images were acquired using a Nikon SIM microscope equipped with a 1.49 NA 100x Oil objective and Andor DU-897 EMCCD camera. Quantification of mitochondrial morphology was performed in NIS-Elements (Nikon) as described previously (193). Mitochondria were segmented in 3D and skeletonized using the resulting binary 3D mask. All mitochondria within each cell were averaged resulting in one data point per cell. Acquisition and analysis of mitochondrial imaging data was performed by a blinded experimenter.

Transcriptional profiling

RNA was extracted was intracellularly infected urothelial cells using TRIzol Reagent (Invitrogen) according to manufacturer's protocols. 20 µg nuclease free glycogen (Millipore Sigma) was added to facilitate RNA precipitation. 100 ng purified RNA (20 ng/µL) was hybridized for 20 hours and analyzed using the nCounter Human Metabolic Pathways Panel (NanoString Technologies) according to manufacturer's protocols. RNA was analyzed from at least three biological replicates per condition. Raw data were normalized and subjected to background thresholding using default settings. Normalized data were analyzed using the nCounter Advanced Analysis platform (v2.0.134) plugin for nSolver using default settings (Benjamini-Yekutieli method). Gene set enrichment analysis were performed as described previously (194). Raw NanoString read counts were normalized using the nSolver Analysis Software (v4.0) and used as input expression files. Data were annotated using the Human Gene Symbol with Remapping MSigDB (v7.4) Chip platform and analyzed under default settings using HALLMARK_GLYCOLYSIS, HALLMARK_HYPOXIA, or SEMENZA_HIF1_TARGETS gene sets obtained from the Broad Institute Molecular Signatures Database (v7.4). Transcriptional profiling data has been deposited in the Gene Expression Omnibus (GEO) database (accession: GSE188981) and is also contained in **Appendix A**.

Flow Cytometry

Urothelial cells were intracellularly infected with UTI89 pCOM::GFP at an MOI 5-10 as described above. Urothelial cells were treated with 100 μM dimethyloxalylglycine (DMOG; Millipore Sigma), 100 nM digoxin (Millipore Sigma), or DMSO vehicle at the time of infection. Infected monolayers were washed in PBS and homogenized with 0.25% Trypsin-EDTA (Gibco). Single cell suspensions were sedimented, washed in cold PBS, sedimented, and stained with Annexin V Pacific Blue (ThermoFisher Scientific) in annexin binding buffer for 15 minutes according to manufacturer's protocols. Cells were analyzed using a MACSQuant 10 Analyzer (Miltenyi Biotec). At least 300,000 cells were analyzed per replicate. Data analysis was performed in FlowJo (v10.0.7r2). Single cells were selected by gating on FSC-A and FSC-H. Debris and bacteria were subsequently excluded by gating out the FSC-A^{low}, SSC-A^{low} population. The remaining population was analyzed for UPEC (GFP) and annexin V (Pacific Blue). Because we are interested in quantifying cell death, dead cells were not specifically excluded from analyses. The gating strategy is depicted in **Figure 29.**

Statistical analyses

All experiments were performed using a minimum of three biological replicates. Power analyses were performed to determine group size for mouse infection and extracellular flux assays using the ClinCalc browser-based calculator. For mouse infections, power analyses indicate a group size of at least seven is sufficient to detect a 25% difference in mean CFU between test groups, assuming a standard deviation equal to 20% the mean with a power of 90%. For extracellular flux assays, power analyses indicate a group size of at least 21 would be sufficient to detect a 10% difference in mean between test groups, assuming a standard deviation equal to 10% the mean with a power of 90%. Odds ratio calculations were performed using the MedCalc browser-based calculator. All other statistical analyses were performed in GraphPad Prism. All statistical tests are two-tailed unless otherwise noted. Details

of group size, test used, error bars, and statistical significance cutoffs are presented in figure legends and text.

ACKNOWLEDGMENTS

The authors would like to thank Kelsey Voss and Hope Woods for technical assistance and helpful advice. This work was supported by National Institutes of Health (NIH) grants F30AI150077 (CJB), T32GM007347 (CJB, BIR), F99NS125829 (GLR), F30CA247202 (BIR), F32CA250258 (AMB), T32AI112541 (GHM), T32GM007569 (JRB), R01AI127793 (WJC), R01AI101171 (WJC), R01DK105550 (JCR), R35GM128915 (VG), RF1MH123971 (VG), R01AI107052 (MH), P20DK123967 (MH), and the Howard Hughes Medical Institute Gilliam Fellowship (GLR). Transmission electron microscopy was performed by Wandy Beatty at the Molecular Microbiology Imaging Facility (Washington University in St. Louis). Confocal laser scanning and structured illumination microscopy were performed at the Vanderbilt Cell Imaging Shared Resource, which is supported by NIH grant DK20593. NanoString analysis was performed at the Vanderbilt Technologies for Advanced Genomics core facility, which is supported by NIH grants UL1RR024975, P30CA68485, P30EY08126, and G20RR030956. Access to the Vanderbilt Advanced Computing Center for Research and Education was supported in part by NIH grants S10RR031634 and S10OD023680. Some images were created using BioRender.com.

CHAPTER 4

Cytochrome *bd* Promotes Biofilm Antibiotic Tolerance by Regulating Accumulation of Noxious Chemicals

Beebout CJ, Sominsky LA, Van Horn GT, and M Hadjifrangiskou. Cytochrome *bd* promotes biofilm antibiotic tolerance by regulating accumulation of noxious chemicals. npj Biofilms and Microbiomes 2021. PMID: 33863914. © 2021 Beebout et al.

ABSTRACT

Nutrient gradients in biofilms cause bacteria to organize into metabolically versatile communities capable of withstanding threats from external agents including bacteriophages, phagocytes, and antibiotics. We previously determined that oxygen availability spatially organizes respiration in uropathogenic *Escherichia coli* biofilms, and that the high affinity respiratory quinol oxidase cytochrome *bd* is necessary for extracellular matrix production and biofilm development. In this study we investigate the physiologic consequences of cytochrome *bd* deficiency in biofilms and determine that loss of cytochrome *bd* induces a biofilm-specific increase in expression of general diffusion porins, leading to elevated outer membrane permeability. In addition, loss of cytochrome *bd* impedes the proton mediated efflux of noxious chemicals by diminishing respiratory flux. As a result, loss of cytochrome bd enhances cellular accumulation of noxious chemicals and increases biofilm susceptibility to antibiotics. These results identify an undescribed link between biofilm respiration and stress tolerance, while suggesting the possibility of inhibiting cytochrome *bd* as an anti-biofilm therapeutic approach.

INTRODUCTION

Biofilms are multicellular bacterial communities commonly encountered in the environment and during infection. Because bacteria in biofilms are intrinsically resistant to a variety of stressors, including antibiotics, phagocytes, and bacteriophages, the ability to form biofilms is a critical bacterial survival strategy (53, 59-61, 195-197). Accordingly, the vast majority of bacteria in the environment and in the human body – up to 80 percent according to recent estimates (198) – are believed to exist in the biofilm state. Due to the stress tolerance of biofilms and the lack of biofilm-specific therapies, a biofilm associated infection typically necessitates chronic suppressive antibiotic treatment or surgical removal of the infected material (199). Improvements in anti-biofilm therapeutics are critically needed and would greatly advance our ability to reduce infection burden.

Within biofilms, bacteria consume or alter chemicals as they diffuse through the community, thus generating a variety of nutrient gradients that ensure individual bacteria are exposed to highly variable local environmental conditions (60). This environmental heterogeneity induces bacteria to differentiate into metabolically distinct, and oftentimes cooperative, subpopulations which enhance the overall resilience and versatility of the community (54, 60, 61, 63, 120). We previously hypothesized that the presence of oxygen gradients in biofilms would generate differentially respiring subpopulations, each of which uniquely contributes to biofilm development. Indeed, our work with uropathogenic *E. coli* (UPEC) – the primary cause of urinary tract infections and one of the most common human bacterial pathogens (10-12) – indicates that differential oxygen availability across biofilm regions leads to heterogenous expression of respiratory enzymes, with the aerobic quinol oxidases being the most abundantly expressed (**Chapter 2**) (95).

E. coli is a facultative anaerobe that encodes a modular electron transport chain containing a multitude of interchangeable dehydrogenases, quinol electron carriers, and terminal oxidases/reductases (91, 93). This architecture provides *E. coli* an enormous degree of metabolic flexibility, allowing bacteria to colonize diverse niches. Despite being a facultative anaerobe, previous

studies establish that UPEC requires aerobic respiration during infection and to form biofilms (**Chapters 2 and 3**) (54, 83, 87-90, 95). During bladder infection, UPEC consumes amino acids which feed into the TCA cycle to energize the aerobic respiratory chain (87-89). UPEC encodes three aerobic respiratory quinol oxidases: one proton pumping heme-copper oxidase, cytochrome *bo*, and two non-proton pumping *bd*-type oxidases, cytochrome *bd* and cytochrome bd_2 (91, 96). Cytochrome *bo* is a low oxygen affinity respiratory oxidase transcriptionally and biochemically optimized for use under atmospheric oxygen tensions (200-202). By contrast, the *bd*-type oxidases have high oxygen affinity and are optimized for use under low oxygen tensions (200-202). Importantly, the *bd*-type oxidases also provide resistance against oxidative and nitrosative stress, suggesting these enzymes may play a critical role in enhancing stress tolerance under microaerobic conditions encountered in biofilms and the urinary tract (99, 102, 103).

Given the importance of aerobic respiration to UPEC pathogenesis and biofilm formation, as well as the oxygen regulated transcriptional control of respiratory oxidases, we previously investigated the spatial distribution of respiration in biofilms (95). In agreement with studies in *Pseudomonas aeruginosa*, we determined that expression of the two most abundant oxidases, cytochrome *bd* and *bo*, is inversely correlated in the community along the biofilm oxygen gradient, suggesting *E. coli* biofilms contain differentially respiring subpopulations (**Chapter 2**) (95, 123). We then sought to disentangle the contributions of each respiratory oxidase to biofilm physiology. Surprisingly, despite robust expression of all three aerobic respiratory oxidases, only loss of cytochrome *bd* has any significant effect on biofilm development. Cytochrome *bd* deficiency induces severe architectural disturbances in biofilms and reduces their ability to prevent external stressors from entering the biomass (95). Deletion of the locus that encodes cytochrome *bd* leads to upregulation of the low-affinity oxidase cytochrome *bo* and impairs biofilm development without compromising ATP levels (95). This study established the presence of differentially respiring subpopulations in *E. coli* biofilms, and argues respiratory heterogeneity is a fundamental contributor to biofilm physiology.

In this work we aimed to determine how cytochrome *bd* expressing biofilm subpopulations contribute to *E. coli* biofilm physiology. To do so, we interrogated and compared the cellular physiology of cytochrome *bd* deficient cells in the planktonic and biofilm state. We determine that loss of cytochrome *bd* increases the abundance of multiple outer membrane proteins in biofilm cells, including general diffusion porins responsible for antibiotic uptake. Consequently, cytochrome *bd* deficient biofilm cells have increased outer membrane permeability and more readily take up noxious chemicals from the environment. In addition to enhancing cellular uptake of noxious chemicals, loss of cytochrome *bd* impairs their efflux by impeding the proton dependent activity of resistance-nodulation-division (RND) efflux pumps and possibly other tripartite export proteins. As a result, loss of cytochrome *bd* increases biofilm susceptibility to multiple clinically relevant antibiotics. Interestingly, this increased sensitivity is a biofilm-specific phenomenon, as deletion of cytochrome *bd* has no effect on antibiotic susceptibility in planktonic cells. This study reveals a previously undescribed link between respiration and biofilm stress tolerance in *E. coli* and suggests the possibility of inhibiting cytochrome *bd* as a therapeutic strategy for preventing and treating urinary tract infections.

RESULTS

Loss of cytochrome *bd* increases biofilm antibiotic sensitivity

We previously determined that uropathogenic *E. coli* (UPEC) exhibits marked respiratory heterogeneity in biofilms, and that loss of cytochrome *bd* – but not other respiratory quinol oxidases – induces significant disruptions to biofilm development and urinary tract infection pathogenesis (**Chapters 2 and 3**) (95). Furthermore, we demonstrated that these disruptions are solely attributable to cytochrome *bd* deficiency, as extrachromosomal complementation of Δ*cydAB* with a plasmid encoding the *cydABX* operon under native transcriptional control fully rescues the observed biofilm deficits (95). Based on these observations, we hypothesized that cytochrome *bd* is necessary for the formation of metabolically versatile biofilm communities capable of withstanding antibiotics and other

external stressors. To test this, we first evaluated the effects of antibiotics on biofilms formed by the well-characterized uropathogenic *E. coli* cystitis isolate UTI89 and an isogenic mutant strain lacking cytochrome *bd* (Δ*cydAB*) (95).

A recent meta-analysis demonstrates that measuring biofilm antimicrobial susceptibility using a single method or a single drug concentration is often inadequate due to a high degree of variability between methods (203). As such, we sought to investigate the susceptibility of Δ*cydAB* biofilms antibiotic susceptibility across a range of conditions. First, we grew polyvinyl chloride (PVC)-associated biofilms for 48 hours, treated with a panel of antibiotics for another 72 hours, and measured overall biofilm abundance by the crystal violet assay (204). Treatment of wild-type biofilms with supralethal doses of β-lactams (ampicillin), aminoglycosides (gentamicin), or fluoroquinolones (ciprofloxacin) led to a 40 – 75 percent reduction in total biomass but did not eradicate the biofilm, highlighting the resilience of biofilms in the face of our current therapeutic strategies (**Figure 31A**). After normalizing biomass to the untreated control of each strain, we determined both strains have similar relative reductions in biomass after treatment with β-lactams or fluoroquinolones, but Δ*cydAB* biofilms are significantly more susceptible to aminoglycosides than the parental strain (**Figure 31A**).

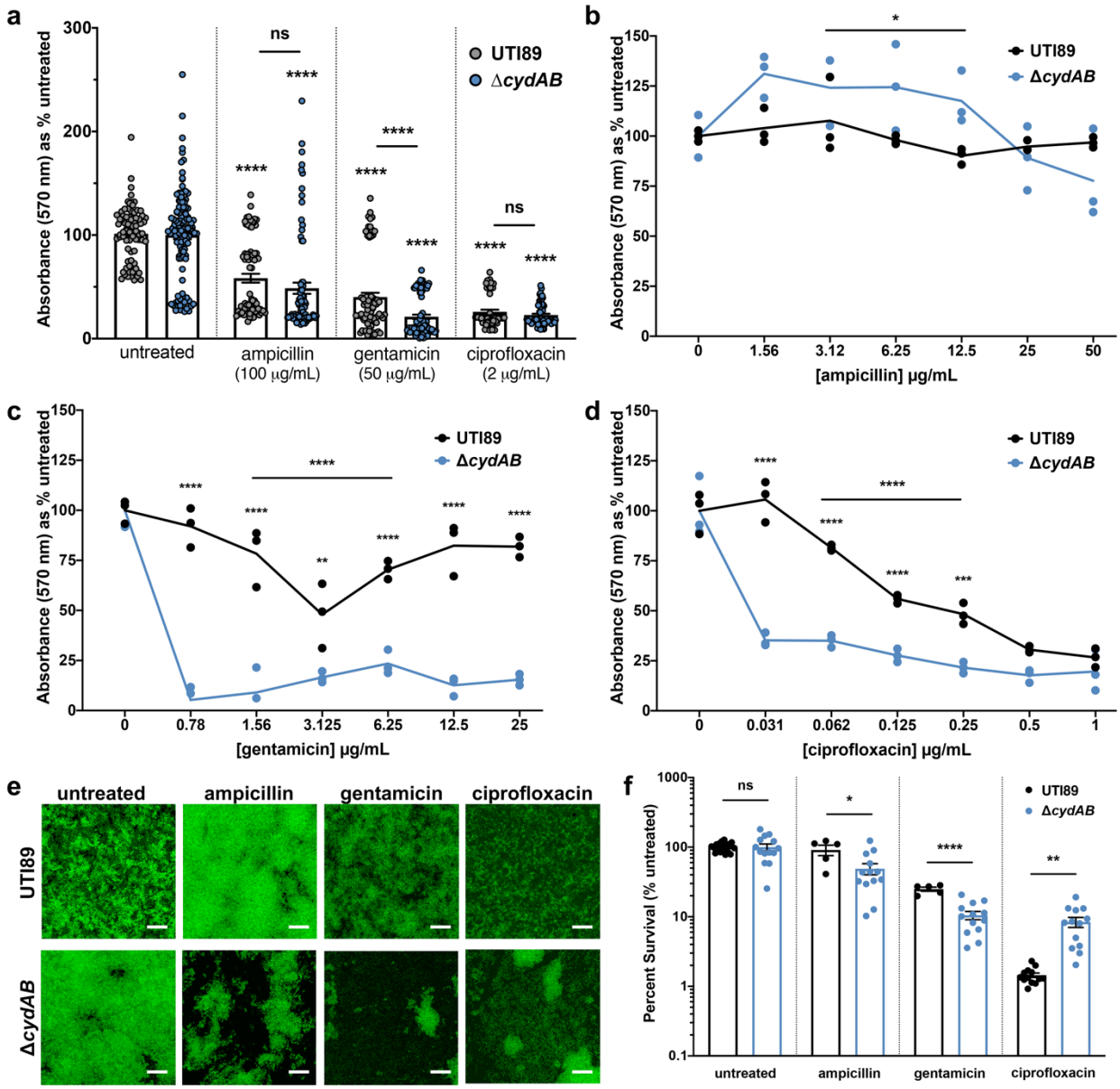

Figure 31: Loss of cytochrome *bd* increases biofilm antibiotic sensitivity. (A) PVC associated air-liquid interface biofilms were grown for 48 hours, treated with antibiotics for 72 hours, and biomass was quantified using the crystal violet assay. Biofilm biomass was quantified for wild-type UTI89 and isogenic cytochrome *bd* deficient strain Δ*cydAB*. Data were normalized to the untreated control of each strain. The mean absorbance value in each treatment group was compared to the untreated control of the same strain (asterisks), and to the mean value of the other strain in the same treatment group (horizontal line with asterisks) using a two-tailed Welch's t test. Data represent at least three biological replicates with at least eight technical replicates each. Each dot represents an independent well. (B-D) Dose response curves depicting the total biomass of biofilms after treatment with decreasing concentrations of ampicillin (B), gentamicin (C), or ciprofloxacin (D). Data were analyzed using a two-way ANOVA to evaluate overall differences between strain across the range of concentrations tested (horizontal line with asterisks), with multiple comparisons used to evaluate differences in mean at each concentration (asterisks). Data represent three biological replicates with three technical replicates each. Each dot represents the mean value of a biological replicate. Solid lines connect mean values at each concentration. (E) Representative images of antibiotic treated biofilms stained with STYO9 and imaged by confocal laser scanning microscopy. At least five images were acquired along the air-liquid interface of three biological replicates. Scale bar is 20 μm. (F) Survival of bacteria in colony biofilms after antibiotic treatment. Colony biofilms were grown on YESCA agar for 72 hours, and biofilms were

transferred to a new plate with or without antibiotics. After 24 hours of antibiotic treatment, biofilms were homogenized and plated to enumerate CFUs. Mean values in each treatment group were statistically compared using a two-tailed unpaired t test. Data are representative of at least five biological replicates. Each dot represents a biological replicate. For all graphs, data are presented as mean ± SEM. * p <0.05, ** p <0.01, *** p <0.001, **** p <0.0001.

To define biofilm antibiotic sensitivity more thoroughly and to more closely approximate antibiotic concentrations encountered by bacteria under clinically relevant conditions, we grew PVC-associated biofilms as previously described and treated with decreasing concentrations of antibiotics (**Figure 31B-D**). Interestingly, at lower β-lactam concentrations we observe minimal effect on total biomass, and Δ*cydAB* biofilms exhibit a small, but statistically significant increase in biomass relative to wild-type (**Figure 31B**). By contrast, Δ*cydAB* biofilms are significantly more sensitive to both aminoglycosides and fluoroquinolones across the range of concentrations tested (**Figure 31C-D**). This effect was most pronounced at lower antibiotic concentrations similar to serum antibiotic concentrations achieved clinically.

Although the crystal violet assay represents a convenient method of assessing biofilm biomass, it does not provide meaningful insights into biofilm architecture or physiology (205). To characterize the structural effect of antibiotics on Δ*cydAB* biofilms, we grew biofilms on PVC coverslips, treated with antibiotics as described above, and imaged the biofilms using confocal laser scanning microscopy (**Figure 31E**). As expected, antibiotic treatment had relatively minor effects on the structural characteristics of wild-type biofilms (**Figure 31E**). Whereas β-lactam treatment led to topographic changes in wild-type biofilms without affecting the apparent density of cells, aminoglycoside or fluoroquinolone treatment had minimal effect (**Figure 31E**). By contrast, treatment with all three classes of antibiotics led to widespread structural disruption of Δ*cydAB* biofilms and reduced cell density (**Figure 31E**), grossly consistent with the reductions in biomass observed by crystal violet assays.

The above data indicate that antibiotic treatment induces a more significant loss of biomass in Δ*cydAB* biofilms as compared to those biofilms formed by the wild-type strain. To determine whether the antibiotic-induced biomass reductions are caused by increased cell death, we quantified percent

survival of biofilm cells after 24 hours of antibiotic treatment in a colony biofilm model (206). Treatment of wild-type biofilms with β-lactams had no significant effect on biofilm CFUs, whereas treatment with aminoglycosides or fluoroquinolones led to significant reductions in CFUs per biofilm (**Figure 31F**). When compared to wild-type, Δ*cydAB* biofilms had significantly reduced cell survival after treatment with β-lactams (91 and 49 percent survival in UTI89 and Δ*cydAB*, respectively) and aminoglycosides (25 and 10 percent survival in UTI89 and Δ*cydAB*, respectively), indicating Δ*cydAB* biofilm cells are more sensitive to antibiotic-induced cell death (**Figure 31F**). By contrast, Δ*cydAB* biofilm cells are somewhat less sensitive to fluoroquinolone treatment than wild-type (2 and 8 percent survival in UTI89 and Δ*cydAB*, respectively) (**Figure 31F**). In total, despite some expected variability between experimental approaches (203), these data demonstrate that loss of cytochrome *bd* renders biofilms more susceptible to the clinically important β-lactam, aminoglycoside, and fluoroquinolone classes of antibiotics.

Cytochrome *bd* does not affect planktonic susceptibility to antibiotics

Our results thus far indicate that cytochrome *bd* affects the ability of biofilms to withstand antibiotics. To determine whether cytochrome *bd* influences antibiotic sensitivity in the planktonic state, we performed broth microdilution assays to measure the minimum inhibitory concentration (MIC) of ampicillin, gentamicin, and ciprofloxacin against each strain (**Figure 32A**). Surprisingly, we observe no significant differences in MIC between strains for ampicillin and ciprofloxacin, and a small increase in MIC for Δ*cydAB* for gentamicin (1.8 and 2.9 μg/mL for UTI89 and Δ*cydAB*, respectively). These MIC values are similar to previously reported values for UTI89, although we observe a somewhat elevated MIC for ampicillin as compared to previous studies (207). Next, to assess antibiotic sensitivity across a range of clinically relevant antibiotics, we performed disk diffusion assays according to Clinical & Laboratory Standards Institute (CLSI) guidelines and procedures followed by the clinical microbiology laboratory at Vanderbilt University Medical Center (208). These analyses revealed that Δ*cydAB* had a slightly larger zone of inhibition for most antibiotics tested (median percent difference: 6.5 percent;

range: 0 – 13 percent) (**Figure 32B and Table 4**). Δ*cydAB* had a significantly larger zone of inhibition after treatment with six antibiotics: meropenem, cefazolin, ceftazidime, aztreonam, sulfamethoxazole-trimethoprim, and nitrofurantoin (**Figure 32B, underlined**). Of note, two of these antibiotics – sulfamethoxazole-trimethoprim and nitrofurantoin – are first line treatments for urinary tract infections (209). Interestingly, we do not observe differences in sensitivity to gentamicin using disk diffusion assays despite the observed increase in MIC, highlighting the effects of distinct growth conditions (static liquid culture versus solid agar surface) on metabolism and antibiotic susceptibility. Although clinical guidelines and CLSI breakpoints would deem both strains equally susceptible to antibiotics (**Table 4**) (208), these analyses reveal a small but consistent trend toward increased antibiotic susceptibility in Δ*cydAB*, which may be indicative of metabolic derangements also present in the planktonic state.

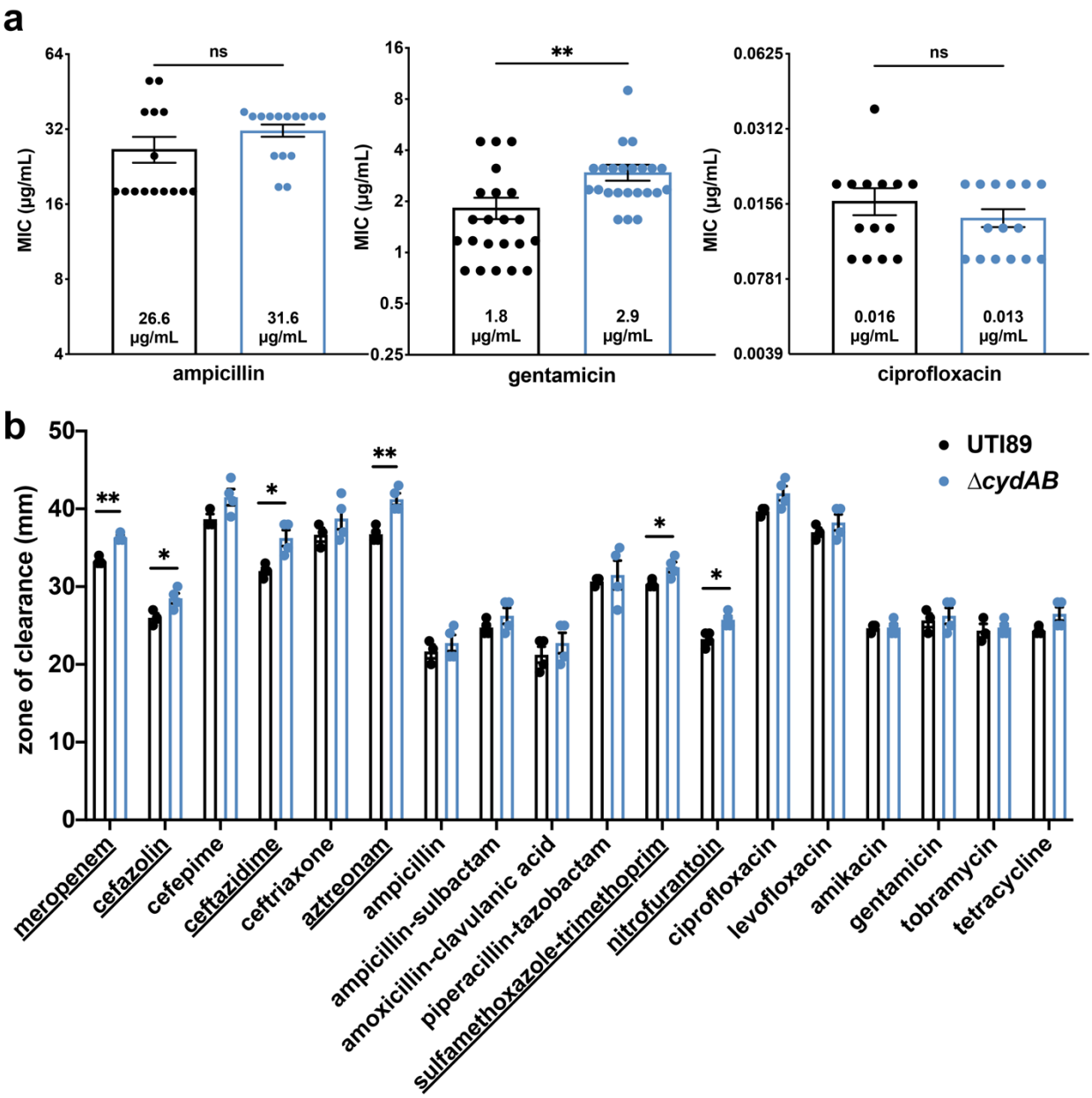

Figure 32: Cytochrome *bd* has minimal effect on planktonic antibiotic susceptibility. (A) Graph depicting minimum inhibitory concentration (MIC) for ampicillin, gentamicin, and ciprofloxacin. Data are representative of at least six biological replicates. Data were analyzed using a two-tailed unpaired t test. (B) Graph depicting the zone of inhibition from disk diffusion assays. Data are representative of at least three biological replicates. Each dot represents a biological replicate. Mean values were statistically compared using two-tailed Welch's t test. Underlined antibiotics attained statistical significance. For all panels, data are presented as mean ± SEM. * p <0.05, ** p <0.01, *** p <0.001, **** p <0.0001.

Antibiotic Name	Antibiotic Class	Mechanism of Action	Breakpoint (mm)	UTI89 (mm)	S/R	Δ*cydAB* (mm)	S/R
meropenem	carbapenem	cell wall inhibitor	16	33.2	S	36.3	S
cefazolin	cephalosporin	cell wall inhibitor	15	26.0	S	28.5	S

cefepime	cephalosporin	cell wall inhibitor	18	38.6	S	41.5	S
ceftazidime	cephalosporin	cell wall inhibitor	21	32.0	S	36.2	S
ceftriaxone	cephalosporin	cell wall inhibitor	23	36.6	S	38.7	S
aztreonam	monobactam	cell wall inhibitor	21	36.7	S	41.2	S
ampicillin	penicillin	cell wall inhibitor	17	21.6	S	22.7	S
ampicillin-sulbactam	penicillin-β lactamase inhibitor	cell wall inhibitor	15	24.7	S	26.2	S
amoxicillin-clavulanic acid	penicillin-β lactamase inhibitor	cell wall inhibitor	18	21.2	S	22.7	S
piperacillin-tazobactam	penicillin-β lactamase inhibitor	cell wall inhibitor	21	30.6	S	31.5	S
sulfamethoxazole-trimethoprim	sulfonamide-dihydrofolate reductase inhibitor	folate biosynthesis inhibitor	16	30.3	S	32.5	S
nitrofurantoin	nitrofuran	reactive cellular damage	17	23.2	S	25.7	S
ciprofloxacin	fluoroquinolone	topoisomerase inhibitor	21	39.6	S	42.0	S
levofloxacin	fluoroquinolone	topoisomerase inhibitor	17	37.0	S	38.2	S
amikacin	aminoglycoside	translation inhibitor	17	24.6	S	24.7	S
gentamicin	aminoglycoside	translation inhibitor	15	25.6	S	26.2	S
tobramycin	aminoglycoside	translation inhibitor	15	24.3	S	24.7	S
tetracycline	tetracycline	translation inhibitor	15	24.3	S	26.5	S

Table 4: Results of disk diffusion assays. Disk diffusion assays were performed to measure antibiotic sensitivity in UTI89 and Δ*cydAB.* CLSI breakpoints were used to determine sensitivity versus resistance to each antibiotic. Reported zone of inhibition is the average of at least three biological replicates.

To determine whether the observed changes in antibiotic sensitivity are physiologically relevant, we performed time kill kinetics assays to measure the rate of antibiotic induced cell death in planktonic cultures (**Figure 33**). Cultures were grown to mid-logarithmic phase, split in two, and one flask was

treated with antibiotics at 5x the minimal inhibitory concentration. The survival curves were analyzed using a two-way ANOVA to statistically compare the rate of antibiotic-induced cell death between strains over time. To fully evaluate the potential role of cytochrome *bd* in planktonic antibiotic sensitivity, these assays were performed on wild-type, Δ*cydAB*, and a strain that encodes cytochrome *bd* as its sole aerobic respiratory oxidase (Δ*appBC*Δ*cyoAB*). These assays revealed no statistically significant differences in the rate of antibiotic killing between strains after treatment with β-lactams, aminoglycosides, fluoroquinolones, or a clinically relevant synergistic combination of β-lactams and aminoglycosides (**Figure 33A-D**). We observe a high degree of variability in survival during the early time points (15 – 30 minutes) of cultures treated with aminoglycosides as compared with other antibiotics, raising the possibility that there is heterogeneous early response to aminoglycoside treatment (**Figure 33B, D**). These results may reflect differences in antibiotic uptake or efficacy resulting from alterations in the electron transport chain composition and proton motive force. In total, these results indicate that, despite small changes in antibiotic susceptibility observed between strains, loss of cytochrome *bd* has no significant or clinically relevant effect on antibiotic susceptibility in the planktonic state. These results are in agreement with recent work in K-12 *E. coli* demonstrating that loss of *cydB* has no discernible effect on planktonic sensitivity to reactive oxygen species or aminoglycosides (210). In combination with previous data, these results demonstrate that loss of cytochrome *bd* specifically increases bacterial susceptibility to antibiotics in the biofilm state.

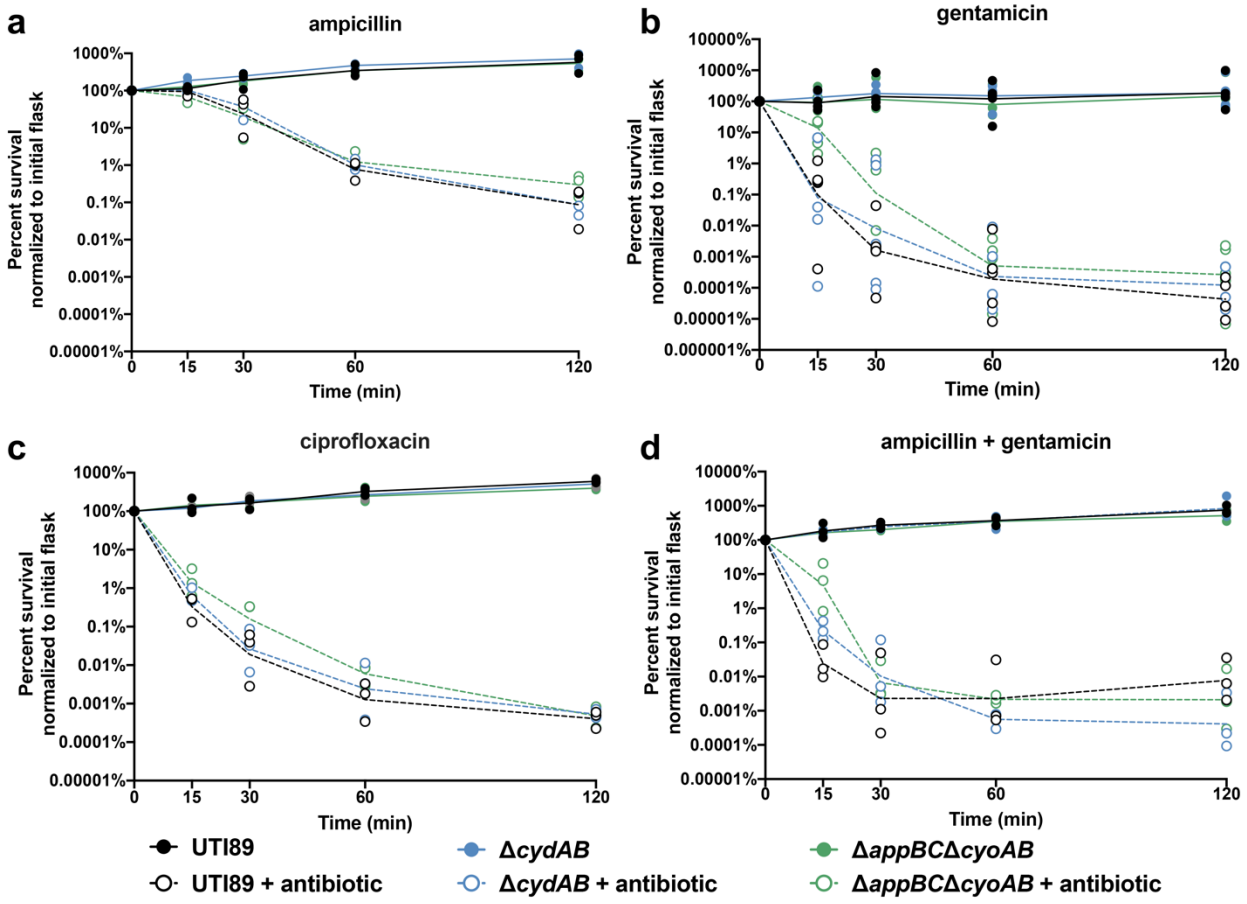

Figure 33: Cytochrome *bd* does not affect the rate of antibiotic-induced cell death in planktonic cells. (A-D) Time kill kinetics assays were performed to evaluate the susceptibility of UTI89 (black), Δ*cydAB* (blue), and Δ*appBC*Δ*cyoAB* (green) to ampicillin (A), gentamicin (B), ciprofloxacin (C), or a combination of ampicillin and gentamicin (D) at 5x MIC. Data were analyzed by a two-way ANOVA with Tukey's multiple comparisons test and determined to have no significant differences between strains. Data are representative of at least three biological replicates. Lines connect geometric mean at each time point. Each dot represents a biological replicate.

Loss of cytochrome *bd* alters the outer membrane of biofilm cells

Our data indicate that loss of cytochrome *bd* increases biofilm sensitivity to antibiotics without significantly affecting planktonic sensitivity. In principle, such a biofilm-specific effect could be caused by changes to the extracellular matrix, outer membrane, or cellular metabolism. In our previous work, we reported that Δ*cydAB* biofilms have changes to the abundance, composition, and organization of the extracellular matrix, suggesting that changes in the extracellular matrix may play a role in antibiotic tolerance by influencing community organization and modulating antibiotic sequestration (**Chapter 2**) (95). In this study, we investigate how cytochrome *bd* impacts biofilm antibiotic tolerance by influencing the outer membrane and cellular energetics.

Prior to import into the cell, antibiotics must interact with and traverse the negatively charged outer membrane. This step is particularly important for charged antibiotics such as cationic aminoglycosides. As such, one possible explanation for the alterations in antibiotic efficacy is that Δ*cydAB* cells have changes to the charge of their outer membrane with consequent effects on antibiotic import. To test this possibility, we measured the interaction of equine cytochrome *c* with the outer membrane of biofilm and planktonic cells (211). Cytochrome *c* is a polycationic molecule known to interact electrostatically with the negatively charged bacterial cell envelope (211). Quantifying the binding of cytochrome *c* to the cell envelope can be used as a proxy for determining the relative charge of the cell envelope, as described previously (211). In planktonic cells, we observe less cytochrome *c* binding to the outer membrane (63 percent of wild-type), suggesting wild-type cells have a more negatively charged outer membrane than Δ*cydAB* (**Figure 34**). However, in biofilm cells, no significant difference in cytochrome *c* binding is observed between wild-type and Δ*cydAB* (**Figure 34**) suggesting the outer membrane has a similar charge in both strains. These results indicate that changes to outer membrane charge cannot explain the altered antibiotic sensitivity of Δ*cydAB* biofilm cells.

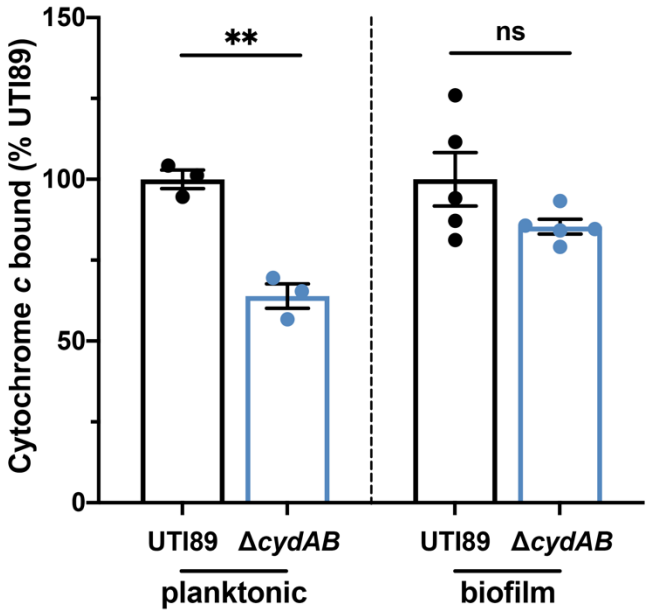

Figure 34: Outer membrane charge is unaffected in Δ*cydAB* biofilm cells. Outer membrane charge was investigated by measuring the binding of cationic cytochrome *c* to planktonic and biofilm cells. Data were analyzed by a two-tailed unpaired t test. Data are representative of at least three biological

replicates, and are presented as mean ± SEM. Each dot represents a biological replicate. * p <0.05, ** p <0.01, *** p <0.001, **** p <0.0001

We next sought to investigate how loss of cytochrome *bd* influences outer membrane permeability. To do so, we extracted the outer membrane and extracellular matrix from colony biofilms using established methods and performed liquid chromatography tandem mass spectrometry (LC-MS/MS) (**Figure 35A and Appendix C**) (131). These experiments identified 30 outer membrane associated or secreted proteins with significantly altered abundance between wild-type and Δ*cydAB* (defined as fold change ≥1.5 and p < 0.05) (**Figure 35A and Appendix C**). Of these, two proteins are of significantly decreased abundance in Δ*cydAB* biofilms, and 28 proteins are of significantly increased abundance. Notably, seven of the 28 proteins with increased abundance in Δ*cydAB* are outer membrane channel proteins responsible for the uptake of environmental compounds (**Figure 35A-B, blue dots and Appendix C**), suggesting Δ*cydAB* biofilm cells may have a more permeable outer membrane. Consistent with this, two proteins with significantly elevated abundance – OmpF and OmpC – are classical general diffusion porins responsible for the non-specific uptake of hydrophilic small molecules including β-lactams, fluoroquinolones, and aminoglycosides (212-214).

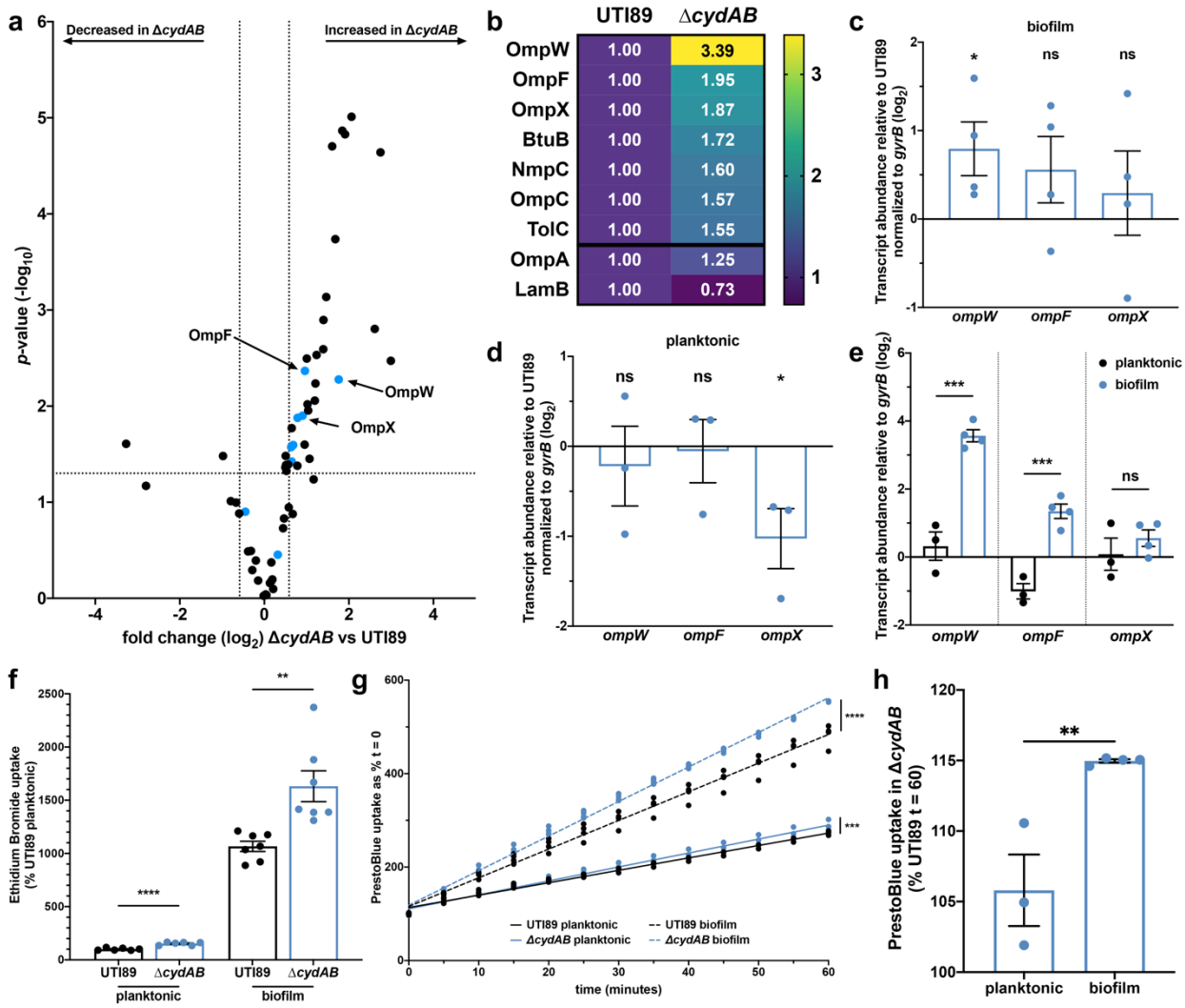

Figure 35: Cytochrome *bd* deficient biofilm cells have elevated uptake of noxious chemicals. (A) Volcano plot depicting all outer membrane or secreted proteins detected by LC-MS/MS performed on outer membrane and extracellular matrix extracts. Blue dots represent outer membrane channel proteins. (B) Heat map depicting the relative difference in abundance of outer membrane proteins in UTI89 and Δ*cydAB*. Each cell contains fold difference in abundance relative to UTI89. OmpA and LamB did not attain statistical significance. Data in (A-B) are representative of three biological replicates per strain. (C-E) RT-qPCR was performed to determine the relative fold difference in outer membrane protein transcript abundance normalized to *gyrB* abundance between UTI89 and Δ*cydAB* in samples derived from homogenized colony biofilms grown on YESCA agar for 11 days (C) and planktonic cells (D). (E) Difference in outer membrane protein transcript abundance between Δ*cydAB* biofilm and planktonic cells was evaluated by comparing the abundance of each transcript to *gyrB* abundance. Data in (C-E) are representative of four biological replicates and were analyzed using a two-tailed unpaired t test. (F) Cellular uptake of membrane impermeant ethidium bromide into planktonic cells and cells extracted from homogenized biofilms. Data are representative of at least six biological replicates and were analyzed by a two-tailed unpaired t test. (G) Cellular uptake of resazurin-based dye PrestoBlue into planktonic cells (solid lines) and cells extracted from homogenized biofilms (dashed lines) was quantified over time. Data were fit to a linear regression model and analyzed by statistically comparing the slope. Data are representative of at least three biological replicates. (H) Percent difference in PrestoBlue uptake at 60 minutes in Δ*cydAB* cells as compared to UTI89. Data were analyzed with a two-tailed unpaired t test. Except where noted all data are presented as mean ± SEM, and each dot represents a biological replicate. * p <0.05, ** p <0.01, *** p <0.001, **** p <0.0001.

To validate the mass spectrometry results, we performed RT-qPCR on RNA extracted from whole, homogenized colony biofilms. Based on the finding that outer membrane channel proteins are significantly more abundant in Δ*cydAB* biofilms, in combination with the known role for this class of proteins in antibiotic uptake, we chose to measure transcript abundance of the three outer membrane proteins with the most increased abundance in Δ*cydAB* (OmpW, OmpF, and OmpX) (**Figure 35B**). Consistent with the proteomics data, RT-qPCR revealed that Δ*cydAB* biofilms have significantly more abundant *ompW* transcript (1.9-fold greater than wild-type), and elevated abundance of both *ompF* and *ompX* transcript (1.6 and 1.4-fold greater than wild-type, respectively), albeit below the threshold of significance (**Figure 35C**). To determine if the observed increase in *omp* transcript is biofilm specific, we performed RT-qPCR targeting the same genes with RNA derived from planktonic cultures (**Figure 35D**). Interestingly, in planktonic cells we observe no significant difference in *ompW* and *ompF* abundance between strains, and significantly decreased *ompX* transcript in Δ*cydAB* (**Figure 35D**). Finally, we compared abundance of each transcript between Δ*cydAB* planktonic and biofilm cells and observe that Δ*cydAB* biofilm cells have significantly elevated steady state transcript of *ompW* and *ompF* as compared to Δ*cydAB* planktonic cells (**Figure 35E**). These results are in agreement with previous studies in K-12 *E. coli* demonstrating that several outer membrane proteins, including OmpC, OmpF, and NmpC, have elevated expression in biofilms relative to planktonic cultures (215). Together these results indicate that cytochrome *bd* deficient cells have elevated expression of several outer membrane proteins in the biofilm state. Guided by these results, we next sought to investigate how loss of cytochrome *bd* influences cellular accumulation of noxious chemicals.

Cytochrome *bd* deficient biofilm cells have enhanced uptake of noxious chemicals

Because outer membrane proteins serve as the primary site of cellular entry for hydrophilic small molecules, the increased abundance of outer membrane proteins suggests that Δ*cydAB* biofilm cells may have a more permissive outer membrane, and therefore increased uptake of antibiotics and other noxious chemicals. To test this, we measured accumulation of ethidium bromide into planktonic cells

as well as cells extracted from colony biofilms (**Figure 35F**). Ethidium bromide is outer membrane impermeant and fluoresces after intercalation into DNA. In planktonic cells we observe a small, but statistically significant increase in ethidium bromide accumulation in Δ*cydAB*. In biofilm cells, ethidium bromide uptake is significantly elevated for both strains and highest in Δ*cydAB* biofilm cells (approximately 10- and 16-fold elevated in UTI89 and Δ*cydAB*, respectively), consistent with the observed increase in outer membrane protein abundance in biofilms (**Figure 35E-F**). These data demonstrate that biofilm cells have elevated outer membrane permeability, higher uptake of noxious chemicals as compared to planktonic cells, and that loss of cytochrome *bd* enhances cellular uptake of these compounds.

The increased ethidium bromide accumulation represents a net increase in uptake and could be explained by alterations to the rate of influx, efflux, or both. To differentiate these possibilities, we quantified influx kinetics using resazurin-based PrestoBlue, a dye that becomes fluorescent after import into the cytosol (216). In planktonic cells we observe a small, but statistically significant increase in the rate of dye influx in Δ*cydAB* relative to wild-type (slope: 2.6 and 3.0 for wild-type and Δ*cydAB*, respectively) (**Figure 35G**). Consistent with ethidium bromide uptake data, in biofilm cells we observe a significant increase in the rate of accumulation for both strains (**Figure 35F-G**). In addition to the overall increase in influx, we observe a significantly increased rate of influx in Δ*cydAB* biofilm cells as compared to wild-type biofilm cells (slope: 6.1 and 7.4 for wild-type and Δ*cydAB*, respectively) (**Figure 35G**). In biofilm cells, the maximal fluorescence value obtained after 60 minutes was 15 percent higher in Δ*cydAB* compared to wild-type – an approximately 2.5-fold greater difference than that observed in planktonic cells (six percent) (**Figure 35H**). Together these results indicate that biofilm cells have an elevated rate of influx compared to planktonic cells, and that loss of cytochrome *bd* enhances cellular influx of noxious compounds.

Loss of cytochrome *bd* impairs efflux of noxious chemicals in biofilm cells

In addition to affecting the rate of antibiotic influx, loss of cytochrome *bd* may also influence the efficiency of efflux. To test this, we measured the rate of ethidium bromide efflux from wild-type and Δ*cydAB* cells. Cells were loaded with ethidium bromide under energy-limited conditions, and efflux was monitored over time using fluorescence based methods (**Figure 36A-B**) (217). Cells were either left in energy-limited conditions as a control for passive decay in signal, or re-energized by the addition of glucose (217). The data were fit to a one phase decay model, and differences between strains were determined by statistically comparing the best fit models.

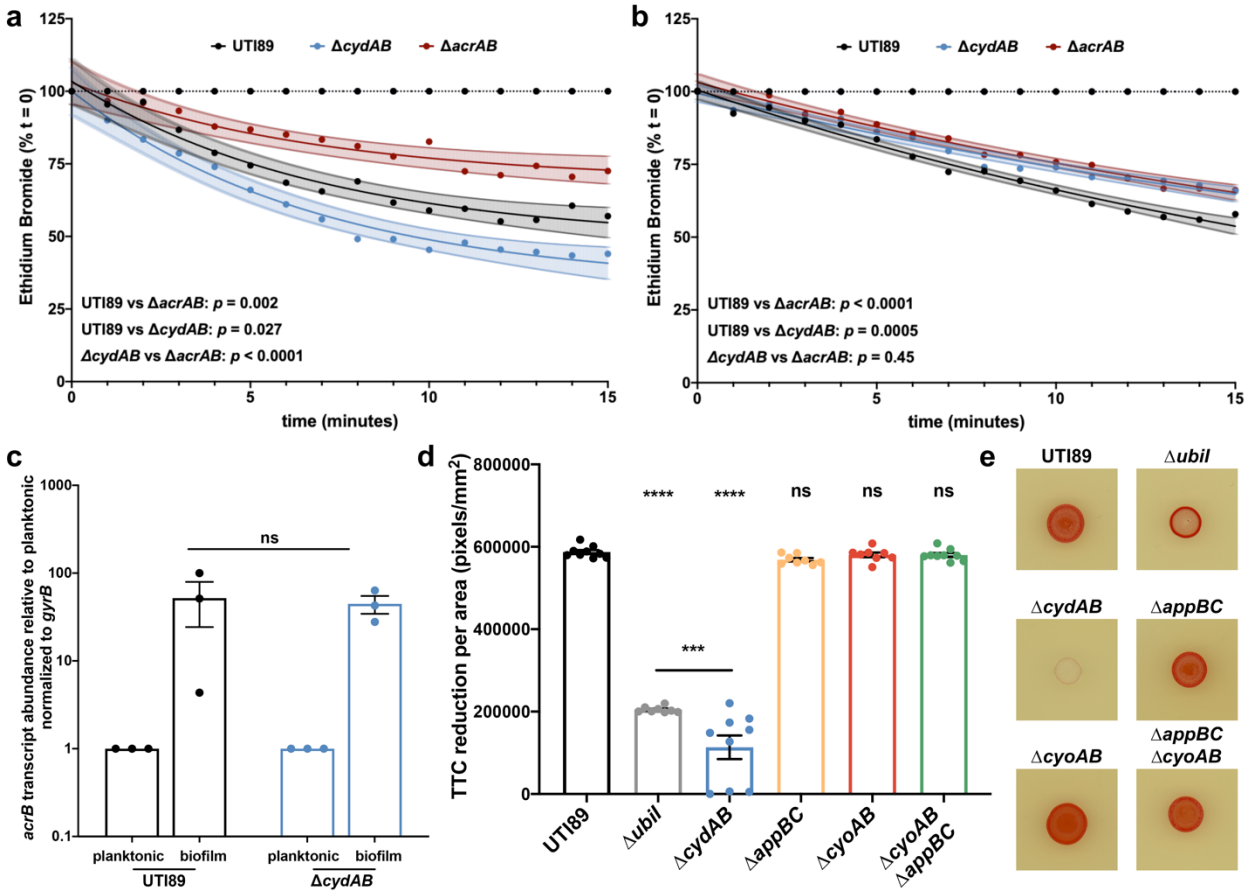

Figure 36: Loss of cytochrome *bd* impairs efflux by diminishing respiratory flux. (A-B) Efflux of ethidium bromide was measured in planktonic cells (A) and cells extracted from homogenized colony biofilms (B). Data were fit to a one phase decay model, and statistical comparisons were made between the curve of best fit for each strain. Data are presented as mean ± 95 percent confidence interval. (C) RT-qPCR was performed to measure *acrB* transcript abundance normalized to *gyrB* abundance in UTI89 and Δ*cydAB* planktonic and biofilm cells. Mean values were statistically compared with a two-tailed unpaired t test. Data are presented as mean ± SEM, and each dot represents a biological replicate. (D-E) Respiratory flux was quantified in wild-type, Δ*ubil* (ubiquinone synthase mutant), and respiratory oxidase mutants by measuring triphenyl tetrazolium chloride (TTC) reduction. (D) Quantification of TTC reduction per unit area in spot colonies. Data were analyzed by a one-way

ANOVA with Dunnett's multiple comparisons test. Data are presented as mean ± SEM, and each dot represents a biological replicate. (E) Representative images of TTC reduction assays. Red color indicates respiratory activity. Data in (A-C) are representative of three biological replicates, and data in (D-E) are representative of at least eight biological replicates. * p <0.05, ** p <0.01, *** p <0.001, **** p <0.0001.

We first measured the rate of efflux in planktonic cells (**Figure 36A**). As expected, the slowest decay in signal was observed in a mutant strain lacking *acrAB*, the resistance-nodulation-division (RND) efflux pump primarily responsible for efflux of ethidium bromide (**Figure 36A**) (217). The rate of efflux was significantly elevated in both wild-type and Δ*cydAB* as compared to Δ*acrAB* (UTI89 vs Δ*acrAB*: p = 0.002; Δ*cydAB* vs Δ*acrAB*: p <0.0001) (**Figure 36A**). Surprisingly, the rate of efflux was significantly elevated in Δ*cydAB* as compared to wild-type (p = 0.02) (**Figure 36A**), indicating loss of cytochrome *bd* enhances efflux under aerobic conditions in planktonic cells.

Next, we homogenized colony biofilms, removed the extracellular matrix, and extracted cells to measure the rate of ethidium bromide efflux in biofilm cells (**Figure 36B**). As expected, Δ*acrAB* biofilm cells again have the slowest rate of efflux, and the rate of efflux did not significantly differ between Δ*acrAB* planktonic and biofilm cells (p = 0.23) (**Figure 36B**). Consistent with data from planktonic cells, we observe a significantly elevated rate of efflux in wild-type biofilm cells as compared to Δ*acrAB* biofilm cells (p < 0.0001) (**Figure 36B**). The rate of efflux did not significantly differ between wild-type planktonic and biofilm cells (p = 0.53). Strikingly, the rate of efflux in Δ*cydAB* biofilm cells was indistinguishable from Δ*acrAB* biofilm cells (p = 0.45) (**Figure 36B**), indicating that loss of cytochrome *bd* functionally inactivates efflux in biofilm cells. Δ*cydAB* biofilm cells have a significant reduction in efflux both compared to Δ*cydAB* planktonic cells (p < 0.0001) and compared to wild-type biofilm cells (p = 0.0005). Although Δ*acrAB* biofilms exhibit some minor structural anomalies relative to wild-type, they are morphologically distinct from Δ*cydAB* biofilms, suggesting a lack of AcrAB efflux activity does not fully explain the biofilm developmental defects observed in Δ*cydAB* (**Figure 37**). These results indicate that loss of cytochrome *bd* impairs efflux of noxious chemicals in a biofilm-specific manner.

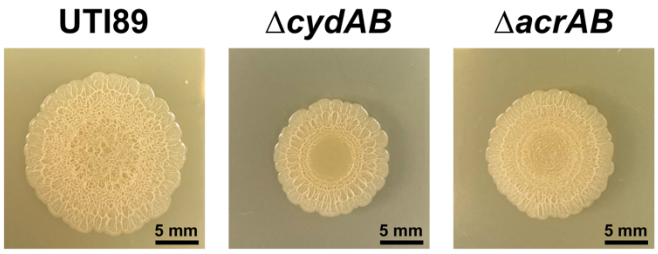

Figure 37: AcrAB inactivation has minor effects on biofilm development. Representative images of UTI89, Δ*cydAB*, and Δ*acrAB* biofilms grown on YESCA agar for 11 days. Data are representative of at least five biological replicates.

Loss of cytochrome *bd* impairs respiratory flux and diminishes the proton motive force

The impaired efflux in Δ*cydAB* biofilm cells could be explained by changes in the expression, abundance, or activity of efflux pumps. To investigate these possibilities, we performed RT-qPCR on samples derived from planktonic and biofilm cells to measure the abundance of *acrB* transcript. Interestingly, *acrB* transcript is approximately 50-fold more abundant in biofilm cells relative to planktonic cells, and we observe no significant difference in abundance between wild-type and Δ*cydAB* (**Figure 36C**). Additionally, our proteomics results reveal no significant difference in AcrA abundance between strains (fold change 0.99 in UTI89 compared to Δ*cydAB*, $p = 0.95$). These data argue the impaired efflux in Δ*cydAB* biofilm cells is not explainable by changes in *acrAB* expression or abundance; rather, loss of cytochrome *bd* appears to reduce the activity of AcrAB – and potentially other proton dependent tripartite exporters – in biofilm cells.

Because cytochrome *bd* is a respiratory quinol oxidase that contributes to electron flow and the establishment of the proton motive force, we hypothesized that loss of cytochrome *bd* would impair respiratory flux, diminish the proton motive force, and consequently impair the proton mediated efflux through RND, major facilitator superfamily (MFS), and multidrug and toxin extrusion (MATE) family transporters (218). To test this hypothesis, we quantified respiratory flux using triphenyl tetrazolium chloride (TTC) reduction assays (**Figure 36D-E**). TTC is a redox sensitive dye that undergoes an irreversible color change upon reduction by NADH dehydrogenase and is commonly used as an indicator of respiratory activity (123). Cells lacking cytochrome *bd* displayed significantly diminished overall TTC reduction as compared to wild-type, indicating that loss of cytochrome *bd* diminishes flux

through the electron transport chain and impairs the generation of the proton motive force (**Figure 36D-E**). Importantly, the diminished TTC reduction in Δ*cydAB* is rescued by extrachromosomal complementation with a plasmid encoding the *cydABX* operon under native transcriptional control (**Figure 38**) (95). Despite the observed impairments in respiratory flux, we observe no significant reduction in ATP levels in Δ*cydAB* colony biofilms (**Figure 39**), consistent with our previous reports (95). This suggests that these cells likely are not fermenting, as under fermentative conditions the F_0F_1-ATPase is reversed and consumes ATP to generate a proton gradient (219). Rather, the reduced respiratory flux is likely due to inefficient respiration in hypoxic biofilm regions where cytochrome *bd* is most highly expressed (95). Consistent with this, loss of cytochrome *bo* or bd_2 did not significantly impact TTC reduction, arguing that cytochrome *bd* is the dominant respiratory enzyme under the conditions tested and its loss cannot be compensated for by expression of other respiratory oxidases (**Figure 36D-E**). Together these data argue that loss of cytochrome *bd* impedes efflux of noxious chemicals by disrupting respiratory flux and impairing the proton dependent activity of efflux pumps.

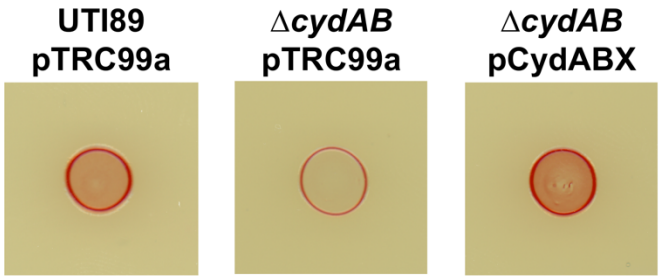

Figure 38: Complementation restores TTC reduction in Δ*cydAB*. Representative images of TTC reduction assays. Red color indicates respiratory activity. Strains were transformed with pTRC99a (empty vector) or pCydABX (*cydABX* operon under native transcriptional control). Data are representative of four biological replicates per strain.

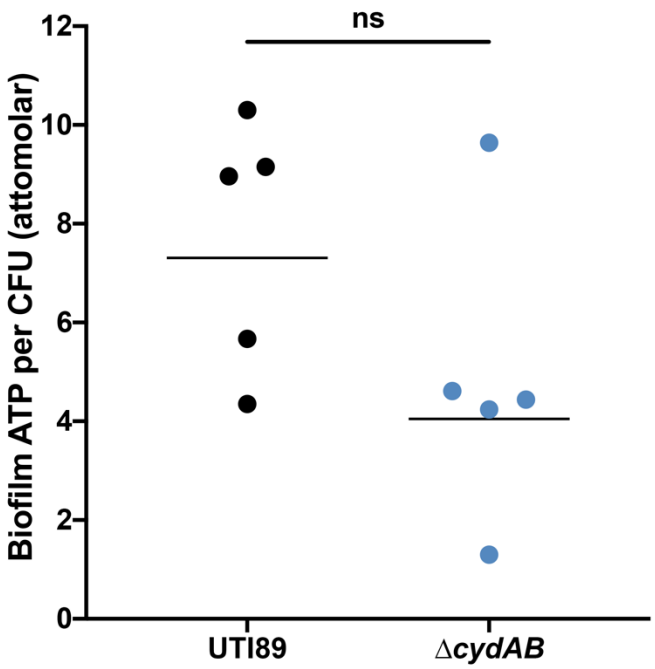

Figure 39: Loss of cytochrome *bd* does not impair ATP generation. Graph depicting ATP concentration in colony biofilms normalized to CFUs in the same biofilm. Line depicts geometric mean. Each dot represents a biological replicate. Data were analyzed by a Mann-Whitney test.

DISCUSSION

Living in spatially structured biofilm communities affords resident bacteria significant protection from a wide array of exogenous threats, including antibiotics and host immune defenses. While this has been demonstrated in several different studies, the composite mechanisms that lead to resilience in the biofilm remain largely uncharacterized. In this work, we build upon our previous findings that revealed a spatial organization in respiratory oxidase expression in *E. coli* biofilms (95). Here, we expand our understanding of how cytochrome *bd* expression influences biofilm-specific resistance to antibiotics. We demonstrate that loss of cytochrome *bd* increases antibiotic susceptibility in a biofilm-specific manner by regulating the cellular accumulation of antibiotics and other noxious chemicals. This enhanced accumulation results from a combination of increased abundance of general diffusion porins and decreased efficiency of proton mediated efflux. Consistent with these findings, alterations in the expression or activity of porins and efflux pumps is a common contributor to antibiotic resistance in clinical isolates (212, 214, 220).

We report that disrupting cytochrome *bd*-mediated respiration in uropathogenic *E. coli* leads to a general enhancement of antibiotic susceptibility specifically when bacteria are found in the biofilm state. A likely explanation for the distinct antibiotic susceptibility phenotypes observed between Δ*cydAB* planktonic and biofilm cells is that *E. coli* encodes a highly flexible respiratory chain – allowing bacteria to adapt to loss of cytochrome *bd* by altering the expression of other oxidases (91, 96) – and that the spatial organization of biofilms imparts unique metabolic constraints not encountered in well-mixed planktonic cultures. Indeed, we previously reported that expression of cytochrome *bo* was increased nearly tenfold in Δ*cydAB* biofilms, indicating that rather than simply impeding respiration, loss of cytochrome *bd* forces bacteria to instead transition to respiring via cytochrome *bo* (95). Such a transition likely has minimal effect in shaking, logarithmic phase planktonic cultures, where all cells are expected to have access to near atmospheric levels of oxygen, as cytochrome *bo* is a low affinity respiratory quinol oxidase optimized for use under atmospheric oxygen tensions (91, 96). In fact, because it is a proton pumping oxidase, cytochrome *bo* is more energetically efficient than cytochrome *bd* (H^+/e^- ratio: 2 and 1 for cytochrome *bo* and *bd*, respectively), potentially explaining the increased efflux observed in Δ*cydAB* planktonic cells. In spatially structured biofilms, by contrast, most cells are exposed to sub-atmospheric oxygen levels (60). As such, cytochrome *bd* is the dominant respiratory enzyme in these cells, and the low oxygen affinity of cytochrome *bo* ensures that simply overexpressing this oxidase cannot compensate for lack of cytochrome *bd.* As a result of the unique biochemistries of these respiratory oxidases and the spatially structured nature of biofilms, loss of cytochrome *bd* reduces the efficiency of respiration and proton mediated efflux in a biofilm-specific manner.

While our results stand in contrast to the antibiotic resistance phenotype generated by respiratory deficiency in small colony variants described in *Staphylococcus aureus* and other species (221), they are consistent with studies in *Mycobacterium tuberculosis* in which targeting of the electron transport chain is a promising avenue for the development of novel classes of antibiotics (168, 169). In recent years two electron transport chain inhibitors – bedaquiline, an ATPase inhibitor, and pretomanid, a nitric oxide donor and respiratory poison – have been approved by the Food and Drug Administration

(FDA) for the treatment of multidrug resistant *M. tuberculosis* (169, 222). Additionally, promising results from a phase 2 clinical trial were recently reported for telacebec (Q203), an inhibitor of the terminal cytochrome oxidase supercomplex bc_1-aa_3 (223). In addition to the known clinical utility of these agents, preclinical studies have identified numerous small molecule inhibitors of all electron transport chain components (NADH dehydrogenases, succinate dehydrogenases, respiratory oxidases, ATPase), some of which are known to eradicate even highly drug resistant isolates (168, 169). Although the potential for disrupting energetics as a therapeutic approach has not been thoroughly evaluated outside *Mycobacterial species*, in combination with our findings these studies raise the possibility of inhibiting cytochrome *bd* to treat or prevent urinary tract infections. Notably, previous work has identified several natural small molecule quinol analogs that serve as potent inhibitors of *E. coli* respiratory oxidases, including several molecules that preferentially inhibit *bd*-type oxidases (167, 169). Importantly, the *bd*-type oxidases are unique to bacteria, suggesting inhibitors of cytochrome *bd* could be used clinically to inhibit biofilm formation, potentiate the effects of antibiotics, and impede virulence in the urinary tract. Together, this work reveals that the spatial stratification of respiration is a fundamental driver of *E. coli* biofilm stress tolerance and suggest the possibility of reprogramming the electron transport chain as an anti-biofilm therapeutic approach.

MATERIALS AND METHODS

Bacterial Strains and Growth Conditions

All studies were performed in uropathogenic *E. coli* cystitis isolate UTI89 (44) and isogenic deletion mutants. For all analyses, strains were propagated from a single colony in Lysogeny broth (LB) (Fisher) at pH 7.4 overnight at 37°C with shaking unless otherwise noted. Genetically manipulated strains were created using λ-red recombinase system (143). Respiratory oxidase mutant strains, *ubiI* mutant strains, and Δ*cydAB* complementation constructs were created in previous studies (89, 95). Primers used for gene deletions and qPCR are listed in **Table 5**.

Primer	Sequence (5' → 3')	Purpose
acrAB_KO_Fwd	TCAATGATGATCGACAGTATGGCTGTGCTCGATAT CTTCATTCTTGCGGCGTGTAGGCTGGAGCTGCTTC	*acrAB* deletion
acrAB_KO_Rev	ATGCCCGCCGTTGGCGTAGTAACAGTCAAAACTGA ACCTCTGCAGATCACCATATGAATATCCTCCTTAG	*acrAB* deletion
acrAB_KOtest_Fwd	TGGTTCAATACTCCTTAATGTTCGTAG	*acrAB* deletion
acrAB_KOtest_Rev	GGCGGTCGTTCTGATGC	*acrAB* deletion
acrB_qPCR_Fwd	GTGTAGTGGTGCGTGCTCT	qPCR
acrB_qPCR_Rev	TATCGTCAGTTCTCCATTACCATTGT	qPCR
ompW_qPCR_Fwd	TATGGCGACCGACAACATTGG	qPCR
ompW_qPCR_Rev	CGTAAGGACGGAATTTGCTGC	qPCR
ompF_qPCR_Fwd	CGTTAGAGCGGCGTGC	qPCR
ompF_qPCR_Rev	CACTGGGTTACACCGATATGCTG	qPCR
ompX_qPCR_Fwd	ACTGGCGGTTACGCACA	qPCR
ompX_qPCR_Rev	CGGACCAGCAGTGATGCC	qPCR

Table 5: Primers used in Chapter 4.

Crystal Violet Biofilm Assays

Determination of biofilm biomass was performed using the crystal violet assay as previously described (204). Overnight cultures were diluted to optical density 600 nm (OD_{600}) = 0.05, and 100 µL of the diluted culture was aliquoted into a 96 well polyvinyl chloride (PVC) plate (Costar). Plates were incubated in a humid chamber at room temperature, washed and stained with crystal violet, and disaggregated using 35 percent acetic acid. For antibiotic assays, biofilms were grown for 48 hours, antibiotics or vehicle was added to each well, and biofilms were grown another 72 hours prior to determining biomass. Total biomass was determined by measuring the absorbance at 570 nm using a SpectraMax i3 microplate reader (Molecular Devices).

Microscopy

Plastic coverslips (Fisher) were placed in the diluted culture in a six well plate and allowed to grow 48 hours at room temperature. Antibiotics were added at 48 hours, and biofilms were allowed to grow another 72 hours before being fixed in 4% PFA and stained with SYTO 9 (ThermoFisher). Images were taken using a Zeiss 710 confocal laser scanning microscope. To obtain a representative sample of the biofilms, at least three images were taken along the air-liquid interface from at least five biological replicates.

Biofilm Survival Assays

Colony biofilm survival assays were performed as previously described (206). Briefly, 10 µL overnight culture was spotted on a piece of filter paper covered in a thin layer of 1.2x yeast extract casamino acids (YESCA) agar and allowed to incubate at room temperature. After 72 hours, biofilms were transferred to new YESCA agar with or without antibiotics. After 24 hours of treatment, biofilms were homogenized by two rounds of vortexing and sonication, serially diluted, and plated to enumerate colony forming units (CFUs).

Disk Diffusion Assays

Antimicrobial susceptibility testing was performed using the Kirby-Bauer disk diffusion method. Testing was performed on 5% Mueller-Hinton agar using commercially available antimicrobial disks (BD) according to Clinical & Laboratory Standard Institute (CLSI) guidelines, M100-ed30 (208). The following disks were used for antimicrobial susceptibility testing: meropenem (10 µg), cefazolin (30 µg), cefepime (30 µg), ceftazidime (30 µg), ceftriaxone (30 µg), aztreonam (30 µg), ampicillin (10 µg), ampicillin-sulbactam (10/10 µg), amoxicillin-clavulanic acid (20/10 µg), piperacillin-tazobactam (100/10 µg), trimethoprim-sulfamethoxazole (1.25/23.75 µg), nitrofurantoin (300 µg), ciprofloxacin (5 µg), levofloxacin (5 µg), amikacin (30 µg), gentamicin (10 µg), tobramycin (10 µg), and tetracycline (30 µg).

Broth Microdilution Assays

Broth microdilution assays were performed to determine the minimum inhibitory concentration (MIC), as previously described (224). Briefly, antibiotics were serially diluted two-fold in a 96-well plate. To increase the precision of the MIC estimate, two independent dilution series were used for each antibiotic. Overnight cultures were diluted to OD = 0.06 in Mueller-Hinton Broth (BD Difco), and 100 µL was added to each well. Cultures were incubated overnight at 37 ˚C, and MIC was determined by assessing the row at which visible growth of bacteria was inhibited.

Time Kill Kinetics Assay

Overnight cultures were subcultured in 20 mL Mueller-Hinton Broth (BD Difco) to an OD_{600} = 0.05 and grown 3-4 hours to mid logarithmic phase. Each strain was normalized to an OD_{600} = 0.5 in PBS and split into two flasks. One flask of each strain was inoculated with antibiotic to a final concentration at 5 times the MIC of wild-type; the other flask served as an untreated control. After addition of the antibiotic, 100 µL of culture was removed from each flask at each time point (0, 15, 30, 60, and 120 minutes) for CFU enumeration.

RT-qPCR

RNA was extracted from day 11 colony biofilms or planktonic cultures using the RNeasy kit (Qiagen). RNA was DNase treated using Turbo DNase I (Invitrogen), and reverse transcribed using SuperScript III Reverse Transcriptase (Invitrogen). cDNA was amplified in an Applied Biosystems StepOne Plus Real-Time PCR machine using SYBR green and primers listed in **Table 5**. All reactions were performed using cDNA from at least three biological replicates. Each reaction was performed in triplicate with at least two different cDNA concentrations. A melt curve analysis was performed using genomic DNA and for every reaction with cDNA to verify primer specificity. Relative fold difference in transcript abundance was determined using the $\Delta\Delta C_T$ method (145). Transcripts were normalized to *gyrB* abundance.

Cytochrome *c* binding assay

Outer membrane charge was assessed by measuring the amount of cationic cytochrome *c* binding to cells, as previously described (211). Planktonic cells were extracted from mid-logarithmic phase cultures. Biofilm cells were extracted from homogenized colony biofilms grown for 11 days on YESCA agar. Cells were normalized to OD = 2.0 and washed twice in 20 mM MOPS (pH 7.0). Cationic equine cytochrome *c* (Sigma) was added to 0.5 mg/mL. Cells were incubated with cytochrome *c* for 10 minutes at room temperature. After incubation, cells were pelleted by centrifugation, and unbound cytochrome *c* was measured from the supernatant by quantifying absorption at 530 nm.

Proteomics

Outer membrane and extracellular matrix samples were extracted as described previously (131). Biofilms were grown for 11 days on 1.2x YESCA agar containing 40 µg/mL Congo Red. Biofilms were homogenized in cold 10 mM Tris-HCl pH 7.4 using an Omni Tissue Homogenizer five times for one minute per cycle. To increase yield and robustness, each sample is a pooled collection of 100 individually grown biofilms. Data is representative of three pooled replicates per strain. The homogenate was centrifuged three times for 10 minutes at 5,000 x *g* to remove cells. NaCl was added to the supernatant (final concentration 170 mM) and centrifuged for one hour at 13,000 x *g* to pellet the extracellular matrix. The extracellular matrix pellet was washed in 10 mM Tris-HCl pH 7.4 with 4% SDS and incubated at room temperature rocking overnight. 25 ug of protein was precipitated by adding 1/3 volume of 100 percent w/v trichloroacetic acid. After washing 2 times with ice cold acetone, the protein pellet was resuspended in 8 M urea 100 mM tris pH 8.5, reduced using TCEP, alkylated with iodoacetamide, diluted back to 2 M urea and digested with 0.5 ug of trypsin overnight at 37 ˚C. Resulting peptides were analyzed by high resolution data dependent LC-MS/MS. Briefly, peptides were autosampled onto a 200 mm by 0.1 mm (Jupiter 3 micron, 300A), self-packed analytical column coupled directly to a Q-exactive plus mass spectrometer (ThermoFisher) using a nanoelectrospray source and resolved using an aqueous to organic gradient. Both the intact masses (MS) and fragmentation patters

(MS/MS) of the peptides were collected in a data dependent manner utilizing dynamic exclusion to maximize depth of proteome coverage. Resulting peptide MS/MS spectral data were searched against the bacterial protein database using MaxQuant-LFQ along with subsequent MS1-based integrations and normalizations (225). Statistical comparisons of resulting normalized protein quantitative values were performed using ProStaR (226). Protein name, gene name, and subcellular localization of each identified peptide was manually determined using the UniProt and EcoCyc databases (227, 228).

Ethidium Bromide Uptake Assay

Colony biofilms were grown at room temperature on YESCA agar. After 11 days, biofilms were homogenized by vortexing and sonication in PBS. After homogenization, a portion of the cellular fraction was removed and normalized to OD_{600} = 0.5 in PBS. Ethidium bromide (Bio-Rad) was added to a final concentration of 10 µg/mL. Cells were then incubated at 37 ˚C for 10 minutes. Next, the suspensions were pelleted, supernatant removed, and cells were resuspended in 300 µL PBS. Fluorescence of ethidium bromide was measured at 360/590 nm. Each fluorescence measurement is the average of three technical replicates.

PrestoBlue Uptake Assay

Uptake of PrestoBlue (Invitrogen) was performed as previously described (216). Planktonic cultures were grown to mid-logarithmic phase and normalized to OD_{600} = 1.0 in PBS. Biofilm cells were extracted from homogenized colony biofilms and normalized to OD_{600} = 1.0 in PBS. For each growth condition, 180 µL of culture was mixed with 20 µL PrestoBlue in a 96-well plate. Fluorescence at 560/590 nm was measured every five minutes for one hour. Each fluorescence measurement is the average of three technical replicates.

Ethidium Bromide Efflux Assay

Efflux of ethidium bromide was performed as described previously (217). Planktonic cultures were grown to mid-logarithmic phase, washed twice in PBS, and normalized to OD_{600} = 0.5. Biofilm cells were extracted from homogenized colony biofilms, washed twice with PBS, and normalized to OD_{600} = 0.5. Cells were loaded with ethidium bromide (10 µg/mL) in energy deplete conditions (PBS with 10 µg/mL proton ionophore carbonyl cyanide m-chlorophenyl hydrazone (CCCP)) for one hour at 37˚C. Cells were washed in PBS and resuspended in PBS ± 0.4% w/v glucose. Efflux was monitored by measuring fluorescence at 360/590 nm in technical triplicate at 37˚C every minute for 15 minutes.

TTC Reduction Assays

Triphenyl tetrazolium chloride (TTC) reduction assays were performed as described previously (123). 10 µL of overnight culture was spotted onto 1.2x YESCA agar containing 0.001% (w/v) TTC. After 24 hours of growth, colonies were imaged using an Epson digital scanner. Images were subjected to automatic thresholding to subtract background, and TTC reduction was quantified by measuring pixel intensity on imageJ. Colony area was determined on Adobe Photoshop.

ATP quantification

ATP quantification was performed on cells extracted from homogenized colony biofilms grown on YESCA agar for 11 days. One aliquot of biofilm cells was removed, and ATP concentration was determined using the Cell-Glo Titer kit (Promega) according to manufacturer's protocols. Briefly, 50 µL of bacterial suspension was mixed with an equal volume of Cell-Glo Titer reagent and incubated with shaking at room temperature for 15 minutes. Luminescence was measured on a SpectraMax i3 plate reader (Molecular Devices) and converted to ATP concentration using a standard curve. A separate aliquot of the same sample was serially diluted for CFU enumeration. To account for differences in the number of cells between samples, ATP concentration was normalized to CFU per biofilm.

Statistical analyses

Statistical analyses were performed in GraphPad Prism. Details of sample size, test used, error bars, and statistical significance cutoffs are presented in the text or Figure legends.

ACKNOWLEDGMENTS

We thank members of the Hadjifrangiskou and Schmitz labs for helpful discussions and critical reading of the manuscript. Proteomics studies were performed at the Vanderbilt Mass Spectrometry Research Center with the help of W. Hayes McDonald, and microscopy was performed at the Vanderbilt Cell Imaging Shared Resource. This work was supported by the National Institutes of Health under the following grants: R01AI107052 (MH), P20DK123967 (MH), T32GM007347 (CJB), and F30AI150077 (CJB).

CHAPTER 5

Conclusions and Future Directions

CONCLUSIONS

Prior to this work, it was unknown exactly why and how UPEC uses aerobic respiration during its lifecycle. Additionally, little was known regarding how UPEC supports its replication during intracellular infection of urothelial cells, and it was completely unknown why host cells tolerate unrestrained intracellular bacterial expansion. My dissertation work has begun to address these gaps in the field. In this work, I demonstrate that UPEC heterogeneously expresses respiratory complexes during both planktonic and biofilm modes of growth, and that this heterogeneity of respiration supports adaptation across niches (**Chapter 2**). These findings are suggestive of a respiratory bet-hedging mechanism in *E. coli*, challenging the previous assumption that respiratory oxidases are expressed solely as a function of oxygen tension. Furthermore, I identify the high affinity respiratory oxidase cytochrome *bd* as a central regulator of biofilm development and pathogenesis in the urinary tract (**Chapters 2 and 3**). Deletion of cytochrome *bd* impedes biofilm development by disrupting the production and organization of the biofilm extracellular matrix – a critical factor that protects biofilm bacteria from external stressors (**Chapter 2**). By disrupting extracellular matrix formation and by altering outer membrane physiology, deletion of cytochrome *bd* increases biofilm sensitivity to a panel of clinically relevant antibiotics (**Chapters 2 and 4**). In addition to impeding biofilm development, loss of cytochrome *bd* exerts profound effects on UPEC during bladder infection (**Chapter 2 and 3**). Through this work I determine that cytochrome *bd* is specifically required during intracellular infection of urothelial cells, and that intracellular aerobic respiration mediated by cytochrome *bd* reprograms host cell metabolism to antagonize apoptosis and preserve the intracellular replicative niche of UPEC in the bladder (**Chapter 3**). This work clarifies the role of aerobic respiration in urinary tract infection and defines a multifaceted role for cytochrome *bd* in UPEC physiology and pathogenesis. Furthermore, by revealing the critical importance of cytochrome *bd* to UPEC biofilm formation and intracellular replication during bladder

infection – both critical components of UPEC pathogenesis – this work identifies cytochrome *bd* as a promising drug target and lays the foundation for future work investigating the possibility of reprogramming bacterial metabolism as a therapeutic strategy for urinary tract infection and other bacterial diseases.

FUTURE DIRECTIONS

This work opens multiple fruitful avenues for further exploration. To facilitate efficient transfer of this information to a future researcher, I have grouped some of the key outstanding areas of interest into broad projects that could be used as the basis for future work in the laboratory. These proposals are intended to serve as a roadmap of future studies, rather than a discrete list of next steps.

Project 1: Characterize the metabolic and immune response of urothelial cells to intracellular infection. Rationale: HIF-1, a hypoxia inducible transcription factor, is a key regulator of central metabolism in humans and has been shown to influence cell survival, particularly in the context of cancer and immune cells (229-232). HIF-1 activity is primarily regulated in a post-translational, oxygen-dependent manner (229-234). Under atmospheric oxygen tensions, prolyl hydroxylases chemically modify the HIF-1α subunit of HIF-1, allowing it to be recognized by the E3 ubiquitin ligase von Hippel-Lindau (VHL) (229-234). Ubiquitylation of HIF-1α by VHL facilitates its proteolytic degradation, thereby maintaining HIF-1 at low basal levels under atmospheric oxygen tensions (229-234). Because prolyl hydroxylases use molecular oxygen as a substrate, decreases in oxygen tension dramatically reduce the efficiency of these enzymes (229-234). Consequently, under low oxygen tensions HIF-1α experiences minimal proteolytic degradation, causing protein levels and HIF-1 activity to rapidly increase (229-234). Upon translocation to the nucleus, HIF-1 acts as a transcription factor which, among other activities, serves to reprogram cellular metabolism and adapt the cell to low oxygen availability by repressing oxidative phosphorylation and inducing aerobic glycolysis. These activities are believed to function both to metabolically adapt cells to lower oxygen availability and to facilitate

cellular growth and proliferation by increasing the availability of anabolic byproducts of central metabolism (229-234). Data presented in this work reveals that intracellular infection of urothelial cells stabilizes HIF-1α, leads to induction of HIF-1 regulated genes, and shifts central metabolism toward a more glycolytic phenotype (**Figures 25-27**). In addition, pharmacologic modulation of HIF-1 modulates urothelial cell death during intracellular infection, implicating HIF-1 as a major regulator of urothelial cell fate (**Figure 28**). In this project, I propose to clarify the mechanism of HIF-1 activation during intracellular infection and define the consequences of HIF-1 regulated metabolic alterations on urothelial cell survival and bacterial pathogenesis in the bladder.

Aim 1: Define the role of HIF-1 in urothelial cell response to infection. My studies demonstrate that HIF-1 is centrally involved in the urothelial cell response to infection. However, several questions regarding the mechanism of activation as well as downstream consequences of HIF-1 dependent metabolic changes on bacterial pathogenesis and urothelial cell survival remain unanswered. To further characterize the influence of HIF-1 on urothelial cell response to infection, I propose to:

1.1) Monitor HIF-1 activation during murine infection using reporter strains, flow cytometry, and immunofluorescence imaging

1.2) Assess the contribution of bacterial oxygen consumption to HIF-1 activation by infecting with a respiratory null strain

1.3) Define HIF-1 dependent metabolic changes using knockout cell culture and mouse lines

1.4) Identify mechanistic links between HIF-1 dependent metabolic changes and urothelial cell apoptosis

1.5) Determine the influence of HIF-1 on bacterial reservoir formation in the bladder

Aim 2: Characterize the influence of immune signaling on urothelial cell metabolic adaptations during intracellular infection. Although the observed transcriptional and metabolic changes are consistent with a model in which intracellular bacterial oxygen consumption stabilizes HIF-1α and

promotes a shift toward aerobic glycolysis – and indeed our data demonstrates cytochrome *bd* mediated aerobic respiration is partially responsible for this metabolic shift (**Figure 27**) – HIF-1 activity is influenced by myriad cellular signaling pathways. Among these pathways include PI3K, mTORC, Akt, and NF-kB, all of which are directly or indirectly activated during bladder infection (74, 161, 229, 235-237). Additionally, cGAS-STING, an innate immune signaling pathway that can detect intracellular pathogens by recognizing cytosolic dsDNA and cyclic dinucleotides, has been shown to stabilize HIF-1α during intracellular infection of macrophages by *Brucella abortus* (238-241). While this pathway is expected to recognize intracellular UPEC, intracellular immune sensing pathways have not been investigated in the context of urinary tract infection. To clarify the immune response to intracellular infection and identify the role of immune signaling in the metabolic response to intracellular infection, I propose to:

2.1) Characterize the influence of TLR-NF-kB signaling on urothelial metabolic adaptations using MyD88 knockout cell culture and mouse lines

2.2) Characterize the influence of PI3K-mTORC-Akt signaling on urothelial metabolic adaptations using chemical inhibitors

2.3) Determine whether cGAS-STING is activated by intracellular infection and investigate functional consequences of cGAS-STING activation during intracellular infection

Aim 3: Determine the impact of glycosuria on urothelial cell survival and intracellular bacterial replication. The results of this work suggest HIF-1 dependent increases in glucose uptake antagonize apoptosis and protect intracellular bacteria from exfoliation (**Figures 28 and 30**). As such, I hypothesize that increases in urinary glucose concentration (glycosuria) increases the risk of urinary tract infection by inhibiting urothelial cell apoptosis, facilitating intracellular bacterial replication, and aiding in the formation of latent bacterial reservoirs in the bladder tissue. Consistent with this, diabetes is a known risk factor for urinary tract infection and increases in hemoglobin A1c are independently associated with a dose-dependent increase in risk of urinary tract infection (20, 170). Additionally, dapagliflozin – a

sodium-glucose transport protein 2 (SGLT2) inhibitor that induces glycosuria – is associated with increased risk of urinary tract infection, and the United States Food and Drug Administration (FDA) warns of increased risk of severe urinary tract infections in patients taking SGLT2 inhibitors (20, 171-173). To clarify the impact of glycosuria on bacterial pathogenesis in the bladder, I propose to:

3.1) Define the impact of extracellular glucose availability and glucose uptake on urothelial cell survival during intracellular infection in cell culture and murine models of glycosuria

3.2) Quantify bacterial bladder colonization and intracellular bacterial community (IBC) formation in murine models of glycosuria

3.3) Perform a retrospective study of the clinical records to assess possible associations of glycosuria with urinary tract infection incidence and recurrence

Completion of this project will define immune and metabolic mechanisms by which intracellular bacterial infection alters urothelial cell physiology and provide translational insights into potential links between glycosuria and urinary tract infection pathogenesis.

Project 2: Investigate the efficacy of inhibiting cytochrome *bd* as an antimicrobial therapeutic strategy for urinary tract infections. Rationale: Cytochrome *bd* is a respiratory quinol oxidase that plays a central role in the physiology and pathogenesis of a diverse group of bacterial pathogens (96, 99). In UPEC, deletion of cytochrome *bd* reduces fitness in the bladder, impairs biofilm formation, and sensitizes bacteria to innate immune defenses and antibiotics (**Figures 8, 9, 13, 16, and 31**) (95, 102, 103, 149). Importantly, deletion of cytochrome *bd* does not kill UPEC, but rather reprograms its metabolism in a manner that impedes virulence in the bladder without influencing its ability to survive in the anaerobic gut (**Figures 8 and 12**) (41, 87, 95, 149). As such, inhibition of cytochrome *bd* is expected to impose relatively minimal selective pressures on UPEC. In combination with data presented in this work, these studies collectively identify cytochrome *bd* as a promising target for the development of antimicrobial approaches to aid in the treatment of urinary tract infection and other

bacterial diseases. In this project, I propose a series of studies that will characterize small molecule inhibitors of cytochrome *bd* and test their efficacy as a standalone therapy for urinary tract infection or in combination with antibiotics.

Aim 1: Characterize small molecule inhibitors of cytochrome *bd in vitro*. Cytochrome *bd* represents a promising target for the development of novel therapeutics for treating urinary tract infections. Indeed, several potent natural small molecule inhibitors of *E. coli* cytochrome *bd* have been identified, and inhibition of cytochrome *bd* is a promising strategy for the treatment of *Mycobacterium tuberculosis* (107, 167-169). To assess the potential efficacy of cytochrome *bd* inhibition for treating urinary tract infections, I propose to:

1.1) Synthesize a panel of natural small molecule inhibitors of cytochrome *bd*

1.2) Quantify the potency and efficacy of cytochrome *bd* inhibitors using purified respiratory oxidases in both membrane preparations and in whole cells

1.3) Determine the effects of cytochrome *bd* inhibitors on UPEC growth and energetics *in vitro*

Aim 2: Determine whether cytochrome *bd* inhibitors potentiate antibiotic treatment. Biofilms are multicellular bacterial communities commonly encountered during infection (57, 59, 195). Biofilms are highly resistant to a variety of external stressors, including immune defenses and antibiotics (60, 61). As such, biofilms are a key bacterial virulence factor and a major contributor to clinical treatment failure (59, 195). In UPEC, deletion of cytochrome *bd* impairs biofilm formation and renders biofilms more susceptible to a wide array of clinically relevant antibiotics (**Figures 8, 9, 13, and 31**) (95, 149). Accordingly, I hypothesize that chemical inhibition of cytochrome *bd* will increase biofilm sensitivity to antibiotics. Indeed, preliminary studies suggest treatment with aurachin C, a potent inhibitor of cytochrome *bd*, increases biofilm sensitivity to gentamicin in a cytochrome *bd*-dependent manner (**Figure 40**). To build upon this work, I propose to:

2.1) Characterize the impact of cytochrome *bd* inhibitors on UPEC biofilm formation

2.2) Determine whether inhibition of cytochrome *bd* increases biofilm sensitivity to clinically relevant antibiotics

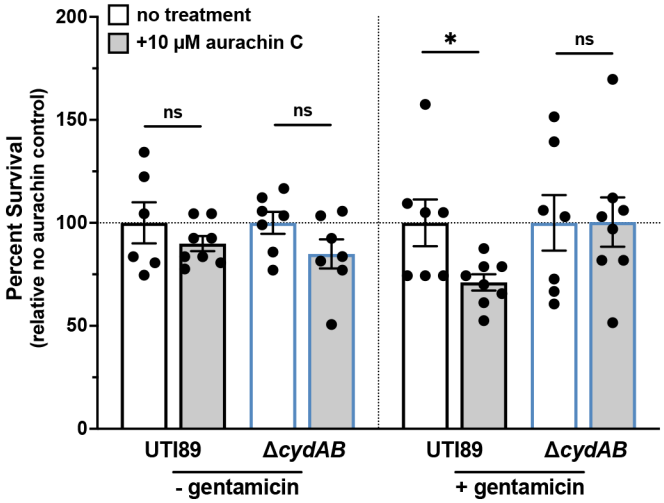

Figure 40: Inhibition of cytochrome *bd* potentiates antibiotics in UPEC colony biofilms. Colony biofilms were grown for 48 hours at room temperature on yeast extract casamino acids (YESCA) agar atop a piece of filter paper covered by a thin layer of agar. After 48 hours, biofilms were transferred to a new YESCA agar plate containing vehicle, 10 μM aurachin C, 50 μg/mL gentamicin, or 10 μM aurachin C and 50 μg/mL gentamicin. After another 24 hours of growth, biofilms were harvested into ice cold sterile PBS and homogenized by two rounds of vortexing and sonication. After homogenization, the number of colony-forming units (CFU) per biofilm was enumerated by serial dilution. The effect of antibiotics and aurachin C was quantified by calculating the percent survival in treated biofilms relative to vehicle treated controls of the same genotype; mean ± SEM; Mann-Whitney test. Each dot represents a biological replicate. * $p < 0.05$, ** $p < 0.01$, *** $p < 0.001$, **** $p < 0.0001$.

Aim 3: Test the efficacy of cytochrome *bd* inhibitors in a murine model of urinary tract infection.

Based on the data from the previous aims, the most promising compounds will be selected for evaluation of efficacy *in vivo*. Using these molecules, I propose to:

3.1) Characterize pharmacokinetics, safety, and toxicity of cytochrome *bd* inhibitors in mice

3.2) Quantify the impact of cytochrome *bd* inhibition on bacterial colonization of the bladder

3.3) Investigate whether cytochrome *bd* inhibitors potentiate antibiotics and aid in the clearance of urinary tract infection

3.4) Characterize off-target effects of cytochrome *bd* inhibitors on the microbiome composition

Completion of this project will characterize a panel of cytochrome *bd* inhibitors and provide a preclinical foundation for further investigation of cytochrome *bd* inhibitors as therapeutics for urinary tract infection.

Project 3: Define mechanisms by which cytochrome *bd* influences the spatial and temporal organization of the biofilm extracellular matrix. Rationale: Biofilms are multicellular bacterial communities commonly encountered in the environment and during infection (57-59, 61, 195, 198). By secreting a highly structured extracellular matrix, bacteria in biofilms organize into robust and metabolically versatile communities capable of withstanding threats from external agents including bacteriophages, phagocytes, and antibiotics (60, 61). Accordingly, the spatiotemporal development of the extracellular matrix is critical for community development and resilience. My studies demonstrate that loss of cytochrome *bd* disrupts the synthesis and organization of the extracellular matrix, consequently impairing the ability for bacteria to resist external stressors (**Figures 8, 9, 13, and 31**) (95). In this project, I propose to define changes to the Δ*cydAB* biofilm extracellular matrix in both space and time and determine the mechanisms by which cytochrome *bd* influences extracellular matrix production and organization.

Aim 1: Characterize the spatial and temporal influence of cytochrome *bd* on extracellular matrix organization. Loss of cytochrome *bd* leads to gross morphological disruptions to biofilm organization and reduced extracellular matrix production (**Figure 8**). Consistent with these changes, scanning electron microscopy and mass spectrometric analysis of purified extracellular matrix reveals dramatic alterations to extracellular matrix composition and organization in cytochrome *bd* deficient biofilms (**Figures 8, 35, and 41**). Additionally, matrix-assisted laser desorption/ionization imaging mass spectrometry (MALDI-IMS) analysis of biofilm cross-sections demonstrates that loss of cytochrome *bd* leads to alterations in the spatial organization of protein expression within the community (**Figure 42)**. To determine the effect of cytochrome *bd* on the spatiotemporal organization of the extracellular matrix, I propose to:

1.1) Identify spatially dysregulated peptide species in biofilm cross-sections using MALDI-IMS

1.2) Characterize changes in extracellular matrix composition across space and time in cytochrome *bd* deficient biofilms using biochemical approaches, transcriptional reporter strains, and chemical probes

1.3) Correlate changes in extracellular matrix production with expression of respiratory oxidases

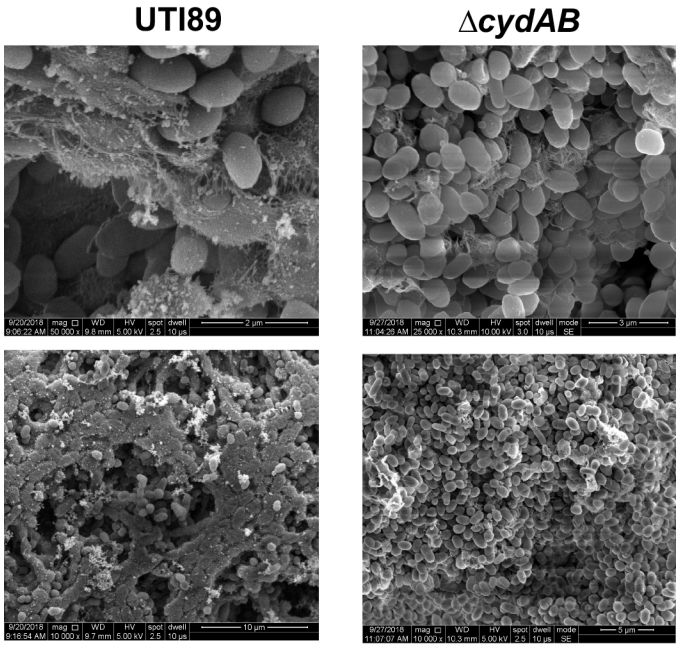

Figure 41: Loss of cytochrome *bd* disrupts extracellular matrix organization. Representative scanning electron micrographs of UPEC colony biofilms grown for 11 days on yeast extract-casamino acids (YESCA) agar and prepared for electron microscopy following previously published methods (242). Consistent with previous studies in K-12 *E. coli*, wild-type UPEC colony biofilms (left) are wrinkled and have a highly structured extracellular matrix ultrastructure (128, 129, 242, 243). Wild-type cells are embedded in a thick extracellular matrix (top) and the surface of the biofilm is coated in a thick layer of curli and phosphoethanolamine (pEtN) cellulose (bottom) (131, 132, 242). By contrast, Δ*cydAB* biofilm cells (right) are largely devoid of extracellular matrix. In Δ*cydAB* biofilms we observe sparse patches of extracellular matrix – grossly similar in structure to the canonical wild-type curli and pEtN cellulose network – as well as individual cells surrounded by a loose network of fibers that are visually consistent with curli fibers. Overall, the extracellular matrix of Δ*cydAB* biofilms is visually disorganized and patchy, in stark contrast with the thick surface coating of extracellular matrix in wild-type biofilms. Images are representative of three biological replicates. Images acquired by John Brannon, PhD.

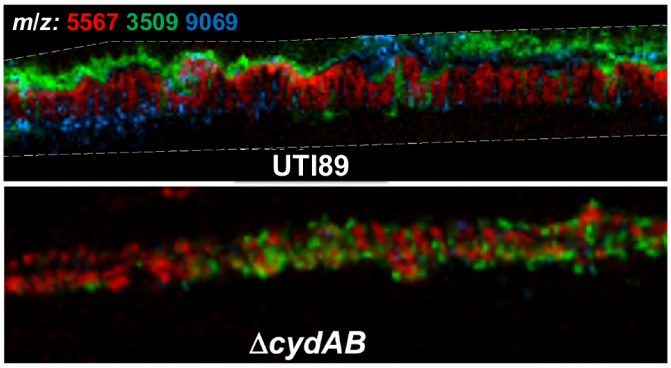

Figure 42: MALDI-IMS analysis of UPEC biofilms reveals spatial dysregulation of peptide species. Colony biofilms were grown for 11 days at room temperature on YESCA agar and flash frozen in Tissue-Tek OCT compound and cryosections. Cryosections were placed on ITO coated slides and analyzed by MALDI-IMS as described previously (54). A subset of *m/z* species with spatially restricted localization patterns in UTI89 biofilms (green – surface, red – interior, blue – throughout) were observed to have spatial delocalization in biofilms lacking cytochrome *bd*. Images are representative of three biological replicates. Images acquired by Jessica Moore, PhD.

Aim 2: Investigate the impact of cytochrome *bd* mediated quinol oxidation on the ArcAB-σ^S signaling axis. Previous work across species has demonstrated links between cellular redox state and extracellular matrix production, and studies in *E. coli* have shown that chemical gradients in biofilms induce a spatial stratification of sigma factor expression and extracellular matrix synthesis that is critical for community structuring (121, 123, 127, 128, 147, 244-246). In UPEC biofilms, respiratory oxidase expression is similarly stratified according to oxygen availability, and cytochrome *bd* is enriched in hypoxic regions of the biofilm (**Figures 2 and 4**). Because cytochrome *bd* is a respiratory oxidase that plays a central role in regulating cellular energetics, I hypothesize that cytochrome *bd* organizes extracellular matrix synthesis by regulating energetics and redox balance in hypoxic regions of the biofilm.

In *E. coli* changes to redox state are sensed by ArcB, a membrane embedded histidine kinase whose activity is regulated by the redox state of the quinone pool (**Figure 43**) (247). Under atmospheric conditions, quinols are rapidly oxidized to quinones by respiratory quinol oxidases such as cytochrome *bd.* Oxidized quinones in turn induce the formation of intermolecular disulfide bonds between ArcB monomers which sterically inhibit the autophosphorylation reaction necessary for ArcB activity (248, 249). Under oxygen-limiting conditions, respiratory efficiency is decreased and there is an accumulation

of quinols. Reduced quinols can donate electrons to cysteine residues in ArcB, thereby reducing the inhibitory disulfide bonds and relieving the repression of ArcB (248, 249). While ArcB is classically thought of as redox sensor that regulates respiration and carbon catabolism, ArcB also regulates the general stress response alternative sigma factor, σ^S – a central regulator of extracellular matrix production (250-255). When activated, the ArcAB system represses transcription of the σ^S encoding gene (*rpoS*) and facilitates the proteolytic degradation of σ^S (**Figure 43**). From this, I hypothesize that ArcB inhibits extracellular matrix production, and that cytochrome *bd* promotes extracellular matrix production in hypoxic biofilm regions by maintaining the quinone pool in an oxidized state, thereby impeding the activation of ArcB. Consistent with this model, preliminary work indicates deletion of cytochrome *bd* decreases the abundance of σ^S and *rpoS* transcript, suggesting cytochrome *bd* inhibits ArcB activation (**Figure 43**). To further investigate possible links between cytochrome *bd*, ArcAB-σ^S, and extracellular matrix production, I propose to:

2.1) Define the energetic state of cytochrome *bd* deficient biofilm cells *in vitro* and *in situ* using chemical probes and microscopy

2.2) Determine the effect of cytochrome *bd* mediated respiration on biofilm formation using a quinol oxidation deficient variant of cytochrome *bd*

2.3) Assess whether cytochrome *bd* mediated quinol oxidation modulates ArcB disulfide bond formation under oxygen limiting conditions

2.4) Investigate the effect of cytochrome *bd* mediated quinol oxidation on σ^S accumulation

2.5) Characterize the influence of the ArcAB-σ^S signaling axis on biofilm development and extracellular matrix production

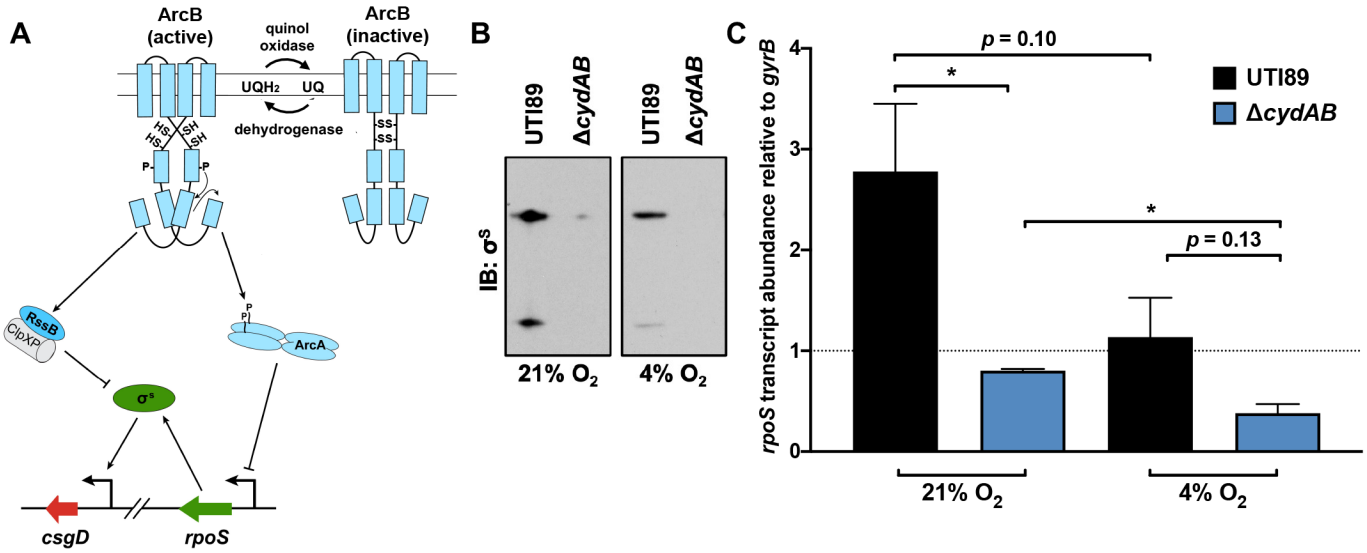

Figure 43: Cytochrome *bd* may regulate σ^S abundance by modulating ArcB activity. (A) Schematic depicting the ArcAB-σ^S signaling network. Under high oxygen tensions, respiratory quinol oxidases rapidly oxidize ubiquinol (UQH_2) into ubiquinone (UQ). By removing electrons from cysteine residues in the histidine kinase ArcB, ubiquinone induces the formation of disulfide bonds that inhibit activation of ArcB. Under conditions of low oxygen tension or decreased respiratory efficiency, reduced ubiquinol accumulates in the membrane. Ubiquinol donates electrons to ArcB, thereby reducing disulfide bonds and relieving repression of ArcB histidine kinase activity. Upon activation, ArcB phosphorylates the response regulator ArcA, which, among other targets, transcriptionally represses the σ^S encoding gene *rpoS*. In addition to phosphorylating ArcA, ArcB phosphorylates RssB. In combination with the ClpXP protease, phosphorylated RssB facilitates the proteolytic degradation of σ^S. I propose that by maintaining the quinone pool in an oxidized state, cytochrome *bd* represses ArcB and indirectly promotes σ^S accumulation. (B) Immunoblots of σ^S in planktonic cells grown at either 21% or 4% oxygen. Cultures were grown to mid-logarithmic phase and normalized prior to loading samples. Similar loading and transfer efficiency was assessed by Ponceau S staining. (C) RT-qPCR analysis of *rpoS* transcript abundance in mid-logarithmic phase bacteria grown at either 21% or 4% oxygen. Dotted line indicates abundance of the housekeeper gene *gyrB*; mean ± SEM; unpaired t test. All experiments were performed on at least three biological replicates. * $p < 0.05$, ** $p < 0.01$, *** $p < 0.001$, **** $p < 0.0001$.

Aim 3: Determine whether cytochrome *bd* influences cyclic di-GMP signaling. Although cytochrome *bd* canonically functions as a respiratory quinol oxidase, this complex also possesses non-respiratory activities including the ability to sequester and degrade nitric oxide (96, 99, 102, 103). Importantly, nitric oxide – a byproduct of anaerobic respiration and a key innate immune effector – activates phosphodiesterase enzymes which degrades cyclic di-GMP, a ubiquitous nucleotide second messenger that promotes bacterial adherence and biofilm formation (141, 256). As such, I hypothesize that cytochrome *bd* promotes extracellular matrix production by degrading endogenously produced nitric oxide and maintaining high levels of cyclic di-GMP in hypoxic biofilm regions. Indeed, preliminary

work demonstrates that deletion of cytochrome *bd* decreases cyclic di-GMP abundance (**Figure 44**) and alters the spatial patterns of cyclic di-GMP accumulation in biofilms (**Figure 45**). To define the role of cytochrome *bd* in cyclic di-GMP signaling, I propose to:

3.1) Determine how cytochrome *bd* influences the accumulation of cyclic di-GMP

3.2) Define the influence of cytochrome *bd* mediated quinol oxidation and nitric oxide tolerance on cyclic di-GMP accumulation using a quinol oxidation deficient variant of cytochrome *bd*

3.3) Characterize and correlate the spatial accumulation of cyclic di-GMP and *cydA* transcript in biofilms

3.4) Perform a transposon mutagenesis screen to identify phosphodiesterases that are involved with the cytochrome *bd*-nitric oxide-cyclic di-GMP signaling axis

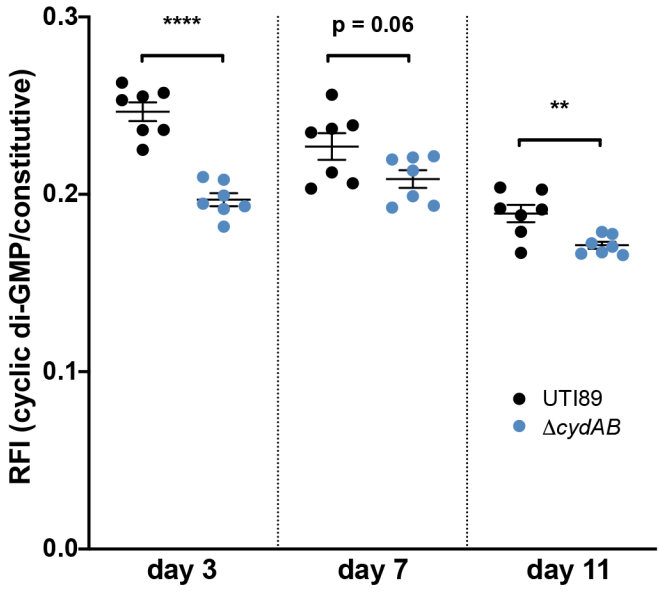

Figure 44: Loss of cytochrome *bd* reduces cyclic di-GMP accumulation in biofilms. To determine whether cytochrome *bd* influences cyclic di-GMP accumulation in biofilms, UTI89 and Δ*cydAB* were transformed with pMMB67EH-Gm-Bc3-5, a reporter plasmid containing a constitutively expressed fluorescent protein and another fluorescent protein under the regulatory control of a cyclic di-GMP responsive riboswitch. Colony biofilms were grown from both strains at room temperature on YESCA agar supplemented with 50 µg/mL gentamicin to maintain the reporter plasmid. At pre-determined time points, were harvested into ice cold sterile PBS and homogenized by two rounds of vortexing and sonication. After homogenization, the cellular fraction was extracted to measure the fluorescence intensity of both fluorescent proteins. Relative fluorescence intensity (RFI) was calculated by quantifying the ratio of cyclic di-GMP dependent fluorescence to constitutive fluorescence; mean ± SEM; unpaired t test. Each dot represents a biological replicate. * $p < 0.05$, ** $p < 0.01$, *** $p < 0.001$, **** $p < 0.0001$.

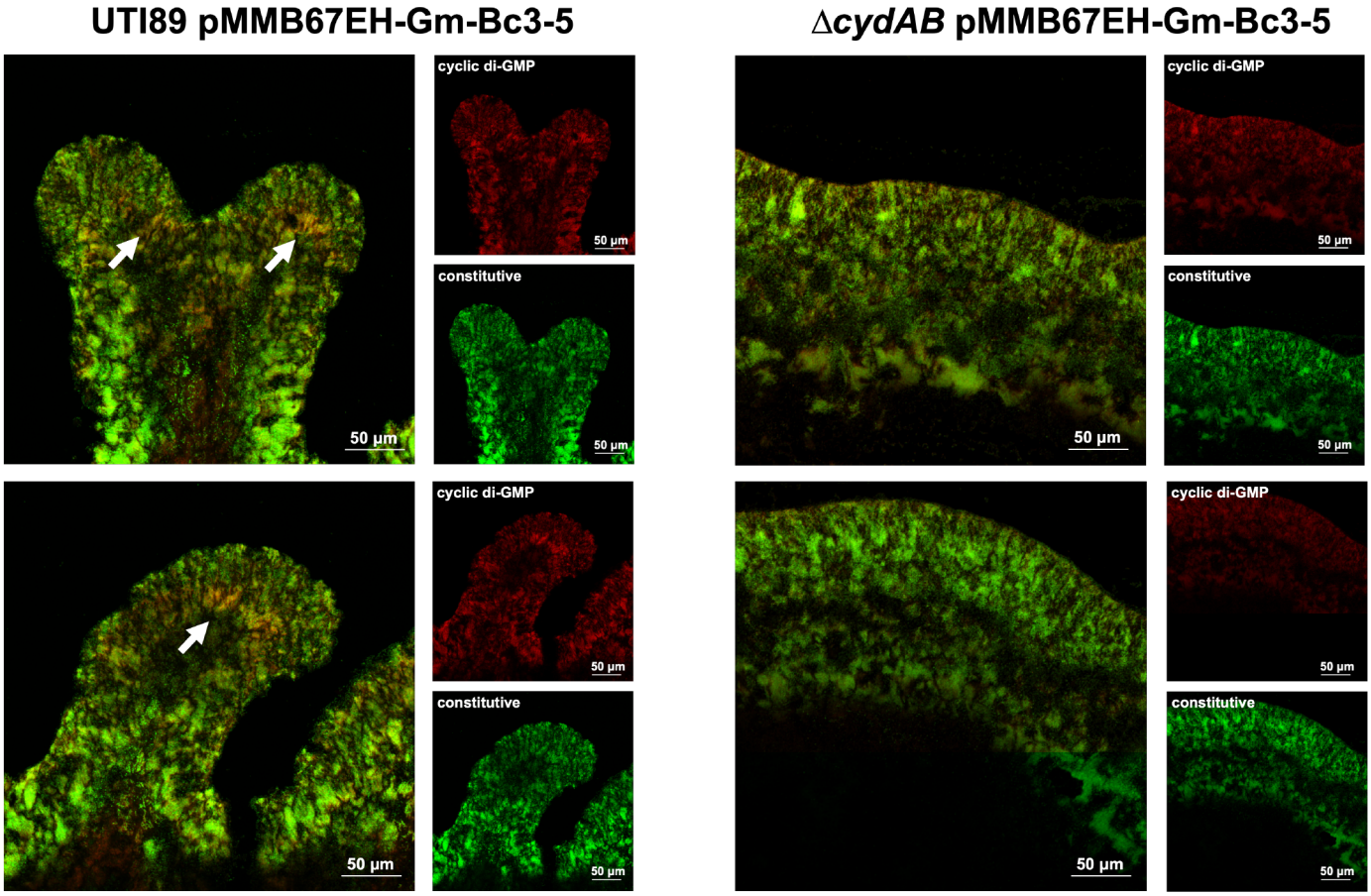

Figure 45: Cytochrome *bd* influences the spatial accumulation of cyclic di-GMP in biofilms. To investigate the spatial patterns of cyclic di-GMP accumulation, I grew biofilms with the pMMB67EH-Gm-Bc3-5 cyclic di-GMP reporter plasmid on YESCA agar. After 11 days, biofilms were flash frozen, and fluorescence was visualized in biofilm cryosections using confocal laser scanning microscopy. Cyclic di-GMP dependent fluorescence (red) accumulates heterogeneously in wild-type biofilms with foci localizing to the interior of biofilm ridges, consistent with the known role for cyclic di-GMP in promoting extracellular matrix production and biofilm wrinkling. By contrast, in Δ*cydAB* biofilms fluorescence accumulates in a relative homogenous manner near the surface of the community, and discrete foci near ridges are not observed. Images are representative of three biological replicates.

Completion of this project will determine the influence of cytochrome *bd* on the spatiotemporal organization of the extracellular matrix and define biochemical mechanisms by which cytochrome *bd* regulates extracellular matrix production.

Project 4: Investigate the contribution of respiratory complexes to UPEC physiology and pathogenesis. Rationale: *E. coli* possesses a modular electron transport chain that affords it a remarkable degree of metabolic flexibility (91, 93). In addition to using oxygen as an electron acceptor via one of three terminal respiratory oxidases, *E. coli* can grow using fermentation or by performing

anaerobic respiration using one of five alternative terminal electron acceptors (nitrate, nitrite, TMAO, DMSO, and fumarate) in tandem with one of seven terminal reductases (90, 91, 93, 95). Although the biochemical activities of each of these respiratory complexes is well-established, we have surprisingly little knowledge regarding precisely how and when UPEC deploys each of these enzymes during physiologically relevant conditions and during infection.

The presence of urinary nitrite – a byproduct of anaerobic nitrate respiration – is a hallmark of infection by Enterobacteriaceae and the basis for a common clinical diagnostic test for urinary tract infection. As such, it has historically been assumed that UPEC subsists off anaerobic nitrate respiration in the bladder. Despite this, work from several groups clearly demonstrates that cytochrome *bd* mediated aerobic respiration is required during bladder infection (41, 87-89, 95, 102, 257). Although cytochrome *bd* has the strongest effect on UPEC pathogenesis, all three respiratory oxidases are expressed during bladder infection (**Figures 13, 16, 21, and 23**)**.** Additionally, we observe robust expression of all three terminal oxidases and two terminal reductases (fumarate reductase and a nitrite reductase) in biofilms (**Figure 2**), suggesting UPEC uses multiple aerobic and anaerobic respiratory pathways within biofilms (95). In this project, I propose several studies that will clarify the role of other respiratory subpopulations in UPEC physiology and pathogenesis.

Aim 1: Determine the influence of cytochrome *bo* on bacterial persistence in the bladder. Although *E. coli* encodes three terminal respiratory oxidases (cytochrome *bo*, *bd*, bd_2), only loss of cytochrome *bd* impairs bacterial colonization of the bladder (**Figure 13 and 16**) (95, 102). Despite this, several lines of evidence suggest cytochrome *bo* also plays an important role during bladder infection. First, deletion of cytochrome *bo* causes subtle, but reproducible alterations to biofilm formation – a key survival strategy used by UPEC to colonize the urinary tract (**Figure 8**). Additionally, UPEC robustly expresses and uses both cytochromes *bd* and *bo* to facilitate aerobic respiration during intracellular infection of urothelial cells (**Figures 21 and 23**). Finally, deletion of cytochromes *bo* and bd_2 alters the kinetics of infection in a murine model of chronic cystitis and reduces bacterial bladder titer four weeks

post-infection (**Figure 46**), suggesting cytochrome *bo* contributes to bacterial persistence in the bladder. To define the role of cytochrome *bo* in UPEC biofilm formation and bladder pathogenesis, I propose to:

1.1) Use transcriptional reporter strains to track expression of respiratory oxidases across niches during infection

1.2) Characterize the contribution of cytochrome *bo* to bacterial colonization and persistence in the urinary tract

1.3) Define the influence of cytochrome *bo* on the biofilm extracellular matrix

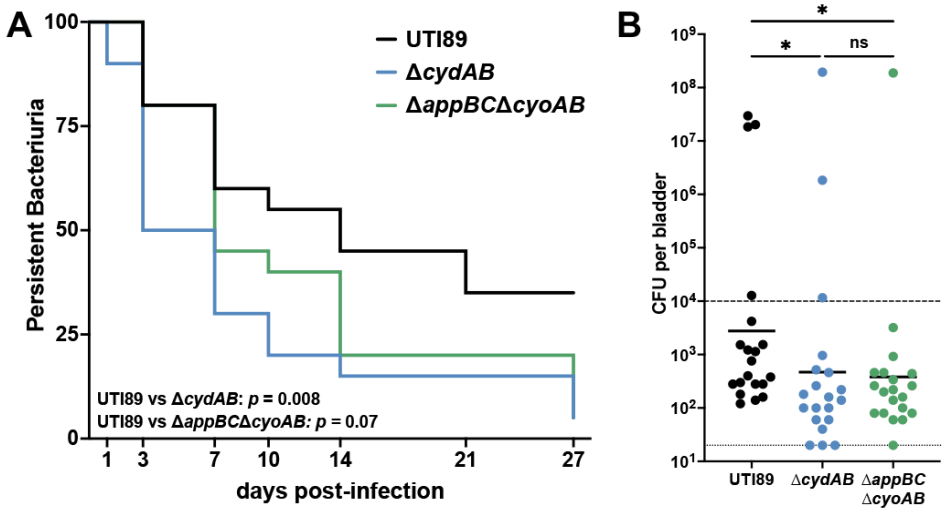

Figure 46: Cytochrome *bd* is necessary but not sufficient for bacterial persistence in the bladder. To investigate the contribution of cytochrome *bd* to bacterial persistence in the bladder, mice were infected with wild-type UTI89, Δ*cydAB*, and Δ*appBC*Δ*cyoAB*. Urine bacterial titer was monitored over time in each mouse, and mice with fewer than 10^4 CFU/mL urine were considered to have resolved bacteriuria. (A) Kaplan-Meier curve depicting the proportion of mice that resolved infection; n = 20 per group; Mantel-Cox test. (B) Bladder titers of mice 28 days post-infection; geometric mean; Mann-Whitney test. Each dot represents a biological replicate. * $p < 0.05$, ** $p < 0.01$, *** $p < 0.001$, **** $p < 0.0001$.

Aim 2: Characterize the contribution of anaerobic respiratory complexes to UPEC pathogenesis and biofilm physiology. Although the urine contains oxygen and cytochrome *bd* is required for efficient bladder colonization, UPEC also respires nitrate during bladder infection (86, 95, 102). Because nitrate respiration is repressed by oxygen, this suggests that oxygen scavenging cytochrome *bd* may be required to deplete urinary oxygen and derepress nitrate respiration. In addition to using anaerobic

respiration during infection of the bladder, UPEC robustly expresses both nitrite and fumarate reductases in biofilms (**Figure 2**) (95). Expression of anaerobic respiratory complexes in the bladder and in biofilms suggests UPEC uses heterogeneous respiratory pathways to support its metabolic needs during its infectious lifecycle. Additionally, the high expression of fumarate reductase in biofilms raises the possibility that a fumarate/succinate cross-feeding interaction exists between aerobic and anerobic biofilm subpopulations (**Figure 47**) (64). To characterize the contribution of these anaerobic respiratory complexes to UPEC pathogenesis and biofilm formation, I propose to:

2.1) Define the role of nitrate respiration in UPEC pathogenesis in the bladder

2.2) Determine whether oxygen scavenging by cytochrome *bd* is required to create an effectively anoxic environment that permits nitrate respiration

2.2) Characterize the spatiotemporal expression patterns of fumarate reductase and nitrite reductase in biofilms

2.3) Determine whether deletion of fumarate reductase and nitrite reductase influences biofilm development and extracellular matrix production

2.4) Investigate a possible cross-feeding interaction between aerobic and anaerobic subpopulations in biofilms

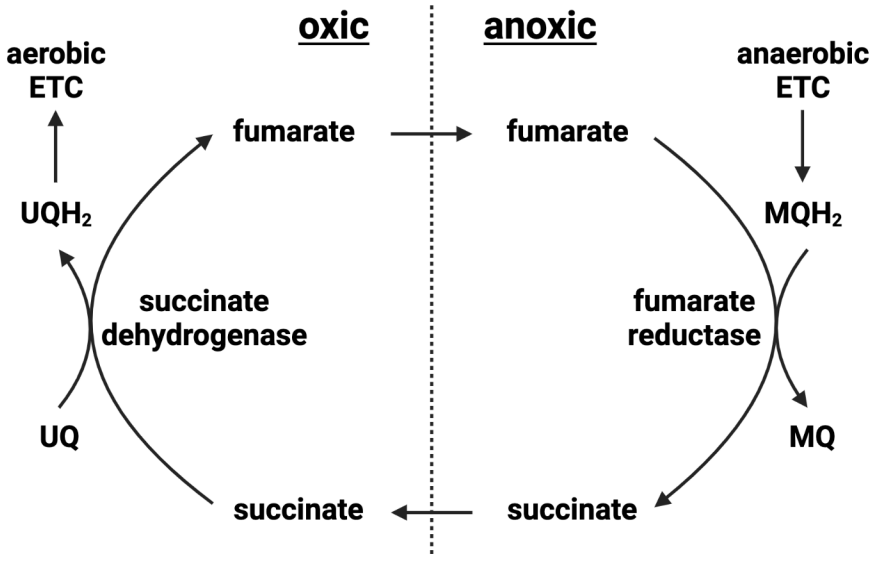

Figure 47: Schematic depicting proposed cross-feeding interactions between oxic and anoxic regions of the biofilm. Under aerobic conditions, succinate is converted to fumarate via succinate

dehydrogenase. Electrons from succinate are transferred onto ubiquinol, which serves as a lipid soluble electron carrier that shuttles electrons to terminal respiratory oxidases. Under anaerobic conditions, fumarate reductase extracts electrons from reduced menaquinol species to generate succinate. I propose that fumarate is exported from cells in oxic biofilm regions via the succinate transporters DauA and DctA and subsequently shuttled to anoxic regions where it is imported and used as an anaerobic terminal electron acceptor. The succinate generated in this reaction is then exported via the anaerobic fumarate/succinate antiporter DcuB and shuttled to oxic biofilm regions where cells take up succinate and use it as an electron donor to facilitate aerobic respiration. Such a fumarate/succinate cross-feeding mechanism would allow for a shuttling of electrons between aerobic and anaerobic biofilm subpopulations, thereby enhancing the efficient of respiration in the community as a whole.

Aim 3: Define mechanisms by which cytochrome *bd* regulates flagellar motility. Flagella are critical bacterial appendages that aid in chemotaxis, attachment to surfaces, and – in the case of urinary tract infection – facilitate bacterial ascension to the kidneys (25). Flagellar motility is energized by the proton motive force, which itself is generated by respiratory oxidases and other components of the electron transport chain. As such, I hypothesized that loss of respiratory oxidases would impair flagellar motility by impairing the generation and maintenance of the proton motive force. Surprisingly, although deletion of cytochrome *bd* ablates flagellar motility, deletion of the other respiratory oxidases has no effect (**Figure 48**), indicating cytochrome *bd* has a unique role in regulating flagellar motility. Interestingly, loss of cytochrome *bd* does not impact biosynthesis of flagella (**Figure 20**), suggesting disruptions to flagellar motility are caused by functional impairments to flagellar rotation. Because cytochrome *bd* is a respiratory oxidase, I hypothesize that cytochrome *bd* promotes flagellar motility in a quinol oxidation-dependent manner by contributing to the proton motive force. Alternatively, cytochrome *bd* may promote accumulation of cyclic di-GMP by sequestering and detoxifying nitric oxide (see also **Project 3**). Because cyclic di-GMP represses flagellar rotation, cytochrome *bd* may also repress flagellar motility in a quinol oxidation-independent manner. To clarify the mechanism by which cytochrome *bd* regulates flagellar motility and functional consequences of impaired motility in UPEC pathogenesis, I propose to:

3.1) Quantify expression of respiratory oxidases in motile populations

3.2) Determine if impaired motility in cytochrome *bd* deficient UPEC is caused by an inability to rotate flagella

3.3) Measure the relative impact of respiration and nitric oxide-cyclic-di-GMP signaling on flagellar motility using a quinol oxidation deficient variant of cytochrome *bd*

3.4) Determine whether loss of cytochrome *bd* impairs flagellum mediated ascension to the kidneys

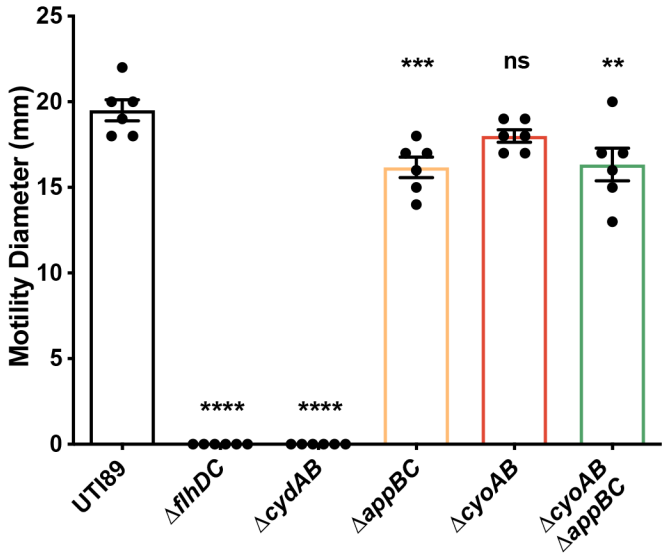

Figure 48: Loss of cytochrome *bd* eliminates flagellar motility. Flagellar motility radius of UTI89 and isogenic mutants lacking the master regulator of flagellar biosynthesis (Δ*flhDC*) or respiratory quinol oxidase performed at 37˚C under aerobic conditions; mean ± SEM; one-way ANOVA. Each dot represents a biological replicate. * $p < 0.05$, ** $p < 0.01$, *** $p < 0.001$, **** $p < 0.0001$.

Aim 4: Characterize the expression and activity of respiratory oxidases on a single cell level. Expression of respiratory enzymes is regulated by a panoply of signaling pathways that respond to the energetic state of the cell as well as the availability of electron acceptors (91, 93). Based on the structure of these regulatory networks, conditions that induce expression of one respiratory pathway typically repress expression of all other respiratory pathways. As such, bacteriologists have historically assumed a mutual exclusivity to respiratory enzyme expression except under transitional states. However, my work has generated several lines of evidence that apparently contradict this paradigm and suggest that individual bacterial cells can use multiple respiratory enzymes simultaneously. First, population level RT-qPCR and *in situ* analysis of gene expression in homogenously aerated planktonic cultures reveals that UPEC robustly expresses all three respiratory oxidases under aerobic conditions, and some cells contain transcript corresponding to all three oxidases simultaneously (**Figures 4 and 13**). Additionally,

deletion of cytochrome *bd*, which canonically is expressed and used only under microaerobic conditions, imparts a significant growth defect on homogenously aerated cultures (**Figure 12**), indicating cytochrome *bd* is used under fully aerobic conditions. Furthermore, loss of cytochrome *bd* impairs proton-dependent flagellar motility without disrupting proton-dependent ATP production (**Figures 12, 19, and 48**), raising the possibility that there exists a functional separation in the energetic inputs to these two processes. Finally, UPEC respires nitrate in the oxygenated bladder despite oxygen repressing nitrate respiration, suggesting oxygen consumption by cytochrome *bd* may deplete cytosolic oxygen, create an effectively anaerobic environment within the cell, and permit nitrate respiration to proceed despite the presence of environmental oxygen.

Together these data suggest that individual cells may use multiple respiratory complexes simultaneously to support different processes within the cell; rather than a single cell using a single respiratory complex to add to a shared proton pool, my work suggests different respiratory complexes co-exist within a given cell, and that each complex may have distinct contributions to energetically intensive processes. Consistent with this hypothesis, super resolution microscopy studies demonstrate that respiratory enzymes are not freely diffusible in the membrane, but instead are localized within discrete membrane microdomains (258-260). The heterogeneity of proton-producing and proton-consuming enzymes suggests that the proton pool is not uniformly distributed but has local maxima and minima near proton-producing and proton-consuming enzymes, respectively (258-260). Consequently, this model predicts that if a particular respiratory enzyme were colocalized within membrane microdomains with a particular proton-consuming enzyme, there should be a functional link between these two enzymes that cannot be compensated for by the activity of other respiratory enzymes. For example, if cytochrome *bd* is colocalized with flagella, we would expect loss of cytochrome *bd* to have an outsized impact on motility even though other respiratory enzymes can in principle generate a proton gradient and energize flagellar rotation. As a precedent for this spatially restricted signaling model, although cyclic di-GMP is freely diffusible in the cytosol, cyclic di-GMP signaling occurs within hyper-localized signaling nodes where individual diguanylate cyclases and

phosphodiesterases specifically regulate a subset of cyclic di-GMP dependent processes without affecting other cyclic di-GMP dependent processes or the cytosolic cyclic di-GMP concentration (246, 261, 262). To investigate this hypothesis and characterize the expression and utilization of respiratory enzymes on a single cell level, I propose to:

4.1) Perform single cell RNA sequencing to quantify respiratory oxidase expression within single cells

4.2) Use translational fusions to visualize expression of respiratory complexes within single cells

4.3) Use fluorescence resonance energy transfer (FRET) and bacterial two-hybrid screens to probe for co-localization of respiratory complexes with the flagellar motor and other proton utilizing proteins

Completion of this project will characterize the role of aerobic and anaerobic respiratory enzymes in the physiology and pathogenesis of UPEC and will determine the single cell expression and utilization patterns of respiratory enzymes.

Probe Name	Accession #	NS Probe ID	Class Name	Analyte Type	mock	mock	mock	mock	UTI89	UTI89	UTI89	UTI89	Δ*cydAB*	Δ*cydAB*	Δ*cydAB*
A2M	NM_000014.4	NM_000014.4:1685	Endogenous	mRNA	20	20	20	20	20	20	20	20	23.04	20	20
AADAT	NM_016228.3	NM_016228.3:1510	Endogenous	mRNA	1088.31	1137.95	1132.48	1118.55	989.54	912.34	993.17	963.52	990.6	948.14	971.89
AANAT	NM_001088.2	NM_001088.2:461	Endogenous	mRNA	20	20	20	20	20	20	20	20	20	20	24.16
ABL1	NM_005157.3	NM_005157.3:3200	Endogenous	mRNA	1068.55	1080.17	1077.96	1015.35	1028.94	1117.42	1102.93	1028.36	1110.4	983.41	1050.96
ACAA2	NM_006111.2	NM_006111.2:450	Endogenous	mRNA	1684.67	1730.43	1693.06	1707.79	1768.56	1765.26	1791.58	1680.65	1814.19	1710.46	1772.46
ACACA	NM_198834.1	NM_198834.1:3681	Endogenous	mRNA	723.34	757.98	718.98	703.53	764.39	742.23	731.7	711.94	844.32	740.61	713.82
ACACB	NM_001093.3	NM_001093.3:3365	Endogenous	mRNA	45.15	42.11	30.86	36.62	49.53	41.95	46.27	53.17	42.62	55.61	35.14
ACADL	NM_001608.3	NM_001608.3:1015	Endogenous	mRNA	20	20	22.63	24.41	20	20	20	20	24.19	20	25.26
ACAP2	NM_012287.5	NM_012287.5:852	Endogenous	mRNA	532.4	503.36	551.32	516	490.83	520.84	543.39	516.12	513.73	545.28	522.73
ACAT1	NM_000019.3	NM_000019.3:282	Endogenous	mRNA	369.67	394.66	344.58	361.75	365.87	342.57	398.13	374.77	380.12	322.83	350.32
ACAT2	NM_005891.2	NM_005891.2:910	Endogenous	mRNA	5068.11	4838.75	4926.94	5098.95	4530.03	4448.69	4562.35	4719.04	4946.11	4693.24	5005.49
ACMSD	NM_138326.2	NM_138326.2:468	Endogenous	mRNA	20	20	20	20	20	20	20	20	20	20	20
ACOT12	NM_130767.2	NM_130767.2:918	Endogenous	mRNA	20	21.54	22.63	33.29	28.14	23.3	23.67	27.23	20	37.98	20
ACOX1	NM_004035.5	NM_004035.5:2950	Endogenous	mRNA	1992.25	1990.93	2008.83	1897.54	2500.3	2488.85	2597.53	2495.04	2660.81	2502.61	2594.99
ACSF3	NR_045667.2	NR_045667.2:2282	Endogenous	mRNA	53.62	46.03	48.34	43.28	50.66	34.96	46.27	38.9	47.23	54.26	49.42
ACY1	NM_000666.2	NM_000666.2:109	Endogenous	mRNA	46.09	45.05	42.17	51.04	43.9	44.28	45.19	53.17	29.95	66.47	35.14
ADA	NM_000022.2	NM_000022.2:1300	Endogenous	mRNA	631.16	639.49	711.78	720.18	643.93	650.18	633.78	600.42	683.06	667.36	649.02
ADAL	NM_001012969.2	NM_001012969.2:890	Endogenous	mRNA	214.46	206.63	177.95	220.82	198.13	180.6	186.15	162.1	167.02	189.9	185.59
ADH1A	NM_000667.3	NM_000667.3:1004	Endogenous	mRNA	20	20	20	20	20	20	20	20	20	20	20
ADH1B	NM_000668.4	NM_000668.4:1532	Endogenous	mRNA	23.52	22.52	23.66	22.19	24.77	20	30.13	28.53	24.19	20	20
ADH1C	NM_000669.3	NM_000669.3:976	Endogenous	mRNA	84.66	113.6	115.2	108.75	95.69	110.69	117.29	111.52	99.06	99.02	103.23
ADH4	NM_000670.3	NM_000670.3:190	Endogenous	mRNA	20	20	20	20	20	20	20	20	20	20	20
ADH6	NM_000672.3	NM_000672.3:35	Endogenous	mRNA	31.04	24.48	29.83	28.85	33.77	40.78	25.82	42.79	20	32.55	36.24
ADH7	NM_000673.3	NM_000673.3:1028	Endogenous	mRNA	20	20	20	20	20	20	20	20	20	20	20
ADK	NM_001123.2	NM_001123.2:355	Endogenous	mRNA	3295.02	3342.37	3448.86	3340.12	3411.03	3532.86	3562.72	3213.46	3167.63	3431.77	3356.03
ADORA2A	NM_000675.3	NM_000675.3:1095	Endogenous	mRNA	27.28	20.57	27.77	31.07	47.28	54.76	50.57	40.2	42.62	55.61	53.81
AFMID	NM_001010982.4	NM_001010982.4:850	Endogenous	mRNA	449.62	437.75	496.81	480.49	521.22	494.04	500.35	513.53	488.39	527.65	530.42
AGXT	NM_000030.2	NM_000030.2:755	Endogenous	mRNA	20	20	20	20	20	20	23.67	27.23	20	20	26.36
AGXT2	NM_031900.3	NM_031900.3:1636	Endogenous	mRNA	20	20	20	20	20	20	26.9	20	20	20	20
AK3	NM_016282.2	NM_016282.2:450	Endogenous	mRNA	1097.71	1046.88	1058.42	1113	1148.27	1130.23	1229.9	1086.72	1180.66	1157.03	1284.87
AKR1C4	NM_001818.2	NM_001818.2:321	Endogenous	mRNA	20	20	20	20	20	20	20	20	20	20	20
AKT1	NM_001014431.1	NM_001014431.1:758	Endogenous	mRNA	1952.75	2114.32	2063.35	1968.56	2201.97	2231.34	2244.59	2300.52	2183.94	2322.21	2196.35
AKT1S1	NM_032375.3	NM_032375.3:1850	Endogenous	mRNA	1059.15	1065.48	1066.65	1110.78	1062.71	1118.58	1097.55	1032.25	1057.41	1117.7	1101.47
AKT2	NM_001626.4	NM_001626.4:699	Endogenous	mRNA	2020.47	2049.69	1905.97	1969.67	1895.77	1937.71	1976.66	2013.92	1995.03	1987.17	1911.93
AKT3	NM_005465.4	NM_005465.4:287	Endogenous	mRNA	2462.57	2392.44	2348.27	2437.95	2697.31	2647.31	2754.63	2749.21	2686.15	2726.42	2562.05
ALDH2	NM_000690.2	NM_000690.2:825	Endogenous	mRNA	26.34	31.34	20	25.52	25.89	25.63	21.52	31.12	28.8	20	21.96
ALDOA	NM_184041.2	NM_184041.2:1455	Endogenous	mRNA	15328.49	16906.72	16796.84	16095.81	25662.68	27787.45	26711.27	25037.24	21618.2	25526.64	20363.5
ALDOB	NM_000035.3	NM_000035.3:1470	Endogenous	mRNA	20	23.5	20	20	20	25.63	22.6	32.42	20	35.27	20
ALOX12	NM_000697.1	NM_000697.1:1945	Endogenous	mRNA	20	20	20	22.19	20	20	20	20	20	20	20
ALOX15	NM_001140.3	NM_001140.3:1910	Endogenous	mRNA	27.28	45.05	23.66	34.4	41.65	33.79	36.58	35.01	40.32	50.19	45.03
ALOX5	NM_000698.2	NM_000698.2:735	Endogenous	mRNA	722.4	754.06	699.44	675.79	809.42	821.46	810.25	702.86	835.1	717.55	843.4
AMDHD1	NM_152435.2	NM_152435.2:1936	Endogenous	mRNA	39.51	55.82	40.11	44.39	73.17	46.61	60.26	58.36	52.99	63.75	54.91
AMPD1	NM_000036.2	NM_000036.2:436	Endogenous	mRNA	20	20	20	20	20	20	20	20	27.64	27.13	20
AMPD2	NM_004037.6	NM_004037.6:3095	Endogenous	mRNA	289.71	335.9	342.52	346.22	342.23	337.91	295.91	282.7	332.89	328.26	336.04
AMPD3	NM_000480.2	NM_000480.2:3033	Endogenous	mRNA	824.93	853.95	804.36	862.22	1415.07	1426.19	1484.92	1234.55	1390.3	1348.29	1261.81
AOC1	NM_001091.2	NM_001091.2:274	Endogenous	mRNA	20	20	20	20	20	20	20	20	20	20	20
AOC3	NM_001277731.1	NM_001277731.1:2582	Endogenous	mRNA	20	20	20	20	20	20	22.6	20	20	20	20
AOX1	NM_001159.3	NM_001159.3:1415	Endogenous	mRNA	60.2	79.32	48.34	61.03	57.41	57.09	63.49	49.28	50.68	61.04	48.32
AP2S1	NM_021575.2	NM_021575.2:665	Endogenous	mRNA	4680.57	4727.11	4731.5	4818.2	4973.58	5100.04	4695.78	4752.76	5007.16	4892.64	4770.48
APOA1	NM_000039.1	NM_000039.1:149	Endogenous	mRNA	20	20	20	20	20	20	20	20	20	20	20
APOA2	NM_001643.1	NM_001643.1:60	Endogenous	mRNA	20	20	20	20	20	20	20	20	20	20	20
APOA4	NM_000482.3	NM_000482.3:1347	Endogenous	mRNA	20	20	20	20	23.64	20	20	20	23.04	20	20
APOB	NM_000384.2	NM_000384.2:2833	Endogenous	mRNA	22.58	22.52	24.69	24.41	32.65	23.3	20	35.01	20	32.55	20
APOC2	NM_000483.3	NM_000483.3:556	Endogenous	mRNA	32.92	44.07	34.97	31.07	46.16	38.45	32.28	49.28	44.92	55.61	42.83
APOC3	NM_000040.1	NM_000040.1:384	Endogenous	mRNA	20	20	20	20	20	20	20	20	20	20	20
APOE	NM_000041.2	NM_000041.2:96	Endogenous	mRNA	75.25	93.03	63.77	78.79	92.31	71.08	75.32	81.7	79.48	99.02	74.68
APOM	NM_019101.2	NM_019101.2:496	Endogenous	mRNA	54.56	69.53	67.89	77.68	104.7	83.89	75.32	80.4	70.26	78.67	84.56
APRT	NM_000485.2	NM_000485.2:662	Endogenous	mRNA	1869.97	1921.4	1862.77	1940.82	1946.43	1990.14	1863.68	1942.6	1905.18	1907.14	1868
AR	NM_000044.2	NM_000044.2:875	Endogenous	mRNA	20	20	20	20	20	20	20	20	20	20	20
ARF5	NM_001662.2	NM_001662.2:36	Endogenous	mRNA	2440.93	2576.55	2549.87	2670.98	2629.76	2607.69	2655.63	2706.41	2565.2	2677.59	2563.15
ARG1	NM_000045.3	NM_000045.3:673	Endogenous	mRNA	20	25.46	20.57	25.52	20	20	20	20	20	27.13	20
ARID1A	NM_006015.4	NM_006015.4:5495	Endogenous	mRNA	1198.36	1314.23	1231.22	1269.47	1316.01	1282.87	1274.01	1339.59	1315.43	1454.09	1284.87
ARID1B	NM_020732.3	NM_020732.3:6335	Endogenous	mRNA	1267.03	1275.06	1296.02	1311.63	1285.61	1408.71	1327.82	1317.54	1339.62	1342.86	1332.09
ARID2	NM_152641.2	NM_152641.2:3355	Endogenous	mRNA	1249.16	1177.12	1229.16	1116.33	1323.89	1381.92	1462.32	1260.49	1322.34	1272.33	1302.44
ARPC4	NM_005718.4	NM_005718.4:970	Endogenous	mRNA	26279.29	26682.15	26215.62	27396.72	28393.75	28669.5	28062.76	28358.34	28146.97	28969.26	29156.6
ASCL1	NM_004316.3	NM_004316.3:1650	Endogenous	mRNA	20	20	20	20	20	20	20	20	20	27.13	20
ASH1L	NM_018489.2	NM_018489.2:5005	Endogenous	mRNA	1703.48	1720.64	1653.97	1536.9	1852.99	1687.19	1849.69	1637.85	1777.33	1702.32	1749.4
ASL	NM_000048.3	NM_000048.3:130	Endogenous	mRNA	1368.61	1385.72	1373.17	1259.48	1374.55	1214.13	1250.34	1263.08	1303.91	1304.88	1178.34
ASMT	NM_001171039.1	NM_001171039.1:80	Endogenous	mRNA	20	20	20	20	20	20	20	20	20	20	20
ASNS	NM_183356.2	NM_183356.2:1644	Endogenous	mRNA	475.96	460.27	453.61	501.57	437.92	450.93	528.33	503.16	468.81	458.47	463.43
ASPA	NM_000049.2	NM_000049.2:635	Endogenous	mRNA	20	20	20	20	20	20	21.52	29.83	20	32.55	20
ASPG	NM_001080464.2	NM_001080464.2:416	Endogenous	mRNA	20	20	20	20	20	20	20	20	20	20	20
ASS1	NM_000050.4	NM_000050.4:1275	Endogenous	mRNA	3247.99	3525.5	3481.77	3530.98	4588.57	4606	4300.88	4499.88	4159.38	4671.54	3771.14
ATF4	NM_001675.2	NM_001675.2:1151	Endogenous	mRNA	13678.62	12912.14	12849.12	13006.48	14266.67	14487.97	14748.01	14075.43	14106.89	14068.88	14500.33
ATF7	NM_001130060.1	NM_001130060.1:203	Endogenous	mRNA	1024.34	1095.84	1017.27	1074.16	1037.94	949.63	996.4	1085.42	964.11	1033.6	913.68
ATF7IP	NM_018179.3	NM_018179.3:2505	Endogenous	mRNA	1336.63	1306.39	1417.39	1252.82	1130.26	1064.98	1122.3	1196.94	1210.61	1138.04	1173.95
ATG101	NM_021934.4	NM_021934.4:939	Endogenous	mRNA	989.54	975.39	1027.56	985.39	1036.82	927.49	1065.27	1030.95	991.76	1081.07	1052.05
ATG2B	NM_018036.5	NM_018036.5:1722	Endogenous	mRNA	609.53	637.53	598.64	571.48	592.15	636.19	653.15	641.91	605.88	611.75	644.63
ATOX1	NM_004045.3	NM_004045.3:143	Endogenous	mRNA	1990.37	1888.1	1826.77	1894.21	1913.78	1871.29	1936.85	1849.23	1947.8	1957.33	1808.7
ATP5F1D	NM_001687.4	NM_001687.4:184	Endogenous	mRNA	1735.46	1927.27	1784.6	1844.28	1876.63	1887.61	1765.76	1840.15	1764.66	1881.37	1607.73
ATP5ME	NM_007100.3	NM_007100.3:184	Endogenous	mRNA	3633.65	3568.59	3680.29	3725.17	3860.21	3788.03	3844.64	3956.52	3604.19	3876.67	3964.42
ATP6V1F	NM_001198909.1	NM_001198909.1:673	Endogenous	mRNA	4404.96	4566.5	4679.05	4934.72	4772.07	4772.62	4750.65	4760.54	4647.77	4999.8	4639.8
ATXN7	NM_001128149.2	NM_001128149.2:3600	Endogenous	mRNA	917.11	829.47	867.1	873.31	955.76	1006.72	954.44	887.01	905.37	961.71	970.79
BAD	NM_004322.3	NM_004322.3:652	Endogenous	mRNA	947.21	994.97	908.24	942.11	1157.27	1109.26	1177.17	1182.68	1188.72	1154.32	1094.88
BCL2	NM_000657.2	NM_000657.2:5	Endogenous	mRNA	126.98	119.48	140.92	132.05	122.71	117.68	118.36	146.54	105.97	130.22	124.09
BCL2A1	NM_004049.2	NM_004049.2:80	Endogenous	mRNA	109.11	99.89	111.09	126.5	368.12	343.73	344.33	418.87	354.77	359.45	325.06
BCL2L1	NM_138578.1	NM_138578.1:1560	Endogenous	mRNA	5644.71	5686.82	5683.98	5818.02	5939.48	5760.7	5740.6	5875.78	5750.11	6173.11	5450.25
BHMT	NM_001713.2	NM_001713.2:40	Endogenous	mRNA	20	20	20	20	20	20	20	20	20	20	20
BHMT2	NM_001178005.1	NM_001178005.1:946	Endogenous	mRNA	20	24.48	21.6	20	22.52	31.46	21.52	20	20	20	21.96
BIRC3	NM_182962.1	NM_182962.1:3	Endogenous	mRNA	20.69	21.54	20	27.74	150.85	138.66	164.63	145.24	139.38	143.78	141.66
BLK	NM_001715.2	NM_001715.2:990	Endogenous	mRNA	20	20	20	20	20	20	20	20	20	20	20
BRAF	NM_004333.3	NM_004333.3:565	Endogenous	mRNA	1157.91	1259.39	1159.22	1085.26	1204.56	1281.71	1381.62	1196.94	1286.63	1313.02	1223.37
BRCA1	NM_007294.3	NM_007294.3:787	Endogenous	mRNA	849.39	848.08	800.24	797.86	810.54	695.62	791.96	785.86	878.87	781.3	833.52
BRCA2	NM_000059.3	NM_000059.3:115	Endogenous	mRNA	210.7	190.96	174.86	180.88	163.23	139.82	150.64	169.88	154.35	169.55	187.79
BRCC3	NM_024332.3	NM_024332.3:458	Endogenous	mRNA	1088.31	1108.57	1142.76	1081.93	1158.4	1218.79	1247.11	1191.76	1103.49	1174.67	1155.28
BRIP1	NM_032043.1	NM_032043.1:1130	Endogenous	mRNA	1755.21	1729.45	1761.97	1743.3	1641.35	1532.22	1572.07	1486.13	1652.93	1474.44	1745
BTK	NM_000061.1	NM_000061.1:570	Endogenous	mRNA	20.69	20	20	20	20	20	20	20	20	20	20
BUB1	NM_004336.3	NM_004336.3:1978	Endogenous	mRNA	1858.68	1767.65	1829.86	1746.63	1882.26	1867.8	1863.68	1696.21	1771.57	1850.17	1768.07
BUB1B	NM_001211.4	NM_001211.4:835	Endogenous	mRNA	1392.13	1447.41	1472.94	1312.74	1261.97	1478.63	1467.7	1355.15	1385.69	1318.45	1388.1

CA12	NM_001218.3	NM_001218.3:2445	Endogenous	mRNA	117.58	135.14	129.6	120.95	166.61	206.24	178.62	171.18	169.32	176.34	121.9
CA9	NM_001216.2	NM_001216.2:960	Endogenous	mRNA	47.03	69.53	56.57	62.14	159.86	215.56	181.85	132.27	85.24	155.99	80.17
CAB39	NM_001130849.1	NM_001130849.1:1238	Endogenous	mRNA	3625.18	3737.03	3503.37	3549.84	3997.55	3726.28	4184.67	4248.3	3969.33	4371.77	4286.19
CACNA1A	NM_001127221.1	NM_001127221.1:4470	Endogenous	mRNA	20	20	20	20	20	20	20	20	20	20	20
CACNA1E	NM_000721.2	NM_000721.2:9325	Endogenous	mRNA	20	20	21.6	20	20	20	20	25.94	20	20	20
CACNB4	NM_000726.3	NM_000726.3:504	Endogenous	mRNA	23.52	36.23	28.8	27.74	33.77	30.29	23.67	27.23	20	28.49	27.45
CACNG2	NM_006078.3	NM_006078.3:3740	Endogenous	mRNA	20	20	20	20	20	20	20	20	20	20	20
CACNG3	NM_006539.2	NM_006539.2:1780	Endogenous	mRNA	20	20	20	20	20	20	20	20	20	27.13	20
CACNG7	NM_031896.3	NM_031896.3:990	Endogenous	mRNA	20	20	20	20	20	20	20	20	20	20	20
CAD	NM_004341.3	NM_004341.3:2380	Endogenous	mRNA	998.01	1109.55	1141.73	982.06	915.24	970.6	982.41	940.18	909.97	1036.31	926.86
CARD11	NM_032415.2	NM_032415.2:1075	Endogenous	mRNA	1299.01	1289.74	1239.45	1266.14	1476.99	1392.4	1365.48	1444.63	1465.17	1417.47	1509.99
CAT	NM_001752.2	NM_001752.2:1130	Endogenous	mRNA	1281.14	1366.13	1395.79	1418.16	1321.63	1451.83	1376.24	1352.56	1284.33	1322.52	1401.27
CBL	NM_005188.2	NM_005188.2:7485	Endogenous	mRNA	525.81	546.45	521.49	504.9	639.43	622.21	630.55	612.09	590.91	667.36	633.65
CBR4	NM_032783.4	NM_032783.4:520	Endogenous	mRNA	2164.39	2091.8	2130.21	2133.9	1923.91	1945.87	2087.49	1868.68	2011.16	1927.49	2110.7
CCL13	NM_005408.2	NM_005408.2:320	Endogenous	mRNA	890.78	865.71	870.19	922.14	937.75	963.61	1023.3	937.58	888.09	967.13	977.38
CCL19	NM_006274.2	NM_006274.2:401	Endogenous	mRNA	20	20	20	20	23.64	20	20	20	20	20	20
CCL4	NM_002984.2	NM_002984.2:201	Endogenous	mRNA	20	20	20	20	20	20	20	20	20	27.13	20
CCL5	NM_002985.2	NM_002985.2:277	Endogenous	mRNA	22.58	30.36	23.66	29.96	112.58	82.73	81.78	132.27	119.79	107.16	84.56
CCNA1	NM_003914.3	NM_003914.3:1605	Endogenous	mRNA	20	20	20	20	20	20	20	20	20	20	20
CCNA2	NM_001237.2	NM_001237.2:1210	Endogenous	mRNA	4863.05	4531.24	4616.3	4653.97	4636.98	4742.32	4827.05	4706.07	4769.87	4586.09	4716.67
CCNB2	NM_004701.2	NM_004701.2:980	Endogenous	mRNA	2582.97	2614.74	2548.84	2659.89	2486.79	2537.78	2789.06	2585.81	2546.77	2517.53	2552.16
CCND1	NM_053056.2	NM_053056.2:690	Endogenous	mRNA	16545.66	16257.44	16538.67	16574.08	16851.4	15721.91	15268.81	16480.98	16915.13	16464.34	17201.85
CD14	NM_000591.2	NM_000591.2:885	Endogenous	mRNA	32.92	44.07	36	56.59	39.4	39.62	35.51	38.9	36.86	36.62	41.73
CD163	NM_004244.4	NM_004244.4:1630	Endogenous	mRNA	20	20	20	20	20	20	20	20	20	20	20
CD180	NM_005582.2	NM_005582.2:1036	Endogenous	mRNA	20	20	20	20	20	20	20	20	20	20	20
CD19	XM_011545981.1	XM_011545981.1:713	Endogenous	mRNA	20	26.44	20	20	20	20	20	20	20	20	20
CD209	NM_001144899.1	NM_001144899.1:950	Endogenous	mRNA	20	20	20	20	20	20	20	20	20	20	20
CD244	NM_001166663.1	NM_001166663.1:22	Endogenous	mRNA	57.38	45.05	45.26	54.37	70.92	86.22	77.47	64.84	86.39	77.32	71.38
CD247	NM_000734.3	NM_000734.3:1350	Endogenous	mRNA	20	21.54	23.66	35.51	20	30.29	34.43	20	20	20	23.06
CD27	NM_001242.4	NM_001242.4:326	Endogenous	mRNA	20	20	20	20	20	20	20	20	20	20	20
CD274	NM_014143.3	NM_014143.3:1243	Endogenous	mRNA	257.73	274.21	256.12	325.13	361.37	291.3	360.47	411.08	400.85	406.93	353.61
CD276	NM_001024736.1	NM_001024736.1:2119	Endogenous	mRNA	2407.07	2617.68	2588.96	2432.4	2948.35	2968.9	3003.19	2963.18	2699.97	3018.05	2965.08
CD28	NM_001243078.1	NM_001243078.1:2065	Endogenous	mRNA	20	21.54	21.6	20	20	20	20	20	20	20	23.06
CD36	NM_000072.3	NM_000072.3:707	Endogenous	mRNA	20	20	20	20	20	20	20	20	20	20	20
CD3D	NM_000732.4	NM_000732.4:110	Endogenous	mRNA	21.63	24.48	20	27.74	25.89	23.3	26.9	20	36.86	32.55	20
CD3E	NM_000733.2	NM_000733.2:75	Endogenous	mRNA	20	20	20	20	20	20	20	20	20	20	20
CD3G	NM_000073.2	NM_000073.2:404	Endogenous	mRNA	20	20	20	20	20	20	20	20	20	20	20
CD4	NM_000616.4	NM_000616.4:975	Endogenous	mRNA	20	20	20	20	20	20	20	20	20	20	20
CD40LG	NM_000074.2	NM_000074.2:1225	Endogenous	mRNA	20	20	20	20	20	20	20	20	20	20	20
CD6	NM_001254751.1	NM_001254751.1:1722	Endogenous	mRNA	41.39	52.88	56.57	46.61	42.78	38.45	39.81	47.98	43.77	66.47	42.83
CD63	NM_001780.4	NM_001780.4:350	Endogenous	mRNA	14144.24	14441.81	14304.57	14985.03	16416.86	15937.47	15787.45	16291.65	15642.32	16235.1	15332.75
CD68	NM_001251.2	NM_001251.2:1140	Endogenous	mRNA	94.06	102.83	102.86	119.84	136.22	134	122.67	128.38	127.86	137	115.31
CD84	NM_001184879.1	NM_001184879.1:28	Endogenous	mRNA	20	20	20	20	20	20	20	20	24.19	20	20
CD8A	NM_001768.6	NM_001768.6:2029	Endogenous	mRNA	20	20	20	20	23.64	20	20	20	20	20	24.16
CD8B	NM_172099.2	NM_172099.2:439	Endogenous	mRNA	25.4	27.42	21.6	39.95	31.52	38.45	22.6	28.53	26.49	29.84	29.65
CDA	NM_001785.2	NM_001785.2:322	Endogenous	mRNA	764.73	740.35	779.67	794.53	806.04	822.62	777.97	772.89	867.35	858.62	792.88
CDC20	NM_001255.2	NM_001255.2:430	Endogenous	mRNA	4783.1	4766.28	4762.36	4690.59	4631.35	4389.27	4462.28	4462.28	4484.21	4660.69	4378.43
CDC45	NM_080668.3	NM_080668.3:308	Endogenous	mRNA	766.61	769.73	782.76	858.89	851.07	794.66	818.86	955.74	802.85	845.06	793.98
CDCA8	NM_018101.2	NM_018101.2:1665	Endogenous	mRNA	1108.06	950.91	1073.85	1025.34	963.64	988.08	991.02	910.35	1051.65	933.22	1059.74
CDK9	NM_001261.2	NM_001261.2:400	Endogenous	mRNA	980.14	1075.28	1036.82	1080.82	958.02	1024.2	1001.78	1085.42	1030.92	964.42	1135.52
CEACAM3	NM_001815.3	NM_001815.3:527	Endogenous	mRNA	20	20	20	20	22.52	20	20	20	20	29.84	20
CENPA	NM_001042426.1	NM_001042426.1:979	Endogenous	mRNA	1802.24	1735.33	1688.94	1852.04	1696.51	1688.36	1751.77	1653.42	1624.13	1698.25	1742.81
CHMP2A	NM_014453.3	NM_014453.3:241	Endogenous	mRNA	1283.96	1322.06	1282.65	1387.09	1426.33	1386.58	1397.76	1394.06	1391.45	1445.95	1411.16
CHMP6	NM_024591.4	NM_024591.4:346	Endogenous	mRNA	1074.2	1133.06	1074.87	1120.77	1123.5	1144.22	1074.95	1073.75	1154.17	1113.63	1095.98
CLOCK	NM_004898.2	NM_004898.2:2350	Endogenous	mRNA	616.11	656.13	601.72	606.99	625.92	626.87	646.69	570.59	611.64	583.26	605.1
CLSPN	NM_022111.2	NM_022111.2:442	Endogenous	mRNA	2527.47	2577.53	2561.18	2591.09	2462.02	2420.1	2444.73	2393.89	2608.97	2513.46	2768.5
CMKLR1	NM_004072.2	NM_004072.2:762	Endogenous	mRNA	20	20	20	20	20	20	20	20	20	20	20
COL4A1	NM_001845.4	NM_001845.4:780	Endogenous	mRNA	3386.26	3450.09	3432.4	3216.94	3583.27	3870.76	3854.33	3750.33	3553.5	3583.69	3785.42
COL6A1	NM_001848.2	NM_001848.2:3665	Endogenous	mRNA	2055.27	2028.14	2207.35	2065.1	2807.63	2723.05	2834.25	2763.47	2825.52	2902.76	2636.72
COL6A3	NM_004369.3	NM_004369.3:2782	Endogenous	mRNA	20	23.5	20.57	29.96	37.15	29.13	33.36	32.42	28.8	20	26.36
COPS6	NM_006833.4	NM_006833.4:860	Endogenous	mRNA	9553.03	9539.41	9543.24	9706.31	9930.27	9986.84	10149.08	9942.54	9897.98	10357.69	9969.25
COX14	NM_001257133.1	NM_001257133.1:672	Endogenous	mRNA	2100.42	2087.88	2174.44	2170.52	2099.53	2233.67	2155.28	2121.56	2144.77	2217.76	2164.51
COX4I1	NM_001318797.1	NM_001318797.1:50	Endogenous	mRNA	10754.21	11208.15	10977.09	11074.54	11793.39	11935.04	11893.32	11668.57	11266.39	12077.64	11120.14
COX5A	NM_004255.3	NM_004255.3:315	Endogenous	mRNA	11981.73	11774.19	11799.96	11926.77	12924.78	13137.52	13129.67	12680.07	12648.63	12856.23	12626.84
COX5B	NM_001862.2	NM_001862.2:240	Endogenous	mRNA	10809.71	10445.27	10507.03	10787.13	11257.53	11477.12	11457.52	11029.25	11176.54	11506.59	10931.25
COX6A1	NM_004373.2	NM_004373.2:260	Endogenous	mRNA	21553.57	20912.08	21187.88	22143.53	22700.82	22509.14	22364.12	22634.28	22321.99	22885.67	23183.62
COX6B1	NM_001863.4	NM_001863.4:264	Endogenous	mRNA	11421.11	11247.32	11325.78	11717.04	12207.67	12478.02	12330.18	12311.78	11730.59	12346.22	12076.65
COX7B	NM_001866.2	NM_001866.2:159	Endogenous	mRNA	13639.12	13158.92	13259.53	13685.6	14049.4	14197.84	14375.71	14241.42	13988.25	14296.76	14063.26
COX7C	NM_001867.2	NM_001867.2:57	Endogenous	mRNA	2376.03	2325.85	2454.21	2515.63	2553.21	2510.98	2545.88	2693.45	2504.15	2719.64	2575.23
COX8A	NM_004074.2	NM_004074.2:0	Endogenous	mRNA	6479.05	6529.03	6535.65	6926.58	7097.88	7390.8	6865.05	6757.6	6817.89	7030.37	6955.85
CPA3	NM_001870.2	NM_001870.2:220	Endogenous	mRNA	20	20	20	20	20	20	20	20	20	20	20
CPS1	NM_001875.3	NM_001875.3:5560	Endogenous	mRNA	26.34	27.42	20	35.51	36.02	24.47	24.75	28.53	20	27.13	26.36
CPT1A	NM_001876.3	NM_001876.3:1355	Endogenous	mRNA	151.44	135.14	166.63	144.26	182.37	154.97	191.53	159.51	172.78	166.84	162.53
CREB3L3	NM_001271995.1	NM_001271995.1:1050	Endogenous	mRNA	22.58	20	20	20	20	20	20	20	20	20	20
CS	NM_004077.2	NM_004077.2:740	Endogenous	mRNA	3614.84	3685.12	3555.83	3529.87	3897.36	3897.56	4191.12	4023.96	3922.1	4090.99	3810.67
CSF3R	NM_000760.3	NM_000760.3:2066	Endogenous	mRNA	20	20	20	20	20	20	20	20	20	20	20
CTCF	NM_001191022.1	NM_001191022.1:490	Endogenous	mRNA	2240.58	2123.13	2094.21	2011.84	2025.23	1962.18	2152.05	2025.6	2065.29	1983.1	2148.03
CTLA4	NM_005214.3	NM_005214.3:405	Endogenous	mRNA	20	20	20	20	20	20	20	20	20	20	20
CTPS1	NM_001301237.1	NM_001301237.1:580	Endogenous	mRNA	3331.71	3609.72	3488.97	3437.77	3179.13	2959.58	3153.83	3060.44	3290.88	3414.13	3161.65
CTSA	NM_001127695.1	NM_001127695.1:1540	Endogenous	mRNA	3271.51	3228.77	3247.25	3302.39	3369.38	3409.35	3349.67	3335.36	3459.05	3387	3443.88
CTSD	NM_001909.3	NM_001909.3:1495	Endogenous	mRNA	8206.99	9698.06	9070.09	9801.74	9404.54	8354.41	8077.73	10047.58	8145.99	10174.57	7985.94
CTSL	NM_001912.4	NM_001912.4:1072	Endogenous	mRNA	1221.88	1181.04	1159.22	1256.15	1153.9	1225.78	1215.91	1226.77	1320.04	1235.71	1262.9
CTSS	NM_004079.3	NM_004079.3:685	Endogenous	mRNA	1562.38	1652.09	1632.37	1673.39	2426	2529.63	2697.6	2533.94	2218.49	2453.78	2478.59
CTSW	NM_001335.3	NM_001335.3:1075	Endogenous	mRNA	22.58	28.4	28.8	26.63	31.52	24.47	31.2	33.72	20	31.2	20
CTSZ	NM_001336.3	NM_001336.3:827	Endogenous	mRNA	5370.05	5704.45	5574.95	5546.15	6003.64	5763.03	6109.68	6041.77	5773.15	6170.4	5412.92
CXCL9	NM_002416.2	NM_002416.2:2012	Endogenous	mRNA	20	21.54	20	25.52	20	20	20	20	20	20	20
CXCR6	NM_006564.1	NM_006564.1:97	Endogenous	mRNA	20	20	20	20	20	20	20	20	20	20	20
CYBB	NM_000397.3	NM_000397.3:2686	Endogenous	mRNA	20	20	20	20	20	20	20	20	20	27.13	20
CYP1A1	NM_000499.3	NM_000499.3:695	Endogenous	mRNA	82.78	50.92	70.97	58.81	55.16	39.62	49.5	49.28	48.38	52.9	91.15
CYP1A2	NM_000761.3	NM_000761.3:617	Endogenous	mRNA	23.52	25.46	36	33.29	31.52	37.29	26.9	40.2	26.49	20	37.34
CYP1B1	NM_000104.3	NM_000104.3:1715	Endogenous	mRNA	672.55	694.33	637.72	668.02	335.47	267.99	303.44	379.96	414.67	367.59	657.81
CYP4A11	NM_000778.3	NM_000778.3:1727	Endogenous	mRNA	20	20	20	20	27.02	20	20	25.94	20	20	20
CYP4A22	NM_001010969.3	NM_001010969.3:285	Endogenous	mRNA	20	20	20	20	20	20	20	20	20	20	20
CYP8B1	NM_004391.2	NM_004391.2:1634	Endogenous	mRNA	20	20	20	20	20	20	20	20	20	20	20
D2HGDH	NM_001287249.1	NM_001287249.1:550	Endogenous	mRNA	79.01	80.3	81.26	62.14	76.55	75.74	72.09	84.29	73.72	74.6	70.28
DAO	NM_001917.4	NM_001917.4:965	Endogenous	mRNA	20	20	20	20	20	20	20	20	20	20	20
DCK	NM_000788.2	NM_000788.2:310	Endogenous	mRNA	1095.83	1197.69	1157.16	1189.57	1214.69	1139.56	1193.31	1163.23	1110.4	1243.85	1128.93
DDC	NM_000790.3	NM_000790.3:803	Endogenous	mRNA	20	20	20	20	20	20	20	20	20	20	31.85
DEPTOR	NM_022783.3	NM_022783.3:790	Endogenous	mRNA	20	21.54	20.57	20	20	20	20	20	20	20	20
DERA	NM_015954.2	NM_015954.2:960	Endogenous	mRNA	1449.51	1429.79	1457.51	1535.79	1497.25	1407.55	1543.02	1556.16	1438.68	1494.78	1401.27

DGLUCY	NM_001102369.2	NM_001102369.2:442	Endogenous	mRNA	583.19	551.35	542.07	503.79	539.24	503.36	573.52	456.47	573.63	537.15	522.73
DGUOK	NM_080916.2	NM_080916.2:902	Endogenous	mRNA	4254.46	4020.05	3970.35	4074.72	3978.41	3938.34	4017.88	4066.75	4258.44	3925.51	4345.49
DMGDH	NM_013391.2	NM_013391.2:1500	Endogenous	mRNA	20	20	20	20	20	20	20	20	20	20	20
DTL	NM_016448.2	NM_016448.2:715	Endogenous	mRNA	349.91	351.57	311.66	361.75	278.06	248.19	303.44	267.14	284.51	336.39	344.83
DUOX1	NM_175940.1	NM_175940.1:4855	Endogenous	mRNA	31.98	26.44	28.8	55.48	27.02	36.12	26.9	40.2	25.34	37.98	31.85
DUOX2	NM_014080.4	NM_014080.4:3320	Endogenous	mRNA	32.92	26.44	26.74	29.96	33.77	34.96	32.28	31.12	35.71	42.05	37.34
ECHS1	NM_004092.3	NM_004092.3:125	Endogenous	mRNA	966.97	1072.34	1021.39	1094.14	1106.62	1060.32	1068.49	1161.93	987.15	1220.79	1043.27
EEA1	NM_003566.3	NM_003566.3:2035	Endogenous	mRNA	1869.97	1915.52	1881.29	1877.57	1820.34	1933.05	2022.93	1825.89	1892.51	1907.14	1970.13
EFNA4	NM_005227.2	NM_005227.2:380	Endogenous	mRNA	131.69	136.12	139.89	148.7	155.35	147.98	147.42	140.05	134.77	204.82	128.49
EGFR	NM_201282.1	NM_201282.1:1354	Endogenous	mRNA	6199.68	6697.47	6499.65	6659.15	8095.29	7778.81	7661.31	7902.68	7234.86	8146.71	7480.78
EHHADH	NM_001166415.1	NM_001166415.1:2022	Endogenous	mRNA	143.92	141.02	168.69	132.05	131.71	145.65	167.86	149.13	172.78	142.43	157.04
EME1	XM_011524392.1	XM_011524392.1:416	Endogenous	mRNA	342.39	382.91	357.95	358.42	352.36	286.64	337.87	282.7	308.7	340.46	331.65
ENO1	NM_001428.2	NM_001428.2:1689	Endogenous	mRNA	14696.38	14308.63	14560.69	14098.4	17215.02	18129.19	18523.79	16671.61	16619.11	17213.09	14943.99
ENO3	NM_001976.4	NM_001976.4:1368	Endogenous	mRNA	44.21	47.99	47.32	44.39	58.54	52.43	51.65	42.79	63.35	35.27	47.22
EOMES	NM_005442.2	NM_005442.2:1670	Endogenous	mRNA	53.62	45.05	58.63	58.81	52.91	48.94	63.49	50.58	58.75	63.75	73.58
EPC1	NM_025209.2	NM_025209.2:1615	Endogenous	mRNA	837.16	923.48	853.73	906.6	726.11	723.58	773.66	704.16	739.5	675.5	818.14
ERCC6	NM_001277058.1	NM_001277058.1:200	Endogenous	mRNA	256.79	261.47	267.43	244.13	225.15	256.34	230.27	201	230.37	240.09	240.5
ERN1	NM_001433.2	NM_001433.2:435	Endogenous	mRNA	529.57	484.76	475.21	513.78	686.71	650.18	677.9	704.16	752.17	754.17	801.67
EXO1	NM_003686.3	NM_003686.3:2715	Endogenous	mRNA	855.03	841.22	787.9	861.11	828.55	745.72	765.05	780.67	745.26	786.73	809.36
EZH2	NM_001203247.1	NM_001203247.1:1121	Endogenous	mRNA	2199.19	2069.27	2104.49	2086.19	2029.73	1934.22	2005.71	2002.25	1913.25	2148.58	1898.75
FABP5	NM_001444.1	NM_001444.1:100	Endogenous	mRNA	13337.18	13060.99	13350.04	13729.99	12605.06	11795.22	12491.59	12324.75	13055.24	12807.4	12406.11
FAH	NM_000137.1	NM_000137.1:920	Endogenous	mRNA	618.93	636.55	632.58	636.95	757.63	746.89	773.66	695.08	668.08	720.26	694.05
FAHD1	NM_031208.3	NM_031208.3:542	Endogenous	mRNA	727.11	713.91	707.67	695.77	730.61	796.99	777.97	783.26	716.46	743.32	695.15
FAM30A	NR_026800.2	NR_026800.2:9125	Endogenous	mRNA	20	20	20	20	24.77	20	20	20	25.34	20	20
FANCA	NM_000135.2	NM_000135.2:798	Endogenous	mRNA	964.14	1016.52	968.93	959.87	990.66	913.51	917.85	920.73	863.9	906.09	892.82
FANCD2	NM_033084.3	NM_033084.3:260	Endogenous	mRNA	9122.22	9189.8	9245.98	9277.98	9452.95	9032.55	9291.48	9039.97	9204.55	9134.19	9278.5
FANCI	NM_001113378.1	NM_001113378.1:541	Endogenous	mRNA	1872.79	1865.58	1732.14	1813.21	1867.62	1882.95	1945.45	1833.67	1939.74	1920.7	1852.62
FASLG	NM_000639.1	NM_000639.1:625	Endogenous	mRNA	20	20	20	20	20	20	20	20	20	20	20
FASN	NM_004104.4	NM_004104.4:5387	Endogenous	mRNA	2511.48	2595.16	2581.76	2495.66	2484.54	2535.45	2356.5	2440.57	2628.56	2540.59	2588.4
FBP1	NM_000507.3	NM_000507.3:590	Endogenous	mRNA	40.45	36.23	51.43	37.73	41.65	36.12	43.04	32.42	42.62	32.55	32.95
FCAR	NM_002000.2	NM_002000.2:1415	Endogenous	mRNA	20	20	20	20	20	20	20	20	20	20	20
FCRL2	NM_001159488.1	NM_001159488.1:132	Endogenous	mRNA	20	20	20	20	20	20	20	20	20	20	20
FDX1	NM_004109.4	NM_004109.4:618	Endogenous	mRNA	1391.19	1375.92	1256.93	1360.46	1200.05	1145.38	1250.34	1235.85	1269.36	1275.04	1258.51
FDXR	NM_004110.3	NM_004110.3:1123	Endogenous	mRNA	128.87	120.45	128.57	127.61	124.96	103.7	131.28	106.34	124.4	155.99	132.88
FGF1	NM_033137.1	NM_033137.1:315	Endogenous	mRNA	20	28.4	20	26.63	20	20	20	20	20	20	23.06
FH	NM_000143.2	NM_000143.2:203	Endogenous	mRNA	4110.55	4161.07	4154.47	4159.06	4020.07	3871.93	4262.14	4132.89	4046.5	4236.13	4187.35
FLT1	NM_002019.4	NM_002019.4:530	Endogenous	mRNA	158.97	164.52	163.55	147.59	392.89	329.75	373.38	381.26	357.08	381.16	341.53
FLT3	NM_004119.2	NM_004119.2:2374	Endogenous	mRNA	20	31.34	27.77	20	32.65	25.63	29.05	38.9	25.34	35.27	23.06
FNIP1	NM_001008738.2	NM_001008738.2:1264	Endogenous	mRNA	607.65	589.54	568.81	602.55	664.19	612.89	671.44	569.29	588.6	569.7	627.06
FNIP2	NM_020840.1	NM_020840.1:1732	Endogenous	mRNA	248.33	295.75	275.66	244.13	280.31	277.32	248.56	247.69	254.56	249.58	249.29
FOLH1	NM_004476.1	NM_004476.1:695	Endogenous	mRNA	20	20	20	20	20	20	20	29.83	20	20	20
FOLH1B	NM_153696.2	NM_153696.2:47	Endogenous	mRNA	20	20	20	20	20	20	21.52	20	20	20	20
FOLR1	NM_000802.2	NM_000802.2:815	Endogenous	mRNA	36.68	44.07	50.4	45.5	42.78	33.79	37.66	49.28	27.64	47.48	20
FOLR3	NM_000804.2	NM_000804.2:469	Endogenous	mRNA	60.2	42.11	40.11	46.61	49.53	69.91	53.8	46.68	49.53	47.48	40.63
FOXM1	NM_202002.1	NM_202002.1:1000	Endogenous	mRNA	934.99	911.73	893.84	850.01	874.71	885.54	888.8	835.14	938.77	855.91	923.57
FOXP3	NM_014009.3	NM_014009.3:1230	Endogenous	mRNA	20	20	20	20	20	20	20	20	24.19	20	20
FPR1	NM_002029.3	NM_002029.3:350	Endogenous	mRNA	20	21.54	20	20	20	20	20	20	20	27.13	20
FTCD	NM_006657.2	NM_006657.2:1173	Endogenous	mRNA	20	20	20	20	20	20	20	20	20	20	20
G6PC	NM_000151.2	NM_000151.2:1155	Endogenous	mRNA	20	20	25.71	32.18	27.02	24.47	20	27.23	20	20	20
GABARAP	NM_007278.1	NM_007278.1:233	Endogenous	mRNA	5790.51	5470.4	5787.86	5840.21	6004.77	6337.47	6243.1	5989.9	6259.23	6033.4	6181.64
GAD1	NM_000817.2	NM_000817.2:575	Endogenous	mRNA	124.16	134.16	148.12	113.19	101.32	115.35	134.5	134.87	95.6	115.3	120.8
GADL1	NM_207359.2	NM_207359.2:1674	Endogenous	mRNA	20	22.52	20	20	20	20	20	20	20	20	20
GAPDH	NM_001256799.1	NM_001256799.1:386	Endogenous	mRNA	78064.66	79365.83	79175.56	78470.54	96824.94	100085.14	100833.32	95096.66	89047.22	97490.62	86723.04
GAPDHS	NM_014364.4	NM_014364.4:297	Endogenous	mRNA	20	20	20	20	20	20	20	20	20	20	20
GAPVD1	NM_001282679.1	NM_001282679.1:380	Endogenous	mRNA	2408.01	2563.82	2581.76	2368.04	2610.62	2709.07	2727.73	2489.85	2471.9	2550.09	2538.99
GART	NM_000819.3	NM_000819.3:370	Endogenous	mRNA	3992.03	4084.68	4079.38	3848.35	4090.99	4376.45	4576.34	4127.7	4098.33	4184.58	4256.53
GATM	NM_001482.2	NM_001482.2:525	Endogenous	mRNA	27.28	23.5	27.77	20	20	23.3	25.82	25.94	20	27.13	20
GBA	NM_001005742.2	NM_001005742.2:1695	Endogenous	mRNA	971.67	975.39	1010.07	1057.52	994.04	1017.21	1014.69	1033.55	994.06	1142.11	1047.66
GCDH	NM_000159.2	NM_000159.2:464	Endogenous	mRNA	273.72	294.77	271.55	292.95	274.68	255.18	258.25	230.83	266.08	250.94	262.46
GCK	NM_000162.4	NM_000162.4:1739	Endogenous	mRNA	20	20	20	24.41	24.77	20	25.82	20	27.64	29.84	20
GCLC	NM_001498.2	NM_001498.2:520	Endogenous	mRNA	668.79	646.34	634.64	624.75	723.86	727.08	710.18	737.88	708.4	729.76	656.71
GDA	NM_001242506.2	NM_001242506.2:861	Endogenous	mRNA	17676.29	16029.27	15932.83	16838.18	18108.87	17541.93	17820.07	18046.21	19654.27	18006.6	20726.99
GLRX	NM_002064.2	NM_002064.2:360	Endogenous	mRNA	1189.9	1134.04	1096.47	1170.71	1326.14	1420.37	1498.9	1364.23	1261.29	1329.3	1212.39
GLS	NM_014905.3	NM_014905.3:985	Endogenous	mRNA	4033.42	4066.07	4040.29	3951.55	4106.75	4200.51	4481.65	4357.23	4166.29	4341.93	4285.09
GLS2	NM_013267.2	NM_013267.2:1945	Endogenous	mRNA	20	27.42	20	20	20	20	20	27.23	20	20	20
GLUD1	NM_005271.2	NM_005271.2:2680	Endogenous	mRNA	2603.66	2523.67	2591.01	2687.63	2464.27	2575.07	2510.37	2421.12	2592.85	2428.01	2590.6
GLUL	NM_001033044.2	NM_001033044.2:2645	Endogenous	mRNA	18166.36	18665.55	18458.01	17563.91	21638.11	23195.43	23861.95	22823.61	21824.38	22671.36	23334.06
GLYAT	NM_005838.3	NM_005838.3:252	Endogenous	mRNA	24.46	26.44	20	20	20	27.96	20	20	20	20	20
GLYCTK	NR_026700.1	NR_026700.1:1336	Endogenous	mRNA	88.42	94.99	102.86	84.34	84.43	99.04	78.55	68.73	94.45	58.33	118.6
GMPR	NM_006877.3	NM_006877.3:325	Endogenous	mRNA	63.96	56.8	66.86	48.83	66.42	73.41	61.33	58.36	62.2	56.97	63.69
GMPR2	NM_001002001.2	NM_001002001.2:392	Endogenous	mRNA	1302.77	1311.29	1316.59	1321.62	1370.04	1293.36	1417.13	1230.66	1451.35	1372.71	1397.98
GMPS	NM_003875.2	NM_003875.2:385	Endogenous	mRNA	1391.19	1467.98	1517.17	1398.19	1490.5	1451.83	1470.93	1464.08	1400.67	1540.9	1346.37
GNG12	NM_018841.3	NM_018841.3:245	Endogenous	mRNA	4324.07	4302.09	4312.87	4392.09	5024.24	5257.34	5542.61	5150.87	5111.98	5165.28	5160.33
GNLY	NM_012483.2	NM_012483.2:880	Endogenous	mRNA	20	25.46	20	22.19	27.02	26.8	20	27.23	28.8	20	31.85
GNS	NM_002076.3	NM_002076.3:1340	Endogenous	mRNA	821.17	887.25	907.21	764.56	889.35	942.64	1023.3	850.7	933.01	914.23	975.18
GOT1	NM_002079.2	NM_002079.2:615	Endogenous	mRNA	747.8	727.62	746.75	807.84	695.72	651.34	688.66	736.58	711.85	697.2	708.32
GOT2	NM_002080.2	NM_002080.2:2145	Endogenous	mRNA	1848.34	1845.01	1960.49	1817.64	1971.19	2143.95	1986.34	1946.49	1901.73	2088.9	2100.81
GPI	NM_000175.2	NM_000175.2:1695	Endogenous	mRNA	1684.67	1906.71	1854.54	1799.89	2809.88	2767.33	2823.49	2749.21	2180.48	2775.25	2055.79
GPS1	NM_004127.4	NM_004127.4:605	Endogenous	mRNA	3723.95	3764.45	3678.23	3785.1	3781.41	3628.4	3648.8	3627.14	3673.3	3811.57	3525.15
GPT	NM_005309.2	NM_005309.2:431	Endogenous	mRNA	20	20	20	20	23.64	20	20	20	20	20	21.96
GPX1	NM_000581.2	NM_000581.2:745	Endogenous	mRNA	1052.56	1035.13	969.96	1076.38	1107.74	1067.31	1137.36	1154.15	1182.97	1154.32	962
GPX4	NM_001039847.1	NM_001039847.1:435	Endogenous	mRNA	7968.07	8073.39	7965.39	8174.96	8734.72	8143.51	8689.99	8879.16	8903.92	9161.32	8085.88
GRAP2	NM_001291826.1	NM_001291826.1:848	Endogenous	mRNA	20	20	20	20	20	20	20	20	20	20	20
GRIN1	NM_000832.5	NM_000832.5:1290	Endogenous	mRNA	20	20	20	20	20	20	20	20	20	20	20
GSK3B	NM_002093.2	NM_002093.2:925	Endogenous	mRNA	2274.44	2499.19	2300.95	2378.03	3280.45	3395.36	3267.89	3300.35	3288.57	3256.79	3065.01
GTSE1	NM_016426.5	NM_016426.5:305	Endogenous	mRNA	1366.73	1229.03	1313.51	1259.48	1234.95	1315.5	1267.56	1221.58	1317.73	1405.26	1269.49
GUSB	NM_000181.3	NM_000181.3:1899	Endogenous	mRNA	3517.95	3490.24	3422.11	3374.52	3543.87	3707.63	3760.71	3546.74	3623.77	3623.02	3673.4
GYS2	NM_021957.3	NM_021957.3:804	Endogenous	mRNA	20	20	20	20	20	20	20	20	20	20	20
GZMA	NM_006144.2	NM_006144.2:155	Endogenous	mRNA	20	20	20	20	20	20	20	20	20	20	20
GZMB	NM_004131.3	NM_004131.3:540	Endogenous	mRNA	27.28	22.52	27.77	34.4	23.64	27.96	29.05	32.42	32.25	20	36.24
GZMH	NM_033423.3	NM_033423.3:705	Endogenous	mRNA	25.4	20	20.57	20	22.52	20	22.6	20	20	20	20
H6PD	NM_004285.3	NM_004285.3:7250	Endogenous	mRNA	181.54	175.3	201.6	205.29	175.62	206.24	223.81	201	207.34	198.04	218.54
HAAO	NM_012205.2	NM_012205.2:243	Endogenous	mRNA	20	20	20	20	20	20	20	20	20	20	20
HACD2	NM_198402.2	NM_198402.2:510	Endogenous	mRNA	1900.07	1859.7	1936.83	1893.1	1830.48	1871.29	1912.1	1816.81	1753.14	1797.27	1827.37
HADH	NM_001184705.2	NM_001184705.2:645	Endogenous	mRNA	2752.28	2854.67	2866.68	2815.24	2751.34	2957.25	2938.63	2729.76	2895.79	2832.22	2832.2
HDC	NM_002112.3	NM_002112.3:1170	Endogenous	mRNA	20	20	20	20	20	20	20	20	20	20	20
HERC1	NM_003922.3	NM_003922.3:300	Endogenous	mRNA	911.47	1015.54	930.87	995.38	990.66	954.29	977.03	993.35	847.77	1002.4	889.52
HEXA	NM_000520.4	NM_000520.4:702	Endogenous	mRNA	1165.44	1235.88	1221.96	1191.79	1274.35	1296.86	1266.48	1256.6	1127.68	1207.22	1225.57
HEXB	NM_000521.3	NM_000521.3:950	Endogenous	mRNA	2547.22	2514.86	2572.5	2501.2	2760.35	2815.1	2964.45	2769.96	2702.28	2739.99	2500.55
HIF1A	NM_001530.2	NM_001530.2:1985	Endogenous	mRNA	6830.85	7048.06	7003.66	6975.41	7106.88	7299.91	7469.77	7149.24	7328.16	7381.69	8016.69

HIF3A	NM_152796.2	NM_152796.2:720	Endogenous	mRNA	20	24.48	20.57	20	33.77	23.3	20	20	20	20	20
HJURP	NM_018410.3	NM_018410.3:1325	Endogenous	mRNA	2086.31	1890.06	1910.09	2059.55	1930.67	1871.29	1900.26	1810.33	1978.9	1913.92	2025.04
HK1	NM_000188.2	NM_000188.2:3355	Endogenous	mRNA	822.11	830.45	898.99	836.69	1125.75	1207.14	1157.8	1148.96	1034.37	1147.54	980.67
HK2	NM_000189.4	NM_000189.4:6880	Endogenous	mRNA	3263.04	3236.6	3321.31	3195.86	6601.42	7798.62	7442.87	6083.27	5442.56	6387.42	5218.54
HK3	NM_002115.1	NM_002115.1:495	Endogenous	mRNA	25.4	28.4	36	23.3	31.52	30.29	39.81	36.31	31.1	33.91	27.45
HLA-A	NM_002116.5	NM_002116.5:1000	Endogenous	mRNA	2262.21	2309.2	2197.06	2288.15	2768.23	2665.95	2620.12	2596.19	2604.37	2668.1	2400.61
HLA-C	NM_002117.4	NM_002117.4:895	Endogenous	mRNA	600.12	690.41	673.73	701.31	699.09	749.22	678.97	797.53	695.73	794.87	856.58
HLA-DQA1	NM_002122.3	NM_002122.3:258	Endogenous	mRNA	20	20	20	20	20	20	20	20	20	20	20
HLA-DRB1	NM_002124.3	NM_002124.3:1016	Endogenous	mRNA	20	20	20	20	20	23.3	20	20	20	20	20
HLA-E	NM_005516.5	NM_005516.5:1287	Endogenous	mRNA	1460.8	1381.8	1330.99	1405.96	1785.45	1684.86	1644.17	1798.66	1777.33	1768.78	1696.68
HMOX1	NM_002133.2	NM_002133.2:781	Endogenous	mRNA	155.2	174.32	171.77	177.55	228.53	209.73	193.68	252.88	193.51	236.02	186.69
HNF4A	NM_178850.1	NM_178850.1:1116	Endogenous	mRNA	20	20	20	20	20	20	20	20	20	20	20
HPD	NM_002150.2	NM_002150.2:288	Endogenous	mRNA	29.16	20	20.57	20	20	20	20	20	23.04	20	26.36
HPRT1	NM_000194.1	NM_000194.1:240	Endogenous	mRNA	3200.96	3255.21	3348.05	3295.73	3878.22	3754.24	3885.53	3842.41	3546.59	3840.05	3685.48
HRAS	NM_005343.2	NM_005343.2:396	Endogenous	mRNA	1549.22	1643.27	1682.77	1643.43	1818.09	1849.16	1803.42	1884.24	1694.39	1859.66	1668.13
HSD11B1	NM_181755.1	NM_181755.1:155	Endogenous	mRNA	20	34.28	22.63	23.3	22.52	24.47	21.52	20	20	33.91	20
HSD17B8	NM_014234.3	NM_014234.3:875	Endogenous	mRNA	110.99	119.48	113.14	112.08	110.32	132.83	132.35	121.9	124.4	119.37	101.03
HSF1	XM_011517006.1	XM_011517006.1:63	Endogenous	mRNA	1443.87	1608.02	1564.48	1513.59	1597.44	1659.23	1600.05	1585.98	1400.67	1585.67	1537.45
HSF2	NM_001135564.1	NM_001135564.1:615	Endogenous	mRNA	504.18	572.89	530.75	483.82	472.82	525.5	536.94	490.19	496.45	463.9	478.81
HSPA2	NM_021979.3	NM_021979.3:2095	Endogenous	mRNA	65.84	55.82	61.72	63.25	41.65	33.79	47.35	62.25	58.75	70.53	71.38
HSPA4	NM_002154.3	NM_002154.3:1225	Endogenous	mRNA	3667.51	3542.15	3508.51	3745.15	3582.15	3508.39	3908.13	3751.63	3795.39	3924.15	3727.21
HSPE1	NM_002157.2	NM_002157.2:607	Endogenous	mRNA	21460.45	20453.77	21014.05	21112.64	21139.4	20936.13	22171.52	21976.8	21403.95	21841.22	23180.32
ICOS	NM_012092.2	NM_012092.2:640	Endogenous	mRNA	20	20	20	22.19	20	20	20	20	20	20	20
IDH1	NM_005896.3	NM_005896.3:418	Endogenous	mRNA	2127.7	2083.96	2040.72	2032.92	1800.08	1774.58	1851.84	1786.98	1900.58	1856.95	1921.81
IDH2	NM_002168.2	NM_002168.2:944	Endogenous	mRNA	6196.86	6450.68	6492.45	6438.32	6781.54	7144.94	6762.82	6738.15	6600.19	6863.53	6491.32
IDH3A	NM_005530.2	NM_005530.2:1521	Endogenous	mRNA	2500.19	2349.35	2468.61	2464.58	2234.62	2260.47	2475.94	2260.32	2352.11	2293.72	2444.54
IDH3B	NM_001258384.1	NM_001258384.1:556	Endogenous	mRNA	3978.86	4209.05	4229.55	4110.23	4298.13	4050.2	4176.06	4371.5	4208.91	4485.71	4011.64
IDH3G	NM_004135.2	NM_004135.2:390	Endogenous	mRNA	1359.21	1438.6	1410.19	1380.43	1466.86	1531.06	1373.01	1429.07	1374.17	1437.81	1295.85
IDNK	NM_001001551.3	NM_001001551.3:272	Endogenous	mRNA	93.12	89.12	85.37	94.32	75.43	85.06	76.4	63.54	78.33	70.53	94.44
IDO1	NM_002164.5	NM_002164.5:52	Endogenous	mRNA	61.14	51.9	76.12	78.79	90.06	80.4	104.37	94.67	67.96	69.18	82.36
IDO2	NM_194294.2	NM_194294.2:1575	Endogenous	mRNA	20	20	20	20	20	20	20	20	20	20	23.06
IFNG	NM_000619.2	NM_000619.2:970	Endogenous	mRNA	27.28	28.4	26.74	23.3	20	50.1	35.51	46.68	41.47	20	36.24
IL10	NM_000572.2	NM_000572.2:230	Endogenous	mRNA	20	20	20	20	20	20	20	20	20	20	20
IL2	NM_000586.2	NM_000586.2:300	Endogenous	mRNA	20	20.57	20	20	22.52	24.47	20	20	28.8	20	27.45
IL21R	NM_021798.2	NM_021798.2:2080	Endogenous	mRNA	20	20	20	20	20	20	20	20	20	20	20
IL2RA	NM_000417.1	NM_000417.1:1000	Endogenous	mRNA	20	20	20	20	23.64	24.47	20	20	20	29.84	20
IL4	NM_000589.2	NM_000589.2:625	Endogenous	mRNA	20	20	20	20	20	20	20	20	20	20	20
IL4I1	NM_152899.1	NM_152899.1:1452	Endogenous	mRNA	38.57	38.19	30.86	31.07	66.42	66.42	79.63	106.34	57.59	61.04	65.89
IL6	NM_000600.3	NM_000600.3:364	Endogenous	mRNA	299.12	283.02	303.43	297.39	717.1	582.59	612.26	737.88	837.41	798.94	923.57
IL7	NM_000880.3	NM_000880.3:516	Endogenous	mRNA	20	28.4	20	20	28.14	20	20	31.12	24.19	32.55	20
IMPDH1	NM_000883.3	NM_000883.3:862	Endogenous	mRNA	1110.88	1091.93	1184.93	1046.42	1164.03	1189.66	1228.82	1168.41	1109.25	1157.03	1069.62
IMPDH2	NM_000884.2	NM_000884.2:545	Endogenous	mRNA	2688.32	2699.94	2647.59	2656.56	2710.81	2730.04	2877.29	2749.21	2615.89	2891.91	2632.33
INMT	NM_006774.4	NM_006774.4:1025	Endogenous	mRNA	20	24.48	20	20	22.52	24.47	20	20	20	20	20
INSR	NM_000208.2	NM_000208.2:525	Endogenous	mRNA	352.74	337.86	325.03	329.57	338.85	408.98	384.14	316.42	285.66	373.02	379.97
IRF1	NM_002198.2	NM_002198.2:15	Endogenous	mRNA	201.29	239.93	236.58	236.36	383.88	435.78	379.84	395.52	374.36	406.93	333.85
IRF4	NM_002460.1	NM_002460.1:325	Endogenous	mRNA	20	20	20	20	20	20	20	20	20	20	20
ITCH	NM_001257138.1	NM_001257138.1:438	Endogenous	mRNA	8301.99	7982.32	7753.5	7712.23	8508.45	8727.27	9016.02	8080.34	8498.46	8450.55	8994.07
ITGA1	NM_181501.1	NM_181501.1:1875	Endogenous	mRNA	1088.31	1113.47	1073.85	1116.33	1356.53	1418.04	1425.73	1353.86	1268.2	1346.93	1311.22
ITGA11	NM_012211.3	NM_012211.3:650	Endogenous	mRNA	20	20	20	20	20	20	20	20	20	20	20
ITGAM	NM_000632.3	NM_000632.3:515	Endogenous	mRNA	20	20	20	20	20	20	20	20	20	20	20
ITGB1	NM_002211.3	NM_002211.3:355	Endogenous	mRNA	14973.87	15686.51	15012.24	15508.79	16289.65	16560.84	17276.67	17043.79	15860.03	17077.44	16816.38
ITGB2	NM_000211.2	NM_000211.2:520	Endogenous	mRNA	117.58	112.62	120.34	118.74	150.85	104.87	156.02	142.65	125.55	176.34	149.35
ITGB5	NM_002213.3	NM_002213.3:2560	Endogenous	mRNA	1604.71	1752.96	1694.08	1668.95	1854.12	1937.71	1913.17	1809.03	1787.69	1707.74	1748.3
ITK	NM_005546.3	NM_005546.3:3430	Endogenous	mRNA	20	20	20	20	20	20	20	20	20	20	20
JAK2	NM_004972.3	NM_004972.3:1464	Endogenous	mRNA	583.19	596.4	545.15	544.85	551.62	583.76	601.5	560.22	634.68	571.06	579.84
KANSL1	NM_001193465.1	NM_001193465.1:1838	Endogenous	mRNA	1659.27	1681.47	1580.94	1536.9	1892.39	1859.64	2005.71	1849.23	1870.63	1816.26	1746.1
KAT6A	NM_001099412.1	NM_001099412.1:550	Endogenous	mRNA	2307.36	2298.43	2260.84	2167.19	2285.28	2274.45	2410.3	2213.63	2293.36	2413.09	2386.34
KDM3B	NM_016604.3	NM_016604.3:4178	Endogenous	mRNA	1166.38	1160.48	1116.02	1116.33	1241.71	1237.43	1218.06	1234.55	1235.95	1341.51	1199.21
KEAP1	NM_012289.3	NM_012289.3:561	Endogenous	mRNA	589.77	582.69	579.1	583.69	575.26	580.26	578.9	595.23	517.19	553.42	524.93
KIF2C	NM_006845.3	NM_006845.3:1940	Endogenous	mRNA	1544.51	1493.44	1477.05	1492.51	1356.53	1387.74	1480.61	1465.38	1468.63	1466.3	1290.36
KIR3DL1/2	NM_001322168.1	NM_001322168.1:466	Endogenous	mRNA	20	20	20	20	20	20	20	20	20	20	20
KIR3DL3	NM_153443.3	NM_153443.3:539	Endogenous	mRNA	20	20	20	20	20	20	20	20	20	20	20
KLRB1	NM_002258.2	NM_002258.2:85	Endogenous	mRNA	20	20	20	20	20	20	20	20	20	20	20
KLRD1	NM_007334.2	NM_007334.2:1252	Endogenous	mRNA	39.51	42.11	47.32	43.28	67.55	48.94	52.73	79.1	34.56	82.74	38.44
KLRK1	NM_007360.1	NM_007360.1:760	Endogenous	mRNA	20	27.42	20.57	26.63	23.64	20	20	27.23	20	46.12	20
KMO	NM_003679.3	NM_003679.3:595	Endogenous	mRNA	27.28	38.19	34.97	35.51	48.41	55.93	63.49	70.03	55.29	61.04	52.71
KMT2A	NM_005933.2	NM_005933.2:14000	Endogenous	mRNA	979.19	899.98	964.82	845.57	1030.06	1075.47	1023.3	998.53	1103.49	994.26	1083.9
KMT2D	NM_003482.3	NM_003482.3:6070	Endogenous	mRNA	803.3	799.11	920.59	752.36	788.03	809.81	828.54	844.21	791.33	899.31	858.77
KMT2E	NM_018682.3	NM_018682.3:1541	Endogenous	mRNA	1082.66	1033.17	1098.53	1107.45	1367.79	1492.61	1544.1	1355.15	1301.61	1418.82	1316.71
KPNA2	NM_002266.2	NM_002266.2:917	Endogenous	mRNA	12834.88	12515.52	12620.78	12621.42	11633.54	11711.32	12208.59	12044.64	11973.64	12119.69	12611.46
KRAS	NM_033360.2	NM_033360.2:267	Endogenous	mRNA	1027.17	1022.39	989.5	1004.25	1304.75	1233.94	1389.15	1322.73	1250.93	1363.21	1224.47
KRT1	NM_006121.2	NM_006121.2:690	Endogenous	mRNA	20	21.54	20	20	20	20	20	25.94	20	20	20
KYAT1	NM_004059.4	NM_004059.4:1557	Endogenous	mRNA	140.15	173.34	151.2	155.35	159.86	152.64	137.73	159.51	120.95	132.93	130.68
KYAT3	NM_001008661.2	NM_001008661.2:1445	Endogenous	mRNA	1614.12	1489.52	1518.2	1609.03	1578.31	1485.62	1546.25	1540.59	1740.47	1557.18	1698.88
KYNU	NM_003937.2	NM_003937.2:738	Endogenous	mRNA	2138.05	2079.06	2119.92	2113.93	4009.93	4143.42	4292.27	4052.49	3813.82	3802.07	3722.82
L2HGDH	NM_024884.2	NM_024884.2:1296	Endogenous	mRNA	268.08	257.56	280.8	255.22	269.06	236.53	246.41	250.28	254.56	253.65	260.27
LAG3	NM_002286.5	NM_002286.5:1736	Endogenous	mRNA	20	26.44	20	20	32.65	23.3	23.67	20	20	37.98	20
LAMA4	NM_001105209.1	NM_001105209.1:287	Endogenous	mRNA	723.34	796.18	842.41	844.46	773.39	727.08	803.79	884.41	686.51	813.86	748.96
LAMB1	NM_002291.2	NM_002291.2:3120	Endogenous	mRNA	4068.22	4196.32	4205.9	3815.06	4079.73	4414.9	4527.92	3970.79	4028.07	4207.64	3971.01
LAMC1	NM_002293.3	NM_002293.3:4915	Endogenous	mRNA	4541.36	4570.42	4549.44	4561.87	5038.87	5129.17	5318.8	5043.24	4933.44	5154.43	5159.24
LAMTOR2	NM_001145264.1	NM_001145264.1:272	Endogenous	mRNA	1473.97	1582.56	1575.8	1571.3	1616.58	1510.09	1547.33	1697.51	1525.07	1732.16	1425.43
LAMTOR4	NM_001008395.2	NM_001008395.2:494	Endogenous	mRNA	3078.68	3114.19	3077.54	3051.6	3244.42	3185.63	3329.22	3226.43	3151.5	3290.7	2848.67
LAMTOR5	NM_006402.2	NM_006402.2:504	Endogenous	mRNA	5431.19	5178.56	5355.86	5446.28	5655.79	5694.28	5729.84	5593.08	5318.16	5669.87	5788.49
LAT	NM_001014987.1	NM_001014987.1:1290	Endogenous	mRNA	266.2	239.93	242.75	316.26	251.04	267.99	267.93	263.25	251.11	297.06	262.46
LCK	NM_005356.2	NM_005356.2:1260	Endogenous	mRNA	65.84	76.39	52.46	73.24	68.67	50.1	49.5	71.32	65.66	84.1	70.28
LDHA	NM_001165414.1	NM_001165414.1:1690	Endogenous	mRNA	37752.14	38610.08	37841.75	36425.02	68967.04	77132.07	79270.84	68302.26	60180.33	69777.43	55468.92
LDHB	NM_001174097.1	NM_001174097.1:586	Endogenous	mRNA	29798.18	29368.38	29476.25	29978.93	30555.2	31451.97	31836.38	31541.97	30262.95	31237.21	32421.48
LDHC	NM_002301.2	NM_002301.2:725	Endogenous	mRNA	21.63	20	20	20	25.89	20	24.75	20	31.1	20	31.85
LEPR	NM_001003679.1	NM_001003679.1:2000	Endogenous	mRNA	104.41	114.58	123.43	109.86	127.21	151.47	144.19	127.09	130.16	130.22	143.86
LTA	NM_000595.2	NM_000595.2:885	Endogenous	mRNA	20	20	20	20	20	20	20	20	20	20	20
LTA4H	NM_001256643.1	NM_001256643.1:1140	Endogenous	mRNA	3850.93	3903.51	3868.52	3965.97	4178.8	4180.7	4284.74	4267.76	3969.33	4408.39	4030.31
LTB	NM_002341.1	NM_002341.1:330	Endogenous	mRNA	20	20	20	20	20	20	20	27.23	20	31.2	20
LTC4S	NM_145867.1	NM_145867.1:31	Endogenous	mRNA	20	20	27.77	20	30.4	26.8	20	28.53	27.64	31.2	24.16
LY86	NM_004271.3	NM_004271.3:255	Endogenous	mRNA	20	20	20	20	20	20	20	20	20	20	20
LY96	NM_015364.2	NM_015364.2:360	Endogenous	mRNA	20.69	20	20	20	20	20	20	20	20	20	20
MAP1LC3B	NM_022818.4	NM_022818.4:1685	Endogenous	mRNA	920.88	952.86	898.99	977.62	1072.84	1134.89	1136.28	1095.79	1057.41	1132.62	1131.12
MAP2K1	NM_002755.2	NM_002755.2:970	Endogenous	mRNA	2156.86	2256.32	2175.46	2187.17	3214.03	3438.48	3504.62	3095.45	2926.89	3420.91	2744.34
MAP2K2	NM_030662.3	NM_030662.3:375	Endogenous	mRNA	1055.39	1179.08	1098.53	1088.59	1197.8	1119.75	1230.97	1327.92	1109.25	1275.04	1065.23
MAP2K3	NM_145109.1	NM_145109.1:370	Endogenous	mRNA	958.5	916.63	974.07	1039.76	1843.98	1722.15	1617.27	1971.13	1731.25	1791.84	1670.33
MAP3K12	NM_006301.2	NM_006301.2:800	Endogenous	mRNA	51.73	63.65	30.86	48.83	55.16	64.09	48.42	51.87	46.07	55.61	53.81

MAPK1	NM_138957.2	NM_138957.2:430	Endogenous	mRNA	4643.88	4698.71	4544.3	4727.21	4876.76	5112.85	5032.57	4925.23	4949.56	5052.7	5128.49
MAPK8	NM_002750.2	NM_002750.2:945	Endogenous	mRNA	889.83	823.6	847.56	845.57	856.7	844.76	943.67	881.82	881.18	908.81	931.25
MAPK8IP1	NM_005456.2	NM_005456.2:259	Endogenous	mRNA	20	20.57	20	20	20	20	20	28.53	20	28.49	21.96
MAPKAP1	NM_001006617.1	NM_001006617.1:1188	Endogenous	mRNA	3080.56	2974.15	3084.74	3039.39	3083.44	3225.25	3229.15	3136.95	3090.45	3088.59	3268.17
MAPT	NM_016834.3	NM_016834.3:1205	Endogenous	mRNA	54.56	63.65	54.52	63.25	56.29	72.24	55.95	72.62	61.05	71.89	50.52
MAT1A	NM_000429.2	NM_000429.2:2275	Endogenous	mRNA	31.98	43.09	30.86	36.62	31.52	39.62	36.58	45.39	32.25	36.62	28.55
MAT2A	NM_005911.4	NM_005911.4:805	Endogenous	mRNA	12843.35	13351.85	13125.81	13447.02	11677.44	10419.13	11236.94	12113.37	11810.07	12670.4	11792.22
MCAT	NM_014507.3	NM_014507.3:378	Endogenous	mRNA	126.04	187.05	150.17	168.67	172.24	149.14	133.43	133.57	126.71	189.9	126.29
ME2	NM_002396.3	NM_002396.3:610	Endogenous	mRNA	521.11	535.68	488.58	517.11	518.97	534.82	556.31	530.39	552.9	548	519.44
MGST3	NM_004528.2	NM_004528.2:195	Endogenous	mRNA	4983.45	4657.57	4819.96	4984.65	5117.68	5402.99	5337.09	5004.34	5296.27	5116.45	5327.26
MKI67	NM_002417.2	NM_002417.2:4020	Endogenous	mRNA	1196.48	1289.74	1359.79	1275.01	1283.36	1250.25	1355.79	1335.7	1206	1329.3	1166.26
MLST8	NM_001199173.1	NM_001199173.1:810	Endogenous	mRNA	374.37	330.03	367.21	351.77	314.09	342.57	323.88	341.06	340.95	310.62	328.35
MLYCD	NM_012213.2	NM_012213.2:1530	Endogenous	mRNA	250.21	264.41	267.43	280.75	231.91	217.89	257.17	221.75	260.32	241.44	241.6
MPC1	NM_016098.2	NM_016098.2:210	Endogenous	mRNA	786.37	802.05	788.93	788.98	719.36	667.65	681.12	692.49	753.32	727.05	729.19
MPC2	NM_001143674.1	NM_001143674.1:285	Endogenous	mRNA	1094.89	1007.7	1073.85	1039.76	991.79	1030.03	1092.17	976.49	1085.06	1032.24	1053.15
MPO	NM_000250.1	NM_000250.1:545	Endogenous	mRNA	20	20	20	20	20	20	20	20	20	27.13	20
MRAS	NM_001085049.2	NM_001085049.2:1700	Endogenous	mRNA	51.73	43.09	42.17	56.59	34.9	38.45	26.9	54.47	36.86	33.91	42.83
MS4A1	NM_152866.2	NM_152866.2:620	Endogenous	mRNA	20.69	20	20	23.3	20	20	20	20	20	33.91	20
MS4A2	NM_000139.3	NM_000139.3:126	Endogenous	mRNA	20	20	20	20	20	20	20	20	20	20	20
MS4A4A	NM_024021.2	NM_024021.2:800	Endogenous	mRNA	20	20	20	20	20	20	20	20	20	20	20
MSH2	NM_000251.1	NM_000251.1:2105	Endogenous	mRNA	2271.62	2354.25	2364.72	2330.31	2388.85	2517.98	2697.6	2441.87	2339.44	2585.35	2502.75
MSRB2	NM_012228.3	NM_012228.3:385	Endogenous	mRNA	484.42	447.54	481.38	479.38	526.85	410.15	487.44	486.3	444.62	496.45	444.76
MTF1	NM_005955.2	NM_005955.2:210	Endogenous	mRNA	895.48	925.44	857.84	895.51	843.19	897.2	855.44	833.84	881.18	883.04	897.21
MTOR	NM_004958.3	NM_004958.3:1865	Endogenous	mRNA	1186.13	1194.75	1131.45	1185.13	1165.15	1103.43	1088.94	1104.87	1129.98	1040.38	1193.72
MYB	NM_001130173.1	NM_001130173.1:183	Endogenous	mRNA	208.82	243.85	231.43	234.14	248.79	217.89	290.53	197.11	226.92	264.5	209.75
MYBL1	NM_001080416.3	NM_001080416.3:1030	Endogenous	mRNA	105.35	121.43	117.26	113.19	118.2	92.05	128.05	124.49	119.79	112.58	119.7
MYBL2	NM_002466.2	NM_002466.2:445	Endogenous	mRNA	4798.15	4854.42	4754.13	4616.24	5045.63	5026.63	5098.21	5069.18	5153.44	5149	4858.34
MYC	NM_002467.3	NM_002467.3:1610	Endogenous	mRNA	7145.02	7261.55	7302.98	7484.75	7466	7602.86	7406.29	7975.3	7148.47	7990.72	7875.03
MYCL	NM_001033081.2	NM_001033081.2:568	Endogenous	mRNA	136.39	129.27	133.72	134.27	118.2	116.52	135.58	125.79	125.55	124.79	124.09
MYCN	NM_005378.4	NM_005378.4:1545	Endogenous	mRNA	51.73	42.11	38.06	39.95	31.52	41.95	30.13	37.61	34.56	31.2	29.65
MYD88	NM_002468.3	NM_002468.3:2145	Endogenous	mRNA	1496.54	1525.76	1505.85	1599.04	1455.6	1526.4	1529.03	1521.14	1584.97	1562.61	1598.95
NAALAD2	NM_005467.3	NM_005467.3:830	Endogenous	mRNA	96.88	94.01	79.2	88.77	79.93	95.55	94.69	77.81	85.24	94.95	96.64
NADK	NM_001198993.1	NM_001198993.1:1558	Endogenous	mRNA	693.24	707.06	792.01	750.14	765.51	734.07	689.73	673.04	645.04	693.14	717.11
NADK2	NM_153013.3	NM_153013.3:315	Endogenous	mRNA	608.59	641.44	673.73	653.6	583.14	565.12	576.75	578.37	587.45	590.05	611.68
NAGLU	NM_000263.3	NM_000263.3:696	Endogenous	mRNA	166.49	210.55	237.6	223.04	189.13	160.8	149.57	182.85	178.54	155.99	168.02
NAT8L	NM_178557.3	NM_178557.3:3021	Endogenous	mRNA	20	20	20	20	20	20	20	20	20	20	20
NCAPH	NM_015341.3	NM_015341.3:1550	Endogenous	mRNA	1368.61	1248.61	1324.82	1290.55	1283.36	1332.98	1371.93	1185.27	1326.95	1170.6	1414.45
NCOA2	NM_006540.2	NM_006540.2:1045	Endogenous	mRNA	517.35	535.68	496.81	504.9	586.52	568.61	576.75	575.78	612.79	625.31	550.19
NCOR1	NM_006311.3	NM_006311.3:1390	Endogenous	mRNA	1340.4	1472.87	1440.02	1367.12	1482.62	1476.3	1581.76	1535.41	1408.73	1563.96	1463.87
NCR1	NM_004829.5	NM_004829.5:602	Endogenous	mRNA	33.86	35.25	32.91	33.29	30.4	32.63	35.51	29.83	28.8	35.27	39.53
NDC1	NM_001168551.1	NM_001168551.1:1845	Endogenous	mRNA	255.85	266.37	271.55	253.01	284.82	313.44	288.37	293.08	294.88	305.2	321.77
NDUFA1	NM_004541.3	NM_004541.3:240	Endogenous	mRNA	10457.91	10039.84	10211.82	10540.79	11107.81	11071.63	11278.9	11086.31	10719.25	11236.66	11392.49
NDUFA11	NM_175614.4	NM_175614.4:115	Endogenous	mRNA	20	20	20	20	20	20	20	20	20	20	20
NDUFA12	NM_018838.3	NM_018838.3:315	Endogenous	mRNA	9124.1	9078.16	9193.52	9368.97	9214.29	9020.9	9586.32	9632.6	9171.15	9608.94	9773.78
NDUFA13	NM_015965.6	NM_015965.6:167	Endogenous	mRNA	6989.81	7464.26	7316.35	7626.78	7730.55	7128.63	7310.52	7680.92	7176.12	8091.1	6730.73
NDUFA2	NM_001185012.1	NM_001185012.1:116	Endogenous	mRNA	425.16	448.52	441.26	469.39	472.82	523.17	477.76	474.63	449.23	496.45	481
NDUFA3	NM_004542.3	NM_004542.3:75	Endogenous	mRNA	2875.5	2879.16	2915.02	2920.66	2903.32	3104.07	2863.31	2950.21	2948.77	2929.89	2966.18
NDUFA4	NM_002489.2	NM_002489.2:35	Endogenous	mRNA	7968.07	7636.62	7960.24	8470.14	8557.98	8423.16	7894.8	8302.09	7795.82	8420.71	8895.23
NDUFA6	NM_002490.3	NM_002490.3:430	Endogenous	mRNA	6460.24	6169.62	6417.36	6340.67	6565.39	6530.89	6840.3	6638.3	6666.99	6658.71	6643.97
NDUFA7	NM_005001.2	NM_005001.2:373	Endogenous	mRNA	2162.51	2163.28	2132.26	2333.64	2217.73	2194.05	2242.44	2268.1	2215.04	2197.42	2160.11
NDUFB1	NM_004545.3	NM_004545.3:270	Endogenous	mRNA	6365.23	5989.43	6136.56	6393.94	6506.86	6643.91	6619.71	6613.66	6457.35	6542.06	6737.32
NDUFB10	NM_004548.2	NM_004548.2:155	Endogenous	mRNA	1784.37	2098.65	1966.66	2081.75	2068.01	1970.34	1970.2	2177.32	1864.87	2205.55	1752.69
NDUFB11	NM_001135998.1	NM_001135998.1:255	Endogenous	mRNA	1979.08	1990.93	1983.12	2145	2248.13	2041.41	2124.08	2095.62	2121.74	2086.19	2041.51
NDUFB2	NM_004546.2	NM_004546.2:230	Endogenous	mRNA	4375.81	4366.72	4271.73	4298.87	4613.34	4599	4477.34	4427.26	4560.23	4415.18	4595.87
NDUFB4	NM_004547.4	NM_004547.4:254	Endogenous	mRNA	11910.24	11541.11	11480.07	11864.62	11970.14	11754.44	12346.32	11922.74	12020.86	12011.18	11792.22
NDUFB7	NM_004146.5	NM_004146.5:239	Endogenous	mRNA	3385.32	3659.66	3682.35	3838.36	3919.87	3679.67	3685.39	3799.61	3668.69	4142.53	3444.98
NDUFB8	NM_001284367.1	NM_001284367.1:204	Endogenous	mRNA	2360.04	2441.41	2368.84	2495.66	2531.82	2473.7	2515.75	2523.57	2421.22	2596.21	2344.61
NDUFS7	NM_024407.4	NM_024407.4:376	Endogenous	mRNA	1032.81	1038.06	1059.45	1118.55	1085.23	1090.62	1012.54	1085.42	1018.25	1066.15	999.34
NDUFS8	NM_002496.3	NM_002496.3:190	Endogenous	mRNA	4910.08	5105.12	4884.76	5042.35	5068.14	4908.94	5124.04	5052.32	5175.33	5319.92	5047.22
NEDD8	NM_006156.2	NM_006156.2:330	Endogenous	mRNA	4373.92	4428.42	4433.21	4604.03	4632.48	4746.98	4646.28	4645.12	4324.1	4626.78	4520.1
NEU1	NM_000434.3	NM_000434.3:1508	Endogenous	mRNA	609.53	730.56	687.1	721.29	745.25	718.92	766.13	697.68	700.33	744.68	703.93
NFAT5	NM_173214.1	NM_173214.1:3290	Endogenous	mRNA	226.69	245.81	244.8	201.96	319.71	283.14	310.97	317.72	358.23	310.62	285.53
NFE2L2	NM_006164.3	NM_006164.3:995	Endogenous	mRNA	3285.62	3203.31	3158.79	3120.4	3354.75	3246.22	3450.82	3409.28	3616.86	3467.03	3626.18
NFKB1	NM_003998.2	NM_003998.2:1675	Endogenous	mRNA	847.51	892.15	843.44	853.34	1935.17	1912.08	1976.66	1936.12	1845.29	1835.25	1771.36
NFKB2	NM_002502.2	NM_002502.2:825	Endogenous	mRNA	447.74	440.69	419.66	430.55	1158.4	1068.48	1084.63	1161.93	1119.61	1119.05	1106.96
NFS1	NM_021100.3	NM_021100.3:1775	Endogenous	mRNA	934.99	1046.88	1080.02	960.98	960.27	989.25	1008.24	986.86	954.9	1002.4	943.33
NGFR	NM_002507.3	NM_002507.3:2730	Endogenous	mRNA	24.46	22.52	20	22.19	20	20	20	29.83	20	27.13	20
NKG7	NM_005601.3	NM_005601.3:633	Endogenous	mRNA	20	20	20	20	20	30.29	20	20	20	20	21.96
NME1	NM_000269.2	NM_000269.2:500	Endogenous	mRNA	13496.14	14048.13	13937.37	14090.63	14319.58	13979.95	14013.09	14457.98	13295.98	14542.28	13899.63
NME2	NM_001018137.2	NM_001018137.2:669	Endogenous	mRNA	56641.84	55932.03	55328.78	57191.45	58175.56	59365.26	60238.09	58488.1	59393.61	60020.63	59342.19
NOD2	NM_001293557.1	NM_001293557.1:652	Endogenous	mRNA	20	20	20	20	20	20	24.75	20	20	29.84	25.26
NOS1	NM_000620.4	NM_000620.4:2212	Endogenous	mRNA	27.28	20	34.97	26.63	34.9	27.96	32.28	20	28.8	28.49	35.14
NOS2	NM_000625.4	NM_000625.4:605	Endogenous	mRNA	29.16	24.48	20	33.29	52.91	41.95	36.58	54.47	36.86	47.48	32.95
NOS3	NM_000603.4	NM_000603.4:1456	Endogenous	mRNA	20	20	20	20	20	20	20	20	20	20	20
NOX1	NM_007052.4	NM_007052.4:455	Endogenous	mRNA	20	20	20	20	20	20	23.67	20	20	20	20
NOX3	NM_015718.2	NM_015718.2:398	Endogenous	mRNA	20.69	28.4	20	20	20	24.47	20	20	20	20	20
NOX4	NM_001143836.2	NM_001143836.2:1795	Endogenous	mRNA	181.54	174.32	147.09	176.44	163.23	146.81	171.09	154.32	156.65	164.13	142.76
NPM1	NM_002520.6	NM_002520.6:910	Endogenous	mRNA	110161.73	107500.27	109161.99	108421.73	108765.8	111971.25	116330.25	111545.21	109828.02	111894.55	115149.35
NPR1	NM_000906.3	NM_000906.3:1120	Endogenous	mRNA	20	20	20	20	20	20	20	20	20	20	20
NPR2	NM_003995.3	NM_003995.3:1085	Endogenous	mRNA	49.85	52.88	47.32	35.51	56.29	48.94	50.57	41.5	56.44	37.98	60.4
NQO1	NM_000903.2	NM_000903.2:790	Endogenous	mRNA	3323.24	3126.92	3156.74	3353.43	3359.25	3273.02	3316.31	3344.44	3489	3502.3	3449.37
NR2F1	NM_005654.4	NM_005654.4:2885	Endogenous	mRNA	104.41	107.72	96.69	107.64	94.56	104.87	118.36	85.59	85.24	103.09	91.15
NRAS	NM_002524.3	NM_002524.3:877	Endogenous	mRNA	1101.48	999.87	1031.67	1006.47	1220.32	1238.6	1360.1	1242.33	1179.51	1155.68	1330.99
NRF1	NM_001040110.1	NM_001040110.1:2910	Endogenous	mRNA	224.81	216.43	217.03	256.33	221.77	238.86	219.51	229.53	220.01	187.19	197.67
NSD1	NM_022455.4	NM_022455.4:3140	Endogenous	mRNA	1265.15	1412.16	1298.08	1266.14	1428.58	1293.36	1366.55	1329.22	1314.28	1364.57	1341.97
NT5E	NM_002526.2	NM_002526.2:1214	Endogenous	mRNA	1617.88	1583.54	1529.51	1474.76	1678.5	1697.68	1892.73	1832.37	1624.13	1782.35	1689
NUP205	NM_015135.1	NM_015135.1:5075	Endogenous	mRNA	3581.91	3503.95	3420.06	3465.51	3578.77	3750.75	3762.86	3555.81	3705.55	3613.53	3600.92
NUP62	NM_016553.3	NM_016553.3:457	Endogenous	mRNA	1622.58	1616.83	1647.8	1714.45	1757.3	1662.73	1704.43	1882.95	1708.22	1843.39	1658.25
OAT	NM_000274.3	NM_000274.3:775	Endogenous	mRNA	1066.67	1078.21	1139.68	1207.32	1195.55	1140.72	1198.69	1251.41	1118.46	1325.23	1210.19
ODC1	NM_002539.1	NM_002539.1:950	Endogenous	mRNA	4661.76	4447.02	4561.79	4817.09	4184.43	3725.11	3845.72	4228.85	4623.59	4240.2	4789.15
OGDH	NM_001003941.2	NM_001003941.2:196	Endogenous	mRNA	3005.31	2969.25	3018.91	3103.76	3110.46	2954.92	3082.81	2943.73	3406.06	3175.4	3189.11
OGDHL	NM_018245.2	NM_018245.2:3615	Endogenous	mRNA	24.46	25.46	24.69	20	27.02	20	20	20	31.1	27.13	26.36
OTC	NM_000531.5	NM_000531.5:544	Endogenous	mRNA	20	20	20	20	22.52	27.96	20	28.53	20	20	20
PAH	NM_000277.1	NM_000277.1:845	Endogenous	mRNA	20	20	20	20	20	20	20	20	20	20	20
PCK1	NM_002591.2	NM_002591.2:1870	Endogenous	mRNA	20	20	20	27.74	20	20	25.82	20	20	20	21.96
PCK2	NM_004563.2	NM_004563.2:795	Endogenous	mRNA	242.68	219.36	176.92	211.95	183.5	213.23	209.83	194.52	237.28	214.32	215.24
PCLAF	NM_014736.5	NM_014736.5:1025	Endogenous	mRNA	262.44	236.01	237.6	277.42	228.53	227.21	258.25	252.88	278.75	252.3	252.58
PDCD1	NM_005018.2	NM_005018.2:310	Endogenous	mRNA	20	20	20	20	20	20	20	20	20	20	20
PDCD1LG2	NM_025239.3	NM_025239.3:235	Endogenous	mRNA	284.07	264.41	248.92	267.43	316.34	297.12	276.54	298.26	322.52	291.63	340.43
PDGFB	NM_033016.2	NM_033016.2:1480	Endogenous	mRNA	35.74	40.15	50.4	34.4	73.17	72.24	67.79	66.14	62.2	62.4	73.58

PDGFRB	NM_002609.3	NM_002609.3:265	Endogenous	mRNA	20	20	20	20	20	20	20	20	20	20	20
PDHA1	NM_000284.3	NM_000284.3:1080	Endogenous	mRNA	1298.07	1396.49	1293.96	1360.46	1407.19	1420.37	1473.08	1470.57	1320.04	1530.05	1474.85
PDK1	NM_002610.3	NM_002610.3:1170	Endogenous	mRNA	543.68	569.96	529.72	509.34	1570.43	1914.41	1826.02	1431.66	1253.23	1557.18	1120.14
PDK2	NM_002611.3	NM_002611.3:435	Endogenous	mRNA	509.82	536.66	571.89	540.41	560.63	538.32	515.42	508.34	501.06	519.51	527.12
PDK3	NM_005391.1	NM_005391.1:585	Endogenous	mRNA	391.3	381.93	433.04	341.78	443.55	454.42	489.59	418.87	408.91	453.05	420.6
PDK4	NM_002612.3	NM_002612.3:1675	Endogenous	mRNA	24.46	34.28	33.94	23.3	29.27	30.29	27.98	31.12	26.49	32.55	20
PDP1	NM_001161778.1	NM_001161778.1:950	Endogenous	mRNA	2202.95	2072.21	2096.26	2093.95	2572.35	2470.2	2608.29	2562.47	2603.21	2624.69	2405.01
PDPK1	NM_002613.3	NM_002613.3:5935	Endogenous	mRNA	732.75	710	736.47	712.41	715.98	708.44	777.97	753.44	790.18	789.44	763.23
PEBP1	NM_002567.2	NM_002567.2:1335	Endogenous	mRNA	4394.62	4560.62	4649.22	4476.42	4500.76	4752.81	4789.39	4751.46	4380.54	4723.09	4862.73
PEMT	NM_148173.1	NM_148173.1:385	Endogenous	mRNA	612.35	670.82	680.93	668.02	679.96	703.77	653.15	683.41	656.56	709.41	641.34
PFKFB1	NM_002625.2	NM_002625.2:564	Endogenous	mRNA	21.63	20.57	27.77	20	27.02	24.47	20	20	32.25	20	21.96
PFKL	NM_001002021.1	NM_001002021.1:2410	Endogenous	mRNA	1474.91	1635.44	1638.54	1525.8	1983.58	1999.47	2037.99	1994.47	1757.75	2064.49	1678.01
PFKM	NM_000289.5	NM_000289.5:2195	Endogenous	mRNA	1413.77	1401.39	1398.88	1432.59	1395.93	1305.01	1373.01	1333.11	1454.81	1416.11	1435.32
PGAM2	NM_000290.3	NM_000290.3:58	Endogenous	mRNA	42.33	52.88	49.37	57.7	64.17	58.26	49.5	57.06	34.56	54.26	43.93
PGD	NM_002631.2	NM_002631.2:1472	Endogenous	mRNA	2990.26	3080.89	3136.16	3171.45	3110.46	3141.35	3092.5	3051.36	3203.34	3062.82	3238.52
PGK1	NM_000291.2	NM_000291.2:1030	Endogenous	mRNA	15576.81	15912.73	15661.28	15558.73	27108.14	30178.42	30004.98	27092.66	22926.72	27520.59	22607.07
PGM2	NM_018290.3	NM_018290.3:295	Endogenous	mRNA	1375.2	1445.45	1485.28	1364.9	1773.06	1917.9	2021.85	1772.72	1745.08	1904.43	1727.43
PHGDH	NM_006623.3	NM_006623.3:1900	Endogenous	mRNA	9447.68	9464.98	8962.09	9241.36	8954.24	9398.42	9436.75	9021.81	9692.94	9166.75	9515.7
PIK3C2A	NM_002645.1	NM_002645.1:3505	Endogenous	mRNA	2669.5	2745.97	2741.19	2699.83	2875.17	2848.89	3145.22	2945.02	2757.56	2939.38	3027.67
PIK3CA	NM_006218.2	NM_006218.2:2445	Endogenous	mRNA	563.44	623.82	609.95	589.24	692.34	709.6	728.47	661.37	655.41	694.49	711.62
PIK3CB	NM_006219.1	NM_006219.1:2945	Endogenous	mRNA	226.69	228.18	237.6	214.17	263.43	243.52	243.18	239.91	253.41	215.67	249.29
PIK3CD	NM_005026.3	NM_005026.3:2978	Endogenous	mRNA	126.98	129.27	154.29	152.03	198.13	216.73	187.23	230.83	194.67	181.76	209.75
PIK3R1	NM_181504.2	NM_181504.2:1105	Endogenous	mRNA	236.1	232.1	242.75	254.12	254.42	227.21	269.01	263.25	239.59	236.02	238.3
PIK3R2	NM_005027.2	NM_005027.2:3100	Endogenous	mRNA	334.86	345.69	360.01	355.1	361.37	318.1	331.42	385.15	298.33	332.33	311.88
PIK3R3	NM_003629.3	NM_003629.3:5016	Endogenous	mRNA	245.5	238.95	271.55	244.13	221.77	252.85	259.32	268.44	225.77	234.66	236.11
PIK3R4	NM_014602.1	NM_014602.1:3620	Endogenous	mRNA	1035.63	1008.68	1022.42	942.11	938.88	1078.97	1113.69	1043.92	994.06	1013.25	1099.28
PKLR	NM_181871.3	NM_181871.3:206	Endogenous	mRNA	21.63	26.44	26.74	28.85	20	23.3	25.82	32.42	27.64	35.27	21.96
PKM	NM_182471.1	NM_182471.1:2105	Endogenous	mRNA	16484.52	16406.3	16326.78	16821.54	19134.43	18495.06	18474.29	18579.2	18920.53	19185.33	17381.95
PLA2G15	NM_012320.3	NM_012320.3:900	Endogenous	mRNA	182.48	191.94	193.37	194.19	201.51	184.1	211.98	213.97	171.63	253.65	166.92
PLCG1	NM_002660.2	NM_002660.2:2290	Endogenous	mRNA	1996.01	2200.5	2139.46	1964.12	2208.73	2208.03	2154.2	2054.12	1895.97	2103.82	1999.78
PLK1	NM_005030.3	NM_005030.3:535	Endogenous	mRNA	2451.28	2422.8	2329.75	2394.67	2341.57	2253.48	2308.08	2374.43	2192	2337.13	2227.1
PNOC	NM_001284244.1	NM_001284244.1:416	Endogenous	mRNA	20	20	20	20	20	20	20	20	20	20	20
PNP	NM_000270.2	NM_000270.2:1150	Endogenous	mRNA	2535.94	2355.23	2408.95	2557.8	2441.76	2300.08	2300.54	2616.93	2625.1	2683.02	2745.44
POLE	NM_006231.3	NM_006231.3:3264	Endogenous	mRNA	1066.67	1028.27	1051.22	907.71	1055.96	1069.64	991.02	977.78	1034.37	1007.83	1108.06
PPARG	NM_005037.5	NM_005037.5:345	Endogenous	mRNA	1669.62	1571.78	1544.94	1522.47	1615.46	1568.35	1653.85	1502.99	1665.6	1642.64	1674.72
PPARGC1A	NM_013261.3	NM_013261.3:1505	Endogenous	mRNA	20	23.5	20	23.3	20	20	20	25.94	23.04	20	21.96
PPAT	NM_002703.3	NM_002703.3:1210	Endogenous	mRNA	1621.64	1596.27	1661.17	1573.52	1469.11	1526.4	1510.74	1392.76	1459.41	1440.53	1583.57
PPM1A	NM_021003.4	NM_021003.4:550	Endogenous	mRNA	1322.52	1372.99	1406.08	1338.27	1449.97	1536.89	1563.47	1508.17	1420.25	1539.55	1417.75
PRDX1	NM_002574.2	NM_002574.2:632	Endogenous	mRNA	26432.61	25084.9	25034.8	25778.82	25829.29	25874.21	26465.94	26511.7	26499.8	25825.05	27180.98
PRDX5	NM_012094.4	NM_012094.4:600	Endogenous	mRNA	11520.82	11440.24	11373.1	11790.28	11859.81	12234.49	12265.62	11767.13	12592.19	12236.35	12251.26
PRF1	NM_005041.3	NM_005041.3:2120	Endogenous	mRNA	20.69	20	20	20	20	26.8	21.52	32.42	27.64	20	25.26
PRIM1	NM_000946.2	NM_000946.2:480	Endogenous	mRNA	1418.47	1444.48	1347.45	1342.7	1212.44	1229.28	1285.85	1171.01	1200.24	1327.94	1301.34
PRIM2	NM_001282488.1	NM_001282488.1:124	Endogenous	mRNA	1277.37	1267.22	1221.96	1270.58	1243.96	1155.87	1218.06	1159.34	1174.9	1277.76	1203.6
PRKAA1	NM_006251.5	NM_006251.5:366	Endogenous	mRNA	3969.45	3988.71	3836.63	3941.56	3802.8	3645.88	3757.48	3658.26	4022.31	3793.93	3804.09
PRKAA2	NM_006252.2	NM_006252.2:975	Endogenous	mRNA	53.62	66.59	68.92	71.02	91.19	83.89	78.55	55.76	58.75	75.96	66.99
PRKAB1	NM_006253.4	NM_006253.4:1550	Endogenous	mRNA	1080.78	1088.01	1091.33	1130.76	1129.13	1119.75	1201.92	1099.68	1100.03	1205.87	1100.37
PRKAB2	NM_005399.3	NM_005399.3:1600	Endogenous	mRNA	514.52	520.01	499.89	481.6	490.83	501.03	503.58	487.6	503.36	489.67	487.59
PRKAG1	NM_002733.3	NM_002733.3:825	Endogenous	mRNA	1004.59	912.71	918.53	924.36	884.84	849.42	879.11	879.23	839.71	864.05	885.13
PRKAG2	NM_016203.3	NM_016203.3:1895	Endogenous	mRNA	1439.16	1480.71	1448.25	1494.73	1499.5	1522.9	1499.98	1343.48	1472.08	1508.35	1509.99
PRKCG	NM_002739.3	NM_002739.3:445	Endogenous	mRNA	60.2	56.8	85.37	66.58	69.8	53.6	58.11	58.36	66.81	92.24	54.91
PRKN	NM_004562.2	NM_004562.2:3386	Endogenous	mRNA	20	20	20	20	20	20	20	20	20	20	20
PRODH2	NM_021232.1	NM_021232.1:428	Endogenous	mRNA	20	20	20	20	20	20	20	20	20	20	20
PRPS1	NM_002764.3	NM_002764.3:1081	Endogenous	mRNA	730.87	708.04	676.81	680.23	607.91	645.52	677.9	691.19	662.32	625.31	643.53
PRR5	NM_015366.3	NM_015366.3:1635	Endogenous	mRNA	59.26	52.88	59.66	51.04	56.29	60.59	52.73	68.73	50.68	73.25	63.69
PSAT1	NM_021154.3	NM_021154.3:1445	Endogenous	mRNA	386.6	411.31	409.38	417.24	360.24	376.36	369.08	370.88	359.38	381.16	406.33
PSMA3	NM_152132.1	NM_152132.1:465	Endogenous	mRNA	6165.82	5857.22	6057.35	5990.02	5977.75	6183.66	6569.14	6267.42	6183.21	5968.29	6144.3
PSMA7	NM_002792.2	NM_002792.2:639	Endogenous	mRNA	18506.87	18023.13	18534.13	18764.57	19105.16	19320.01	19518.04	19073.28	19617.41	19577.34	19721.06
PSMB1	NM_002793.2	NM_002793.2:0	Endogenous	mRNA	4191.44	4294.25	4160.64	4145.74	4479.37	4599	4503.17	4349.45	4521.07	4402.97	4198.33
PSMB10	NM_002801.3	NM_002801.3:249	Endogenous	mRNA	305.7	344.72	315.78	348.44	371.5	362.37	329.26	346.24	324.83	416.42	296.51
PSMB3	NM_002795.3	NM_002795.3:22	Endogenous	mRNA	6607.92	6486.92	6481.13	6537.08	6996.56	7037.75	7205.07	6956.01	6976.85	7054.79	6519.88
PSMC1	NM_002802.2	NM_002802.2:58	Endogenous	mRNA	2851.05	3022.14	3095.02	3098.21	3126.22	2996.87	3143.07	3324.99	2984.48	3346.31	3114.43
PSMD13	NM_175932.2	NM_175932.2:668	Endogenous	mRNA	3379.68	3387.42	3362.45	3342.34	3426.79	3479.26	3914.58	3698.46	3524.71	3525.36	3531.74
PSME2	NM_002818.2	NM_002818.2:315	Endogenous	mRNA	4808.49	5072.8	5121.34	5020.16	5477.92	5801.48	5794.4	5721.46	5389.58	5751.26	5532.62
PSPH	NM_004577.3	NM_004577.3:225	Endogenous	mRNA	215.4	203.7	240.69	218.61	195.88	235.37	222.74	217.86	228.07	242.8	219.64
PTEN	NM_000314.3	NM_000314.3:1675	Endogenous	mRNA	1774.03	1728.47	1713.63	1718.88	1752.8	1808.37	2032.61	1783.09	1760.05	1936.98	1798.81
PTGER4	NM_000958.2	NM_000958.2:976	Endogenous	mRNA	59.26	66.59	58.63	66.58	46.16	69.91	44.12	71.32	59.9	80.03	60.4
PTGES	NM_004878.4	NM_004878.4:303	Endogenous	mRNA	2734.41	2902.66	2849.19	2806.36	2948.35	2876.85	2842.86	3181.04	2752.96	3172.69	2843.18
PTGS1	NM_000962.2	NM_000962.2:700	Endogenous	mRNA	21.63	38.19	24.69	34.4	47.28	51.27	45.19	42.79	34.56	40.69	40.63
PTGS2	NM_000963.1	NM_000963.1:495	Endogenous	mRNA	10271.67	8924.41	8970.32	9355.66	11474.8	11118.24	10991.61	11410.51	13032.2	11472.68	13954.54
PTK2	NM_005607.4	NM_005607.4:3466	Endogenous	mRNA	1885.02	1962.53	2024.26	2014.06	2289.78	2248.82	2270.41	2161.76	2081.42	2258.45	2327.04
PTK6	NM_001256358.1	NM_001256358.1:291	Endogenous	mRNA	151.44	167.46	122.4	184.21	165.49	122.34	158.18	171.18	158.96	188.54	162.53
PTPN5	NM_001039970.1	NM_001039970.1:2354	Endogenous	mRNA	20	20	20	20	20	20	20	25.94	20	20	25.26
PTPRC	NM_080923.2	NM_080923.2:154	Endogenous	mRNA	20	20	20	20	20	20	20	20	20	20	20
PUDP	NM_001178135.1	NM_001178135.1:425	Endogenous	mRNA	190.95	188.03	188.23	203.07	164.36	163.13	191.53	189.33	187.75	172.27	180.1
PYCR1	NM_006907.2	NM_006907.2:513	Endogenous	mRNA	181.54	215.45	186.17	170.89	202.64	200.41	170.01	225.64	178.54	214.32	206.46
PYCR2	NM_013328.2	NM_013328.2:1250	Endogenous	mRNA	1917	1768.62	1913.17	1945.26	1683	1568.35	1767.91	1666.38	1667.9	1734.87	1827.37
PYCR3	NM_023078.2	NM_023078.2:1145	Endogenous	mRNA	392.24	362.34	373.38	337.34	300.58	346.06	309.9	311.23	367.44	301.13	340.43
RAD51	NM_133487.2	NM_133487.2:566	Endogenous	mRNA	342.39	308.48	299.32	329.57	378.25	336.74	322.81	347.54	365.14	341.82	347.02
RAD51AP1	NM_001130862.1	NM_001130862.1:1125	Endogenous	mRNA	945.33	985.18	968.93	909.93	889.35	906.52	955.51	875.34	830.49	877.61	1013.62
RANBP2	NM_006267.4	NM_006267.4:5384	Endogenous	mRNA	3657.16	3674.35	3772.86	3680.79	3764.52	3664.52	3853.25	3743.85	3925.56	3844.12	3910.61
RB1CC1	NM_001083617.1	NM_001083617.1:1860	Endogenous	mRNA	1036.57	1015.54	987.44	1006.47	1120.12	1285.2	1277.24	1073.75	1126.52	1193.66	1083.9
RBBP5	NM_005057.2	NM_005057.2:325	Endogenous	mRNA	1050.68	1016.52	987.44	917.7	1008.68	920.5	984.56	916.83	1068.93	977.99	1013.62
RBKS	NM_022128.2	NM_022128.2:914	Endogenous	mRNA	102.53	94.01	97.72	110.97	128.34	90.88	103.3	106.34	87.54	126.15	101.03
RBP4	NM_006744.3	NM_006744.3:793	Endogenous	mRNA	122.28	121.43	139.89	129.83	109.2	107.2	121.59	127.09	140.53	124.79	113.11
RELA	NM_021975.3	NM_021975.3:1990	Endogenous	mRNA	1258.56	1213.36	1185.96	1196.23	1492.75	1491.44	1388.07	1470.57	1436.38	1481.22	1461.67
REST	NM_001193508.1	NM_001193508.1:1140	Endogenous	mRNA	1568.97	1487.56	1528.48	1599.04	1648.1	1691.86	1800.19	1706.58	1677.12	1741.65	1631.89
RGN	NM_152869.3	NM_152869.3:1190	Endogenous	mRNA	20	22.52	20	20	24.77	20	20	20	20	33.91	20
RICTOR	NM_152756.3	NM_152756.3:3097	Endogenous	mRNA	1194.6	1184.96	1137.62	1228.41	1257.47	1373.76	1498.9	1331.81	1262.44	1380.84	1325.5
RIMKLA	NM_173642.3	NM_173642.3:2324	Endogenous	mRNA	20	22.52	20	20	20	23.3	22.6	28.53	20	20	20
RIMKLB	NM_020734.2	NM_020734.2:1840	Endogenous	mRNA	1472.08	1281.91	1291.91	1491.4	1251.84	1181.5	1257.87	1260.49	1335.01	1258.77	1373.82
RPIA	NM_144563.2	NM_144563.2:1588	Endogenous	mRNA	2554.75	2567.74	2569.41	2637.69	2431.63	2562.25	2700.83	2537.83	2547.93	2525.67	2712.5
RPL23	NM_000978.3	NM_000978.3:71	Endogenous	mRNA	60874.67	61290.79	59786.68	61258.4	66253.98	68811.45	69159.41	67468.41	65404.04	68265.01	63828.25
RPLP0	NM_001002.3	NM_001002.3:250	Endogenous	mRNA	83656.7	83805.02	83774.38	84637	89393.84	93729.04	93438.88	91403.38	88728.15	92576.29	85524.93
RPS6KA1	NM_002953.3	NM_002953.3:2000	Endogenous	mRNA	1136.28	1188.88	1172.59	1061.96	1295.74	1376.09	1421.43	1343.48	1293.54	1329.3	1282.67
RPS6KB1	NM_003161.2	NM_003161.2:310	Endogenous	mRNA	2741.93	2729.32	2718.56	2675.42	2600.49	2844.23	2863.31	2646.76	2666.57	2521.6	2865.14
RPS6KB2	NM_003952.2	NM_003952.2:980	Endogenous	mRNA	559.67	558.2	554.41	531.53	585.39	426.46	579.98	566.7	569.02	573.77	478.81
RPTOR	NM_020761.2	NM_020761.2:6665	Endogenous	mRNA	406.35	448.52	433.04	429.44	484.07	392.67	411.04	451.29	433.1	485.6	445.86
RRAGC	NM_022157.2	NM_022157.2:1199	Endogenous	mRNA	541.8	643.4	676.81	646.94	691.21	676.98	733.85	679.52	590.91	678.21	649.02
RRM1	NM_001033.3	NM_001033.3:2444	Endogenous	mRNA	3128.53	3048.58	3099.14	3127.06	3304.09	3250.88	3496.01	3217.35	3309.31	3214.74	3320.89
RRM2	NM_001034.1	NM_001034.1:1615	Endogenous	mRNA	8349.96	7912.79	7974.64	8172.74	9063.44	9228.3	9268.89	8688.53	9193.03	9162.68	9040.19

RUNX1	NM_001754.4	NM_001754.4:635	Endogenous	mRNA	2118.3	2261.22	2270.09	2040.69	2046.62	2090.35	2084.26	1976.32	1982.36	1996.66	1917.42
RUNX2	NM_001024630.3	NM_001024630.3:34	Endogenous	mRNA	20	21.54	20	20	20	20	20	20	26.49	20	20
S100A1	NM_006271.1	NM_006271.1:221	Endogenous	mRNA	20	20	20	20	20	20	20	20	20	20	20
S100A12	NM_005621.1	NM_005621.1:260	Endogenous	mRNA	24.46	39.17	37.03	44.39	60.79	37.29	37.66	54.47	50.68	52.9	38.44
SCD	NM_005063.4	NM_005063.4:2025	Endogenous	mRNA	4762.4	4829.93	4889.91	4835.96	4822.73	4957.88	5103.59	4929.12	4818.25	4815.32	4656.27
SDHB	NM_003000.2	NM_003000.2:245	Endogenous	mRNA	3832.12	3899.59	4046.47	4137.97	4246.34	4099.14	3973.76	4228.85	3881.78	4374.48	4059.96
SDHC	NM_001035511.1	NM_001035511.1:615	Endogenous	mRNA	1937.7	1894.96	1933.75	1926.39	2090.52	1991.31	1989.57	2046.34	2003.09	2111.96	1715.35
SDS	NM_006843.2	NM_006843.2:1165	Endogenous	mRNA	20	20	20	20	20	20	20	20	20	20	20
SDSL	NM_138432.2	NM_138432.2:303	Endogenous	mRNA	103.47	91.08	110.06	114.3	93.44	90.88	114.06	111.52	119.79	90.88	105.43
SEC13	NM_001136026.2	NM_001136026.2:400	Endogenous	mRNA	17638.67	17549.15	17384.17	17346.41	17364.75	17466.2	17181.98	17137.16	17516.41	17523.71	16858.12
SELENOK	NM_021237.3	NM_021237.3:42	Endogenous	mRNA	86.54	100.87	100.8	88.77	108.07	95.55	100.07	84.29	95.6	103.09	87.85
SEM1	NM_001201451.1	NM_001201451.1:716	Endogenous	mRNA	20	20	20	20	20	20	24.75	20	20	20	20
SERINC1	NM_020755.2	NM_020755.2:95	Endogenous	mRNA	3970.39	3777.18	3803.72	3692.99	4193.43	4080.49	4283.66	4088.8	4286.09	3936.36	4145.62
SERINC2	NM_018565.3	NM_018565.3:795	Endogenous	mRNA	6506.33	6548.61	6756.79	6351.77	6897.49	7055.22	6851.06	6664.24	6548.35	6820.13	6769.16
SERINC3	NM_006811.2	NM_006811.2:185	Endogenous	mRNA	4218.72	4408.83	4383.84	4450.9	4725.91	4786.6	4792.62	4721.63	4463.48	4757	4710.08
SERINC5	NM_001174071.2	NM_001174071.2:526	Endogenous	mRNA	2090.08	2130.97	2049.98	2151.66	2224.49	2265.13	2251.05	2240.86	2354.41	2229.97	2256.75
SH2D1A	NM_002351.4	NM_002351.4:495	Endogenous	mRNA	20	20	20	20	20	20	20	20	20	20	20
SHMT1	NM_148918.1	NM_148918.1:1800	Endogenous	mRNA	409.17	377.03	387.78	378.4	345.61	372.86	418.57	373.48	421.58	383.87	417.31
SHMT2	NM_001166356.1	NM_001166356.1:1460	Endogenous	mRNA	1536.05	1586.47	1609.74	1665.62	1685.25	1534.55	1508.59	1627.48	1566.54	1654.84	1514.39
SIGLEC5	NM_003830.3	NM_003830.3:1405	Endogenous	mRNA	20	20	20	20	20	24.47	20	20	31.1	20	23.06
SLC16A1	NM_003051.3	NM_003051.3:635	Endogenous	mRNA	4052.23	3961.29	3949.78	3836.14	4236.21	4492.97	4621.53	4154.93	4519.92	4336.5	4291.68
SLC16A11	NM_153357.1	NM_153357.1:1039	Endogenous	mRNA	20	20	20	20	20	20	20	20	20	20	20
SLC16A13	NM_201566.2	NM_201566.2:355	Endogenous	mRNA	35.74	38.19	55.54	37.73	52.91	45.44	47.35	62.25	61.05	58.33	56.01
SLC16A2	NM_006517.3	NM_006517.3:2465	Endogenous	mRNA	490.07	469.09	443.32	439.43	496.46	455.59	435.79	413.68	453.83	434.06	408.52
SLC16A3	NM_004207.2	NM_004207.2:370	Endogenous	mRNA	2339.34	2464.91	2483.01	2489	4367.92	4671.25	4153.46	4186.06	3505.12	4215.78	3423.02
SLC16A6	NM_001174166.1	NM_001174166.1:855	Endogenous	mRNA	27.28	35.25	25.71	37.73	48.41	34.96	27.98	55.76	51.83	61.04	47.22
SLC16A7	NM_001270623.1	NM_001270623.1:5460	Endogenous	mRNA	423.28	396.62	392.92	377.29	379.38	372.86	386.29	320.31	359.38	381.16	421.7
SLC16A8	NM_013356.2	NM_013356.2:1613	Endogenous	mRNA	20	20	20	20	20	20	20	20	20	20	20
SLC1A5	NM_001145144.1	NM_001145144.1:180	Endogenous	mRNA	530.51	543.51	510.18	519.33	521.22	485.88	494.97	535.58	577.08	625.31	518.34
SLC25A1	NM_005984.2	NM_005984.2:964	Endogenous	mRNA	1115.59	1100.74	1164.36	1096.36	1121.25	1120.91	1149.2	1077.64	1121.92	1190.94	1138.81
SLC27A1	NM_198580.1	NM_198580.1:1927	Endogenous	mRNA	22.58	34.28	36	26.63	30.4	20	24.75	31.12	23.04	33.91	20
SLC2A1	NM_006516.2	NM_006516.2:2500	Endogenous	mRNA	1434.46	1521.84	1514.08	1472.54	2448.51	2728.87	2598.6	2253.83	2068.75	2373.75	1846.04
SLC2A14	NM_001286234.1	NM_001286234.1:606	Endogenous	mRNA	36.68	46.03	46.29	42.17	114.83	171.28	168.94	101.15	79.48	158.7	62.6
SLC2A3	NM_006931.2	NM_006931.2:35	Endogenous	mRNA	20	20	20	20	20	20	20	20	20	20	20
SLC2A5	NM_003039.2	NM_003039.2:711	Endogenous	mRNA	22.58	27.42	25.71	28.85	31.52	20	22.6	31.12	24.19	20	20
SLC2A6	NM_001145099.1	NM_001145099.1:174	Endogenous	mRNA	177.78	182.15	195.43	163.12	468.31	488.21	442.25	429.24	444.62	459.83	398.64
SLC2A8	NM_014580.3	NM_014580.3:1777	Endogenous	mRNA	375.31	402.49	401.15	378.4	335.47	321.59	335.72	307.34	376.66	337.75	350.32
SLC3A1	NM_000341.3	NM_000341.3:1010	Endogenous	mRNA	20	24.48	20	20	20	20	20	20	20	20	20
SLC3A2	NM_001012662.2	NM_001012662.2:1505	Endogenous	mRNA	5947.6	5706.41	5870.15	5913.45	5519.57	5138.49	5398.42	5301.3	5761.63	5576.28	5723.7
SLC6A12	NM_003044.3	NM_003044.3:969	Endogenous	mRNA	20	20	20	20	20	20	20	20	20	20	20
SLC6A18	NM_182632.2	NM_182632.2:1502	Endogenous	mRNA	20.69	20.57	21.6	25.52	25.89	20	25.82	33.72	20	32.55	24.16
SLC6A19	NM_001003841.2	NM_001003841.2:1515	Endogenous	mRNA	39.51	44.07	39.09	34.4	55.16	48.94	36.58	45.39	34.56	31.2	40.63
SLC7A11	NM_014331.3	NM_014331.3:636	Endogenous	mRNA	750.62	694.33	646.98	720.18	389.51	401.99	441.17	403.3	468.81	439.48	512.85
SLC7A5	NM_003486.5	NM_003486.5:785	Endogenous	mRNA	15647.36	16063.54	16063.46	15725.18	13979.61	13399.68	13958.21	14183.06	14408.68	14615.52	15723.7
SLC7A9	NM_014270.4	NM_014270.4:530	Endogenous	mRNA	20	20	20	20	25.89	23.3	20	20	20	20	20
SMAD2	NM_005901.5	NM_005901.5:1678	Endogenous	mRNA	3227.3	3202.33	3120.74	3111.52	3409.91	3360.41	3626.21	3247.18	3457.9	3327.32	3374.7
SMAD3	NM_005902.3	NM_005902.3:4220	Endogenous	mRNA	3129.47	3112.23	3023.02	2999.45	5627.64	5619.71	5659.9	5466	5455.23	5607.48	5523.83
SMAD4	NM_005359.3	NM_005359.3:1370	Endogenous	mRNA	1155.09	1307.37	1222.99	1171.81	1308.13	1233.94	1485.99	1453.71	1245.17	1467.66	1318.91
SNF8	NM_001317192.1	NM_001317192.1:234	Endogenous	mRNA	5970.17	6023.71	5902.04	5782.51	5850.54	5667.48	6058.03	6076.79	5838.8	6406.41	5792.88
SOD1	NM_000454.4	NM_000454.4:245	Endogenous	mRNA	4425.66	4447.02	4340.64	4462	4620.09	4462.68	4695.78	4687.92	4656.99	5002.51	4326.82
SOD2	NM_000636.2	NM_000636.2:201	Endogenous	mRNA	1885.96	2004.64	2080.83	2079.53	7760.94	7950.09	7787.2	8735.22	6491.91	7671.96	5934.55
SOD3	NM_003102.2	NM_003102.2:139	Endogenous	mRNA	25.4	20	20	20	20	20	25.82	27.23	20	20	27.45
SOS1	NM_005633.2	NM_005633.2:1635	Endogenous	mRNA	745.92	831.43	743.67	762.35	851.07	924	1029.76	929.8	898.45	915.59	901.6
SOS2	NM_006939.2	NM_006939.2:3845	Endogenous	mRNA	290.65	368.22	348.69	317.37	378.25	406.65	393.83	370.88	363.99	355.38	408.52
SOX2	NM_003106.2	NM_003106.2:151	Endogenous	mRNA	98.77	169.42	172.8	159.79	59.66	64.09	61.33	68.73	79.48	65.11	82.36
SPIB	NM_003121.3	NM_003121.3:1029	Endogenous	mRNA	20	20	20	20	20	20	20	20	20	20	20
SQSTM1	NM_003900.3	NM_003900.3:1445	Endogenous	mRNA	2159.68	2078.09	2192.95	2188.28	3713.86	3623.74	3546.58	3420.95	3368.05	3423.63	3172.63
SREBF1	NM_001005291.1	NM_001005291.1:1392	Endogenous	mRNA	1585.9	1585.49	1647.8	1521.36	1640.22	1548.54	1527.96	1617.1	1556.17	1614.15	1540.74
SREBF2	NM_004599.2	NM_004599.2:665	Endogenous	mRNA	3183.09	3118.11	3191.71	3311.26	3355.87	3326.62	3316.31	3358.7	3446.38	3362.59	3391.17
SRM	NM_003132.2	NM_003132.2:254	Endogenous	mRNA	3786.03	4105.25	4175.04	3942.67	3896.23	3677.34	3682.16	3623.25	3687.12	3876.67	3555.9
SRR	NM_021947.1	NM_021947.1:560	Endogenous	mRNA	143.92	155.71	145.03	159.79	163.23	139.82	140.96	145.24	137.07	138.36	146.06
STAM2	NM_005843.4	NM_005843.4:1455	Endogenous	mRNA	973.55	912.71	902.07	933.24	891.6	856.41	840.38	909.05	930.71	869.47	969.69
STAT1	NM_007315.3	NM_007315.3:239	Endogenous	mRNA	1677.14	1573.74	1528.48	1614.57	1581.68	1595.14	1647.4	1458.9	1733.56	1565.32	1712.06
STAT3	NM_003150.3	NM_003150.3:2060	Endogenous	mRNA	3596.96	3522.56	3619.6	3553.17	3955.9	4102.63	4112.57	4136.78	4098.33	3997.4	4106.08
STAT5A	NM_003152.2	NM_003152.2:3460	Endogenous	mRNA	135.45	149.83	162.52	155.35	330.97	301.78	300.21	309.93	337.5	322.83	315.18
STAT6	NM_003153.3	NM_003153.3:2030	Endogenous	mRNA	1754.27	1766.67	1714.66	1825.41	2232.37	2198.71	2062.74	2151.38	2087.18	2201.48	2082.14
STK11	NM_000455.4	NM_000455.4:2060	Endogenous	mRNA	584.13	692.37	689.15	686.89	724.99	741.06	655.3	721.02	724.52	686.35	697.34
STK3	NM_006281.3	NM_006281.3:1295	Endogenous	mRNA	1610.36	1558.07	1583	1661.18	1703.27	1632.43	1730.25	1570.42	1610.31	1654.84	1616.52
TALDO1	NM_006755.1	NM_006755.1:262	Endogenous	mRNA	6445.19	6754.27	6537.71	6755.69	6855.84	6924.72	7089.94	6762.79	6927.32	7115.83	6400.18
TBK1	NM_013254.2	NM_013254.2:1610	Endogenous	mRNA	1086.43	983.22	975.1	1053.08	1124.63	1219.95	1167.49	1194.35	1273.96	1231.64	1273.89
TBX21	NM_013351.1	NM_013351.1:890	Endogenous	mRNA	20	20	20	20	20	20	20	20	20	20	20
TBXAS1	NM_001130966.2	NM_001130966.2:1030	Endogenous	mRNA	20	20	20	20	20	20	20	20	20	20	20
TCL1A	NR_049726.1	NR_049726.1:543	Endogenous	mRNA	20	20	20	25.52	20	20	20	20	20	20	20
TDO2	NM_005651.2	NM_005651.2:495	Endogenous	mRNA	20	20	20.57	20	20	20	22.6	20	20	20	20
TECR	NR_038104.1	NR_038104.1:574	Endogenous	mRNA	4126.54	4127.77	4096.87	4079.16	4159.66	4251.78	4039.4	4140.67	4237.71	4082.85	4254.34
TELO2	NM_016111.3	NM_016111.3:294	Endogenous	mRNA	182.48	176.27	203.66	164.23	173.37	163.13	150.64	185.44	171.63	174.98	180.1
TET2	NM_001127208.2	NM_001127208.2:2882	Endogenous	mRNA	1270.79	1297.58	1283.68	1302.76	1361.04	1363.27	1493.52	1304.58	1407.58	1283.18	1406.76
TF	NM_001063.2	NM_001063.2:640	Endogenous	mRNA	20	20	20	20	20	20	20	20	20	20	20
TFAM	NM_003201.1	NM_003201.1:85	Endogenous	mRNA	1023.4	965.59	979.22	967.64	924.24	930.99	925.38	915.54	933.01	911.52	906
TFRC	NM_003234.1	NM_003234.1:1220	Endogenous	mRNA	6717.03	6931.52	6865.83	6812.28	7365.81	7499.16	7914.17	7684.81	7720.95	7883.57	8060.62
TH	NM_000360.3	NM_000360.3:1306	Endogenous	mRNA	240.8	230.14	197.49	246.35	207.14	198.08	173.24	186.74	236.13	184.47	227.32
THBS1	NM_003246.2	NM_003246.2:3465	Endogenous	mRNA	39154.61	43625.11	43236.7	43378.23	26589.17	24757.96	24398.89	26554.49	25825.96	27470.4	28582.26
THBS2	NM_003247.2	NM_003247.2:4460	Endogenous	mRNA	202.24	167.46	194.4	179.77	227.4	234.2	259.32	233.42	222.31	279.42	264.66
TIGAR	NM_020375.2	NM_020375.2:5245	Endogenous	mRNA	106.29	133.19	136.8	117.63	133.96	127.01	154.95	119.31	127.86	127.5	96.64
TIGIT	NM_173799.2	NM_173799.2:1968	Endogenous	mRNA	20	23.5	21.6	20	20	20	20	20	20	20	20
TIMELESS	NM_003920.2	NM_003920.2:1185	Endogenous	mRNA	1410.94	1463.08	1453.39	1412.61	1350.9	1369.1	1311.68	1237.14	1388	1364.57	1373.82
TK1	NM_003258.1	NM_003258.1:1215	Endogenous	mRNA	900.18	964.62	984.36	976.51	1030.06	1000.9	922.15	1071.15	983.69	1097.35	902.7
TK2	NM_004614.3	NM_004614.3:2165	Endogenous	mRNA	52.68	44.07	39.09	58.81	38.28	24.47	47.35	41.5	35.71	52.9	37.34
TKT	NM_001064.2	NM_001064.2:1235	Endogenous	mRNA	2453.16	2541.3	2613.64	2625.49	2747.96	2695.08	2425.36	2719.38	2394.73	2681.66	2407.2
TLR10	NM_030956.2	NM_030956.2:2246	Endogenous	mRNA	20	26.44	20	25.52	20	20	20	33.72	31.1	20	20
TLR2	NM_003264.3	NM_003264.3:2402	Endogenous	mRNA	182.48	209.57	176.92	193.08	749.75	786.5	720.94	775.48	625.46	716.19	555.68
TLR4	NM_138554.2	NM_138554.2:2570	Endogenous	mRNA	260.55	241.89	261.26	266.32	211.64	226.05	217.36	219.16	231.52	217.03	264.66
TLR7	NM_016562.3	NM_016562.3:4120	Endogenous	mRNA	20	20	20	20	20	20	20	20	20	20	20
TNF	NM_000594.2	NM_000594.2:1010	Endogenous	mRNA	20	20	20	22.19	77.68	81.56	76.4	57.06	94.45	67.82	85.66
TNFRSF17	NM_001192.2	NM_001192.2:635	Endogenous	mRNA	20	20	20	23.3	20	20	20	20	20	20	20
TNFRSF4	NM_003327.3	NM_003327.3:981	Endogenous	mRNA	20	20	20	24.41	20	20	20	20	20	20	20
TP53	NM_000546.2	NM_000546.2:1330	Endogenous	mRNA	3087.14	3106.36	3119.71	3135.94	3674.46	3753.08	3540.13	3676.42	3548.9	3602.68	3405.45
TP63	NM_003722.4	NM_003722.4:1295	Endogenous	mRNA	2011.06	2260.24	2288.61	2076.2	1755.05	1846.83	1933.62	1785.69	1757.75	1719.95	1855.92
TPH1	NM_004179.1	NM_004179.1:335	Endogenous	mRNA	56.44	45.05	40.11	54.37	50.66	48.94	41.97	31.12	62.2	51.54	58.2
TPR	NM_003292.2	NM_003292.2:6825	Endogenous	mRNA	2705.25	2700.92	2659.93	2579.99	2758.1	2876.85	2922.49	2684.37	2815.16	2794.24	2870.64

TPSAB1/B2	NM_003294.3	NM_003294.3:579	Endogenous	mRNA	20	20	20	22.19	20	20	29.05	20	20	20	20
TPX2	NM_012112.4	NM_012112.4:2975	Endogenous	mRNA	2486.08	2698.96	2716.5	2602.18	2682.67	2631	2784.76	2623.42	2492.64	2689.8	2585.11
TRAF1	NM_005658.3	NM_005658.3:3735	Endogenous	mRNA	100.65	84.22	91.54	97.65	431.16	446.27	420.73	391.63	443.47	402.86	424.99
TRAF6	NM_145803.2	NM_145803.2:745	Endogenous	mRNA	950.04	956.78	938.07	960.98	954.64	993.91	991.02	972.6	996.36	961.71	978.48
TRAT1	NM_016388.2	NM_016388.2:770	Endogenous	mRNA	101.59	100.87	105.94	106.53	136.22	142.15	164.63	141.35	119.79	139.71	121.9
TTPA	NM_000370.3	NM_000370.3:1656	Endogenous	mRNA	24.46	20	20	20	20	20	23.67	20	20	20	20
TTR	NM_000371.3	NM_000371.3:199	Endogenous	mRNA	22.58	20	21.6	32.18	20	27.96	30.13	20	32.25	20	24.16
TXN	NM_003329.2	NM_003329.2:55	Endogenous	mRNA	28743.73	28479.17	28797.38	30315.16	30583.34	30070.05	30724.85	30942.85	29263.13	31397.26	30722.6
TXN2	NM_012473.3	NM_012473.3:192	Endogenous	mRNA	1946.16	2016.39	1989.29	1974.11	1985.83	1875.96	1952.99	2002.25	1878.69	1987.17	1940.48
TXNRD1	NM_001093771.1	NM_001093771.1:1009	Endogenous	mRNA	3867.87	3844.75	3696.75	3983.73	4884.64	4656.1	4733.44	4927.83	4784.85	4917.06	5002.2
TYMP	NM_001953.3	NM_001953.3:719	Endogenous	mRNA	22.58	22.52	20	23.3	28.14	20	27.98	32.42	20	31.2	20
TYMS	NM_001071.2	NM_001071.2:1110	Endogenous	mRNA	3629.89	3339.43	3279.14	3325.69	3373.88	3157.66	3589.62	3537.66	3434.86	3593.18	3335.16
UBE2C	NM_007019.2	NM_007019.2:561	Endogenous	mRNA	5418.02	5083.57	5379.52	5543.93	5667.04	5705.93	5536.15	5375.22	5615.34	5649.53	6134.42
UBE2T	NM_014176.3	NM_014176.3:595	Endogenous	mRNA	1648.92	1647.19	1689.97	1764.38	1639.1	1604.47	1535.49	1613.21	1569.99	1707.74	1712.06
UCK1	NM_031432.3	NM_031432.3:232	Endogenous	mRNA	998.95	998.89	984.36	925.47	896.1	883.21	1025.45	1028.36	972.17	1013.25	953.22
UCK2	NM_012474.3	NM_012474.3:730	Endogenous	mRNA	2460.68	2631.39	2640.39	2466.8	2441.76	2537.78	2611.52	2414.63	2423.52	2601.63	2510.43
UCKL1	NM_001193379.1	NM_001193379.1:825	Endogenous	mRNA	2583.91	2593.2	2580.73	2571.11	2580.23	2513.31	2636.26	2527.46	2597.46	2662.67	2633.43
UMPS	NM_000373.2	NM_000373.2:2445	Endogenous	mRNA	725.22	666.91	651.1	665.8	710.35	623.38	661.76	583.56	624.31	706.7	673.18
UPP1	NM_003364.2	NM_003364.2:925	Endogenous	mRNA	2340.28	2369.92	2362.67	2426.86	2575.72	2484.18	2424.29	2729.76	2398.18	2668.1	2331.43
UPP2	NM_001135098.1	NM_001135098.1:594	Endogenous	mRNA	20	20	20	20	20	20	20	20	20	20	20
UQCR10	NM_001003684.1	NM_001003684.1:40	Endogenous	mRNA	1793.78	1686.36	1709.51	1713.34	1756.18	1730.31	1737.78	1783.09	1780.78	1696.89	1797.72
UQCR11	NM_006830.2	NM_006830.2:360	Endogenous	mRNA	140.15	162.56	174.86	168.67	140.72	168.95	156.02	143.94	149.74	157.35	169.12
UQCRQ	NM_014402.4	NM_014402.4:172	Endogenous	mRNA	11001.59	10855.6	10980.18	11664.88	11545.73	11537.71	11924.52	11952.57	11047.54	12107.49	11819.68
USP8	NM_001128610.1	NM_001128610.1:1160	Endogenous	mRNA	1437.28	1511.07	1494.54	1461.44	1518.64	1562.52	1578.53	1525.03	1488.21	1633.14	1564.9
VEGFA	NM_001025366.1	NM_001025366.1:1325	Endogenous	mRNA	1291.48	1228.05	1203.45	1165.16	3143.1	3239.23	2969.83	2871.11	3039.77	3099.44	2676.26
VHL	NM_000551.2	NM_000551.2:1280	Endogenous	mRNA	11101.3	10853.64	10833.09	11029.04	14649.43	14425.05	14694.21	14168.79	14867.12	15069.93	14128.05
VPS28	NM_016208.3	NM_016208.3:416	Endogenous	mRNA	1519.12	1490.5	1527.45	1577.96	1447.72	1369.1	1419.28	1353.86	1511.25	1387.63	1348.56
WASHC4	NM_015275.1	NM_015275.1:1485	Endogenous	mRNA	1330.05	1398.45	1435.91	1347.14	1574.93	1568.35	1620.5	1502.99	1461.72	1523.27	1502.31
WDR45	NM_007075.3	NM_007075.3:1390	Endogenous	mRNA	442.1	399.56	504.01	466.06	514.47	485.88	484.21	490.19	495.3	411	490.89
WNT1	NM_005430.2	NM_005430.2:350	Endogenous	mRNA	20	20	20	20	20	20	20	20	20	20	20
WNT2	NM_003391.2	NM_003391.2:2014	Endogenous	mRNA	20	20	20	20	20	20	20	20	20	20	20
WRN	NM_000553.4	NM_000553.4:2944	Endogenous	mRNA	713	662.01	703.55	743.48	618.04	665.32	701.57	644.51	670.39	633.45	722.6
XCL1/2	NM_003175.3	NM_003175.3:377	Endogenous	mRNA	73.37	81.28	76.12	77.68	78.8	89.72	74.25	71.32	78.33	89.52	82.36
XDH	NM_000379.3	NM_000379.3:1325	Endogenous	mRNA	1267.97	1196.71	1204.48	1158.5	1024.44	1044.01	1003.93	1137.29	1067.78	1119.05	1195.91
XRCC2	NM_005431.1	NM_005431.1:600	Endogenous	mRNA	1066.67	1043.94	1018.3	1003.14	1033.44	1104.6	1027.6	982.97	992.91	1020.03	1018.01
YWHAZ	NM_003406.2	NM_003406.2:2345	Endogenous	mRNA	19996.83	20048.33	20303.3	21042.73	22490.3	22062.87	22288.8	22798.97	22537.39	23238.34	25032.95
ZAP70	NM_001079.3	NM_001079.3:1175	Endogenous	mRNA	20	20	20	20	20	20	20	20	20	20	20
ZNF100	NM_173531.3	NM_173531.3:36	Endogenous	mRNA	155.2	136.12	148.12	146.48	169.99	137.49	145.26	127.09	153.2	123.44	136.17
ZNF136	NM_003437.2	NM_003437.2:385	Endogenous	mRNA	561.56	535.68	525.61	543.74	525.73	503.36	538.01	527.8	580.54	543.93	602.9
ZNF253	NM_021047.2	NM_021047.2:1327	Endogenous	mRNA	1014.94	966.57	1006.99	1002.03	917.49	838.94	858.67	864.96	890.39	919.66	923.57
ZNF254	NM_203282.3	NM_203282.3:1986	Endogenous	mRNA	1315.94	1286.81	1290.88	1304.98	1194.42	1145.38	1178.25	1289.02	1239.41	1247.91	1227.76
ZNF43	NM_003423.2	NM_003423.2:3835	Endogenous	mRNA	1992.25	2849.78	2680.5	2760.87	3026.03	2169.58	2370.49	4164.01	2106.76	4227.99	1600.04
ZNF610	NM_001161427.1	NM_001161427.1:454	Endogenous	mRNA	20	21.54	26.74	35.51	24.77	20	20	20	20	28.49	20
ZNF675	NM_138330.2	NM_138330.2:851	Endogenous	mRNA	701.71	717.83	690.18	734.6	647.31	601.24	609.03	609.49	601.27	638.88	661.1
ZNF682	NM_001077349.1	NM_001077349.1:1465	Endogenous	mRNA	418.58	419.14	415.55	392.82	353.49	351.89	354.01	338.46	362.84	325.54	386.56
ZNF708	NM_021269.2	NM_021269.2:488	Endogenous	mRNA	574.72	541.56	547.21	560.38	529.1	541.81	554.15	526.5	507.97	584.62	520.54
ZNF85	NM_001256171.1	NM_001256171.1:275	Endogenous	mRNA	367.79	376.05	368.23	369.52	334.35	307.61	341.1	334.57	345.56	317.4	337.14
ZNF91	NM_003430.2	NM_003430.2:4472	Endogenous	mRNA	1259.5	1254.49	1197.28	1247.27	1224.82	1215.29	1367.63	1185.27	1201.4	1273.69	1226.66
ZNF93	NM_031218.3	NM_031218.3:2314	Endogenous	mRNA	228.57	202.72	212.92	249.68	240.91	216.73	191.53	167.29	231.52	203.46	254.78
ABCF1	NM_001090.2	NM_001090.2:857	Housekeeping	mRNA	1806.01	1813.67	1927.57	1807.66	1812.46	2021.6	1878.74	1807.73	1804.97	2003.45	1822.97
AGK	NM_018238.3	NM_018238.3:816	Housekeeping	mRNA	1774.97	1765.69	1799	1712.23	1707.77	1704.67	1692.59	1676.76	1840.68	1707.74	1854.82
COG7	NM_153603.3	NM_153603.3:1492	Housekeeping	mRNA	538.98	526.87	557.49	501.57	551.62	629.2	574.6	574.48	531.01	590.05	566.66
DHX16	NM_001164239.1	NM_001164239.1:2490	Housekeeping	mRNA	422.34	428.94	479.32	443.87	454.8	454.42	421.8	409.79	501.06	434.06	437.07
DNAJC14	NM_032364.5	NM_032364.5:1166	Housekeeping	mRNA	312.29	324.15	284.92	331.79	296.07	292.46	312.05	306.04	300.64	268.57	296.51
EDC3	NM_001142443.1	NM_001142443.1:1024	Housekeeping	mRNA	1826.7	1861.66	1825.74	1702.24	1741.54	1640.59	1738.86	1628.78	1745.08	1702.32	1798.81
FCF1	NM_015962.4	NM_015962.4:1022	Housekeeping	mRNA	3581.91	3424.63	3344.97	3211.39	3504.47	3358.08	3555.19	3201.79	3393.39	3461.61	3320.89
G6PD	NM_000402.4	NM_000402.4:923	Housekeeping	mRNA	1113.7	1237.84	1170.53	1186.24	1167.41	1169.85	1083.56	1295.5	1143.8	1250.63	1111.36
MRPS5	NM_031902.3	NM_031902.3:390	Housekeeping	mRNA	2623.41	2583.41	2566.33	2647.68	2513.81	2509.82	2594.3	2397.78	2592.85	2440.22	2691.63
NRDE2	NM_017970.3	NM_017970.3:3233	Housekeeping	mRNA	493.83	454.4	450.52	525.99	431.16	389.17	416.42	474.63	465.35	431.34	478.81
OAZ1	NM_004152.2	NM_004152.2:313	Housekeeping	mRNA	17411.98	17476.68	17209.31	17481.79	18791.08	19090.47	18909	18657.01	18434.45	19049.69	17967.28
POLR2A	NM_000937.2	NM_000937.2:3775	Housekeeping	mRNA	1848.34	1858.72	1837.06	1838.73	1928.42	1916.74	1743.16	1933.52	1931.68	1936.98	2065.67
SAP130	NM_024545.3	NM_024545.3:3090	Housekeeping	mRNA	1459.86	1496.38	1467.8	1438.14	1367.79	1447.17	1495.68	1444.63	1444.44	1374.06	1399.08
SDHA	NM_004168.3	NM_004168.3:342	Housekeeping	mRNA	1619.76	1746.1	1793.86	1836.51	1805.71	1893.43	1798.04	1793.47	1694.39	1886.79	1760.38
STK11IP	NM_052902.2	NM_052902.2:565	Housekeeping	mRNA	135.45	126.33	136.8	125.39	136.22	82.73	126.97	141.35	110.58	116.65	97.74
TBC1D10B	NM_015527.3	NM_015527.3:2915	Housekeeping	mRNA	295.36	297.71	293.15	310.71	310.71	389.17	308.82	315.12	297.18	311.98	341.53
TBP	NM_001172085.1	NM_001172085.1:587	Housekeeping	mRNA	1552.04	1534.57	1425.62	1431.48	1470.23	1454.16	1522.58	1427.77	1584.97	1398.48	1506.7
TLK2	XM_011524223.1	XM_011524223.1:383	Housekeeping	mRNA	1884.08	1844.03	1888.49	1967.45	2017.35	2176.57	2115.47	2002.25	1924.77	2170.29	2062.38
UBB	NM_018955.3	NM_018955.3:1052	Housekeeping	mRNA	21665.5	21703.36	21546.86	22183.48	21179.93	21399.88	20962.06	21018.47	21990.25	22017.56	21542.94
USP39	NM_001256725.1	NM_001256725.1:806	Housekeeping	mRNA	2286.67	2226.94	2245.41	2223.79	2245.88	2392.13	2323.14	2259.02	2273.78	2234.04	2186.47
NEG_A	ERCC_00096.1	ERCC_00096.1:230	Negative	SYSTEM	8	15	10	12	9	15	8	14	5	11	8
NEG_B	ERCC_00041.1	ERCC_00041.1:440	Negative	SYSTEM	12	12	14	13	20	16	18	17	10	22	12
NEG_C	ERCC_00019.1	ERCC_00019.1:140	Negative	SYSTEM	18	12	14	11	23	15	13	16	13	20	17
NEG_D	ERCC_00076.1	ERCC_00076.1:355	Negative	SYSTEM	12	23	15	13	14	20	13	10	17	13	11
NEG_E	ERCC_00098.1	ERCC_00098.1:785	Negative	SYSTEM	11	22	20	16	20	14	22	14	14	20	10
NEG_F	ERCC_00126.1	ERCC_00126.1:220	Negative	SYSTEM	16	26	18	20	23	13	23	26	17	17	12
NEG_G	ERCC_00144.1	ERCC_00144.1:15	Negative	SYSTEM	6	8	5	11	12	7	8	5	6	10	6
NEG_H	ERCC_00154.1	ERCC_00154.1:115	Negative	SYSTEM	17	8	8	19	3	9	15	17	10	9	5
POS_A	ERCC_00117.1	ERCC_00117.1:385	Positive	SYSTEM	24552	39441	34608	34760	37763	22178	24104	45351	19508	45363	18199
POS_B	ERCC_00112.1	ERCC_00112.1:695	Positive	SYSTEM	7418	11957	10698	10917	11406	6738	7497	13869	5880	14248	5488
POS_C	ERCC_00002.1	ERCC_00002.1:850	Positive	SYSTEM	2170	3494	3089	3083	3326	2026	2417	4112	1684	3880	1684
POS_D	ERCC_00092.1	ERCC_00092.1:540	Positive	SYSTEM	518	856	737	705	794	460	511	914	429	955	405
POS_E	ERCC_00035.1	ERCC_00035.1:485	Positive	SYSTEM	111	178	148	166	145	110	92	183	85	181	86
POS_F	ERCC_00034.1	ERCC_00034.1:195	Positive	SYSTEM	37	55	54	67	58	32	50	83	31	84	34

Appendix A: Normalized transcript counts of intracellularly infected urothelial cells. Normalized read counts of all transcripts in the NanoString nCounter Human Metabolic Pathways Panel. Urothelial cells were intracellularly infected with wild-type UPEC, Δ*cydAB*, or mock infected. See also Chapter 3, Materials and Methods.

Gene Name	probe.ID	Log2 fold change	Linear fold change	std error (log2)	P-value
TNF	NM_000594.2:1010	4.21	18.5	0.488	0.000134
BIRC3	NM_182962.1:3	4.15	17.8	0.297	8.33E-06
CCL5	NM_002985.2:277	2.77	6.83	0.289	7.33E-05
TRAF1	NM_005658.3:3735	2.36	5.12	0.0889	1.91E-07
SLC2A14	NM_001286234.1:606	2.1	4.28	0.258	0.000186
TLR2	NM_003264.3:2402	2.07	4.21	0.0597	3.82E-08
SOD2	NM_000636.2:201	2.01	4.02	0.052	2.01E-08
BCL2A1	NM_004049.2:80	1.85	3.61	0.104	1.98E-06
CA9	NM_001216.2:960	1.78	3.45	0.204	0.000124
PDK1	NM_002610.3:1170	1.66	3.16	0.105	4.00E-06
IL4I1	NM_152899.1:1452	1.6	3.04	0.257	0.000783
SLC2A6	NM_001145099.1:174	1.41	2.66	0.0776	1.78E-06
NFKB2	NM_002502.2:825	1.39	2.62	0.0382	2.88E-08
VEGFA	NM_001025366.1:1325	1.33	2.51	0.0513	2.17E-07
ADORA2A	NM_000675.3:1095	1.31	2.48	0.287	0.00386
FLT1	NM_002019.4:530	1.28	2.43	0.0721	2.02E-06
NOS2	NM_000625.4:605	1.25	2.38	0.313	0.00716
NFKB1	NM_003998.2:1675	1.19	2.28	0.0207	1.90E-09
IL6	NM_000600.3:364	1.19	2.28	0.0883	1.04E-05
STAT5A	NM_003152.2:3460	1.1	2.15	0.0649	2.64E-06
HK2	NM_000189.4:6880	1.1	2.14	0.0828	1.14E-05
KMO	NM_003679.3:595	1.08	2.11	0.2	0.00168
PDGFB	NM_033016.2:1480	1.05	2.08	0.217	0.00284
PTGS1	NM_000962.2:700	0.98	1.97	0.31	0.0194
KYNU	NM_003937.2:738	0.968	1.96	0.0238	1.46E-08
LDHA	NM_001165414.1:1690	0.961	1.95	0.0577	3.00E-06
MAP2K3	NM_145109.1:370	0.884	1.85	0.0724	1.83E-05
SMAD3	NM_005902.3:4220	0.87	1.83	0.0193	7.92E-09
PGK1	NM_000291.2:1030	0.866	1.82	0.0443	1.17E-06
SLC16A3	NM_004207.2:370	0.831	1.78	0.0443	1.47E-06
IRF1	NM_002198.2:15	0.832	1.78	0.0755	3.32E-05
IFNG	NM_000619.2:970	0.794	1.73	0.549	0.199
SLC2A1	NM_006516.2:2500	0.755	1.69	0.0634	2.11E-05
AMPD3	NM_000480.2:3033	0.736	1.67	0.0636	2.50E-05
SQSTM1	NM_003900.3:1445	0.733	1.66	0.0313	4.00E-07
ALDOA	NM_184041.2:1455	0.692	1.62	0.0465	5.79E-06
CD244	NM_001166663.1:22	0.664	1.58	0.195	0.0143
CTSS	NM_004079.3:685	0.646	1.56	0.0381	2.71E-06
GPI	NM_000175.2:1695	0.626	1.54	0.0392	3.87E-06
KLRD1	NM_007334.2:1252	0.625	1.54	0.21	0.0247
MAP2K1	NM_002755.2:970	0.595	1.51	0.0446	1.10E-05
PIK3CD	NM_005026.3:2978	0.595	1.51	0.106	0.00134
CA12	NM_001218.3:2445	0.544	1.46	0.0933	0.00112
IDO1	NM_002164.5:52	0.531	1.44	0.208	0.0431
SLC16A6	NM_001174166.1:855	0.531	1.44	0.346	0.176
TRAT1	NM_016388.2:770	0.518	1.43	0.0765	0.000505
GSK3B	NM_002093.2:925	0.488	1.4	0.0327	5.69E-06
HK1	NM_000188.2:3355	0.456	1.37	0.0372	1.80E-05
AMDHD1	NM_152435.2:1936	0.453	1.37	0.205	0.0696
S100A12	NM_005621.1:260	0.45	1.37	0.294	0.177
ERN1	NM_001433.2:435	0.446	1.36	0.0447	5.88E-05
NFAT5	NM_173214.1:3290	0.434	1.35	0.0841	0.0021
COL6A1	NM_001848.2:3665	0.415	1.33	0.0305	9.88E-06
KMT2E	NM_018682.3:1541	0.414	1.33	0.053	0.000233
VHL	NM_000551.2:1280	0.403	1.32	0.0149	1.71E-07
PGM2	NM_018290.3:295	0.4	1.32	0.0558	0.000372
ASS1	NM_000050.4:1275	0.385	1.31	0.0363	4.16E-05
HMOX1	NM_002133.2:781	0.384	1.31	0.0929	0.00612
KRAS	NM_033360.2:267	0.377	1.3	0.0378	5.85E-05
THBS2	NM_003247.2:4460	0.368	1.29	0.087	0.00551
APOM	NM_019101.2:496	0.363	1.29	0.168	0.074
ACOX1	NM_004035.5:2950	0.354	1.28	0.0244	6.75E-06
PFKL	NM_001002021.1:2410	0.355	1.28	0.0387	9.47E-05
CD274	NM_014143.3:1243	0.354	1.28	0.133	0.037
ACACB	NM_001093.3:3365	0.347	1.27	0.222	0.168
ITGA1	NM_181501.1:1875	0.339	1.26	0.0246	9.03E-06
GLUL	NM_001033044.2:2645	0.329	1.26	0.0353	8.76E-05
GAPDH	NM_001256799.1:386	0.318	1.25	0.0207	4.84E-06
TXNRD1	NM_001093771.1:1009	0.319	1.25	0.0292	3.45E-05
CD68	NM_001251.2:1140	0.32	1.25	0.0814	0.00774
SLC16A13	NM_201566.2:355	0.328	1.25	0.228	0.201
HLA-E	NM_005516.5:1287	0.309	1.24	0.0424	0.000339
STAT6	NM_003153.3:2030	0.292	1.22	0.0309	8.02E-05
BAD	NM_004322.3:652	0.287	1.22	0.034	0.000151
ENO1	NM_001428.2:1689	0.29	1.22	0.0372	0.000238
GLRX	NM_002064.2:360	0.288	1.22	0.0475	0.000912
NRAS	NM_002524.3:877	0.29	1.22	0.0496	0.00111
PDP1	NM_001161778.1:950	0.271	1.21	0.0265	5.07E-05
EGFR	NM_201282.1:1354	0.271	1.21	0.0304	0.00011
GNG12	NM_018841.3:245	0.274	1.21	0.031	0.000117
SOS1	NM_005633.2:1635	0.274	1.21	0.0688	0.00726
LEPR	NM_001003679.1:2000	0.277	1.21	0.0996	0.0321
HK3	NM_002115.1:495	0.272	1.21	0.309	0.412
RELA	NM_021975.3:1990	0.267	1.2	0.0318	0.000157
PTGS2	NM_000963.1:495	0.264	1.2	0.0494	0.00175
CBL	NM_005188.2:7485	0.254	1.19	0.0288	0.000118
RPS6KA1	NM_002953.3:2000	0.254	1.19	0.0472	0.0017
TP53	NM_000546.2:1330	0.234	1.18	0.0181	1.35E-05
HLA-A	NM_002116.5:1000	0.233	1.18	0.0258	0.000102
CD276	NM_001024736.1:2119	0.243	1.18	0.0314	0.000242
MAP1LC3B	NM_022818.4:1685	0.243	1.18	0.0335	0.00035
FAH	NM_000137.1:920	0.233	1.18	0.0367	0.000711
KANSL1	NM_001193465.1:1838	0.236	1.18	0.0412	0.00124
PRKAA2	NM_006252.2:975	0.24	1.18	0.205	0.287
HPRT1	NM_000194.1:240	0.229	1.17	0.0177	1.31E-05
PIK3CA	NM_006218.2:2445	0.225	1.17	0.0449	0.00244
RB1CC1	NM_001083617.1:1860	0.228	1.17	0.0697	0.017
SOS2	NM_006939.2:3845	0.228	1.17	0.0835	0.0343
PDK3	NM_005391.1:585	0.223	1.17	0.091	0.0497

ITGB2	NM_000211.2:520	0.213	1.16	0.151	0.208
TBK1	NM_013254.2:1610	0.199	1.15	0.0467	0.00525
RICTOR	NM_152756.3:3097	0.199	1.15	0.0586	0.0145
SLC6A19	NM_001003841.2:1515	0.2	1.15	0.244	0.443
STAT3	NM_003150.3:2060	0.19	1.14	0.0173	3.40E-05
PSME2	NM_002818.2:315	0.187	1.14	0.0279	0.000541
PTK2	NM_005607.4:3466	0.185	1.14	0.0299	0.000817
WASHC4	NM_015275.1:1485	0.184	1.14	0.0345	0.00175
NT5E	NM_002526.2:1214	0.193	1.14	0.0521	0.0101
ARID2	NM_152641.2:3355	0.184	1.14	0.0603	0.0226
CPT1A	NM_001876.3:1355	0.193	1.14	0.114	0.142
ZNF43	NM_003423.2:3835	0.189	1.14	0.211	0.405
FOLR3	NM_000804.2:469	0.187	1.14	0.266	0.509
PKM	NM_182471.1:2105	0.177	1.13	0.0152	2.43E-05
LAMC1	NM_002293.3:4915	0.171	1.13	0.0185	9.10E-05
HRAS	NM_005343.2:396	0.173	1.13	0.0286	0.000913
SMAD4	NM_005359.3:1370	0.17	1.13	0.0754	0.0644
RPL23	NM_000978.3:71	0.16	1.12	0.0165	6.94E-05
AKT3	NM_005465.4:287	0.169	1.12	0.0203	0.000162
GCLC	NM_001498.2:520	0.169	1.12	0.0256	0.000585
NCOA2	NM_006540.2:1045	0.164	1.12	0.0257	0.000698
RRM2	NM_001034.1:1615	0.161	1.12	0.0279	0.00117
ITGB5	NM_002213.3:2560	0.16	1.12	0.0349	0.00376
COL4A1	NM_001845.4:780	0.158	1.12	0.0349	0.00392
NDC1	NM_001168551.1:1845	0.165	1.12	0.0434	0.00902
CAB39	NM_001130849.1:1238	0.163	1.12	0.0471	0.0136
KMT2A	NM_005933.2:14000	0.162	1.12	0.0563	0.0283
APOC2	NM_000483.3:556	0.161	1.12	0.279	0.584
CD63	NM_001780.4:350	0.155	1.11	0.0223	0.000441
TFRC	NM_003234.1:1220	0.156	1.11	0.0244	0.000694
HEXB	NM_000521.3:950	0.157	1.11	0.026	0.000942
CS	NM_004077.2:740	0.153	1.11	0.0286	0.00172
CARD11	NM_032415.2:1075	0.155	1.11	0.0297	0.00199
PPM1A	NM_021003.4:550	0.154	1.11	0.0311	0.0026
AKT1	NM_001014431.1:758	0.148	1.11	0.0303	0.00273
REST	NM_001193508.1:1140	0.145	1.11	0.0356	0.00654
SLC16A1	NM_003051.3:635	0.146	1.11	0.0399	0.0105
PDCD1LG2	NM_025239.3:235	0.15	1.11	0.0593	0.0444
RRAGC	NM_022157.2:1199	0.149	1.11	0.0761	0.0971
RPLP0	NM_001002.3:250	0.131	1.1	0.0164	0.000199
YWHAZ	NM_003406.2:2345	0.139	1.1	0.0196	0.000394
ATF4	NM_001675.2:1151	0.135	1.1	0.0255	0.00186
ITGB1	NM_002211.3:355	0.134	1.1	0.0256	0.0019
MAP2K2	NM_030662.3:375	0.138	1.1	0.0608	0.0643
ALOX5	NM_000698.2:735	0.136	1.1	0.0658	0.085
COX5A	NM_004255.3:315	0.127	1.09	0.0136	8.49E-05
SERINC3	NM_006811.2:185	0.123	1.09	0.0178	0.000441
SERINC1	NM_020755.2:95	0.126	1.09	0.0279	0.00396
BRCC3	NM_024332.3:458	0.121	1.09	0.0299	0.00679
PIK3C2A	NM_002645.1:3505	0.12	1.09	0.0338	0.0121
CCL13	NM_005408.2:320	0.119	1.09	0.0374	0.0193
NDUFA2	NM_001185012.1:116	0.12	1.09	0.0466	0.0416
AFMID	NM_001010982.4:850	0.118	1.09	0.0464	0.0442
ATXN7	NM_001128149.2:3600	0.122	1.09	0.0504	0.0519
HLA-C	NM_002117.4:895	0.13	1.09	0.0723	0.122
WDR45	NM_007075.3:1390	0.124	1.09	0.0763	0.156
GNS	NM_002076.3:1340	0.13	1.09	0.0831	0.17
PGAM2	NM_000290.3:58	0.13	1.09	0.14	0.389
MAP3K12	NM_006301.2:800	0.119	1.09	0.274	0.68
LTA4H	NM_001256643.1:1140	0.117	1.08	0.0132	0.000114
PSMB3	NM_002795.3:22	0.11	1.08	0.0131	0.000152
COX6B1	NM_001863.4:264	0.11	1.08	0.0144	0.000271
NDUFA1	NM_004541.3:240	0.111	1.08	0.0173	0.000681
KDM3B	NM_016604.3:4178	0.111	1.08	0.019	0.00111
CTSZ	NM_001336.3:827	0.107	1.08	0.0256	0.00571
FAHD1	NM_031208.3:542	0.115	1.08	0.0321	0.0119
PDHA1	NM_000284.3:1080	0.108	1.08	0.0312	0.0135
SMAD2	NM_005901.5:1678	0.106	1.08	0.0363	0.0268
GDA	NM_001242506.2:861	0.106	1.08	0.0366	0.0269
NCOR1	NM_006311.3:1390	0.111	1.08	0.0395	0.0307
GPX1	NM_000581.2:745	0.109	1.08	0.0405	0.0357
ITCH	NM_001257138.1:438	0.112	1.08	0.0416	0.036
GOT2	NM_002080.2:2145	0.105	1.08	0.0405	0.0406
MSH2	NM_000251.1:2105	0.105	1.08	0.0408	0.0413
PSMD13	NM_175932.2:668	0.105	1.08	0.0444	0.0558
PIK3CB	NM_006219.1:2945	0.115	1.08	0.0502	0.0612
BRAF	NM_004333.3:565	0.117	1.08	0.0667	0.131
RAD51	NM_133487.2:566	0.105	1.08	0.0686	0.176
COX4I1	NM_001318797.1:50	0.103	1.07	0.0145	0.00038
SERINC5	NM_001174071.2:526	0.0914	1.07	0.0162	0.00132
MAPK1	NM_138957.2:430	0.0991	1.07	0.0199	0.00251
PSMB1	NM_002793.2:0	0.0938	1.07	0.0204	0.00371
IDH2	NM_002168.2:944	0.1	1.07	0.0252	0.00737
GABARAP	NM_007278.1:233	0.102	1.07	0.03	0.0144
GPX4	NM_001039847.1:435	0.0971	1.07	0.0288	0.015
RRM1	NM_001033.3:2444	0.0956	1.07	0.0285	0.0153
MGST3	NM_004528.2:195	0.101	1.07	0.0352	0.0287
UPP1	NM_003364.2:925	0.102	1.07	0.0385	0.0381
GART	NM_000819.3:370	0.0997	1.07	0.0434	0.0612
IMPDH1	NM_000883.3:862	0.098	1.07	0.0429	0.0622
TET2	NM_001127208.2:2882	0.0952	1.07	0.0428	0.068
PSMB10	NM_002801.3:249	0.0914	1.07	0.0598	0.177
CDCA5	NM_080668.3:308	0.1	1.07	0.0696	0.199
STK11	NM_000455.4:2060	0.0971	1.07	0.0714	0.223
HSD17B8	NM_014234.3:875	0.0951	1.07	0.0832	0.297
GMPR	NM_006877.3:325	0.094	1.07	0.203	0.659
ARPC4	NM_005718.4:970	0.0907	1.06	0.0159	0.00125
LDHB	NM_001174097.1:586	0.0798	1.06	0.0145	0.00153
MYBL2	NM_002466.2:445	0.089	1.06	0.0163	0.00157
COX7B	NM_001866.2:159	0.0814	1.06	0.0159	0.00215

COX5B	NM_001862.2:240	0.0876	1.06	0.0186	0.00332
LAMTOR5	NM_006402.2:504	0.0822	1.06	0.0185	0.00436
ATP5ME	NM_007100.3:184	0.0799	1.06	0.0184	0.00489
HEXA	NM_000520.4:702	0.0788	1.06	0.0213	0.0101
NDUFB1	NM_004545.3:270	0.0843	1.06	0.0235	0.0116
CHMP2A	NM_014453.3:241	0.0855	1.06	0.0274	0.0205
GLS	NM_014905.3:985	0.0901	1.06	0.0295	0.0223
UQCRQ	NM_014402.4:172	0.0776	1.06	0.0272	0.0291
COX7C	NM_001867.2:57	0.0901	1.06	0.0333	0.0352
COX8A	NM_004074.2:0	0.0859	1.06	0.0364	0.0559
AK3	NM_016282.2:450	0.0864	1.06	0.0441	0.0979
GAPVD1	NM_001282679.1:380	0.0856	1.06	0.0442	0.101
NUP62	NM_016553.3:457	0.0829	1.06	0.043	0.102
OAT	NM_000274.3:775	0.0898	1.06	0.0489	0.116
PTEN	NM_000314.3:1675	0.0849	1.06	0.0507	0.145
ECHS1	NM_004092.3:125	0.0793	1.06	0.0488	0.155
ASH1L	NM_018489.2:5005	0.0846	1.06	0.0598	0.207
NEU1	NM_000434.3:1508	0.0892	1.06	0.0666	0.229
FNIP1	NM_001008738.2:1264	0.0797	1.06	0.0626	0.25
INSR	NM_000208.2:525	0.09	1.06	0.0965	0.387
TIGAR	NM_020375.2:5245	0.0892	1.06	0.134	0.53
ALOX15	NM_001140.3:1910	0.0837	1.06	0.303	0.791
LAMTOR4	NM_001008395.2:494	0.0744	1.05	0.0148	0.00239
NME2	NM_001018137.2:669	0.0698	1.05	0.0154	0.00397
SDHC	NM_001035511.1:615	0.0756	1.05	0.0187	0.00678
COX6A1	NM_004373.2:260	0.0725	1.05	0.0184	0.00771
NDUFB2	NM_004546.2:230	0.0645	1.05	0.0171	0.00927
NEDD8	NM_006156.2:330	0.0651	1.05	0.0179	0.0108
TXN	NM_003329.2:55	0.0726	1.05	0.0222	0.0169
NDUFA6	NM_002490.3:430	0.0654	1.05	0.0211	0.0212
USP8	NM_001128610.1:1160	0.0646	1.05	0.0214	0.0232
NFE2L2	NM_006164.3:995	0.0751	1.05	0.0252	0.0245
GUSB	NM_000181.3:1899	0.0754	1.05	0.0264	0.0288
SERINC2	NM_018565.3:795	0.0697	1.05	0.0252	0.0326
NUP205	NM_015135.1:5075	0.067	1.05	0.0263	0.0439
TPR	NM_003292.2:6825	0.0767	1.05	0.0329	0.0587
HSF1	XM_011517006.1:63	0.0704	1.05	0.0365	0.102
NDUFB11	NM_001135998.1:255	0.0696	1.05	0.0406	0.137
PTGES	NM_004878.4:303	0.0671	1.05	0.0405	0.148
PLA2G15	NM_012320.3:900	0.0709	1.05	0.0534	0.232
TK1	NM_003258.1:1215	0.0681	1.05	0.054	0.254
ENO3	NM_001976.4:1368	0.07	1.05	0.186	0.72
COPS6	NM_006833.4:860	0.061	1.04	0.00946	0.000658
PSMA7	NM_002792.2:639	0.0609	1.04	0.0145	0.00575
SREBF2	NM_004599.2:665	0.0602	1.04	0.0185	0.0173
SOD1	NM_000454.4:245	0.0621	1.04	0.0191	0.0174
PRDX5	NM_012094.4:600	0.0609	1.04	0.0191	0.0191
HIF1A	NM_001530.2:1985	0.0585	1.04	0.0191	0.0219
NDUFB8	NM_001284367.1:204	0.0542	1.04	0.02	0.035
MAPKAP1	NM_001006617.1:1188	0.0563	1.04	0.0208	0.0354
TALDO1	NM_006755.1:262	0.0603	1.04	0.0223	0.0354
MYC	NM_002467.3:1610	0.0599	1.04	0.0275	0.0726
PEBP1	NM_002567.2:1335	0.0549	1.04	0.0272	0.0898
UBE2C	NM_007019.2:561	0.0564	1.04	0.0332	0.14
ARID1A	NM_006015.4:5495	0.0538	1.04	0.0323	0.147
SDHB	NM_003000.2:245	0.0554	1.04	0.0334	0.148
PSMA3	NM_152132.1:465	0.0534	1.04	0.0324	0.151
PSMC1	NM_002802.2:58	0.06	1.04	0.0414	0.197
IDH3G	NM_004135.2:390	0.0501	1.04	0.0378	0.234
NDUFA4	NM_002489.2:35	0.0504	1.04	0.0398	0.252
ATG2B	NM_018036.5:1722	0.0561	1.04	0.047	0.277
NDUFB7	NM_004146.5:239	0.0504	1.04	0.0433	0.288
PLCG1	NM_002660.2:2290	0.0546	1.04	0.0469	0.289
EFNA4	NM_005227.2:380	0.0606	1.04	0.0527	0.293
LAMB1	NM_002291.2:3120	0.0595	1.04	0.0563	0.331
PIK3R1	NM_181504.2:1105	0.0537	1.04	0.0628	0.425
PIK3R4	NM_014602.1:3620	0.053	1.04	0.0636	0.436
H6PD	NM_004285.3:7250	0.0569	1.04	0.101	0.595
PYCR1	NM_006907.2:513	0.0627	1.04	0.116	0.609
CTSA	NM_001127695.1:1540	0.0438	1.03	0.01	0.00469
IMPDH2	NM_000884.2:545	0.0479	1.03	0.0208	0.061
NPM1	NM_002520.6:910	0.0432	1.03	0.0214	0.0895
NDUFB4	NM_004547.4:254	0.0361	1.03	0.0202	0.125
ARF5	NM_001662.2:36	0.0491	1.03	0.0287	0.137
ACAA2	NM_006111.2:450	0.037	1.03	0.0225	0.152
ARID1B	NM_020732.3:6335	0.0486	1.03	0.0308	0.166
PRKAB1	NM_006253.4:1550	0.0474	1.03	0.0321	0.191
HSPE1	NM_002157.2:607	0.0366	1.03	0.025	0.193
FANCI	NM_001113378.1:541	0.0462	1.03	0.0321	0.201
AP2S1	NM_021575.2:665	0.0408	1.03	0.0293	0.214
NQO1	NM_000903.2:790	0.0359	1.03	0.027	0.231
CDA	NM_001785.2:322	0.0411	1.03	0.0316	0.242
ME2	NM_002396.3:610	0.0464	1.03	0.0361	0.246
STK3	NM_006281.3:1295	0.0464	1.03	0.038	0.267
ATP6V1F	NM_001198909.1:673	0.0364	1.03	0.0343	0.329
PEMT	NM_148173.1:385	0.0422	1.03	0.0407	0.339
MAPK8	NM_002750.2:945	0.0449	1.03	0.0441	0.349
TKT	NM_001064.2:1235	0.0463	1.03	0.0475	0.367
NSD1	NM_022455.4:3140	0.0452	1.03	0.0486	0.388
NDUFB10	NM_004548.2:155	0.0453	1.03	0.0635	0.503
MAPT	NM_016834.3:1205	0.0494	1.03	0.15	0.753
TRAF6	NM_145803.2:745	0.0353	1.02	0.016	0.0695
BCL2L1	NM_138578.1:1560	0.0294	1.02	0.0149	0.0953
SCD	NM_005063.4:2025	0.0354	1.02	0.0187	0.106
NME1	NM_000269.2:500	0.0305	1.02	0.0185	0.149
PRDX1	NM_002574.2:632	0.0328	1.02	0.0212	0.172
RANBP2	NM_006267.4:5384	0.022	1.02	0.0181	0.268
APRT	NM_000485.2:662	0.0254	1.02	0.0243	0.336
NDUFA12	NM_018838.3:315	0.0259	1.02	0.0249	0.338
NDUFA3	NM_004542.3:75	0.0263	1.02	0.0263	0.355

IDH3B	NM_001258384.1:556	0.0306	1.02	0.0313	0.366
TPX2	NM_012112.4:2975	0.0285	1.02	0.0355	0.453
LAMTOR2	NM_001145264.1:272	0.0351	1.02	0.0438	0.454
ADK	NM_001123.2:355	0.029	1.02	0.0371	0.464
GMPS	NM_003875.2:385	0.0234	1.02	0.0311	0.481
DERA	NM_015954.2:960	0.0285	1.02	0.0396	0.499
PDPK1	NM_002613.3:5935	0.0251	1.02	0.0358	0.51
HSPA4	NM_002154.3:1225	0.0264	1.02	0.0413	0.546
KAT6A	NM_001099412.1:550	0.0216	1.02	0.0338	0.546
MKI67	NM_002417.2:4020	0.0265	1.02	0.0464	0.588
ATG101	NM_021934.4:939	0.0238	1.02	0.0476	0.635
RBKS	NM_022128.2:914	0.0335	1.02	0.131	0.807
PRR5	NM_015366.3:1635	0.0266	1.02	0.147	0.862
MYB	NM_001130173.1:183	0.0216	1.02	0.142	0.884
UQCR10	NM_001003684.1:40	0.0195	1.01	0.0222	0.413
TECR	NR_038104.1:574	0.0128	1.01	0.0159	0.451
CCNA2	NM_001237.2:1210	0.0185	1.01	0.0251	0.49
NDUFS8	NM_002496.3:190	0.0144	1.01	0.02	0.5
NDUFA7	NM_005001.2:373	0.0201	1.01	0.031	0.54
NDUFA13	NM_015965.6:167	0.0214	1.01	0.0388	0.601
DCK	NM_000788.2:310	0.0184	1.01	0.035	0.617
ACACA	NM_198834.1:3681	0.0169	1.01	0.0324	0.62
HERC1	NM_003922.3:300	0.0198	1.01	0.0387	0.627
BUB1	NM_004336.3:1978	0.018	1.01	0.0426	0.686
COX14	NM_001257133.1:672	0.0107	1.01	0.0253	0.688
GBA	NM_001005742.2:1695	0.0123	1.01	0.0302	0.697
ATP5F1D	NM_001687.4:184	0.0136	1.01	0.0389	0.738
HADH	NM_001184705.2:645	0.0088	1.01	0.0337	0.803
RPS6KB1	NM_003161.2:310	0.00892	1.01	0.0369	0.817
GMPR2	NM_001002001.2:392	0.0105	1.01	0.0464	0.828
JAK2	NM_004972.3:1464	0.00982	1.01	0.0466	0.84
EEA1	NM_003566.3:2035	0.00726	1.01	0.038	0.855
POLE	NM_006231.3:3264	0.0119	1.01	0.0646	0.86
CAT	NM_001752.2:1130	0.00761	1.01	0.0434	0.867
ASNS	NM_183356.2:1644	0.00912	1.01	0.0736	0.906
ABL1	NM_005157.3:3200	0.00716	1	0.0401	0.864
TYMS	NM_001071.2:1110	0.00705	1	0.0536	0.9
NDUFS7	NM_024407.4:376	0.00418	1	0.0364	0.912
PPARG	NM_005037.5:345	0.00436	1	0.043	0.923
ZNF91	NM_003430.2:4472	0.00431	1	0.05	0.934
RPTOR	NM_020761.2:6665	0.0036	1	0.074	0.963
ADH1C	NM_000669.3:976	0.00627	1	0.134	0.964
PGD	NM_002631.2:1472	0.000733	1	0.0204	0.973
XRCC2	NM_005431.1:600	0.000392	1	0.0418	0.993
CHMP6	NM_024591.4:346	6.46E-06	1	0.0307	1
FANCD2	NM_033084.3:260	-0.00149	0.999	0.0169	0.933
AKT1S1	NM_032375.3:1850	-0.00182	0.999	0.031	0.955
MSRB2	NM_012228.3:385	-0.00122	0.999	0.0833	0.989
SNF8	NM_001317192.1:234	-0.00276	0.998	0.0269	0.922
OGDH	NM_001003941.2:196	-0.00244	0.998	0.0247	0.925
CTSL	NM_001912.4:1072	-0.00244	0.998	0.0336	0.944
ACAT1	NM_000019.3:282	-0.00266	0.998	0.0622	0.967
SREBF1	NM_001005291.1:1392	-0.0045	0.997	0.0343	0.9
CCNB2	NM_004701.2:980	-0.004	0.997	0.0386	0.921
PRKAG2	NM_016203.3:1895	-0.00419	0.997	0.0448	0.929
KMT2D	NM_003482.3:6070	-0.00413	0.997	0.0669	0.953
ATOX1	NM_004045.3:143	-0.00744	0.995	0.0304	0.815
SLC25A1	NM_005984.2:964	-0.00682	0.995	0.0292	0.823
EHHADH	NM_001166415.1:2022	-0.0102	0.993	0.122	0.936
APOE	NM_000041.2:96	-0.0107	0.993	0.158	0.948
KEAP1	NM_012289.3:561	-0.0118	0.992	0.012	0.365
UCKL1	NM_001193379.1:825	-0.0122	0.992	0.0162	0.48
NPR2	NM_003995.3:1085	-0.0122	0.992	0.228	0.959
PHGDH	NM_006623.3:1900	-0.0125	0.991	0.027	0.66
SHMT2	NM_001166356.1:1460	-0.0134	0.991	0.044	0.771
CLOCK	NM_004898.2:2350	-0.0152	0.99	0.0507	0.775
LAMA4	NM_001105209.1:287	-0.015	0.99	0.0788	0.855
SELENOK	NM_021237.3:42	-0.014	0.99	0.123	0.913
SEC13	NM_001136026.2:400	-0.0162	0.989	0.00866	0.11
RPIA	NM_144563.2:1588	-0.0164	0.989	0.0331	0.637
PIK3R2	NM_005027.2:3100	-0.017	0.988	0.0657	0.805
PIK3R3	NM_003629.3:5016	-0.0182	0.987	0.079	0.826
KYAT3	NM_001008661.2:1445	-0.0213	0.985	0.0349	0.565
NCAPH	NM_015341.3:1550	-0.0216	0.985	0.0557	0.712
BUB1B	NM_001211.4:835	-0.0211	0.985	0.0667	0.762
TXN2	NM_012473.3:192	-0.0228	0.984	0.023	0.36
AKT2	NM_001626.4:699	-0.0246	0.983	0.0297	0.439
D2HGDH	NM_001287249.1:550	-0.0247	0.983	0.141	0.866
MYD88	NM_002468.3:2145	-0.0257	0.982	0.0273	0.382
GPS1	NM_004127.4:605	-0.0274	0.981	0.017	0.158
FH	NM_000143.2:203	-0.0283	0.981	0.0298	0.379
NRF1	NM_001040110.1:2910	-0.0275	0.981	0.0661	0.692
DGUOK	NM_080916.2:902	-0.0293	0.98	0.024	0.269
UCK2	NM_012474.3:730	-0.0296	0.98	0.0388	0.474
STAT1	NM_007315.3:239	-0.0291	0.98	0.0481	0.568
NFS1	NM_021100.3:1775	-0.0312	0.979	0.052	0.571
FNIP2	NM_020840.1:1732	-0.0312	0.979	0.0871	0.732
LAT	NM_001014987.1:1290	-0.0312	0.979	0.0991	0.764
ACAP2	NM_012287.5:852	-0.0319	0.978	0.0448	0.502
PNP	NM_000270.2:1150	-0.0326	0.978	0.0528	0.559
HACD2	NM_198402.2:510	-0.0334	0.977	0.0214	0.169
PRKAB2	NM_005399.3:1600	-0.0336	0.977	0.0304	0.312
PDK2	NM_002611.3:435	-0.034	0.977	0.048	0.506
PSPH	NM_004577.3:225	-0.0352	0.976	0.0842	0.691
CCND1	NM_053056.2:690	-0.0366	0.975	0.0329	0.308
UCK1	NM_031432.3:232	-0.0361	0.975	0.0665	0.607
CTSD	NM_001909.3:1495	-0.0381	0.974	0.0941	0.7
GTSE1	NM_016426.5:305	-0.04	0.973	0.0431	0.389
MYBL1	NM_001080416.3:1030	-0.0393	0.973	0.13	0.772
CDK9	NM_001261.2:400	-0.0418	0.971	0.049	0.426

SLC16A2	NM_006517.3:2465	-0.0456	0.969	0.0715	0.547
NADK	NM_001198993.1:1558	-0.0472	0.968	0.0622	0.477
FOXM1	NM_202002.1:1000	-0.049	0.967	0.0382	0.246
MPC2	NM_001143674.1:285	-0.0495	0.966	0.0467	0.33
PLK1	NM_005030.3:535	-0.0514	0.965	0.0224	0.0617
RPS6KB2	NM_003952.2:980	-0.0516	0.965	0.114	0.667
MAT1A	NM_000429.2:2275	-0.0508	0.965	0.24	0.839
XCL1/2	NM_003175.3:377	-0.0523	0.964	0.108	0.646
FASN	NM_004104.4:5387	-0.0555	0.962	0.0266	0.0825
CTCF	NM_001191022.1:490	-0.0552	0.962	0.0433	0.249
ATF7	NM_001130060.1:203	-0.0559	0.962	0.048	0.288
SHMT1	NM_148918.1:1800	-0.0566	0.962	0.0687	0.442
HSF2	NM_001135564.1:615	-0.0563	0.962	0.0709	0.457
PTK6	NM_001256358.1:291	-0.056	0.962	0.148	0.718
ZNF708	NM_021269.2:488	-0.0577	0.961	0.0288	0.0913
SLC1A5	NM_001145144.1:180	-0.0572	0.961	0.0373	0.176
RBBP5	NM_005057.2:325	-0.0575	0.961	0.0561	0.345
ZNF136	NM_003437.2:385	-0.0589	0.96	0.03	0.0968
KYAT1	NM_004059.4:1557	-0.059	0.96	0.0806	0.491
ZNF100	NM_173531.3:36	-0.061	0.959	0.117	0.62
GLUD1	NM_005271.2:2680	-0.0639	0.957	0.0271	0.0562
CENPA	NM_001042426.1:979	-0.0627	0.957	0.0345	0.119
PFKM	NM_000289.5:2195	-0.0671	0.955	0.0232	0.0278
MTF1	NM_005955.2:210	-0.0662	0.955	0.0333	0.0941
FANCA	NM_000135.2:798	-0.0693	0.953	0.034	0.0877
RAD51AP1	NM_001130862.1:1125	-0.0774	0.948	0.0388	0.0929
SRR	NM_021947.1:560	-0.0779	0.947	0.0644	0.272
CLSPN	NM_022111.2:442	-0.0799	0.946	0.0117	0.000477
MTOR	NM_004958.3:1865	-0.0794	0.946	0.0281	0.0304
UBE2T	NM_014176.3:595	-0.0821	0.945	0.0304	0.0357
PRIM2	NM_001282488.1:124	-0.0818	0.945	0.0307	0.0373
PRKAA1	NM_006251.5:366	-0.0839	0.944	0.0195	0.00506
KIF2C	NM_006845.3:1940	-0.0831	0.944	0.034	0.0505
HJURP	NM_018410.3:1325	-0.083	0.944	0.0423	0.0974
ASL	NM_000048.3:130	-0.0834	0.944	0.0509	0.152
UMPS	NM_000373.2:2445	-0.0826	0.944	0.0729	0.3
AMPD2	NM_004037.6:3095	-0.083	0.944	0.0955	0.418
CDC20	NM_001255.2:430	-0.0841	0.943	0.0176	0.00309
RUNX1	NM_001754.4:635	-0.086	0.942	0.0425	0.0894
EZH2	NM_001203247.1:1121	-0.0883	0.941	0.0252	0.0127
IDH3A	NM_005530.2:1521	-0.0871	0.941	0.0404	0.0743
DGLUCY	NM_001102369.2:442	-0.0879	0.941	0.0885	0.359
KPNA2	NM_002266.2:917	-0.0887	0.94	0.0182	0.0028
BCL2	NM_000657.2:5	-0.0889	0.94	0.097	0.395
PCLAF	NM_014736.5:1025	-0.0914	0.939	0.0785	0.288
SDSL	NM_138432.2:303	-0.0916	0.938	0.13	0.509
TFAM	NM_003201.1:85	-0.0967	0.935	0.0221	0.00469
STAM2	NM_005843.4:1455	-0.0964	0.935	0.0358	0.0361
PRPS1	NM_002764.3:1081	-0.103	0.931	0.0504	0.0879
BRCA1	NM_007294.3:787	-0.105	0.93	0.0565	0.111
ADA	NM_000022.2:1300	-0.104	0.93	0.0575	0.121
SRM	NM_003132.2:254	-0.107	0.929	0.0392	0.0343
L2HGDH	NM_024884.2:1296	-0.108	0.928	0.0546	0.0959
EXO1	NM_003686.3:2715	-0.109	0.927	0.0438	0.0477
PCK2	NM_004563.2:795	-0.111	0.926	0.119	0.386
PRKAG1	NM_002733.3:825	-0.113	0.925	0.0366	0.0218
WRN	NM_000553.4:2944	-0.112	0.925	0.054	0.0837
CDCA8	NM_018101.2:1665	-0.115	0.924	0.0582	0.096
ZNF254	NM_203282.3:1986	-0.119	0.921	0.0369	0.0177
FABP5	NM_001444.1:100	-0.121	0.92	0.0259	0.00347
EOMES	NM_005442.2:1670	-0.122	0.919	0.193	0.551
ACY1	NM_000666.2:109	-0.123	0.918	0.104	0.28
MLST8	NM_001199173.1:810	-0.125	0.917	0.0553	0.064
NAALAD2	NM_005467.3:830	-0.124	0.917	0.139	0.406
NR2F1	NM_005654.4:2885	-0.125	0.917	0.14	0.407
CBR4	NM_032783.4:520	-0.127	0.916	0.0362	0.0127
UQCR11	NM_006830.2:360	-0.127	0.916	0.102	0.261
ACAT2	NM_005891.2:910	-0.128	0.915	0.0251	0.00222
TIMELESS	NM_003920.2:1185	-0.129	0.914	0.0363	0.0119
VPS28	NM_016208.3:416	-0.134	0.911	0.0287	0.00337
PPAT	NM_002703.3:1210	-0.134	0.911	0.0354	0.00902
SLC3A2	NM_001012662.2:1505	-0.136	0.91	0.0256	0.00184
NOX4	NM_001143836.2:1795	-0.135	0.91	0.0927	0.195
GOT1	NM_002079.2:615	-0.138	0.909	0.0483	0.029
SLC16A7	NM_001270623.1:5460	-0.146	0.904	0.0788	0.114
MCAT	NM_014507.3:378	-0.146	0.904	0.14	0.338
TELO2	NM_016111.3:294	-0.15	0.901	0.0995	0.183
PSAT1	NM_021154.3:1445	-0.156	0.898	0.0263	0.00104
GAD1	NM_000817.2:575	-0.156	0.898	0.151	0.342
CAD	NM_004341.3:2380	-0.157	0.897	0.0602	0.0406
FDX1	NM_004109.4:618	-0.162	0.894	0.0438	0.0102
RIMKLB	NM_020734.2:1840	-0.164	0.893	0.0636	0.0422
MYCL	NM_001033081.2:568	-0.164	0.893	0.0643	0.0439
PUDP	NM_001178135.1:425	-0.164	0.893	0.0721	0.0639
CTPS1	NM_001301237.1:580	-0.169	0.889	0.0335	0.00234
BRIP1	NM_032043.1:1130	-0.171	0.888	0.0317	0.00167
NADK2	NM_153013.3:315	-0.173	0.887	0.0316	0.00154
ZNF93	NM_031218.3:2314	-0.176	0.885	0.146	0.273
PYCR2	NM_013328.2:1250	-0.179	0.883	0.0477	0.00952
GCDH	NM_000159.2:464	-0.184	0.88	0.0659	0.0316
PRIM1	NM_000946.2:480	-0.187	0.879	0.0397	0.00332
FDXR	NM_004110.3:1123	-0.187	0.878	0.109	0.135
ZNF85	NM_001256171.1:275	-0.192	0.875	0.0343	0.00137
SLC7A5	NM_003486.5:785	-0.194	0.874	0.0202	7.22E-05
IDH1	NM_005896.3:418	-0.204	0.868	0.021	6.80E-05
ZNF253	NM_021047.2:1327	-0.206	0.867	0.0323	0.000689
XDH	NM_000379.3:1325	-0.205	0.867	0.0485	0.00545
RBP4	NM_006744.3:793	-0.208	0.866	0.0837	0.0473
MPC1	NM_016098.2:210	-0.209	0.865	0.0233	0.000107
ODC1	NM_002539.1:950	-0.213	0.863	0.0512	0.00594

ERCC6	NM_001277058.1:200	-0.213	0.863	0.0896	0.0552
ADAL	NM_001012969.2:890	-0.215	0.862	0.103	0.0811
ZNF675	NM_138330.2:851	-0.218	0.86	0.0304	0.000377
MAT2A	NM_005911.4:805	-0.218	0.86	0.0487	0.00421
AADAT	NM_016228.3:1510	-0.223	0.857	0.0316	0.000408
EME1	XM_011524392.1:416	-0.226	0.855	0.0929	0.0513
MLYCD	NM_012213.2:1530	-0.23	0.852	0.0676	0.0143
PYCR3	NM_023078.2:1145	-0.233	0.851	0.0707	0.0165
ATF7IP	NM_018179.3:2505	-0.242	0.846	0.0512	0.00327
TP63	NM_003722.4:1295	-0.241	0.846	0.0556	0.00487
ZNF682	NM_001077349.1:1465	-0.259	0.836	0.0322	2.00E-04
PTGER4	NM_000958.2:976	-0.263	0.833	0.215	0.268
TLR4	NM_138554.2:2570	-0.274	0.827	0.0416	0.000591
AOX1	NM_001159.3:1415	-0.276	0.826	0.197	0.212
EPC1	NM_025209.2:1615	-0.277	0.825	0.0449	0.000829
GLYCTK	NR_026700.1:1336	-0.282	0.822	0.175	0.157
SLC2A8	NM_014580.3:1777	-0.287	0.82	0.0442	0.000639
PRKCG	NM_002739.3:445	-0.297	0.814	0.199	0.186
TH	NM_000360.3:1306	-0.301	0.812	0.0969	0.0211
LCK	NM_005356.2:1260	-0.313	0.805	0.188	0.148
BRCA2	NM_000059.3:115	-0.338	0.791	0.0925	0.0107
NAGLU	NM_000263.3:696	-0.343	0.788	0.141	0.0513
FOLR1	NM_000802.2:815	-0.359	0.78	0.198	0.119
DTL	NM_016448.2:715	-0.362	0.778	0.0807	0.00418
FBP1	NM_000507.3:590	-0.373	0.772	0.259	0.2
CD14	NM_000591.2:885	-0.379	0.769	0.223	0.14
TPH1	NM_004179.1:335	-0.415	0.75	0.284	0.194
IDNK	NM_001001551.3:272	-0.418	0.748	0.142	0.0256
ACSF3	NR_045667.2:2282	-0.432	0.741	0.247	0.131
NCR1	NM_004829.5:602	-0.444	0.735	0.21	0.0794
CD6	NM_001254751.1:1722	-0.485	0.715	0.148	0.0168
MYCN	NM_005378.4:1545	-0.675	0.626	0.25	0.0356
MRAS	NM_001085049.2:1700	-0.685	0.622	0.295	0.059
CYP1A1	NM_000499.3:695	-0.719	0.607	0.242	0.0248
THBS1	NM_003246.2:3465	-0.728	0.604	0.0497	6.33E-06
HSPA2	NM_021979.3:2095	-0.732	0.602	0.216	0.0148
TK2	NM_004614.3:2165	-0.752	0.594	0.32	0.0569
SLC7A11	NM_014331.3:636	-0.814	0.569	0.0625	1.27E-05
CYP1B1	NM_000104.3:1715	-1.12	0.462	0.112	6.06E-05
SOX2	NM_003106.2:151	-1.56	0.339	0.203	0.000255

Appendix B: Differential gene expression during intracellular infection of urothelial cells. Differential expression of all genes in the NanoString nCounter Human Metabolic Pathways Panel. Urothelial cells were intracellularly infected with wild-type UPEC or mock infected and transcript abundance was compared to determine differential expression. Genes are ordered according to linear fold change. See also Chapter 3, Materials and Methods.

UniProt ID	Protein Name	Gene Name	Subcellular Location	Fold Change UTI89 vs Δ*cydAB*	Log2 (Fold Change)	P Value	Log10 (P Value)
tr|Q1R227|Q1R227_ECOUT	Putative exported protein	UTI89_P011	extracellular space	0.125525147	-2.993951676	0.003376482	2.471535568
tr|Q1R8P4|Q1R8P4_ECOUT	Beta-barrel assembly-enhancing protease	*yfgC*	periplasm, membrane	0.148786374	-2.748685687	2.28517E-05	4.641081337
tr|Q1RD49|Q1RD49_ECOUT	Penicillin-binding protein activator	*lpoB*	outer membrane	0.163411049	-2.613422558	0.001571569	2.803666525
tr|Q1R968|Q1R968_ECOUT	Bifunctional long-chain fatty acids transporter	*fadL*	outer membrane	0.239537481	-2.061676679	9.7553E-06	5.010759345
tr|Q1RE62|Q1RE62_ECOUT	Arginine-binding periplasmic protein 1	*artI*	periplasm, membrane	0.266055743	-1.910199551	1.48274E-05	4.828935705
tr|Q1R6J1|Q1R6J1_ECOUT	Putative periplasmic protein	*yraP*	periplasm, outer membrane	0.278227955	-1.845660714	1.36264E-05	4.865617625
tr|Q1RCH8|Q1RCH8_ECOUT	Outer membrane protein W	*ompW*	outer membrane	0.295345369	-1.759525104	0.005280296	2.277341724
tr|Q1R3A8|Q1R3A8_ECOUT	outer membrane lipoprotein Blc	*blc*	outer membrane, cytosol	0.312269546	-1.679136215	0.000183133	3.737233729
tr|Q1R8T9|Q1R8T9_ECOUT	uncharacterized lipoprotein	*yfeY*	outer membrane	0.328622813	-1.605495458	1.97706E-05	4.703980148
tr|Q1R208|Q1R208_ECOUT	enterotoxin TieB	*senB*	extracellular space	0.362473728	-1.464051661	0.000731952	3.135517179
tr|Q1R5B1|Q1R5B1_ECOUT	Starvation induced outer membrane protein	*slp*	outer membrane	0.379379633	-1.398285865	0.001269212	2.896465692
tr|Q1RFZ2|Q1RFZ2_ECOUT	Outer membrane lipoprotein	*rcsF*	outer membrane	0.380701995	-1.393265964	0.002558941	2.591939804
tr|Q1R1Q3|Q1R1Q3_ECOUT	TraT complement resistance protein	*traT*	outer membrane	0.424135876	-1.237401574	0.002933558	2.532605306
tr|Q1RD74|Q1RD74_ECOUT	Flagellar hook-associated protein 3	*flgL*	outer membrane	0.432483284	-1.209283722	0.005806429	2.236090876
tr|Q1R8M1|Q1R8M1_ECOUT	Outer membrane protein assembly factor BamB	*yfgL*	outer membrane	0.436351795	-1.196436363	0.008763172	2.057338657
tr|Q1REY0|Q1REY0_ECOUT	Ferrienterobactin receptor	*fepA*	outer membrane	0.445534911	-1.166389611	0.057785816	1.238178746
sp|Q1RGE3|LPTD_ECOUT	LPS-assembly protein	*lptD*	outer membrane	0.476631728	-1.069053105	0.03527219	1.452567577
tr|Q1R572|Q1R572_ECOUT	Glucanase	*yhjM*	extracellular space	0.486676187	-1.03896591	0.011089604	1.955083959
tr|Q1RBF4|Q1RBF4_ECOUT	Outer membrane lipoprotein	*slyB*	outer membrane	0.492971306	-1.020424419	0.009578436	2.018705394
tr|Q1RCP9|Q1RCP9_ECOUT	Putative outer membrane receptor	*prrA*	outer membrane	0.498638965	-1.003932473	0.003197881	2.495137683
tr|Q1RDS8|Q1RDS8_ECOUT	Outer membrane protein F	*ompF*	outer membrane	0.514037016	-0.960055844	0.00429467	2.367070229
tr|Q1R7V0|Q1R7V0_ECOUT	Lipoprotein	*nlpD*	outer membrane	0.516877617	-0.952105365	0.025155953	1.599359224
tr|Q1REB0|Q1REB0_ECOUT	Outer membrane protein X	*ompX*	outer membrane	0.533727755	-0.905824059	0.012573301	1.900550698
sp|Q1R3U1|BTUB_ECOUT	Vitamin B12 transporter	*btuB*	outer membrane	0.579775036	-0.786434879	0.013235181	1.878270114
tr|Q1RES9|Q1RES9_ECOUT	Endolytic peptidoglycan transglycosylase	*rlpA*	outer membrane	0.581569816	-0.781975701	0.041737973	1.379468645
tr|Q1RCY1|Q1RCY1_ECOUT;tr|Q1RAK8|Q1RAK8_ECOUT	Outer membrane porin protein	*nmpC*	outer membrane	0.623544333	-0.681435958	0.025400875	1.595151319
tr|Q1R573|Q1R573_ECOUT	Cellulose synthase operon protein C	*bcsC*	outer membrane	0.627095163	-0.673243703	0.13242154	0.878041367
tr|Q1REF8|Q1REF8_ECOUT	Pectinesterase	*ybhC*	outer membrane	0.637639149	-0.649187886	0.016912693	1.771787222
tr|Q1R9K0|Q1R9K0_ECOUT;tr|Q1RC18|Q1RC18_ECOUT	Outer membrane protein 1b	*ompC*	outer membrane	0.638605134	-0.647003943	0.037681089	1.423876549
tr|Q1R6U8|Q1R6U8_ECOUT	Outer membrane protein	*tolC*	outer membrane	0.643739109	-0.635451977	0.026690802	1.57363837
tr|Q1RAF5|Q1RAF5_ECOUT	Putative pesticin receptor	*fyuA*	outer membrane	0.670084888	-0.577584223	0.113158809	0.946311633
tr|Q1RAL6|Q1RAL6_ECOUT	Flagellar hook-associated protein 2	*fliD*	outer membrane	0.675164748	-0.566688516	0.040526139	1.392264766
tr|Q1REI3|Q1REI3_ECOUT	Peptidoglycan-associated protein	*pal*	outer membrane	0.696262048	-0.522297707	0.04713933	1.32661659
tr|Q1RD80|Q1RD80_ECOUT	Flagellar basal body protein	*flgF*	outer membrane	0.700667349	-0.513198427	0.041052256	1.386662971
tr|Q1RD75|Q1RD75_ECOUT	Flagellar hook-associated protein 1	*flgK*	outer membrane	0.704544719	-0.505236814	0.03292098	1.482527244
tr|Q1R8Q0|Q1R8Q0_ECOUT	Outer membrane protein assembly factor BamC	*nlpB*	outer membrane	0.708268662	-0.497631384	0.043418765	1.362322534
tr|Q1R2T5|Q1R2T5_ECOUT	Hemolysin A	*hlyA*	extracellular space	0.723240021	-0.467453583	0.147643036	0.830787033
tr|Q1R8N7|Q1R8N7_ECOUT	Polyphosphate kinase	*ppk*	outer membrane, inner membrane	0.73509184	-0.444003588	0.18628135	0.729830624
tr|Q1RDQ7|Q1RDQ7_ECOUT	Outer membrane protein A	*ompA*	outer membrane	0.801838419	-0.31861655	0.351423101	0.454169693
tr|Q1R3B0|Q1R3B0_ECOUT	Putative toxin of osmotically regulated toxin-antitoxin system	*ecnB*	outer membrane, inner membrane	0.864984147	-0.209254402	0.799347027	0.097264636
tr|Q1RBB9|Q1RBB9_ECOUT	Murein lipoprotein	*lpp*	outer membrane, inner membrane, periplasm	0.875936704	-0.191101472	0.635111624	0.197149939
tr|Q1RDC4|Q1RDC4_ECOUT	Curli production assembly/transport component	*csgG*	outer membrane, inner membrane, periplasm	0.891002758	-0.166498197	0.663248379	0.178323803
sp|Q1RG12|BAMA_ECOUT	Outer membrane protein assembly factor	*bamA*	outer membrane	0.891893486	-0.165056667	0.422418782	0.37425678
tr|Q1RBD1|Q1RBD1_ECOUT	Pertactin domain-containing protein	*ydhQ*	outer membrane	0.912285994	-0.132441927	0.69261387	0.159508816
tr|Q1R5W6|Q1R5W6_ECOUT	DNA-binding protein HU-alpha	*hupA*	extracellular space, cytosol	0.966763547	-0.04876502	0.924455781	0.034113857
tr|Q1R386|Q1R386_ECOUT	Protein HflK	*hflK*	periplasm, inner membrane, cytosol	0.977974497	-0.032131251	0.910348205	0.04079246
sp|Q1R7R4|ENO_ECOUT	enolase	*eno*	extracellular space, cytosol	1.010975792	0.015748452	0.942214231	0.025850341
tr|Q1REI6|Q1REI6_ECOUT	Membrane spanning protein	*tolA*	outer membrane, inner membrane	1.107158163	0.146861333	0.653096549	0.185022611
sp|Q1R6U6|YGIB_ECOUT	UPF0441 protein	*ygiB*	outer membrane	1.148782818	0.200106077	0.403807232	0.393825907
tr|Q1R2K0|Q1R2K0_ECOUT	Type 1 fimbriae major subunit FimA	*fimA*	outer membrane	1.217698428	0.284156883	0.507506973	0.294557987
tr|Q1R8L2|Q1R8L2_ECOUT	Alpha-2-macroglobulin	*yfhM*	extracellular space	1.245572315	0.316808784	0.320499999	0.494171967
tr|Q1RD79|Q1RD79_ECOUT	Flagellar basal-body rod protein	*flgG*	outer membrane	1.304408614	0.383395873	0.324757135	0.488441298
sp|Q1R3Q0|LAMB_ECOUT	Maltoporin	*lamB*	outer membrane	1.366544176	0.450532098	0.125376938	0.901782342
tr|Q1RD81|Q1RD81_ECOUT	Flagellar hook protein	*flgE*	outer membrane	1.510549001	0.595072985	0.130688641	0.883762158
tr|Q1RF95|Q1RF95_ECOUT	DNA-binding protein HU-beta, NS1 (HU-1)	*hupB*	extracellular space, cytosol	1.587862307	0.667085813	0.100837375	0.996378469
tr|Q1R2V4|Q1R2V4_ECOUT	Putative F17-like fimbrial subunit	UTI89_C4907	outer membrane	1.73218426	0.792592404	0.097361165	1.011614237
tr|Q1RAL7|Q1RAL7_ECOUT	Flagellin	*fliC*	outer membrane	1.970314662	0.978426049	0.03304911	1.480840229
tr|Q1RDB7|Q1RDB7_ECOUT	Curlin major subunit	*csgA*	outer membrane	6.964677933	2.80005664	0.067618674	1.169933348
tr|Q1RDB8|Q1RDB8_ECOUT	Minor curlin subunit	*csgB*	outer membrane	9.63756597	3.26866883	0.024631056	1.608516969

Appendix C: Biofilm mass spectrometry data. Table lists all detected outer membrane or secreted proteins detected by mass spectrometry, fold change in UTI89 relative to Δ*cydAB,* and *p* value. Data are representative of three biological replicates. See also Chapter 4, Materials and Methods.

REFERENCES

1. Drew GC, Stevens EJ, King KC. 2021. Microbial evolution and transitions along the parasite-mutualist continuum. Nat Rev Microbiol 19:623-638.
2. Armstrong GL, Conn LA, Pinner RW. 1999. Trends in infectious disease mortality in the United States during the 20th century. JAMA 281:61-6.
3. Fredricks DN, Relman DA. 1996. Sequence-based identification of microbial pathogens: a reconsideration of Koch's postulates. Clin Microbiol Rev 9:18-33.
4. Falkow S. 2004. Molecular Koch's postulates applied to bacterial pathogenicity--a personal recollection 15 years later. Nat Rev Microbiol 2:67-72.
5. Falkow S. 1988. Molecular Koch's postulates applied to microbial pathogenicity. Rev Infect Dis 10 Suppl 2:S274-6.
6. Byndloss MX, Baumler AJ. 2018. The germ-organ theory of non-communicable diseases. Nat Rev Microbiol 16:103-110.
7. Banerjee S, Schlaeppi K, van der Heijden MGA. 2018. Keystone taxa as drivers of microbiome structure and functioning. Nat Rev Microbiol 16:567-576.
8. Coyte KZ, Schluter J, Foster KR. 2015. The ecology of the microbiome: Networks, competition, and stability. Science 350:663-6.
9. Gilbert JA, Lynch SV. 2019. Community ecology as a framework for human microbiome research. Nat Med 25:884-889.
10. Foxman B. 2010. The epidemiology of urinary tract infection. Nat Rev Urol 7:653-60.
11. Klein RD, Hultgren SJ. 2020. Urinary tract infections: microbial pathogenesis, host-pathogen interactions and new treatment strategies. Nat Rev Microbiol 18:211-226.
12. Flores-Mireles AL, Walker JN, Caparon M, Hultgren SJ. 2015. Urinary tract infections: epidemiology, mechanisms of infection and treatment options. Nat Rev Microbiol 13:269-84.

13. Sahl JW, Morris CR, Rasko DA. 2013. Chapter 2 - Comparative genomics of pathogenic Escherichia coli, p 21-43. *In* Donnenberg MS (ed), Escherichia coli (Second Edition) doi:https://doi.org/10.1016/B978-0-12-397048-0.00002-4. Academic Press, Boston.

14. Spurbeck RR, Mobley HLT. 2013. Chapter 9 - Uropathogenic Escherichia coli, p 275-304. *In* Donnenberg MS (ed), Escherichia coli (Second Edition) doi:https://doi.org/10.1016/B978-0-12-397048-0.00009-7. Academic Press, Boston.

15. Hagan EC, Lloyd AL, Rasko DA, Faerber GJ, Mobley HL. 2010. Escherichia coli global gene expression in urine from women with urinary tract infection. PLoS Pathog 6:e1001187.

16. Schreiber HL, Conover MS, Chou WC, Hibbing ME, Manson AL, Dodson KW, Hannan TJ, Roberts PL, Stapleton AE, Hooton TM, Livny J, Earl AM, Hultgren SJ. 2017. Bacterial virulence phenotypes of Escherichia coli and host susceptibility determine risk for urinary tract infections. Sci Transl Med 9.

17. Eberly AR, Beebout CJ, Carmen Tong CM, Van Horn GT, Green HD, Fitzgerald MJ, De S, Apple EK, Schrimpe-Rutledge AC, Codreanu SG, Sherrod SD, McLean JA, Clayton DB, Stratton CW, Schmitz JE, Hadjifrangiskou M. 2020. Defining a Molecular Signature for Uropathogenic versus Urocolonizing Escherichia coli: The Status of the Field and New Clinical Opportunities. J Mol Biol 432:786-804.

18. Hooton TM. 2012. Clinical practice. Uncomplicated urinary tract infection. N Engl J Med 366:1028-37.

19. Foxman B. 2014. Urinary tract infection syndromes: occurrence, recurrence, bacteriology, risk factors, and disease burden. Infect Dis Clin North Am 28:1-13.

20. Gupta K, Trautner BW. 2018. Urinary Tract Infections, Pyelonephritis, and Prostatitis. *In* Jameson JL, Fauci AS, Kasper DL, Hauser SL, Longo DL, Loscalzo J (ed), Harrison's Principles of Internal Medicine, 20e. McGraw-Hill Education, New York, NY.

21. Gupta K, Hooton TM, Naber KG, Wullt B, Colgan R, Miller LG, Moran GJ, Nicolle LE, Raz R, Schaeffer AJ, Soper DE, America IDSo, Diseases ESfM, Infectious. 2011. International clinical

practice guidelines for the treatment of acute uncomplicated cystitis and pyelonephritis in women: A 2010 update by the Infectious Diseases Society of America and the European Society for Microbiology and Infectious Diseases. Clin Infect Dis 52:e103-20.

22. Nicolle LE, Gupta K, Bradley SF, Colgan R, DeMuri GP, Drekonja D, Eckert LO, Geerlings SE, Köves B, Hooton TM, Juthani-Mehta M, Knight SL, Saint S, Schaeffer AJ, Trautner B, Wullt B, Siemieniuk R. 2019. Clinical Practice Guideline for the Management of Asymptomatic Bacteriuria: 2019 Update by the Infectious Diseases Society of Americaa. Clin Infect Dis 68:1611-1615.
23. Hooton TM, Roberts PL, Stapleton AE. 2021. Asymptomatic Bacteriuria and Pyuria in Premenopausal Women. Clin Infect Dis 72:1332-1338.
24. Johnson JR, Russo TA. 2018. Acute Pyelonephritis in Adults. N Engl J Med 378:48-59.
25. Lane MC, Alteri CJ, Smith SN, Mobley HL. 2007. Expression of flagella is coincident with uropathogenic Escherichia coli ascension to the upper urinary tract. Proc Natl Acad Sci U S A 104:16669-74.
26. Singer M, Deutschman CS, Seymour CW, Shankar-Hari M, Annane D, Bauer M, Bellomo R, Bernard GR, Chiche JD, Coopersmith CM, Hotchkiss RS, Levy MM, Marshall JC, Martin GS, Opal SM, Rubenfeld GD, van der Poll T, Vincent JL, Angus DC. 2016. The Third International Consensus Definitions for Sepsis and Septic Shock (Sepsis-3). JAMA 315:801-10.
27. Wagenlehner FME, Pilatz A, Weidner W, Naber KG. 2015. Urosepsis: Overview of the Diagnostic and Treatment Challenges. Microbiol Spectr 3.
28. Nicolle LE. 2013. Urinary tract infection. Crit Care Clin 29:699-715.
29. Hooton TM, Roberts PL, Cox ME, Stapleton AE. 2013. Voided midstream urine culture and acute cystitis in premenopausal women. N Engl J Med 369:1883-91.
30. Kolter R. 2021. The History of Microbiology-A Personal Interpretation. Annu Rev Microbiol 75:1-17.
31. Ullmann A. 2011. Escherichia coli and the Emergence of Molecular Biology. EcoSal Plus 4.

32. Ullmann A. 2010. Escherichia coli and the French School of Molecular Biology. EcoSal Plus 4.

33. Gordon DM. 2013. Chapter 1 - The ecology of Escherichia coli, p 3-20. *In* Donnenberg MS (ed), Escherichia coli (Second Edition) doi:https://doi.org/10.1016/B978-0-12-397048-0.00001-2. Academic Press, Boston.

34. Chattopadhyay S, Sokurenko EV. 2013. Chapter 3 - Evolution of pathogenic Escherichia coli, p 45-71. *In* Donnenberg MS (ed), Escherichia coli (Second Edition) doi:https://doi.org/10.1016/B978-0-12-397048-0.00003-6. Academic Press, Boston.

35. Denamur E, Clermont O, Bonacorsi S, Gordon D. 2021. The population genetics of pathogenic Escherichia coli. Nat Rev Microbiol 19:37-54.

36. Touchon M, Hoede C, Tenaillon O, Barbe V, Baeriswyl S, Bidet P, Bingen E, Bonacorsi S, Bouchier C, Bouvet O, Calteau A, Chiapello H, Clermont O, Cruveiller S, Danchin A, Diard M, Dossat C, Karoui ME, Frapy E, Garry L, Ghigo JM, Gilles AM, Johnson J, Le Bouguenec C, Lescat M, Mangenot S, Martinez-Jehanne V, Matic I, Nassif X, Oztas S, Petit MA, Pichon C, Rouy Z, Ruf CS, Schneider D, Tourret J, Vacherie B, Vallenet D, Medigue C, Rocha EP, Denamur E. 2009. Organised genome dynamics in the Escherichia coli species results in highly diverse adaptive paths. PLoS Genet 5:e1000344.

37. Walk ST, Alm EW, Gordon DM, Ram JL, Toranzos GA, Tiedje JM, Whittam TS. 2009. Cryptic lineages of the genus Escherichia. Appl Environ Microbiol 75:6534-44.

38. Mikkelsen H, McMullan R, Filloux A. 2011. The Pseudomonas aeruginosa reference strain PA14 displays increased virulence due to a mutation in ladS. PLoS One 6:e29113.

39. Thurlow LR, Joshi GS, Richardson AR. 2012. Virulence strategies of the dominant USA300 lineage of community-associated methicillin-resistant Staphylococcus aureus (CA-MRSA). FEMS Immunol Med Microbiol 65:5-22.

40. Sarkar S, Hutton ML, Vagenas D, Ruter R, Schuller S, Lyras D, Schembri MA, Totsika M. 2018. Intestinal Colonization Traits of Pandemic Multidrug-Resistant Escherichia coli ST131. J Infect Dis 218:979-990.

41. Alteri CJ, Mobley HL. 2012. Escherichia coli physiology and metabolism dictates adaptation to diverse host microenvironments. Curr Opin Microbiol 15:3-9.

42. Chen SL, Hung CS, Xu J, Reigstad CS, Magrini V, Sabo A, Blasiar D, Bieri T, Meyer RR, Ozersky P, Armstrong JR, Fulton RS, Latreille JP, Spieth J, Hooton TM, Mardis ER, Hultgren SJ, Gordon JI. 2006. Identification of genes subject to positive selection in uropathogenic strains of Escherichia coli: a comparative genomics approach. Proc Natl Acad Sci U S A 103:5977-82.

43. Mysorekar IU, Hultgren SJ. 2006. Mechanisms of uropathogenic Escherichia coli persistence and eradication from the urinary tract. Proc Natl Acad Sci U S A 103:14170-5.

44. Mulvey MA, Schilling JD, Hultgren SJ. 2001. Establishment of a persistent Escherichia coli reservoir during the acute phase of a bladder infection. Infect Immun 69:4572-9.

45. Zhou G, Mo WJ, Sebbel P, Min G, Neubert TA, Glockshuber R, Wu XR, Sun TT, Kong XP. 2001. Uroplakin Ia is the urothelial receptor for uropathogenic Escherichia coli: evidence from in vitro FimH binding. J Cell Sci 114:4095-103.

46. Eto DS, Jones TA, Sundsbak JL, Mulvey MA. 2007. Integrin-mediated host cell invasion by type 1-piliated uropathogenic Escherichia coli. PLoS Pathog 3:e100.

47. Martinez JJ, Mulvey MA, Schilling JD, Pinkner JS, Hultgren SJ. 2000. Type 1 pilus-mediated bacterial invasion of bladder epithelial cells. Embo J 19:2803-12.

48. Mulvey MA, Lopez-Boado YS, Wilson CL, Roth R, Parks WC, Heuser J, Hultgren SJ. 1998. Induction and evasion of host defenses by type 1-piliated uropathogenic Escherichia coli. Science 282:1494-7.

49. Connell I, Agace W, Klemm P, Schembri M, Marild S, Svanborg C. 1996. Type 1 fimbrial expression enhances Escherichia coli virulence for the urinary tract. Proc Natl Acad Sci U S A 93:9827-32.

50. Hultgren SJ, Schwan WR, Schaeffer AJ, Duncan JL. 1986. Regulation of production of type 1 pili among urinary tract isolates of Escherichia coli. Infect Immun 54:613-20.

51. Waksman G, Hultgren SJ. 2009. Structural biology of the chaperone-usher pathway of pilus biogenesis. Nat Rev Microbiol 7:765-74.

52. Hung CS, Bouckaert J, Hung D, Pinkner J, Widberg C, DeFusco A, Auguste CG, Strouse R, Langermann S, Waksman G, Hultgren SJ. 2002. Structural basis of tropism of Escherichia coli to the bladder during urinary tract infection. Mol Microbiol 44:903-15.

53. Kostakioti M, Hadjifrangiskou M, Hultgren SJ. 2013. Bacterial biofilms: development, dispersal, and therapeutic strategies in the dawn of the postantibiotic era. Cold Spring Harb Perspect Med 3:a010306.

54. Floyd KA, Moore JL, Eberly AR, Good JA, Shaffer CL, Zaver H, Almqvist F, Skaar EP, Caprioli RM, Hadjifrangiskou M. 2015. Adhesive fiber stratification in uropathogenic Escherichia coli biofilms unveils oxygen-mediated control of type 1 pili. PLoS Pathog 11:e1004697.

55. Hung C, Zhou Y, Pinkner JS, Dodson KW, Crowley JR, Heuser J, Chapman MR, Hadjifrangiskou M, Henderson JP, Hultgren SJ. 2013. Escherichia coli Biofilms Have an Organized and Complex Extracellular Matrix Structure. MBio 4.

56. Hadjifrangiskou M, Hultgren SJ. 2012. What does it take to stick around? Molecular insights into biofilm formation by uropathogenic Escherichia coli. Virulence 3:231-3.

57. O'Toole G, Kaplan HB, Kolter R. 2000. Biofilm formation as microbial development. Annu Rev Microbiol 54:49-79.

58. Costerton JW. 1999. Introduction to biofilm. Int J Antimicrob Agents 11:217-21; discussion 237-9.

59. Costerton JW, Stewart PS, Greenberg EP. 1999. Bacterial biofilms: a common cause of persistent infections. Science 284:1318-22.

60. Stewart PS, Franklin MJ. 2008. Physiological heterogeneity in biofilms. Nat Rev Microbiol 6:199-210.

61. Flemming HC, Wingender J, Szewzyk U, Steinberg P, Rice SA, Kjelleberg S. 2016. Biofilms: an emergent form of bacterial life. Nat Rev Microbiol 14:563-75.

62. Flemming HC, Wingender J. 2010. The biofilm matrix. Nat Rev Microbiol 8:623-33.

63. Nadell CD, Drescher K, Foster KR. 2016. Spatial structure, cooperation and competition in biofilms. Nat Rev Microbiol 14:589-600.

64. Evans CR, Kempes CP, Price-Whelan A, Dietrich LEP. 2020. Metabolic Heterogeneity and Cross-Feeding in Bacterial Multicellular Systems. Trends Microbiol 28:732-743.

65. Anderson GG, Palermo JJ, Schilling JD, Roth R, Heuser J, Hultgren SJ. 2003. Intracellular bacterial biofilm-like pods in urinary tract infections. Science 301:105-7.

66. Schilling JD, Mulvey MA, Vincent CD, Lorenz RG, Hultgren SJ. 2001. Bacterial invasion augments epithelial cytokine responses to Escherichia coli through a lipopolysaccharide-dependent mechanism. J Immunol 166:1148-55.

67. Dhakal BK, Kulesus RR, Mulvey MA. 2008. Mechanisms and consequences of bladder cell invasion by uropathogenic Escherichia coli. Eur J Clin Invest 38 Suppl 2:2-11.

68. Eto DS, Sundsbak JL, Mulvey MA. 2006. Actin-gated intracellular growth and resurgence of uropathogenic Escherichia coli. Cell Microbiol 8:704-17.

69. Mulvey MA. 2002. Adhesion and entry of uropathogenic Escherichia coli. Cell Microbiol 4:257-71.

70. Thumbikat P, Berry RE, Zhou G, Billips BK, Yaggie RE, Zaichuk T, Sun TT, Schaeffer AJ, Klumpp DJ. 2009. Bacteria-induced uroplakin signaling mediates bladder response to infection. PLoS Pathog 5:e1000415.

71. Abraham SN, Miao Y. 2015. The nature of immune responses to urinary tract infections. Nat Rev Immunol 15:655-63.

72. Song J, Bishop BL, Li G, Grady R, Stapleton A, Abraham SN. 2009. TLR4-mediated expulsion of bacteria from infected bladder epithelial cells. Proc Natl Acad Sci U S A 106:14966-71.

73. Bishop BL, Duncan MJ, Song J, Li G, Zaas D, Abraham SN. 2007. Cyclic AMP-regulated exocytosis of Escherichia coli from infected bladder epithelial cells. Nat Med 13:625-30.

74. Lacerda Mariano L, Ingersoll MA. 2020. The immune response to infection in the bladder. Nat Rev Urol 17:439-458.

75. Hannan TJ, Mysorekar IU, Hung CS, Isaacson-Schmid ML, Hultgren SJ. 2010. Early severe inflammatory responses to uropathogenic E. coli predispose to chronic and recurrent urinary tract infection. PLoS Pathog 6:e1001042.

76. Anderson GG, Dodson KW, Hooton TM, Hultgren SJ. 2004. Intracellular bacterial communities of uropathogenic Escherichia coli in urinary tract pathogenesis. Trends Microbiol 12:424-30.

77. Schwartz DJ, Chen SL, Hultgren SJ, Seed PC. 2011. Population Dynamics and Niche Distribution of Uropathogenic E. coli during Acute and Chronic Urinary Tract Infection. Infect Immun doi:IAI.05339-11 [pii] 10.1128/IAI.05339-11.

78. Hannan TJ, Totsika M, Mansfield KJ, Moore KH, Schembri MA, Hultgren SJ. 2012. Host-pathogen checkpoints and population bottlenecks in persistent and intracellular uropathogenic Escherichia coli bladder infection. FEMS Microbiol Rev 36:616-48.

79. Wright KJ, Seed PC, Hultgren SJ. 2007. Development of intracellular bacterial communities of uropathogenic Escherichia coli depends on type 1 pili. Cell Microbiol 9:2230-41.

80. Justice SS, Hunstad DA, Seed PC, Hultgren SJ. 2006. Filamentation by Escherichia coli subverts innate defenses during urinary tract infection. Proc Natl Acad Sci U S A 103:19884-9.

81. Reigstad CS, Hultgren SJ, Gordon JI. 2007. Functional genomic studies of uropathogenic Escherichia coli and host urothelial cells when intracellular bacterial communities are assembled. J Biol Chem 282:21259-67.

82. Conover MS, Hadjifrangiskou M, Palermo JJ, Hibbing ME, Dodson KW, Hultgren SJ. 2016. Metabolic Requirements of Escherichia coli in Intracellular Bacterial Communities during Urinary Tract Infection Pathogenesis. mBio 7:e00104-16.

83. Hadjifrangiskou M, Gu AP, Pinkner JS, Kostakioti M, Zhang EW, Greene SE, Hultgren SJ. 2012. Transposon mutagenesis identifies uropathogenic Escherichia coli biofilm factors. J Bacteriol 194:6195-205.

84. Fabich AJ, Jones SA, Chowdhury FZ, Cernosek A, Anderson A, Smalley D, McHargue JW, Hightower GA, Smith JT, Autieri SM, Leatham MP, Lins JJ, Allen RL, Laux DC, Cohen PS, Conway T. 2008. Comparison of carbon nutrition for pathogenic and commensal Escherichia coli strains in the mouse intestine. Infect Immun 76:1143-52.

85. Chang DE, Smalley DJ, Tucker DL, Leatham MP, Norris WE, Stevenson SJ, Anderson AB, Grissom JE, Laux DC, Cohen PS, Conway T. 2004. Carbon nutrition of Escherichia coli in the mouse intestine. Proc Natl Acad Sci U S A 101:7427-32.

86. Wang ZJ, Joe BN, Coakley FV, Zaharchuk G, Busse R, Yeh BM. 2008. Urinary oxygen tension measurement in humans using magnetic resonance imaging. Acad Radiol 15:1467-73.

87. Alteri CJ, Smith SN, Mobley HL. 2009. Fitness of Escherichia coli during urinary tract infection requires gluconeogenesis and the TCA cycle. PLoS Pathog 5:e1000448.

88. Hadjifrangiskou M, Kostakioti M, Chen SL, Henderson JP, Greene SE, Hultgren SJ. 2011. A central metabolic circuit controlled by QseC in pathogenic Escherichia coli. Mol Microbiol 80:1516-29.

89. Floyd KA, Mitchell CA, Eberly AR, Colling SJ, Zhang EW, DePas W, Chapman MR, Conover M, Rogers BR, Hultgren SJ, Hadjifrangiskou M. 2016. The UbiI (VisC) Aerobic Ubiquinone Synthase Is Required for Expression of Type 1 Pili, Biofilm Formation, and Pathogenesis in Uropathogenic Escherichia coli. J Bacteriol 198:2662-72.

90. Eberly AR, Floyd KA, Beebout CJ, Colling SJ, Fitzgerald MJ, Stratton CW, Schmitz JE, Hadjifrangiskou M. 2017. Biofilm Formation by Uropathogenic Escherichia coli Is Favored under Oxygen Conditions That Mimic the Bladder Environment. Int J Mol Sci 18.

91. Borisov VB, Verkhovsky MI. 2015. Oxygen as Acceptor. EcoSal Plus 6.

92. Kaila VRI, Wikstrom M. 2021. Architecture of bacterial respiratory chains. Nat Rev Microbiol 19:319-330.

93. Unden G, Bongaerts J. 1997. Alternative respiratory pathways of Escherichia coli: energetics and transcriptional regulation in response to electron acceptors. Biochim Biophys Acta 1320:217-34.

94. Mitchell P, Moyle J. 1967. Chemiosmotic hypothesis of oxidative phosphorylation. Nature 213:137-9.

95. Beebout CJ, Eberly AR, Werby SH, Reasoner SA, Brannon JR, De S, Fitzgerald MJ, Huggins MM, Clayton DB, Cegelski L, Hadjifrangiskou M. 2019. Respiratory Heterogeneity Shapes Biofilm Formation and Host Colonization in Uropathogenic Escherichia coli. MBio 10.

96. Borisov VB, Gennis RB, Hemp J, Verkhovsky MI. 2011. The cytochrome bd respiratory oxygen reductases. Biochim Biophys Acta 1807:1398-413.

97. Morris RL, Schmidt TM. 2013. Shallow breathing: bacterial life at low O(2). Nat Rev Microbiol 11:205-12.

98. Forte E, Borisov VB, Vicente JB, Giuffre A. 2017. Cytochrome bd and Gaseous Ligands in Bacterial Physiology. Adv Microb Physiol 71:171-234.

99. Giuffrè A, Borisov VB, Arese M, Sarti P, Forte E. 2014. Cytochrome bd oxidase and bacterial tolerance to oxidative and nitrosative stress. Biochim Biophys Acta 1837:1178-87.

100. Borisov VB, Forte E, Davletshin A, Mastronicola D, Sarti P, Giuffrè A. 2013. Cytochrome bd oxidase from Escherichia coli displays high catalase activity: an additional defense against oxidative stress. FEBS Lett 587:2214-8.

101. Giuffre A, Borisov VB, Mastronicola D, Sarti P, Forte E. 2012. Cytochrome bd oxidase and nitric oxide: from reaction mechanisms to bacterial physiology. FEBS Lett 586:622-9.

102. Shepherd M, Achard ME, Idris A, Totsika M, Phan MD, Peters KM, Sarkar S, Ribeiro CA, Holyoake LV, Ladakis D, Ulett GC, Sweet MJ, Poole RK, McEwan AG, Schembri MA. 2016. The cytochrome bd-I respiratory oxidase augments survival of multidrug-resistant Escherichia coli during infection. Sci Rep 6:35285.

103. Mason MG, Shepherd M, Nicholls P, Dobbin PS, Dodsworth KS, Poole RK, Cooper CE. 2009. Cytochrome bd confers nitric oxide resistance to Escherichia coli. Nat Chem Biol 5:94-6.

104. Grund TN, Radloff M, Wu D, Goojani HG, Witte LF, Josting W, Buschmann S, Muller H, Elamri I, Welsch S, Schwalbe H, Michel H, Bald D, Safarian S. 2021. Mechanistic and structural diversity between cytochrome bd isoforms of Escherichia coli. Proc Natl Acad Sci U S A 118.

105. Shepherd M, Sanguinetti G, Cook GM, Poole RK. 2010. Compensations for diminished terminal oxidase activity in Escherichia coli: cytochrome bd-II-mediated respiration and glutamate metabolism. J Biol Chem 285:18464-72.

106. Borisov VB, Murali R, Verkhovskaya ML, Bloch DA, Han H, Gennis RB, Verkhovsky MI. 2011. Aerobic respiratory chain of Escherichia coli is not allowed to work in fully uncoupled mode. Proc Natl Acad Sci U S A 108:17320-4.

107. Radloff M, Elamri I, Grund TN, Witte LF, Hohmann KF, Nakagaki S, Goojani HG, Nasiri H, Hideto M, Bald D, Xie H, Sakamoto J, Schwalbe H, Safarian S. 2021. Short-chain aurachin D derivatives are selective inhibitors of E. coli cytochrome bd-I and bd-II oxidases. Sci Rep 11:23852.

108. Chanin RB, Winter MG, Spiga L, Hughes ER, Zhu W, Taylor SJ, Arenales A, Gillis CC, Buttner L, Jimenez AG, Smoot MP, Santos RL, Winter SE. 2020. Epithelial-Derived Reactive Oxygen Species Enable AppBCX-Mediated Aerobic Respiration of Escherichia coli during Intestinal Inflammation. Cell Host Microbe 28:780-788 e5.

109. Chandel NS. 2021. Metabolism of Proliferating Cells. Cold Spring Harb Perspect Biol 13.

110. Steinert EM, Vasan K, Chandel NS. 2021. Mitochondrial Metabolism Regulation of T Cell-Mediated Immunity. Annu Rev Immunol 39:395-416.

111. Singer BD, Chandel NS. 2019. Immunometabolism of pro-repair cells. J Clin Invest 129:2597-2607.

112. Mehta MM, Weinberg SE, Chandel NS. 2017. Mitochondrial control of immunity: beyond ATP. Nat Rev Immunol 17:608-620.

113. Makowski L, Chaib M, Rathmell JC. 2020. Immunometabolism: From basic mechanisms to translation. Immunol Rev 295:5-14.

114. Siska PJ, Rathmell JC. 2015. T cell metabolic fitness in antitumor immunity. Trends Immunol 36:257-64.

115. MacIver NJ, Michalek RD, Rathmell JC. 2013. Metabolic regulation of T lymphocytes. Annu Rev Immunol 31:259-83.

116. Reinfeld BI, Rathmell WK, Kim TK, Rathmell JC. 2022. The therapeutic implications of immunosuppressive tumor aerobic glycolysis. Cell Mol Immunol 19:46-58.

117. Bader JE, Voss K, Rathmell JC. 2020. Targeting Metabolism to Improve the Tumor Microenvironment for Cancer Immunotherapy. Mol Cell 78:1019-1033.

118. Vlamakis H, Aguilar C, Losick R, Kolter R. 2008. Control of cell fate by the formation of an architecturally complex bacterial community. Genes Dev 22:945-53.

119. van Gestel J, Vlamakis H, Kolter R. 2015. Division of Labor in Biofilms: the Ecology of Cell Differentiation. Microbiol Spectr 3:MB-0002-2014.

120. Dragoš A, Kiesewalter H, Martin M, Hsu CY, Hartmann R, Wechsler T, Eriksen C, Brix S, Drescher K, Stanley-Wall N, Kümmerli R, Kovács Á. 2018. Division of Labor during Biofilm Matrix Production. Curr Biol 28:1903-1913.e5.

121. Dietrich LE, Okegbe C, Price-Whelan A, Sakhtah H, Hunter RC, Newman DK. 2013. Bacterial community morphogenesis is intimately linked to the intracellular redox state. J Bacteriol 195:1371-80.

122. DePas WH, Hufnagel DA, Lee JS, Blanco LP, Bernstein HC, Fisher ST, James GA, Stewart PS, Chapman MR. 2013. Iron induces bimodal population development by Escherichia coli. Proc Natl Acad Sci U S A 110:2629-34.

123. Jo J, Cortez KL, Cornell WC, Price-Whelan A, Dietrich LE. 2017. An orphan cbb3-type cytochrome oxidase subunit supports Pseudomonas aeruginosa biofilm growth and virulence. Elife 6.

124. Cegelski L, Pinkner JS, Hammer ND, Cusumano CK, Hung CS, Chorell E, Aberg V, Walker JN, Seed PC, Almqvist F, Chapman MR, Hultgren SJ. 2009. Small-molecule inhibitors target Escherichia coli amyloid biogenesis and biofilm formation. Nat Chem Biol 5:913-9.

125. Rapsinski GJ, Wynosky-Dolfi MA, Oppong GO, Tursi SA, Wilson RP, Brodsky IE, Tükel Ç. 2015. Toll-like receptor 2 and NLRP3 cooperate to recognize a functional bacterial amyloid, curli. Infect Immun 83:693-701.

126. Jurcisek JA, Brockman KL, Novotny LA, Goodman SD, Bakaletz LO. 2017. Nontypeable. Proc Natl Acad Sci U S A 114:E6632-E6641.

127. Klauck G, Serra DO, Possling A, Hengge R. 2018. Spatial organization of different sigma factor activities and c-di-GMP signalling within the three-dimensional landscape of a bacterial biofilm. Open Biol 8.

128. Serra DO, Klauck G, Hengge R. 2015. Vertical stratification of matrix production is essential for physical integrity and architecture of macrocolony biofilms of Escherichia coli. Environ Microbiol 17:5073-88.

129. Serra DO, Richter AM, Hengge R. 2013. Cellulose as an architectural element in spatially structured Escherichia coli biofilms. J Bacteriol 195:5540-54.

130. Lin YC, Sekedat MD, Cornell WC, Silva GM, Okegbe C, Price-Whelan A, Vogel C, Dietrich LEP. 2018. Phenazines regulate Nap-dependent denitrification in. J Bacteriol doi:10.1128/JB.00031-18.

131. McCrate OA, Zhou X, Reichhardt C, Cegelski L. 2013. Sum of the parts: composition and architecture of the bacterial extracellular matrix. J Mol Biol 425:4286-94.

132. Thongsomboon W, Serra DO, Possling A, Hadjineophytou C, Hengge R, Cegelski L. 2018. Phosphoethanolamine cellulose: A naturally produced chemically modified cellulose. Science 359:334-338.

133. Hufnagel DA, Depas WH, Chapman MR. 2015. The Biology of the Escherichia coli Extracellular Matrix. Microbiol Spectr 3.

134. Hobley L, Ostrowski A, Rao FV, Bromley KM, Porter M, Prescott AR, MacPhee CE, van Aalten DM, Stanley-Wall NR. 2013. BslA is a self-assembling bacterial hydrophobin that coats the Bacillus subtilis biofilm. Proc Natl Acad Sci U S A 110:13600-5.

135. Asally M, Kittisopikul M, Rué P, Du Y, Hu Z, Çağatay T, Robinson AB, Lu H, Garcia-Ojalvo J, Süel GM. 2012. Localized cell death focuses mechanical forces during 3D patterning in a biofilm. Proc Natl Acad Sci U S A 109:18891-6.

136. Cutruzzolà F, Frankenberg-Dinkel N. 2016. Origin and Impact of Nitric Oxide in Pseudomonas aeruginosa Biofilms. J Bacteriol 198:55-65.

137. Lindqvist A, Membrillo-Hernańdez J, Poole RK, Cook GM. 2000. Roles of respiratory oxidases in protecting Escherichia coli K12 from oxidative stress. Antonie Van Leeuwenhoek 78:23-31.

138. Taniguchi Y, Choi PJ, Li GW, Chen H, Babu M, Hearn J, Emili A, Xie XS. 2010. Quantifying E. coli proteome and transcriptome with single-molecule sensitivity in single cells. Science 329:533-8.

139. Silander OK, Nikolic N, Zaslaver A, Bren A, Kikoin I, Alon U, Ackermann M. 2012. A genome-wide analysis of promoter-mediated phenotypic noise in Escherichia coli. PLoS Genet 8:e1002443.

140. Huh D, Paulsson J. 2011. Non-genetic heterogeneity from stochastic partitioning at cell division. Nat Genet 43:95-100.

141. Barraud N, Schleheck D, Klebensberger J, Webb JS, Hassett DJ, Rice SA, Kjelleberg S. 2009. Nitric oxide signaling in Pseudomonas aeruginosa biofilms mediates phosphodiesterase activity, decreased cyclic di-GMP levels, and enhanced dispersal. J Bacteriol 191:7333-42.

142. Hengge R. 2009. Principles of c-di-GMP signalling in bacteria. Nat Rev Microbiol 7:263-73.

143. Murphy KC, Campellone KG. 2003. Lambda Red-mediated recombinogenic engineering of enterohemorrhagic and enteropathogenic E. coli. BMC Mol Biol 4:11.

144. Shaffer CL, Zhang EW, Dudley AG, Dixon BR, Guckes KR, Breland EJ, Floyd KA, Casella DP, Algood HM, Clayton DB, Hadjifrangiskou M. 2017. Purine Biosynthesis Metabolically Constrains Intracellular Survival of Uropathogenic Escherichia coli. Infect Immun 85.

145. Pfaffl MW. 2001. A new mathematical model for relative quantification in real-time RT-PCR. Nucleic Acids Res 29:e45.

146. Almeida C, Azevedo NF, Santos S, Keevil CW, Vieira MJ. 2011. Discriminating multi-species populations in biofilms with peptide nucleic acid fluorescence in situ hybridization (PNA FISH). PLoS One 6:e14786.

147. Okegbe C, Fields BL, Cole SJ, Beierschmitt C, Morgan CJ, Price-Whelan A, Stewart RC, Lee VT, Dietrich LEP. 2017. Electron-shuttling antibiotics structure bacterial communities by modulating cellular levels of c-di-GMP. Proc Natl Acad Sci U S A 114:E5236-E5245.

148. Hung CS, Dodson KW, Hultgren SJ. 2009. A murine model of urinary tract infection. Nat Protoc 4:1230-43.

149. Beebout CJ, Sominsky LA, Eberly AR, Van Horn GT, Hadjifrangiskou M. 2021. Cytochrome bd promotes Escherichia coli biofilm antibiotic tolerance by regulating accumulation of noxious chemicals. NPJ Biofilms Microbiomes 7:35.

150. Haugan MS, Charbon G, Frimodt-Møller N, Løbner-Olesen A. 2018. Chromosome replication as a measure of bacterial growth rate during Escherichia coli infection in the mouse peritonitis model. Sci Rep 8:14961.

151. Mogi T, Akimoto S, Endou S, Watanabe-Nakayama T, Mizuochi-Asai E, Miyoshi H. 2006. Probing the ubiquinol-binding site in cytochrome bd by site-directed mutagenesis. Biochemistry 45:7924-30.

152. Safarian S, Hahn A, Mills DJ, Radloff M, Eisinger ML, Nikolaev A, Meier-Credo J, Melin F, Miyoshi H, Gennis RB, Sakamoto J, Langer JD, Hellwig P, Kuhlbrandt W, Michel H. 2019. Active site rearrangement and structural divergence in prokaryotic respiratory oxidases. Science 366:100-104.

153. Friedrich T, van Heek P, Leif H, Ohnishi T, Forche E, Kunze B, Jansen R, Trowitzsch-Kienast W, Höfle G, Reichenbach H. 1994. Two binding sites of inhibitors in NADH: ubiquinone oxidoreductase (complex I). Relationship of one site with the ubiquinone-binding site of bacterial glucose:ubiquinone oxidoreductase. Eur J Biochem 219:691-8.

154. Degli Esposti M. 1998. Inhibitors of NADH-ubiquinone reductase: an overview. Biochim Biophys Acta 1364:222-35.

155. Yao CH, Wang R, Wang Y, Kung CP, Weber JD, Patti GJ. 2019. Mitochondrial fusion supports increased oxidative phosphorylation during cell proliferation. Elife 8.

156. Tiku V, Tan MW, Dikic I. 2020. Mitochondrial Functions in Infection and Immunity. Trends Cell Biol 30:263-275.

157. Marchi S, Morroni G, Pinton P, Galluzzi L. 2021. Control of host mitochondria by bacterial pathogens. Trends Microbiol doi:10.1016/j.tim.2021.09.010.

158. Krab K, Kempe H, Wikström M. 2011. Explaining the enigmatic K(M) for oxygen in cytochrome c oxidase: a kinetic model. Biochim Biophys Acta 1807:348-58.

159. Vander Heiden MG, Plas DR, Rathmell JC, Fox CJ, Harris MH, Thompson CB. 2001. Growth factors can influence cell growth and survival through effects on glucose metabolism. Mol Cell Biol 21:5899-912.

160. Rathmell JC, Fox CJ, Plas DR, Hammerman PS, Cinalli RM, Thompson CB. 2003. Akt-directed glucose metabolism can prevent Bax conformation change and promote growth factor-independent survival. Mol Cell Biol 23:7315-28.

161. Hoxhaj G, Manning BD. 2020. The PI3K-AKT network at the interface of oncogenic signalling and cancer metabolism. Nat Rev Cancer 20:74-88.

162. Lin AE, Beasley FC, Olson J, Keller N, Shalwitz RA, Hannan TJ, Hultgren SJ, Nizet V. 2015. Role of Hypoxia Inducible Factor-1α (HIF-1α) in Innate Defense against Uropathogenic Escherichia coli Infection. PLoS Pathog 11:e1004818.

163. Lopatkin AJ, Bening SC, Manson AL, Stokes JM, Kohanski MA, Badran AH, Earl AM, Cheney NJ, Yang JH, Collins JJ. 2021. Clinically relevant mutations in core metabolic genes confer antibiotic resistance. Science 371.

164. Stokes JM, Lopatkin AJ, Lobritz MA, Collins JJ. 2019. Bacterial Metabolism and Antibiotic Efficacy. Cell Metab 30:251-259.

165. Kohanski MA, Dwyer DJ, Collins JJ. 2010. How antibiotics kill bacteria: from targets to networks. Nat Rev Microbiol 8:423-35.

166. Cook GM, Greening C, Hards K, Berney M. 2014. Energetics of pathogenic bacteria and opportunities for drug development. Adv Microb Physiol 65:1-62.

167. Mogi T, Ui H, Shiomi K, Omura S, Miyoshi H, Kita K. 2009. Antibiotics LL-Z1272 identified as novel inhibitors discriminating bacterial and mitochondrial quinol oxidases. Biochim Biophys Acta 1787:129-33.

168. Lee BS, Hards K, Engelhart CA, Hasenoehrl EJ, Kalia NP, Mackenzie JS, Sviriaeva E, Chong SMS, Manimekalai MSS, Koh VH, Chan J, Xu J, Alonso S, Miller MJ, Steyn AJC, Grüber G, Schnappinger D, Berney M, Cook GM, Moraski GC, Pethe K. 2020. Dual inhibition of the terminal oxidases eradicates antibiotic-tolerant Mycobacterium tuberculosis. EMBO Mol Med doi:10.15252/emmm.202013207:e13207.

169. Bajeli S, Baid N, Kaur M, Pawar GP, Chaudhari VD, Kumar A. 2020. Terminal Respiratory Oxidases: A Targetables Vulnerability of Mycobacterial Bioenergetics? Front Cell Infect Microbiol 10:589318.

170. Lenherr SM, Clemens JQ, Braffett BH, Cleary PA, Dunn RL, Hotaling JM, Jacobson AM, Kim C, Herman W, Brown JS, Wessells H, Sarma AV, Group DER. 2016. Glycemic Control and Urinary Tract Infections in Women with Type 1 Diabetes: Results from the DCCT/EDIC. J Urol 196:1129-35.

171. Geerlings S, Fonseca V, Castro-Diaz D, List J, Parikh S. 2014. Genital and urinary tract infections in diabetes: impact of pharmacologically-induced glucosuria. Diabetes Res Clin Pract 103:373-81.

172. Puckrin R, Saltiel MP, Reynier P, Azoulay L, Yu OHY, Filion KB. 2018. SGLT-2 inhibitors and the risk of infections: a systematic review and meta-analysis of randomized controlled trials. Acta Diabetol 55:503-514.

173. Zaccardi F, Webb DR, Htike ZZ, Youssef D, Khunti K, Davies MJ. 2016. Efficacy and safety of sodium-glucose co-transporter-2 inhibitors in type 2 diabetes mellitus: systematic review and network meta-analysis. Diabetes Obes Metab 18:783-94.

174. Hartmann R, Jeckel H, Jelli E, Singh PK, Vaidya S, Bayer M, Rode DKH, Vidakovic L, Díaz-Pascual F, Fong JCN, Dragoš A, Lamprecht O, Thöming JG, Netter N, Häussler S, Nadell CD, Sourjik V, Kovács Á, Yildiz FH, Drescher K. 2021. Quantitative image analysis of microbial communities with BiofilmQ. Nat Microbiol 6:151-156.

175. Brannon JR, Dunigan TL, Beebout CJ, Ross T, Wiebe MA, Reynolds WS, Hadjifrangiskou M. 2020. Invasion of vaginal epithelial cells by uropathogenic Escherichia coli. Nat Commun 11:2803.

176. Pinkner JS, Remaut H, Buelens F, Miller E, Aberg V, Pemberton N, Hedenstrom M, Larsson A, Seed P, Waksman G, Hultgren SJ, Almqvist F. 2006. Rationally designed small compounds inhibit pilus biogenesis in uropathogenic bacteria. Proc Natl Acad Sci U S A 103:17897-902.

177. Leaver-Fay A, Tyka M, Lewis SM, Lange OF, Thompson J, Jacak R, Kaufman K, Renfrew PD, Smith CA, Sheffler W, Davis IW, Cooper S, Treuille A, Mandell DJ, Richter F, Ban YE, Fleishman SJ, Corn JE, Kim DE, Lyskov S, Berrondo M, Mentzer S, Popovic Z, Havranek JJ, Karanicolas J, Das R, Meiler J, Kortemme T, Gray JJ, Kuhlman B, Baker D, Bradley P. 2011. ROSETTA3: an object-oriented software suite for the simulation and design of macromolecules. Methods Enzymol 487:545-74.

178. Song Y, DiMaio F, Wang RY, Kim D, Miles C, Brunette T, Thompson J, Baker D. 2013. High-resolution comparative modeling with RosettaCM. Structure 21:1735-42.

179. Thesseling A, Rasmussen T, Burschel S, Wohlwend D, Kagi J, Muller R, Bottcher B, Friedrich T. 2019. Homologous bd oxidases share the same architecture but differ in mechanism. Nat Commun 10:5138.

180. Alford RF, Koehler Leman J, Weitzner BD, Duran AM, Tilley DC, Elazar A, Gray JJ. 2015. An Integrated Framework Advancing Membrane Protein Modeling and Design. PLoS Comput Biol 11:e1004398.

181. Koehler Leman J, Mueller BK, Gray JJ. 2017. Expanding the toolkit for membrane protein modeling in Rosetta. Bioinformatics 33:754-756.

182. Ashkenazy H, Abadi S, Martz E, Chay O, Mayrose I, Pupko T, Ben-Tal N. 2016. ConSurf 2016: an improved methodology to estimate and visualize evolutionary conservation in macromolecules. Nucleic Acids Res 44:W344-50.

183. Landau M, Mayrose I, Rosenberg Y, Glaser F, Martz E, Pupko T, Ben-Tal N. 2005. ConSurf 2005: the projection of evolutionary conservation scores of residues on protein structures. Nucleic Acids Res 33:W299-302.

184. Glaser F, Pupko T, Paz I, Bell RE, Bechor-Shental D, Martz E, Ben-Tal N. 2003. ConSurf: identification of functional regions in proteins by surface-mapping of phylogenetic information. Bioinformatics 19:163-4.

185. Park H, Bradley P, Greisen P, Jr., Liu Y, Mulligan VK, Kim DE, Baker D, DiMaio F. 2016. Simultaneous Optimization of Biomolecular Energy Functions on Features from Small Molecules and Macromolecules. J Chem Theory Comput 12:6201-6212.

186. Frenz B, Lewis SM, King I, DiMaio F, Park H, Song Y. 2020. Prediction of Protein Mutational Free Energy: Benchmark and Sampling Improvements Increase Classification Accuracy. Front Bioeng Biotechnol 8:558247.

187. Conway P, Tyka MD, DiMaio F, Konerding DE, Baker D. 2014. Relaxation of backbone bond geometry improves protein energy landscape modeling. Protein Sci 23:47-55.

188. Khatib F, Cooper S, Tyka MD, Xu K, Makedon I, Popovic Z, Baker D, Players F. 2011. Algorithm discovery by protein folding game players. Proc Natl Acad Sci U S A 108:18949-53.

189. Nivon LG, Moretti R, Baker D. 2013. A Pareto-optimal refinement method for protein design scaffolds. PLoS One 8:e59004.

190. Tyka MD, Keedy DA, Andre I, Dimaio F, Song Y, Richardson DC, Richardson JS, Baker D. 2011. Alternate states of proteins revealed by detailed energy landscape mapping. J Mol Biol 405:607-18.

191. Voss K, Hong HS, Bader JE, Sugiura A, Lyssiotis CA, Rathmell JC. 2021. A guide to interrogating immunometabolism. Nat Rev Immunol doi:10.1038/s41577-021-00529-8.

192. Dwyer DJ, Belenky PA, Yang JH, MacDonald IC, Martell JD, Takahashi N, Chan CT, Lobritz MA, Braff D, Schwarz EG, Ye JD, Pati M, Vercruysse M, Ralifo PS, Allison KR, Khalil AS, Ting AY, Walker GC, Collins JJ. 2014. Antibiotics induce redox-related physiological alterations as part of their lethality. Proc Natl Acad Sci U S A 111:E2100-9.

193. Rasmussen ML, Taneja N, Neininger AC, Wang L, Robertson GL, Riffle SN, Shi L, Knollmann BC, Burnette DT, Gama V. 2020. MCL-1 Inhibition by Selective BH3 Mimetics Disrupts Mitochondrial Dynamics Causing Loss of Viability and Functionality of Human Cardiomyocytes. iScience 23:101015.

194. Subramanian A, Tamayo P, Mootha VK, Mukherjee S, Ebert BL, Gillette MA, Paulovich A, Pomeroy SL, Golub TR, Lander ES, Mesirov JP. 2005. Gene set enrichment analysis: a knowledge-based approach for interpreting genome-wide expression profiles. Proc Natl Acad Sci U S A 102:15545-50.

195. Hall-Stoodley L, Costerton JW, Stoodley P. 2004. Bacterial biofilms: from the natural environment to infectious diseases. Nat Rev Microbiol 2:95-108.

196. Donlan RM, Costerton JW. 2002. Biofilms: survival mechanisms of clinically relevant microorganisms. Clin Microbiol Rev 15:167-93.

197. Vidakovic L, Singh PK, Hartmann R, Nadell CD, Drescher K. 2018. Dynamic biofilm architecture confers individual and collective mechanisms of viral protection. Nat Microbiol 3:26-31.

198. Flemming HC, Wuertz S. 2019. Bacteria and archaea on Earth and their abundance in biofilms. Nat Rev Microbiol 17:247-260.

199. Mermel LA, Allon M, Bouza E, Craven DE, Flynn P, O'Grady NP, Raad II, Rijnders BJ, Sherertz RJ, Warren DK. 2009. Clinical practice guidelines for the diagnosis and management of intravascular catheter-related infection: 2009 Update by the Infectious Diseases Society of America. Clin Infect Dis 49:1-45.

200. Cotter PA, Melville SB, Albrecht JA, Gunsalus RP. 1997. Aerobic regulation of cytochrome d oxidase (cydAB) operon expression in Escherichia coli: roles of Fnr and ArcA in repression and activation. Mol Microbiol 25:605-15.

201. Cotter PA, Gunsalus RP. 1992. Contribution of the fnr and arcA gene products in coordinate regulation of cytochrome o and d oxidase (cyoABCDE and cydAB) genes in Escherichia coli. FEMS Microbiol Lett 70:31-6.

202. Cotter PA, Chepuri V, Gennis RB, Gunsalus RP. 1990. Cytochrome o (cyoABCDE) and d (cydAB) oxidase gene expression in Escherichia coli is regulated by oxygen, pH, and the fnr gene product. J Bacteriol 172:6333-8.

203. Stewart PS, Parker AE. 2019. Measuring Antimicrobial Efficacy against Biofilms: a Meta-analysis. Antimicrob Agents Chemother 63.

204. O'Toole GA, Pratt LA, Watnick PI, Newman DK, Weaver VB, Kolter R. 1999. Genetic approaches to study of biofilms. Methods Enzymol 310:91-109.

205. Kragh KN, Alhede M, Kvich L, Bjarnsholt T. 2019. Into the well—A close look at the complex structures of a microtiter biofilm and the crystal violet assay. Biofilm 1.

206. Schiessl KT, Hu F, Jo J, Nazia SZ, Wang B, Price-Whelan A, Min W, Dietrich LEP. 2019. Phenazine production promotes antibiotic tolerance and metabolic heterogeneity in Pseudomonas aeruginosa biofilms. Nat Commun 10:762.

207. Goneau LW, Yeoh NS, MacDonald KW, Cadieux PA, Burton JP, Razvi H, Reid G. 2014. Selective target inactivation rather than global metabolic dormancy causes antibiotic tolerance in uropathogens. Antimicrob Agents Chemother 58:2089-97.

208. CLSI. Performance Standards for Antimicrobial Susceptibility Testing. 30th ed. CLSI supplement M100. Wayne, PA: Clinical and Laboratory Standards Instititute; 2020.

209. Gupta K, Hooton TM, Naber KG, Wullt B, Colgan R, Miller LG, Moran GJ, Nicolle LE, Raz R, Schaeffer AJ, Soper DE, America IDSo, Diseases ESfMaI. 2011. International clinical practice guidelines for the treatment of acute uncomplicated cystitis and pyelonephritis in women: A 2010 update by the Infectious Diseases Society of America and the European Society for Microbiology and Infectious Diseases. Clin Infect Dis 52:e103-20.

210. Mironov A, Seregina T, Shatalin K, Nagornykh M, Shakulov R, Nudler E. 2020. CydDC functions as a cytoplasmic cystine reductase to sensitize. Proc Natl Acad Sci U S A doi:10.1073/pnas.2007817117.

211. Vadyvaloo V, Arous S, Gravesen A, Héchard Y, Chauhan-Haubrock R, Hastings JW, Rautenbach M. 2004. Cell-surface alterations in class IIa bacteriocin-resistant Listeria monocytogenes strains. Microbiology (Reading) 150:3025-3033.

212. Nikaido H. 2003. Molecular basis of bacterial outer membrane permeability revisited. Microbiol Mol Biol Rev 67:593-656.

213. Delcour AH. 2009. Outer membrane permeability and antibiotic resistance. Biochim Biophys Acta 1794:808-16.

214. Nikaido H, Pagès JM. 2012. Broad-specificity efflux pumps and their role in multidrug resistance of Gram-negative bacteria. FEMS Microbiol Rev 36:340-63.

215. Schembri MA, Kjaergaard K, Klemm P. 2003. Global gene expression in Escherichia coli biofilms. Mol Microbiol 48:253-67.

216. Bhattacharyya S, Walker DM, Harshey RM. 2020. Dead cells release a 'necrosignal' that activates antibiotic survival pathways in bacterial swarms. Nat Commun 11:4157.

217. Paixão L, Rodrigues L, Couto I, Martins M, Fernandes P, de Carvalho CC, Monteiro GA, Sansonetty F, Amaral L, Viveiros M. 2009. Fluorometric determination of ethidium bromide efflux kinetics in Escherichia coli. J Biol Eng 3:18.

218. Du D, Wang-Kan X, Neuberger A, van Veen HW, Pos KM, Piddock LJV, Luisi BF. 2018. Multidrug efflux pumps: structure, function and regulation. Nat Rev Microbiol 16:523-539.

219. Sielaff H, Duncan TM, Börsch M. 2018. The regulatory subunit ε in Escherichia coli F. Biochim Biophys Acta Bioenerg 1859:775-788.

220. Pagès JM, James CE, Winterhalter M. 2008. The porin and the permeating antibiotic: a selective diffusion barrier in Gram-negative bacteria. Nat Rev Microbiol 6:893-903.

221. Proctor RA, von Eiff C, Kahl BC, Becker K, McNamara P, Herrmann M, Peters G. 2006. Small colony variants: a pathogenic form of bacteria that facilitates persistent and recurrent infections. Nat Rev Microbiol 4:295-305.

222. Conradie F, Diacon AH, Ngubane N, Howell P, Everitt D, Crook AM, Mendel CM, Egizi E, Moreira J, Timm J, McHugh TD, Wills GH, Bateson A, Hunt R, Van Niekerk C, Li M, Olugbosi M, Spigelman M, Team N-TT. 2020. Treatment of Highly Drug-Resistant Pulmonary Tuberculosis. N Engl J Med 382:893-902.

223. de Jager VR, Dawson R, van Niekerk C, Hutchings J, Kim J, Vanker N, van der Merwe L, Choi J, Nam K, Diacon AH. 2020. Telacebec (Q203), a New Antituberculosis Agent. N Engl J Med 382:1280-1281.

224. Wiegand I, Hilpert K, Hancock RE. 2008. Agar and broth dilution methods to determine the minimal inhibitory concentration (MIC) of antimicrobial substances. Nat Protoc 3:163-75.

225. Cox J, Hein MY, Luber CA, Paron I, Nagaraj N, Mann M. 2014. Accurate proteome-wide label-free quantification by delayed normalization and maximal peptide ratio extraction, termed MaxLFQ. Mol Cell Proteomics 13:2513-26.

226. Wieczorek S, Combes F, Lazar C, Giai Gianetto Q, Gatto L, Dorffer A, Hesse AM, Couté Y, Ferro M, Bruley C, Burger T. 2017. DAPAR & ProStaR: software to perform statistical analyses in quantitative discovery proteomics. Bioinformatics 33:135-136.

227. Keseler IM, Mackie A, Santos-Zavaleta A, Billington R, Bonavides-Martínez C, Caspi R, Fulcher C, Gama-Castro S, Kothari A, Krummenacker M, Latendresse M, Muñiz-Rascado L, Ong Q, Paley S, Peralta-Gil M, Subhraveti P, Velázquez-Ramírez DA, Weaver D, Collado-Vides J, Paulsen I, Karp PD. 2017. The EcoCyc database: reflecting new knowledge about Escherichia coli K-12. Nucleic Acids Res 45:D543-D550.

228. Consortium U. 2019. UniProt: a worldwide hub of protein knowledge. Nucleic Acids Res 47:D506-D515.

229. Semenza GL. 2003. Targeting HIF-1 for cancer therapy. Nat Rev Cancer 3:721-32.

230. Semenza GL. 2007. Hypoxia-inducible factor 1 (HIF-1) pathway. Sci STKE 2007:cm8.

231. Semenza GL. 2001. HIF-1 and mechanisms of hypoxia sensing. Curr Opin Cell Biol 13:167-71.

232. Semenza GL. 1999. Regulation of mammalian O2 homeostasis by hypoxia-inducible factor 1. Annu Rev Cell Dev Biol 15:551-78.

233. Epstein AC, Gleadle JM, McNeill LA, Hewitson KS, O'Rourke J, Mole DR, Mukherji M, Metzen E, Wilson MI, Dhanda A, Tian YM, Masson N, Hamilton DL, Jaakkola P, Barstead R, Hodgkin J, Maxwell PH, Pugh CW, Schofield CJ, Ratcliffe PJ. 2001. C. elegans EGL-9 and mammalian homologs define a family of dioxygenases that regulate HIF by prolyl hydroxylation. Cell 107:43-54.

234. Weidemann A, Johnson RS. 2008. Biology of HIF-1alpha. Cell Death Differ 15:621-7.

235. Rius J, Guma M, Schachtrup C, Akassoglou K, Zinkernagel AS, Nizet V, Johnson RS, Haddad GG, Karin M. 2008. NF-kappaB links innate immunity to the hypoxic response through transcriptional regulation of HIF-1alpha. Nature 453:807-11.

236. Hayes BW, Abraham SN. 2016. Innate Immune Responses to Bladder Infection. Microbiol Spectr 4.

237. D'Ignazio L, Bandarra D, Rocha S. 2016. NF-kappaB and HIF crosstalk in immune responses. FEBS J 283:413-24.

238. Ablasser A, Goldeck M, Cavlar T, Deimling T, Witte G, Rohl I, Hopfner KP, Ludwig J, Hornung V. 2013. cGAS produces a 2'-5'-linked cyclic dinucleotide second messenger that activates STING. Nature 498:380-4.

239. Hopfner KP, Hornung V. 2020. Molecular mechanisms and cellular functions of cGAS-STING signalling. Nat Rev Mol Cell Biol 21:501-521.

240. Eaglesham JB, Kranzusch PJ. 2020. Conserved strategies for pathogen evasion of cGAS-STING immunity. Curr Opin Immunol 66:27-34.

241. Gomes MTR, Guimaraes ES, Marinho FV, Macedo I, Aguiar E, Barber GN, Moraes-Vieira PMM, Alves-Filho JC, Oliveira SC. 2021. STING regulates metabolic reprogramming in macrophages via HIF-1alpha during Brucella infection. PLoS Pathog 17:e1009597.

242. Serra DO, Richter AM, Klauck G, Mika F, Hengge R. 2013. Microanatomy at cellular resolution and spatial order of physiological differentiation in a bacterial biofilm. MBio 4:e00103-13.

243. Hung C, Zhou Y, Pinkner JS, Dodson KW, Crowley JR, Heuser J, Chapman MR, Hadjifrangiskou M, Henderson JP, Hultgren SJ. 2013. Escherichia coli biofilms have an organized and complex extracellular matrix structure. MBio 4:e00645-13.

244. Arnaouteli S, Ferreira AS, Schor M, Morris RJ, Bromley KM, Jo J, Cortez KL, Sukhodub T, Prescott AR, Dietrich LEP, MacPhee CE, Stanley-Wall NR. 2017. Bifunctionality of a biofilm matrix protein controlled by redox state. Proc Natl Acad Sci U S A 114:E6184-E6191.

245. Mashruwala AA, Guchte AV, Boyd JM. 2017. Impaired respiration elicits SrrAB-dependent programmed cell lysis and biofilm formation in. Elife 6.

246. Serra DO, Hengge R. 2019. A c-di-GMP-Based Switch Controls Local Heterogeneity of Extracellular Matrix Synthesis which Is Crucial for Integrity and Morphogenesis of Escherichia coli Macrocolony Biofilms. J Mol Biol doi:10.1016/j.jmb.2019.04.001.

247. Georgellis D, Kwon O, Lin EC. 2001. Quinones as the redox signal for the arc two-component system of bacteria. Science 292:2314-6.

248. Peña-Sandoval GR, Georgellis D. 2010. The ArcB sensor kinase of Escherichia coli autophosphorylates by an intramolecular reaction. J Bacteriol 192:1735-9.

249. Malpica R, Franco B, Rodriguez C, Kwon O, Georgellis D. 2004. Identification of a quinone-sensitive redox switch in the ArcB sensor kinase. Proc Natl Acad Sci U S A 101:13318-23.

250. Mika F, Hengge R. 2005. A two-component phosphotransfer network involving ArcB, ArcA, and RssB coordinates synthesis and proteolysis of sigmaS (RpoS) in E. coli. Genes Dev 19:2770-81.

251. Dorich V, Brugger C, Tripathi A, Hoskins JR, Tong S, Suhanovsky MM, Sastry A, Wickner S, Gottesman S, Deaconescu AM. 2019. Structural basis for inhibition of a response regulator of σ S stability by a ClpXP antiadaptor. Genes Dev 33:718-732.

252. Battesti A, Hoskins JR, Tong S, Milanesio P, Mann JM, Kravats A, Tsegaye YM, Bougdour A, Wickner S, Gottesman S. 2013. Anti-adaptors provide multiple modes for regulation of the RssB adaptor protein. Genes Dev 27:2722-35.

253. Battesti A, Majdalani N, Gottesman S. 2011. The RpoS-mediated general stress response in Escherichia coli. Annu Rev Microbiol 65:189-213.

254. Pesavento C, Becker G, Sommerfeldt N, Possling A, Tschowri N, Mehlis A, Hengge R. 2008. Inverse regulatory coordination of motility and curli-mediated adhesion in Escherichia coli. Genes Dev 22:2434-46.

255. Weber H, Pesavento C, Possling A, Tischendorf G, Hengge R. 2006. Cyclic-di-GMP-mediated signalling within the sigma network of Escherichia coli. Mol Microbiol 62:1014-34.

256. Lahiri T, Luan B, Raleigh DP, Boon EM. 2014. A structural basis for the regulation of an H-NOX-associated cyclic-di-GMP synthase/phosphodiesterase enzyme by nitric oxide-bound H-NOX. Biochemistry 53:2126-35.

257. Hagan EC, Mobley HL. 2007. Uropathogenic Escherichia coli outer membrane antigens expressed during urinary tract infection. Infect Immun 75:3941-9.

258. Lenn T, Leake MC. 2016. Single-molecule studies of the dynamics and interactions of bacterial OXPHOS complexes. Biochim Biophys Acta 1857:224-31.

259. Llorente-Garcia I, Lenn T, Erhardt H, Harriman OL, Liu LN, Robson A, Chiu SW, Matthews S, Willis NJ, Bray CD, Lee SH, Shin JY, Bustamante C, Liphardt J, Friedrich T, Mullineaux CW, Leake MC. 2014. Single-molecule in vivo imaging of bacterial respiratory complexes indicates delocalized oxidative phosphorylation. Biochim Biophys Acta 1837:811-24.

260. Lenn T, Leake MC, Mullineaux CW. 2008. Clustering and dynamics of cytochrome bd-I complexes in the Escherichia coli plasma membrane in vivo. Mol Microbiol 70:1397-407.

261. Sarenko O, Klauck G, Wilke FM, Pfiffer V, Richter AM, Herbst S, Kaever V, Hengge R. 2017. More than Enzymes That Make or Break Cyclic Di-GMP-Local Signaling in the Interactome of GGDEF/EAL Domain Proteins of. MBio 8.

262. Hengge R, Gründling A, Jenal U, Ryan R, Yildiz F. 2016. Bacterial Signal Transduction by Cyclic Di-GMP and Other Nucleotide Second Messengers. J Bacteriol 198:15-26.